

# **Diffusive properties of the system water/ethanol/triethylene glycol in microgravity and ground conditions**

**Von der Universität Bayreuth  
zur Erlangung des Grades eines  
Doktors der Naturwissenschaften (Dr. rer. nat.)  
genehmigte Abhandlung**

von

**Thomas Triller**

geboren in Hof (Saale)

am 28.11.1986

1. Gutachter: Prof. Dr. Werner Köhler
2. Gutachter: Prof. Dr. Matthias Weiß

Tag der Einreichung: 03.05.2018  
Tag des Kolloquiums: 23.07.2018



Meinen Großeltern





# Abstract

Thermodiffusion (also called Ludwig-Soret effect) describes the diffusive motion of molecules due to a temperature gradient and is a typical example of cross-coupling between fluxes in non-equilibrium thermodynamics. Experiments in liquids typically revolve around applying a temperature gradient to a sample and monitoring the concentration changes from the resulting demixing. Since such additional fluxes in a non-isothermal liquid bulk can easily lead to gravitational instabilities (convection), measurement of the effect on ground is not always easily possible. Careful experiment design can prevent such instabilities in some cases, but slow advective fluxes are not necessarily detectable in a measurement and can lead to erroneous data. The best option for reliable data is to completely suppress gravitational effects by measuring in microgravity, i.e. aboard the International Space Station. The “Diffusion and thermodiffusion Coefficients Measurements in ternary mIXtures” (DCMIX) project is an international collaboration between ESA and several research teams to further the understanding of thermo-diffusive processes in ternary liquid mixtures. It tries to compile reference data for different classes of molecular mixtures in microgravity via phase-shifting interferometry, utilizing the Selectable Optical Diagnostics Instrument (SODI) aboard the space station.

This work presents results obtained from the DCMIX3 campaign, investigating the system water/ethanol/triethylene glycol; the preparations, operations and data evaluation are described in detail. Processing of the SODI interferograms has first been implemented and tested on DCMIX1 data, which is compared to results from other DCMIX teams and literature. A special focus is laid on the error propagation in the data; since optical methods detect concentration changes in a sample via refractive index measurements, thermophysical data of the sample (so-called contrast factors) are necessary for this conversion. In ternary mixtures, this involves the inversion of a numerically ill-conditioned matrix, which leads to more complexity in the interpretation of results compared to the binary case. The experience from DCMIX1 is then applied to data evaluation of DCMIX3, which comprises the first analysis of microgravity data in the system water/ethanol/triethylene glycol. Additionally, ground-measurements have been performed with Optical Beam Deflection (OBD), including the necessary contrast factor measurements. This allows for a direct comparison between microgravity and ground results.



# Kurzdarstellung

Thermodiffusion (auch Ludwig-Soret Effekt genannt) beschreibt die diffusive Bewegung von Molekülen aufgrund eines Temperaturgradienten und ist ein typisches Beispiel für Kreuz-Kopplungen von Flüssen innerhalb der Nichtgleichgewichtsthermodynamik. Die zugehörigen Experimente in Flüssigkeiten basieren darauf, dass einer Probe ein Temperaturgradient aufgeprägt wird und man die Konzentrationsänderungen durch die entstehende Entmischung beobachtet. Da diese zusätzlichen Flüsse innerhalb einer nicht-isothermen Flüssigkeit leicht zu Instabilitäten innerhalb des Schwerfelds der Erde (Konvektion) führen können, ist die Messung des Effekts am Boden nicht immer problemlos möglich. Eine entsprechend sorgfältige Planung von Experimenten kann solche Instabilitäten in manchen Fällen verhindern, aber langsame advective Flüsse sind nicht zwingend in einer Messung erkennbar und können zu verfälschten Ergebnissen führen. Daher ist die beste Option, um verlässliche Daten zu erhalten, Gravitations-Effekte durch Messungen in Mikrogravitation, insbesondere auf der Internationalen Raumstation, komplett auszuschalten. Das "Diffusion and thermodiffusion Coefficients Measurements in ternary mIXtures" (DCMIX) Projekt ist eine internationale Kollaboration zwischen der ESA und mehreren Forschungsgruppen, dessen Ziel es ist das Verständnis von thermodiffusiven Prozessen in ternären Flüssigkeitsmischungen zu fördern. Es versucht Referenz-Daten zu verschiedenen molekularen Mischungen in Mikrogravitation durch Phasenverschiebungs-Interferometrie zu sammeln; dazu wird das Selectable Optical Diagnostics Instrument (SODI) auf der Raumstation verwendet.

Diese Arbeit präsentiert Ergebnisse, die im Rahmen der DCMIX3 Kampagne im System Wasser/Ethanol/Triethylenglycol gesammelt wurden; es werden sowohl Vorbereitung und Durchführung der Messungen als auch die Datenauswertung detailliert beschrieben. Die Auswertung der SODI Interferogramme wurde zuerst für DCMIX1 Daten implementiert und getestet, welche mit Ergebnissen anderer DCMIX Teams als auch Literatur verglichen werden. Besonderes Augenmerk wird dabei auf die Fehlerfortpflanzung in der Analyse gelegt; da optische Experimente Konzentrationsänderungen über Brechungsindex-Messungen detektieren, werden für die Umrechnung thermophysikalische Eigenschaften der Probe (sogenannte Kontrast-Faktoren) benötigt. In ternären Mischungen muss dazu eine numerisch schlecht konditionierte Matrix invertiert werden, was zu mehr Komplexität bei der Interpretation der Ergebnisse führt, besonders im Vergleich mit dem binären Fall. Die Erfahrungen aus DCMIX1 werden bei der Auswertung von DCMIX3 angewandt, welche die erste Analyse von Mikrogravitations-Daten im System Wasser/Ethanol/Triethylenglycol darstellt. Zusätzlich wurden Boden-

Messungen mittels Optical Beam Deflection (OBD) durchgeführt, inklusive der notwendigen Kontrast-Faktor Messungen. Dies erlaubt einen direkten Vergleich zwischen Ergebnissen aus Mikrogravations- und Boden-Messungen.

# Contents

<b>Abstract</b>	<b>i</b>
<b>Kurzdarstellung</b>	<b>iii</b>
<b>1 Introduction</b>	<b>1</b>
<b>2 Thermodiffusion in Ternary Liquids</b>	<b>5</b>
2.1 Experiments in Multi-Component Mixtures . . . . .	5
2.1.1 Phenomenological Equations . . . . .	5
2.1.2 Quasi-Stationary State . . . . .	9
2.1.3 Diffusion Equation . . . . .	9
2.2 Optical Methods . . . . .	12
2.3 Need for Microgravity Data . . . . .	15
<b>3 The DCMIX Project</b>	<b>19</b>
3.1 DCMIX1 . . . . .	21
3.2 DCMIX2 . . . . .	24
3.3 DCMIX3 . . . . .	24
3.3.1 DCMIX3a . . . . .	25
3.3.2 DCMIX3b . . . . .	28
3.3.3 Sample Preparation . . . . .	28
3.3.4 Cell Filling . . . . .	32
3.3.5 Operations on the ISS . . . . .	33
3.4 DCMIX4 . . . . .	40
<b>4 Experimental Methods</b>	<b>43</b>
4.1 Optical Beam Deflection . . . . .	43
4.1.1 Setup . . . . .	43
4.1.2 Dimensionless Analysis . . . . .	48
4.2 Contrast Factor Measurements . . . . .	52
4.2.1 Solutal Contrast Factor . . . . .	52
4.2.2 Thermal Contrast Factor . . . . .	53
4.2.3 Refractive Index Parametrization . . . . .	55
4.3 Selectable Optical Diagnostics Instrument . . . . .	55
4.3.1 Components . . . . .	55
4.3.2 Phase-Shifting Interferometry . . . . .	58
4.3.3 Phase-Shifting Interferometry in the Case of SODI . . . . .	64

4.3.4	Dimensionless Analysis . . . . .	69
<b>5</b>	<b>Results and Discussion</b>	<b>73</b>
5.1	DCMIX1 . . . . .	73
5.1.1	Contrast Factors . . . . .	73
5.1.2	SODI-DCMIX1 . . . . .	77
5.1.3	Comparison Microgravity and Ground Results . . . . .	85
5.2	DCMIX3 . . . . .	96
5.2.1	Contrast Factors . . . . .	96
5.2.2	Optical Beam Deflection . . . . .	101
5.2.3	SODI-DCMIX3 . . . . .	105
5.2.4	Comparison Microgravity and Ground Results . . . . .	115
<b>6</b>	<b>Summary and Conclusions</b>	<b>123</b>
<b>A</b>	<b>Thermophysical Data</b>	<b>127</b>
<b>B</b>	<b>Fit Coefficients</b>	<b>139</b>
<b>C</b>	<b>Parametrization</b>	<b>143</b>
<b>D</b>	<b>Software and Sources</b>	<b>147</b>
D.1	Plots . . . . .	147
D.2	Data Analysis . . . . .	147
D.3	Source Paths . . . . .	148
D.3.1	Software . . . . .	148
D.3.2	Data . . . . .	148
	<b>Bibliography</b>	<b>149</b>
	<b>List of Publications &amp; Funding</b>	<b>161</b>
	<b>List of Acronyms</b>	<b>163</b>
	<b>List of Figures</b>	<b>165</b>
	<b>List of Tables</b>	<b>167</b>
	<b>Acknowledgments</b>	<b>169</b>

# 1 Introduction

Diffusive motion of molecules in a gradient of chemical potential is a well studied process and has already been described by Fick in the 19th century [1]. Still, diffusive processes in multi-component systems are non-trivial and can have many counter-intuitive effects: when looking at different molecule species, cross-coupling between the fluxes leads to movements not only driven by the gradient in the component itself but also in all other components. Furthermore, gradients in other state variables (temperature, electrical potential etc.) can also cross-couple and drive fluxes, e.g., heat flux due to electrical voltage (thermoelectric effect) [2]. Such effects have been studied extensively at the beginning of the 20th century, with the works of Onsager, Meixner, de Groot, Prigogine and others laying the foundations of non-equilibrium thermodynamics and the description of irreversible processes [3]. While these theories offer a phenomenological description of the macroscopic fluxes, the underlying microscopic forces driving these fluxes are still not well understood in some cases. This is especially true for thermodiffusion (or Ludwig-Soret effect), which was first described by Karl Ludwig and Charles Soret in the 19th century as a diffusive mass flux due to a gradient in temperature [4, 5]. Over the years, the importance of this effect has been established in a variety of systems, e.g. biochemical reactions [6], thermohaline circulation in the oceans [7], stratification in crude-oil reservoirs [8] and many more [9]. While simple kinetic models are available for gases, no comprehensive microscopic theory for thermodiffusion in liquids is available. Therefore, to gain a quantitative understanding for mixtures of different molecule species, extensive experimental studies are necessary.

Over the course of the last decades, focus was almost exclusively on binary mixtures and different experimental techniques have been devised for measuring thermodiffusive effects. In-situ methods rely mainly on optical detection mechanisms, utilizing the local changes of refractive index resulting from concentration changes. One example of this is Optical Beam Deflection (OBD), in which a light beam passes through a transparent sample and its position is detected on a line camera. As soon as (thermo)diffusive fluxes are induced in the sample, a refractive index gradient is established and the beam is deflected. Since an analytical connection between the amount of deflection and the diffusive quantities of the sample can be found, this offers a way to measure (thermo)diffusion in different systems, as long as their refractive index change is large enough (often referred to as contrast factor). Another optical method is Thermal Diffusion Forced Rayleigh Scattering (TDFRS): via holography, a laser-light grating is created inside a sample. Due to absorption (mostly enhanced by added dye), a temperature modula-

tion inside the sample is established, driving the Soret effect and in turn creating a local refractive index modulation. The detectable quantity is then the diffraction efficiency of this refractive index grating, leading to a similar description as in the case of OBD. Still another example is Optical Digital Interferometry (ODI), which visualizes refractive index changes directly via phase-stepping interferometry. Apart from such optical methods, a different class of experiments is based on convective coupling, with the most important example being the so-called Thermo-Gravitational Column (TGC). As the name implies, a column (aligned vertically) is filled with the liquid mixture under study and a horizontal temperature gradient is applied, leading to convection. Now, since the Soret effect drives a demixing along the temperature gradient, different components are advected differently along the column, which leads to a stratification of the sample in vertical direction. Via ports in different heights of the column, small quantities of the sample can be extracted and analyzed ex-situ. From the concentration of the sample along the height (determined e.g. via refractive index and density measurements), the thermodiffusion coefficient can then be deduced.

Even though such experiments have proven successful in binary mixtures, to reach an understanding in real-world processes, multi-component mixtures and the resulting cross-couplings have to be considered. Of course, such a drastic increase in complexity makes quantitative experiments much more difficult; so, as a first step to more realistic cases, study of ternary systems has increased in the last years, since these already display multi-component behaviour while still being manageable. But first measurements proved problematic: for one, agreement between the different techniques was only marginal. Also, gravitational instabilities cannot be excluded in all cases, due to cross-diffusion and possibly destabilizing effects of the denser component migrating anti-parallel to the temperature gradient; in the worst case, such effects can lead to wrong data. These problems led to benchmarking efforts in order to provide reliable reference data and validate experimental techniques. The arguably most important of these collaborations in recent years has been the DCMIX project, in which teams from different nations are working with ESA and Roscosmos to measure ternary liquid mixtures aboard the International Space Station. Utilizing a phase-stepping interferometer (SODI), different ternary model systems are analyzed and compared with accompanying ground-measurements. Starting in 2011, already two DCMIX campaigns have been performed, generating data for the systems tetralin/*n*-dodecane/*iso*-butylbenzene and toluene/methanol/cyclohexane. The third campaign DCMIX3 focuses on the aqueous system water/ethanol/triethylene glycol and was scheduled for 2014, but, unfortunately, a failure of the launch vehicle destroyed the first samples. After a delay of two years, the measurements could finally be performed in 2016.

This work now presents the first analysis of the data gathered during DCMIX3, juxtaposing them to measurements performed with OBD on ground and, where possible, literature data. It is structured as follows: in Chapter 2, the general phenomenological description of multi-component systems will be recapitulated and



---

the underlying principles of optical methods in ternary systems explained. Furthermore, the need for microgravity data will be formulated in more detail. Chapter 3 gives an overview of the DCMIX project; since the author was part of the team responsible for preparations and operations of DCMIX3, these will be described in detail. Chapter 4 explains the experimental setups relevant for this work, OBD and SODI with focus on the dimensionless analysis first proposed by Gebhardt and Köhler. Finally, Chapter 5 summarizes the results. Since the implemented analysis for SODI was first tested on DCMIX1 data, this is presented first, comparing it to results from other teams and literature data. This allows to demonstrate the capability of the proposed method, as well as to discuss the asymmetric nature of error-propagation, due to the numerical ill-conditioning of the so-called contrast factors. After that, the results from SODI and OBD measurements in the DCMIX3 system, as well as contrast factor measurements necessary for interpretation, conclude the work; this represents the first comparison of diffusive properties of the system water/ethanol/triethylene glycol under microgravity and ground conditions.



## 2 Thermodiffusion in Ternary Liquids

This chapter will recapitulate some basic principles regarding thermodiffusion in liquids, with focus on ternary and higher multi-component mixtures. Since the phenomenological equations and their foundation in non-equilibrium thermodynamics is well documented in the literature [2, 10, 11] and other theses [12, 13], in the first section only important results will be summarized. With the governing equations of Optical Beam Deflection relying on the solution of the dimensionless diffusion equations [14, 15], this will also be presented to form the basis for the discussions about the measured signal in Section 4.1, as well as the evaluation of microgravity data chosen for this work. The second section will then focus on important aspects of optical methods for the measurement of thermodiffusive quantities, as they relate to this work. Especially the transformation between refractive index space, in which measurements are performed, and concentration space, in which the quantities of interest are defined, will be discussed. Since this poses a numerically ill-conditioned problem, the implications for optical methods are far-reaching and much work in the literature is devoted to this challenging task [15–17]. The last section will make the argument for microgravity measurements, as the implications of multi-component effects can be subtle and a clear understanding of limitations with ground-based measurements is necessary to gain insights to mixtures with more than two components.

### 2.1 Experiments in Multi-Component Mixtures

#### 2.1.1 Phenomenological Equations

When an initially homogeneous mixture of two (or more) different kinds of molecules is subjected to an external temperature gradient, one can observe a mass flux inside the bulk arising. The simplest description of this (thermo)diffusive mass transport is an extension of Fick's first law of diffusion for a binary mixture,

$$\underline{j} = -\rho D \underline{\nabla} c - \rho D_T c (1 - c) \underline{\nabla} T. \quad (2.1)$$

This describes the 3-dimensional mass flux  $\underline{j}$  of one independent component with mass fraction  $c$  (the other one is fixed due to conservation of mass  $\sum_k c_k = 1$ ), with  $D$  being the diffusion coefficient and  $D_T$  the thermodiffusion coefficient of this

component.  $\rho$  is the average density of the mixture. Since the frame of reference is important when describing fluxes, it shall be noted that here the velocity of the center of mass is taken as reference [18]. Equation (2.1) is a phenomenological description, which has first been derived in this form by Charles Soret in 1879 [5] and is still used today. What his experiments, along with those performed by Karl Ludwig some years earlier [4], had shown was that not only a gradient in the component concentration (i.e. differences in chemical potential) leads to a force on the molecules (known as Fickian diffusion), but also an external temperature gradient can act as a thermodynamic force for mass diffusion. Of course, binary mixtures are the simplest case to study, so a more general description has to consider the  $K$ -component case (with a total  $K - 1$  of independent components):

$$\underline{j}_i = -\rho \sum_{k=1}^{K-1} D_{ik} \underline{\nabla} c_k - \rho D'_{T,i} \underline{\nabla} T \quad (2.2)$$

Here,  $\underline{j}_i$  is the mass flux of component  $i$ . For this work, the ternary case ( $K = 3$ ) is the most relevant one:

$$\begin{pmatrix} j_1 \\ j_2 \end{pmatrix} = -\rho \begin{pmatrix} D_{11} \underline{\nabla} c_1 + D_{12} \underline{\nabla} c_2 + D'_{T,1} \underline{\nabla} T \\ D_{21} \underline{\nabla} c_1 + D_{22} \underline{\nabla} c_2 + D'_{T,2} \underline{\nabla} T \end{pmatrix}. \quad (2.3)$$

Looking at the problem as a set of vectors in the space of independent concentrations  $c_k$ , it is obvious that every component has a unique thermodiffusion coefficient  $D'_{T,i}$ , driven by the same temperature gradient  $\underline{\nabla} T$ . The prime denotes that the concentration dependent factor, which was written as  $c(1-c)$  in Eq. (2.1) and is much more complicated in the multi-component case, is subsumed into the definition of the thermodiffusion coefficient. However, since the concentration gradient is now a vector itself, diffusion is no longer describable by a single coefficient, but by a  $(K - 1) \times (K - 1)$  matrix  $D_{ik}$ . The diagonal terms of the matrix ( $k = i$ ) still describe Fickian diffusion, so a mass flux in component  $i$  due to a concentration gradient in the same component. But the off-diagonal terms ( $k \neq i$ ) incorporate a new effect, not present in binary mixtures: fluxes of component  $i$  due to a gradient of component  $k$ , the so-called multi-component diffusion, which is sometimes described in the framework of the Stefan-Maxwell equations [11, 19]. This introduces considerably more complexity than in the binary case, since cross-effects lead to (at first glance) counter-intuitive behaviour. As visualized in Fig. 2.1, e.g. a diffusion barrier can hinder a mass flux of component  $i$ , even though a gradient in that component exists, while inverse diffusion changes the direction of the mass flux into the gradient direction. Inversely, osmotic diffusion leads to a mass flux even in absence of a gradient, driven only by gradients in the other components [10].

Theoretical treatments of (thermo)diffusion are rooted in (linear) non-equilibrium thermodynamics, which looks at systems that are globally out of equilibrium, but can be assumed to be in local equilibrium states. An important trait of Eq. (2.2),

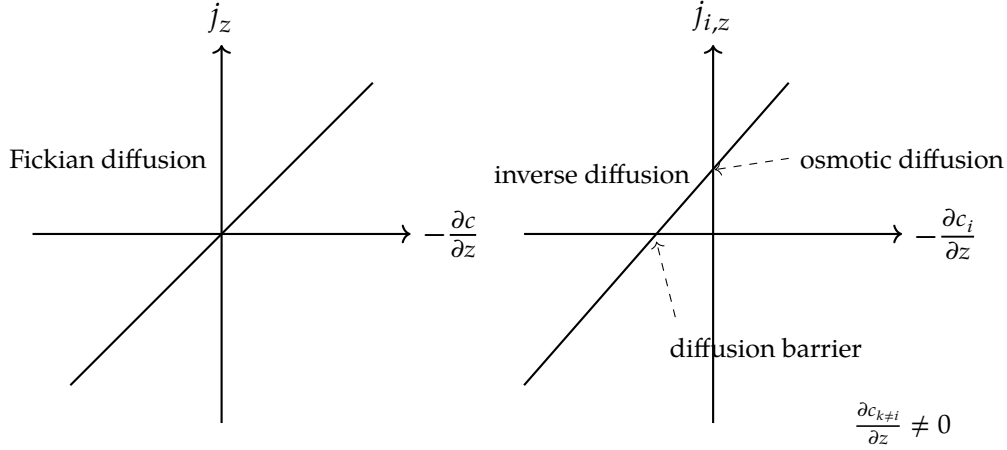


**Figure 2.1:** A simple visualization of the different diffusive behaviours in binary (left) and multi-component mixtures (right), analogous to a similar drawing in [10]. For simplicity, only the spatial components in  $z$ -direction are shown, for an arbitrary mixture component  $i$ . What is important to note is that in the multi-component case new effects arise, not present in the binary case.

and consequently Eqs. (2.1) and (2.3), is that they appear in a form shared by all phenomenological equations describing molecular transport phenomena; they represent a linear relationship between a flux and a thermodynamic force:

$$J_i = \sum_k L_{ik} X_k. \quad (2.4)$$

$J_i$  are the generalized fluxes (i.e. heat or mass),  $X_k$  the thermodynamic forces (i.e. gradients in temperature or chemical potential) and  $L_{ik}$  are the so-called *phenomenological coefficients*, or *Onsager coefficients*. The set of equations (2.4) are also often described as *linear equations of irreversible processes*. When looking at the internal entropy production  $\sigma$  of the system, this takes the form

$$\sigma = \sum_i J_i \cdot X_i \geq 0, \quad (2.5)$$

due to the second law of thermodynamics. Equation (2.5) is sometimes called the *dissipation function* [3]. Inserting expression (2.4) into Eq. (2.5),

$$\sigma = \sum_{i,k} L_{ik} X_i \cdot X_k \geq 0, \quad (2.6)$$

allows to make statements about properties of the Onsager coefficients  $L$ , since the thermodynamic forces appear in a quadratic term. The matrix  $L$  has to be positive-definite; also Onsager showed that  $L_{ik} = L_{ki}$  due to symmetry under time-reversal [20, 21]. For this symmetry, the name *Onsager reciprocal relations* is often used in the literature and Onsager received the Nobel price in 1968 for this work.

But it is also important to note that different constraints apply when looking at the diffusion coefficients, which are defined from the Onsager coefficients via

$$D_{ik} = \sum_{j=1}^{K-1} L_{ij} G_{jk}, \quad (2.7)$$

where  $G$  is the Hessian matrix of the Gibbs free energy [2]; so the diffusion coefficient matrix can be split into a kinetic ( $L$ ) and a thermodynamic part ( $G$ ). Explicitly,

$$D_{ik} = \frac{1}{\rho T} \sum_{j,l=1}^{K-1} L_{ij} \left( \delta_{jl} + \frac{c_l}{c_K} \right) \left( \frac{\partial \mu_l}{\partial c_k} \right)_{p,T}, \quad (2.8)$$

with  $\delta_{jl}$  the Kronecker delta and  $\mu_l$  the chemical potential per unit mass of component  $l$ . Even though the diffusion coefficients in binary systems have to be positive, no such necessity follows for the diagonal elements  $D_{ii}$  in the multi-component case; they can indeed have negative signs. Also, the diffusion matrix is not necessarily symmetric. The properties of the diffusion matrix in a thermodynamically stable system, based on literature [18, 22, 23], can be summarized as

- $\sum_{i=1}^{K-1} D_{ii} > 0$
- $\det(D) > 0$
- $\left( \sum_{i=1}^{K-1} D_{ii} \right)^2 - 4 \det(D) > 0$
- $\hat{D}_i > 0, \quad i = 1, \dots, K-1$

with  $\hat{D}_i$  being the eigenvalues of the diffusion matrix. It should be noted that Ref. [23] discusses some examples of complex eigenvalues in hydrocarbon and aqueous liquid mixtures, but for most examples the reported accuracies of the diffusion matrix could also allow for real eigenvalues. Due to these properties, multi-component diffusion coefficients can generally not be compared with binary diffusion coefficients, especially since multi-component coefficients are dependent on the choice of reference frame and the independent concentrations. Only the eigenvalues of the diffusion matrix are invariant to transformations and therefore comparable to the binary coefficients.

The thermodiffusion coefficients are related to the Onsager coefficients via

$$D'_{T,i} = \frac{L_{iq}}{\rho T^2}, \quad (2.9)$$

where  $L_{iq}$  are the Onsager coefficients coupling the heat flux (driven by the external temperature gradient) to a mass flux of component  $i$ . This makes it obvious, that Eqs. (2.4) allow for cross-effects between all fluxes. Conversely, the Dufour effect (described by the coefficient  $L_{qi}$ ) is the transport of heat due to gradients in

the concentration (and mostly neglected in liquids). Another example for this includes the Peltier effect (heat flux due to voltage differences) and the Seebeck effect (electrical currents due to temperature differences). Due to Eq. (2.9), it is clear that  $D'_{T,i}$  can be negative or positive, meaning that molecules can move either parallel or anti-parallel to the imposed temperature gradient.

### 2.1.2 Quasi-Stationary State

When looking at the long-term evolution of a system driven by an external temperature gradient, since Fickian diffusion tries to equilibrate any concentration differences, while thermodiffusion is a forced demixing, most systems will achieve a quasi-stationary state on sufficiently long timescales. This means, that all mass fluxes die off ( $j_i = 0 \forall i$ ) and constant concentration gradients  $\nabla c_{\infty,i}$  will establish across the system. The magnitude of these gradients is directly coupled to the external temperature gradient via

$$\Delta c_{\infty,i} = -S'_{T,i} \Delta T, \quad (2.10)$$

with the proportionality constant  $S'_{T,i}$ , also called *Soret coefficient*. The prime again denotes the subsumption of a concentration-dependent factor into the definition of the coefficient, resulting from the relation to  $D'_T$ :

$$S'_{T,i} = \sum_k^{K-1} (D)_{ik}^{-1} D'_{T,k}. \quad (2.11)$$

Just as the diffusion coefficients  $D_{ik}$  and  $D'_{T,i}$ , the Soret coefficients  $S'_{T,i}$  are a property of the specific mixture under investigation, and their precise determination is one of the aims of quantitative studies. An illustrative interpretation of  $S'_T$  is to look at it as a measure of the amount of demixing achievable in a specific mixture, when a constant temperature gradient is applied, since it is defined as the ratio of a demixing effect  $D'_T$  (thermodiffusion) to a mixing effect  $D$  (diffusion). The same convention as for  $D'_{T,i}$  applies to the Soret coefficient: a negative sign signals parallel movement, a positive sign anti-parallel movement with respect to the temperature gradient (typically with regard to the denser component). Due to conservation of mass, it also follows that

$$\sum_{k=1}^{K-1} S'_{T,k} = 0. \quad (2.12)$$

### 2.1.3 Diffusion Equation

Apart from the quasi-stationary state, to extract the diffusion coefficients  $D_{ik}$  and  $D'_{T,i}$  the time dependent evolution of the system has to be monitored. The general principle for most (optical) experiments investigating this transient evolution

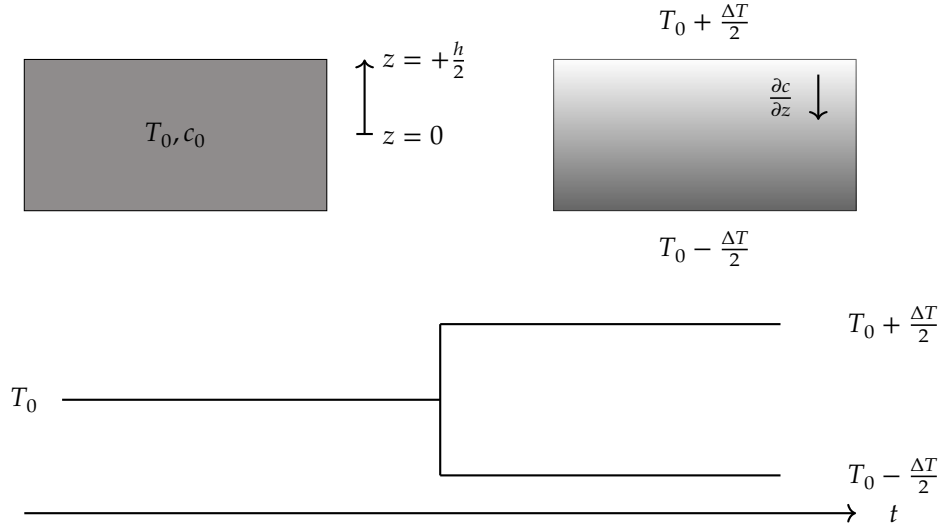


**Figure 2.2:** The general principle of a Soret cell experiment. A parallelepipedic sample volume (height  $h$ , ideally infinite in lateral dimensions) with a liquid mixture is first brought to an equilibrium state (bulk with homogeneous temperature  $T_0$ , concentration  $c_0$ ). Then a Heaviside-like temperature gradient is applied to the sample, monitoring the ensuing transient concentration gradient  $\partial c / \partial z$ .

is sketched in Fig. 2.2. A parallelepipedic sample volume between two materials with high thermal conductivity, also called Soret cell, is subjected to a linear temperature gradient (typically anti-parallel to gravity), modelled after a Heaviside function in the time domain. The system will respond with mass fluxes Eq. (2.2), leading to a time-dependent concentration gradient along the direction of the temperature gradient inside the bulk. Since Eq. (2.4) is a linear relationship, such an experiment is a typical example of linear response theory, with a system reacting linearly to an external driving force.

To find the time-dependence of Eq. (2.2), the appropriate governing equation is the continuity equation

$$\rho \frac{\partial c_i}{\partial t} + \nabla \cdot \underline{j}_i = 0, \quad (2.13)$$

otherwise local conservation of mass would be violated [2, 11]. Inserting Eq. (2.2) into Eq. (2.13) yields a coupled system of differential equations:

$$\frac{\partial c_i}{\partial t} = \sum_{k=1}^{K-1} D_{ik} \nabla^2 c_k + D'_{T,i} \nabla^2 T, \quad (2.14)$$

with  $\nabla^2$  being the Laplace operator. This system of equations has to be solved for the specific boundary conditions applicable in the respective experiments to yield expressions for deducing the diffusion coefficients. For the general case of a parallelepipedic Soret cell with a binary mixture this was already done by Bierlein in 1955 [24], and the resulting equation has been successfully applied for beam deflection experiments [25, 26]. But for ternary mixtures, no such description was



available until 2006, when Haugen and Firoozabadi presented an analytical solution for the multi-component case [14, 27], which will be shortly summarized in the following.

In general, the thermal diffusion is much faster than mass diffusion, meaning that when applying an external linear gradient  $\Delta T$ , it will have stabilized long before substantial demixing occurs. A measure for this timescale separation is the Lewis number

$$Le = \frac{D}{\alpha}, \quad (2.15)$$

which gives the ratio between mass diffusivity  $D$  and thermal diffusivity  $\alpha$ ; typically  $Le \ll 1$  in liquids and  $Le \approx 1$  in gases [11]. Taking  $\nabla^2 T = 0$ , Eq. (2.14) can then be simplified as

$$\frac{\partial c_i}{\partial t} = \sum_{k=1}^{K-1} D_{ik} \nabla^2 c_k. \quad (2.16)$$

An approach to solving such a coupled system of equations is to find a transformation such that the coefficients matrix is diagonalized [18],

$$\frac{\partial C_i}{\partial t} = \sum_{k=1}^{K-1} \hat{D}_{ik} \nabla^2 C_k \quad (2.17)$$

with the transformation matrix  $V$  defined by

$$\sum_{k,l=1}^{K-1} V_{ik}^{-1} D_{kl} V_{lj} = \hat{D}_{ij} \quad (2.18)$$

and

$$C_i = \sum_{k=1}^{K-1} V_{ik}^{-1} c_k. \quad (2.19)$$

$\hat{D}$  contains the eigenvalues of the diffusion matrix  $D$  in the diagonal entries and zero otherwise, therefore decoupling the system. So the diffusion equations have now been transformed into the coordinate system of the eigenvectors of  $D$ . Since the concentration gradients will achieve stationary values  $\Delta C_{\infty,i}$  when approaching the quasi-stationary state, one can normalize the  $C_i$  to these amplitudes

$$\tilde{C}_i = \frac{C_i}{\Delta C_{\infty,i}}. \quad (2.20)$$

Another justified simplification is to only look at concentration changes in  $z$ -direction, assuming a homogeneous temperature gradient solely along the cell height. The position  $z$  can be normalized on the cell height  $h$  and the time  $t$  on the inherent timescales of the involved process:

$$\tilde{z} = \frac{z}{h} \quad (2.21)$$

$$\tilde{t}_i = \frac{t \hat{D}_i}{h^2}. \quad (2.22)$$

This yields a dimensionless form of the diffusion equation:

$$\frac{\partial \tilde{C}_i}{\partial \tilde{t}_i} = \frac{\partial^2 \tilde{C}_i}{\partial \tilde{z}^2}. \quad (2.23)$$

As already mentioned, most experiments can be described via linear response theory, so Eq. (2.23) can be solved via a Green's function approach with the method of images [11]. The general solution to Eq. (2.23) in the case of a parallelepipedic Soret cell is then:

$$\begin{aligned} \tilde{C}_i - \tilde{C}_{i,0} = & \tilde{z} + \frac{1}{2} \sum_{n=-N}^N (\tilde{z} - n)(-1)^n \left[ \operatorname{erf} \left( \frac{2\tilde{z} - 2n - 1}{4\sqrt{\tilde{t}_i}} \right) - \operatorname{erf} \left( \frac{2\tilde{z} - 2n + 1}{4\sqrt{\tilde{t}_i}} \right) \right] + \\ & + \sum_{n=-N}^N (-1)^n \sqrt{\frac{\tilde{t}_i}{\pi}} \left[ \exp \left( -\frac{(2\tilde{z} - 2n - 1)^2}{16\tilde{t}_i} \right) - \exp \left( -\frac{(2\tilde{z} - 2n + 1)^2}{16\tilde{t}_i} \right) \right], \end{aligned} \quad (2.24)$$

with  $\tilde{C}_{i,0}$  the concentration at time  $\tilde{t} = 0$ . The gradient along  $\tilde{z}$  is then given by:

$$\begin{aligned} \frac{\partial \tilde{C}_i}{\partial \tilde{z}} = & 1 + \frac{1}{2} \sum_{n=-N}^N (-1)^n \left[ \operatorname{erf} \left( \frac{2\tilde{z} - 2n - 1}{4\sqrt{\tilde{t}_i}} \right) - \operatorname{erf} \left( \frac{2\tilde{z} - 2n + 1}{4\sqrt{\tilde{t}_i}} \right) \right] + \\ & + \sum_{n=-N}^N (-1)^n \frac{1}{4\sqrt{\pi\tilde{t}_i}} \left[ \exp \left( -\frac{(2\tilde{z} - 2n - 1)^2}{16\tilde{t}_i} \right) + \exp \left( -\frac{(2\tilde{z} - 2n + 1)^2}{16\tilde{t}_i} \right) \right]. \end{aligned} \quad (2.25)$$

Note: the solution is exact for  $N \rightarrow \infty$ , but can be truncated to a finite  $N$  for most cases. Figure 2.3 shows a plot of this analytical solution. For more details, see the relevant works of Haugen and Firoozabadi [14, 27].

## 2.2 Optical Methods

The most straightforward way to measure the concentration gradient inside a Soret cell in situ is by means of optical methods (e.g. Optical Beam Deflection or Thermal Diffusion Forced Rayleigh Scattering), making use of the dependence of the refractive index  $n$  of a liquid on the local concentrations. Additionally,  $n$  is a function of temperature  $T$ , pressure  $p$  and wavelength  $\lambda$  as well:

$$n = n(T, p, \lambda, c_1, c_2, \dots), \quad (2.26)$$

while in the case of a Soret cell, isobaric conditions can be assumed. The quantity of interest is the gradient along the cell height, so

$$\frac{\partial n_\lambda}{\partial z} = \left( \frac{\partial n_\lambda}{\partial T} \right)_{p, c_i} \frac{\partial T}{\partial z} + \sum_{k=1}^{K-1} \left( \frac{\partial n_\lambda}{\partial c_k} \right)_{p, T, c_{j \neq k}} \frac{\partial c_k}{\partial z}, \quad (2.27)$$

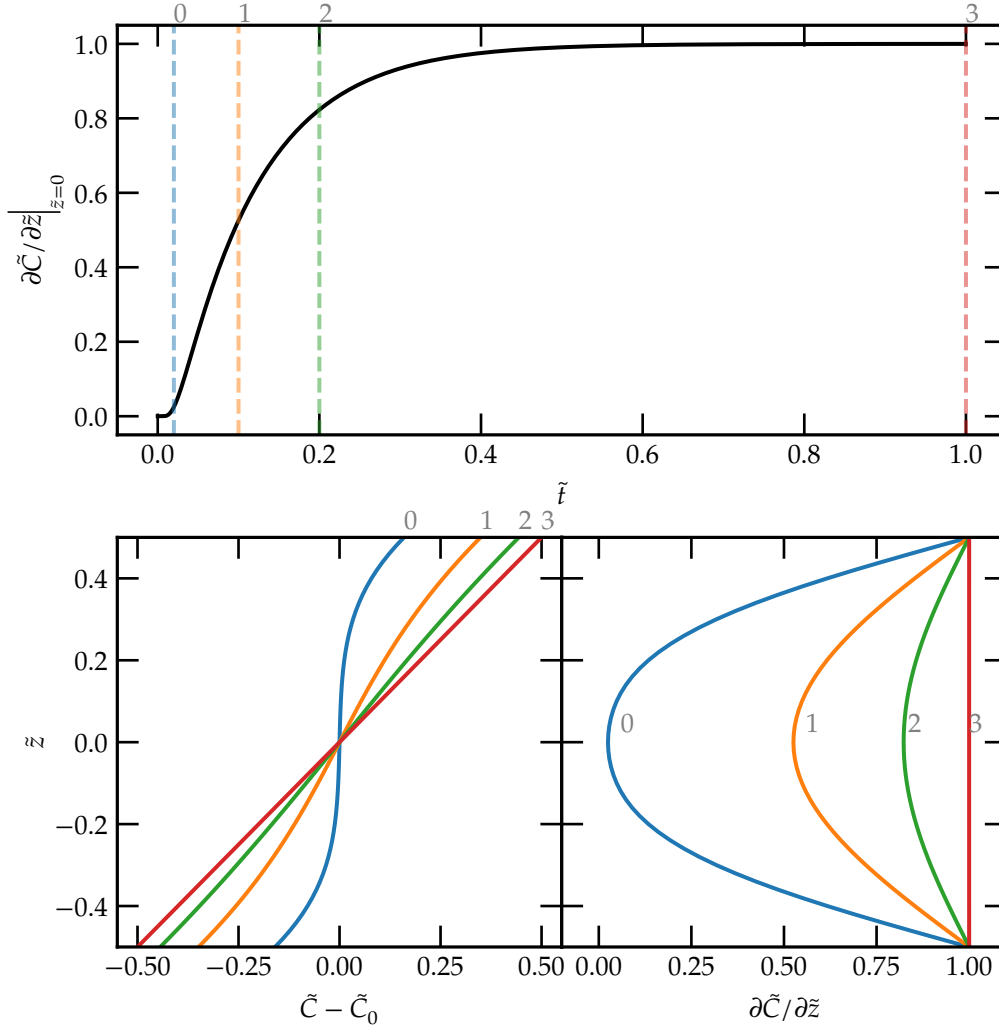


**Figure 2.3:** Top: plot of Eq. (2.25) for  $N = 10$ ,  $\hat{D} = 5 \times 10^{10} \text{ m}^2 \text{ s}^{-1}$  and  $h = 5 \text{ mm}$  (binary case). The dashed lines mark several points in time, for which the concentration difference to  $\tilde{t} = 0$  — Eq. (2.24) — as well the gradient along the cell height are shown in the lower two plots.

where the subscript indicates the dependence on the wavelength. As has been proposed by Haugen and Firoozabadi [14] for the analysis of mixtures with  $K - 1$  components,  $K - 1$  wavelengths can be employed, utilizing the dispersion  $n(\lambda)$  to be able to separate the different concentration contributions. To signal this, we rewrite Eq. (2.27) with a new subscript

$$\frac{\partial n_i}{\partial z} = \left( \frac{\partial n_i}{\partial T} \right)_{p, c_i} \frac{\partial T}{\partial z} + \sum_{k=1}^{K-1} \left( \frac{\partial n_i}{\partial c_k} \right)_{p, T, c_{j \neq k}} \frac{\partial c_k}{\partial z}. \quad (2.28)$$

$n_i$  is the refractive index of the  $i$ -th employed wavelength  $\lambda_i$ . The occurring derivatives  $(\partial n_i / \partial T)_{p, c_i}$  and  $(\partial n_i / \partial c_j)_{p, T, c_{k \neq j}}$  are often referred to as *optical contrast fac-*

tors. They are a thermophysical property of the liquid mixture under investigation and have to be measured separately with high precision, to be able to make the connection between refractive index and concentration gradient in Eq. (2.28) [15–17]. Note: in the rest of this work, the subscripts indicating constant pressure etc. on the contrast factors are mostly omitted for brevity. The temperature gradient  $\partial T / \partial z$  is assumed to be known, since it is a prescribed experimental parameter. Ignoring the temperature contribution for now, we write Eq. (2.28) in matrix-vector notation for a ternary system:

$$\begin{pmatrix} \Delta n_1 \\ \Delta n_2 \end{pmatrix} = \underbrace{\begin{pmatrix} \partial n_1 / \partial c_1 & \partial n_1 / \partial c_2 \\ \partial n_2 / \partial c_1 & \partial n_2 / \partial c_2 \end{pmatrix}}_{N_c} \cdot \begin{pmatrix} \Delta c_1 \\ \Delta c_2 \end{pmatrix}. \quad (2.29)$$

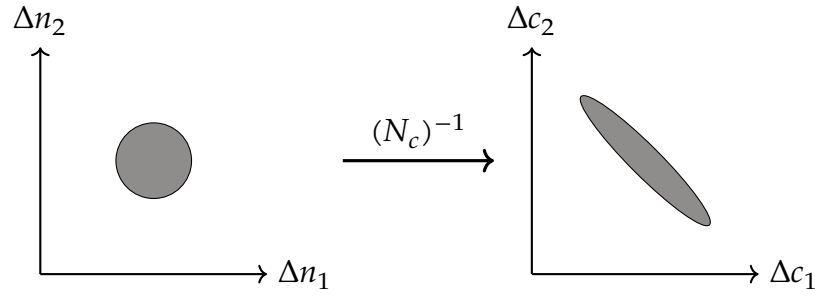


**Figure 2.4:** Visualization of the error propagation through inversion of the contrast factor matrix.

As is obvious from Eq. (2.29), to deduce concentration gradients from optical measurements, the contrast factor matrix  $N_c$  has to be inverted. This is not always possible; and also for some matrices which are in principle invertible, numerical problems might arise in practice. In numerical analysis, such problems are tied to their *conditioning*, or *condition number*, which gives information about the influence of errors in the input on the result of a calculation. In the specific case of matrix inversion, the condition number of a matrix is a measure how small uncertainties in the elements can propagate during inversion. Since the exact determination of contrast factors is non-trivial, this conditioning becomes a major concern for all optical experiments in multi-component systems.

The definition of the condition number of a square matrix  $A$  is given by

$$\text{cond}(A) = \|A\| \cdot \|A^{-1}\|, \quad (2.30)$$

with  $\|A\|$  the norm of the matrix  $A$  [28]. The norm can be defined in different ways, but in this work it will be exclusively defined as  $l_2$ -norm, equivalent to the Euclidean norm for vectors. A condition number of unity indicates that the inversion process can be performed with the same precision as the input data. In contrast, the higher the number, the more the input errors are amplified. Such a

matrix is also described as *ill-conditioned*. Using the  $l_2$ -norm, the condition number can also be defined via

$$\text{cond}(A) = \frac{\sigma_{\max}(A)}{\sigma_{\min}(A)}, \quad (2.31)$$

with  $\sigma_{\max}/\sigma_{\min}$  being the maximum/minimum singular values of a matrix  $A$  [28]. The singular values have a quite apparent geometric meaning: suppose we let matrix  $A$  operate on a unit sphere in two-dimensional space. This operation (excluding the identity matrix) will deform the sphere to an ellipsoid, with the lengths of the principal semiaxes given by the singular values  $\sigma_1$  and  $\sigma_2$ , which leads to an important property of the error propagation of contrast factor matrices: it is inherently asymmetric in concentration space. Figure 2.4 gives a visualization of this: we assume two measured values  $\Delta n_1$  and  $\Delta n_2$  with Gaussian noise. When applying the inversion of the contrast factor matrix to these values, to transform them into values  $\Delta c_1$  and  $\Delta c_2$ , the sphere of possible values in refractive index space is elongated to an ellipsoid shape in concentration space. So the condition number lends itself for the interpretation as the eccentricity of the ellipsoid of possible values in concentration space.

The importance of the condition number of the contrast factor matrix  $N_c$  has already been recognized early in the literature, when optical experiments in ternary mixtures were first discussed [29]. Especially when comparing results from different experiments, each with its unique contrast factor matrix, this cannot be neglected. Even minimal errors in the measured refractive index amplitudes can lead to large asymmetric errors in concentration space. So, a direct comparison of e.g. Soret coefficients in ternary systems can give strongly varying results, possibly effecting misleading interpretations. One way to account for this is by Monte-Carlo simulation, adding noise either to the elements of  $N_c$  or the refractive index amplitudes (see the works of Khlybov [30] and Gebhardt [31] for examples of this approach). This would have the same effect as presented in Fig. 2.4, producing an elliptical shape in the concentration space, which contains possible combinations of coefficients. Since each experiment would have its own ellipsoid of compatible coefficients, a simple interpretation of results offers itself: even though individual values might differ, different experiments are compatible if (and only if) the ellipsoids overlap.

## 2.3 Need for Microgravity Data

One of the tenets of most diffusion experiments is the assumption, that no undesired advective fluxes exist inside the system, so mass transport is only facilitated by diffusive processes. Especially in the case of an external temperature gradient, the possibility of gravitational instabilities has to be considered, since a density gradient anti-parallel to gravitational acceleration  $\underline{g}$  is prone to buoyancy. A first

approach to this problem is to analyze the Rayleigh number,

$$Ra = \frac{g\beta_T\Delta TL^3}{\nu\alpha} \quad (2.32)$$

which gives a measure how influential heat transport via convection is in contrast to conduction for a simple liquid layer, heated between two plates (infinite in lateral dimensions), see also Ref. [32]. Here,  $g$  is the gravitational acceleration,  $\beta_T$  the thermal expansion,  $\Delta T$  the applied temperature gradient,  $L$  the characteristic length scale (height of the liquid layer),  $\nu$  the kinematic viscosity and  $\alpha$  the thermal diffusivity. The critical threshold in a simple liquid is  $Ra = 1708$  [32], marking the transition from mainly conductive heat transport to a convective state. Dependent on the experiment parameters (the external temperature gradient  $\Delta T$  and the layer height  $L$ ), as soon as the Rayleigh number rises above this critical threshold, convection can develop in the cell. So, to reduce the Rayleigh number, one can either measure at lower gradients or reduce the characteristic length. But all the above considerations assume a typical Rayleigh-Bernard configuration with heating from below, so by applying a temperature gradient anti-parallel to the gravitational acceleration (heating from above), convection can be suppressed in a simple liquid even for large values of  $L$  and  $\Delta T$ .

Of course, when studying thermo(diffusion) in a binary mixture, the assumption of a simple liquid no longer applies and a much more complex behaviour arises. Apart from thermal ( $\alpha$ ) and momentum ( $\nu$ ) diffusivity, mass diffusivity ( $D$ ) has to be considered also. This is further complicated by the Soret effect, leading to additional density shifts inside the liquid not effected by thermal expansion. In this case, the so-called solutal Rayleigh number

$$Ra_s = \frac{\Psi}{Le} Ra = -\frac{c(1-c)S_T\beta_c g\Delta TL^3}{\nu D} \quad (2.33)$$

is a new measure for convection onset, with  $\beta_c$  being the solutal expansion coefficient [33];  $\Psi = -\frac{\beta_c}{\beta_T}c(1-c)S_T$  is the so-called separation ratio, describing the ratio between the concentration-induced and the temperature-induced density gradient. If heating from below and  $\Psi > 0$ , the density gradient introduced by thermal expansion is further amplified by the Soret effect (with the denser component migrating to the cold wall), effectively decreasing the critical threshold value [32]; above this new critical value, a stationary instability occurs. Inversely, for  $\Psi < 0$  an oscillatory mode can be found [34]. Due to these different classes of possible instabilities and pattern formation behaviour, binary mixtures with  $\Psi < 0$  (i.e. water/ethanol) have been studied extensively over the years [33, 35–40].

These studies lead to a surprising result: when looking at the situation of heating from above — which is stable in the simple case — binary mixtures can become unstable if  $\Psi < 0$  (see especially Refs. [36–38]). The implications for Soret cell experiments are important: such an instability could be very hard to discern as

such, since the effect on the observed signal is hard to predict. It is indeed imaginable that a shift in the quasi-steady state in Soret measurements, driven by slow advective fluxes, would not be discerned as such, but could lead to wrong values for the Soret coefficients (see Fig. 2.5 for an example).

In the ternary case, even more complexity is induced by the cross-diffusion effects. The stability criteria of ternary and higher-component mixtures, and the accompanying viable parameters spaces, are still subject to active research [41–43]. Of course, a simple way to reduce the Rayleigh number is by reducing the characteristic length or the applied temperature gradient. But even when a safe range of parameters is found, depending on the separation ratio, these parameters might not be easily realized and can severely impact the signal-to-noise ratio of the experiment, as is obvious from Eq. (2.10). Consequently, the best way to validate measurements would be to compare them to reference data that are guaranteed to be free from gravitational instabilities. The only way to achieve this is by performing measurements in microgravity, where no such instabilities can develop, which is currently done in the DCMIX project; this will be presented in the next chapter, as the current work was carried out in the framework of DCMIX3.

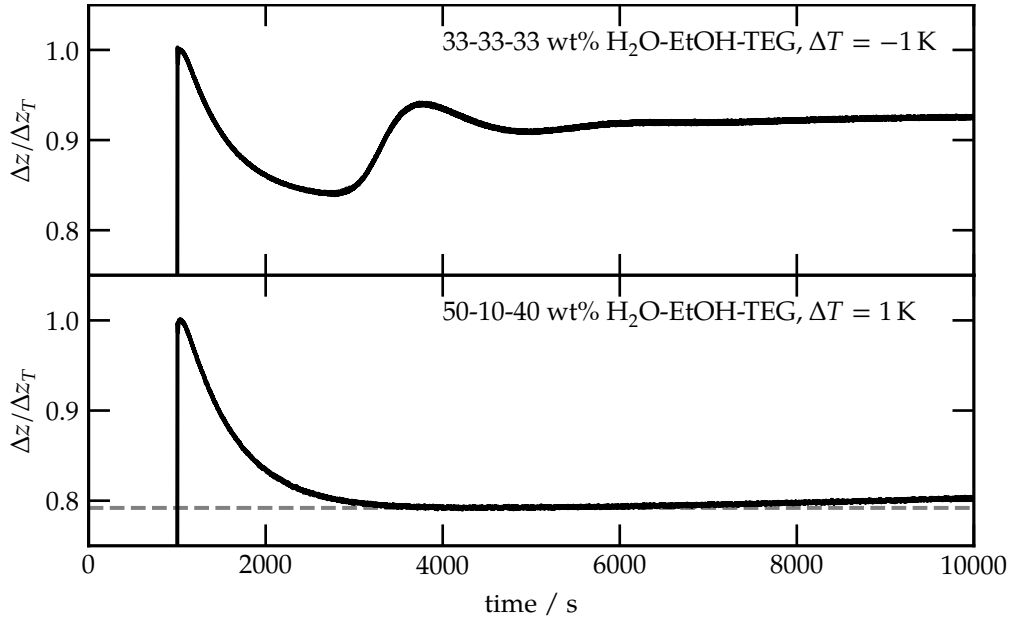


**Figure 2.5:** Examples of instabilities in the DCMIX3-system water, ethanol and triethylene glycol during Optical Beam Deflection experiments (signals are normalized on the thermal amplitude). Top: the equi-mass mixture exhibits an oscillatory mode when heated from below. Bottom: the 50-10-40 wt% mixture can be unstable even when heated from above. This kind of solutal instability can be hard to discern and critically affect ground-based measurements.





### 3 The DCMIX Project

At least since the 1990s, different research teams have intensified their work on thermodiffusive transport in ternary liquids [44]. Due to a missing fundamental theoretical description for multi-component systems, many applications rely on limited molecular dynamics simulations or quantitative experimental studies. But simulations have not yet been able to consistently make predictions for different multi-component mixtures; also, older experimental values on identical systems, even in binary cases, sometimes differ considerably. Therefore, before the jump to multi-component systems can be made, a clear understanding of the performance of different experimental techniques is necessary. To remedy this situation and provide reliable data from different methods for the same liquids, several teams agreed to work simultaneously on a benchmark system and compare their results. This effort has become known as *Fontainebleau* benchmark, named after the location of the initial workshop on the subject, which studied the binary systems of 1,2,3,4-tetrahydronaphthalene (tetralin), n-dodecane and isobutylbenzene at equi-mass fractions and 25 °C. Through this systematic study, sources for errors could be identified and all teams converged to common benchmark values, validating the experimental methods [45–50].

Still, as acknowledged in the *Fontainebleau* benchmark papers, ground experiments struggle with gravity-induced instabilities. As elaborated in Section 2.3, parallel-plate type Soret cells have to be designed carefully to avoid dimensions prone to gravitational convection. These design constraints can in turn influence other experimental parameters, such as the feasible range of temperature gradients. In general, a smaller cell design can help to reduce the possibility of convection onset by reducing the associated Rayleigh number, but there is no guarantee for ground-experiments that convection can always be avoided or, much worse, be discerned as such [36, 37]. Especially in ternary mixtures, the presence of slow advective fluxes could effectively shift the quasi-steady state, without manifesting itself as a deformation of the overall signal shape, therefore not becoming obvious as such. This would lead to the interpretation that no gravitational convection takes place and produce wrong values for diffusive transport coefficients like the Soret coefficients.

Already before the *Fontainebleau* benchmark, some teams formulated ideas for thermodiffusive experiments in microgravity. This would allow to avoid gravitational instabilities altogether, therefore providing guaranteed advection-free reference data, and to validate ground-based experiments. Many platforms for such experiments exist: sounding rocket, drop tower, parabolic flight etc; but microgravity on these persists only for some seconds to minutes, definitely not sufficient

for the timescales involved in thermodiffusive processes. Only the International Space Station (ISS) or unmanned satellites offer such a high-quality microgravity platform as required for thermodiffusion experiments. Simple estimates for the required experiment times are based on the diffusion coefficients:

$$\tau = \frac{L^2}{\pi^2 D} \quad (3.1)$$

with  $L$  the typical lengthscale of the experimental volume and  $D$  the Fickian diffusion coefficient of the studied mixture. Values for  $L$  are in the order of several millimeters, e.g.  $L = 5$  mm. Diffusion coefficients for aqueous mixtures can be estimated as  $D = 5 \times 10^{-10} \text{ m}^2 \text{ s}^{-1}$ , which leads to an experimental timescale of  $\tau \approx 5000$  s, during which ambient conditions should not vary. Two independent proposals were made to ESA for experiments to be carried out on the ISS (AO-2009-858 “Transport phenomena in multicomponent mixtures” and AO-2009-1056 “Diffusion and Thermodiffusion Coefficient Measurements”) [51]. The underlying principle for both relied on optical methods also used in ground-based experiments: the concentration changes introduced due to thermodiffusion inside a parallel-plate Soret cell always lead to changes in the refractive index (see Section 2.2). These refractive index modulations can be visualized in different ways, i.e. an interferometer, and allow to deduce the local concentration changes, which gives a direct way to compute the Soret coefficients. Due to the common goals of the proposals, together with an older proposal (A0-1999-111 “Diffusion and Soret Coefficients Measurement for Improvement of Oil Recovery”), they were combined into the DCMIX project (“Diffusion and thermodiffusion Coefficients Measurements in ternary mIXtures”), which is jointly sponsored by ESA as well as Roscosmos. The experiment itself to be carried out under the DCMIX project was originally designated as “Diffusion and Soret Coefficients measurement” (DSC), a description which can still be found in some documents; but today most literature refers just to DCMIX or SODI-DCMIX [52]. SODI (Selectable Optical Diagnostics Instrument), a Mach-Zehnder type interferometer on the ISS working at two wavelengths (670 nm and 935 nm), was chosen as experiment platform. A modular design allows the placement of different types of measurement cells into the beam, making SODI a flexible instrument suitable for investigations on liquid media, as already proven by the IVIDIL project [29, 53–56] (Influence of VIBrations on DIffusion in LIquids); detailed descriptions of SODI and the cell design can be found in Section 4.3.

The number of participating groups at the start of the project was around a dozen, with researchers from Belgium, Canada, France, Germany, Japan, Russia and Spain; the represented fields range from experimentalists with experience in ground or space research to theoreticians. In general, experiments on the space station require a lot of preparations and experience, so the approach for most proposals is to delegate certain parts (especially regarding engineering and equipment operation) to external service providers or dedicated User Support and Operations Centers (USOC). Scientific supervision of all steps meanwhile resides

with a Principal Investigator (PI), a position which would be rotated through the DCMIX team for the different campaigns. The tasks of a PI include providing necessary documentation for all liquids, the sample preparation and acting as advisor during operations. Furthermore, the preliminary evaluation of the data during and shortly after operations is performed by the PI team, to maximize the scientific value and provide guidelines for future analysis.

Due to the inherent restrictions of microgravity experiments, only a small number of samples could be investigated per campaign. For SODI, a maximum of five different sample cells could be accommodated, so the DCMIX team had to choose five mixtures in the ternary composition space. As already discussed in Section 2.2, optical experiments are always dependent on the refractive index of the sample, or, more explicitly, on the change of refractive index between two compositions. The transformation between refractive index space and composition space is a numerically ill-posed problem, due to the necessary inversion of the contrast factor matrix. To remedy this problem, one can calculate the condition number of this matrix across the composition space and look for global minima of the condition number. Thus the points in concentration space are identified, which are most accessible by optical experiments. This approach was followed in all DCMIX campaigns, with preliminary experiments on ground measuring the contrast factor matrix for the relevant wavelengths. The DCMIX team identified ternary systems representing different classes of liquids (or exhibiting unique properties) to be investigated in up to five measurement campaigns. As of end of 2017, three measurement campaigns could be performed on the ISS: DCMIX1, DCMIX2 and DCMIX3, with preparations for the DCMIX4 measurements already ongoing. The next sections will give a summary of these DCMIX campaigns, with special focus on the DCMIX3 operations, as the group of W. Köhler was designated PI for this campaign, responsible for sample preparation and first evaluation of the data. Additionally, accompanying ground experiments have been performed with the DCMIX3 system utilizing the Optical Beam Deflection technique.

### 3.1 DCMIX1

The choice for DCMIX1 was also tetralin (THN), n-dodecane (nC12) and isobutylbenzene (IBB), as in the Fontainebleau benchmark, because of the experience with this model system. Also, the system is representative for hydrocarbon mixtures as found in oil reservoirs, where hundreds or even thousands of different molecule species undergo thermodiffusive processes, making it a common choice for studies in the oil industry [57]. Furthermore, hydrocarbons form the building blocks for all organic matter, giving it significance in basic research far beyond industry applications. The measurements of DCMIX1 took place at the end of 2011/2012, with the teams of Stefan Van Vaerenbergh (Université Libre de Bruxelles, Belgium) and Ziad Saghir (Ryerson University, Canada) acting as PI. All experiments were defined in a similar pattern as during ground measurements: after a equilibra-

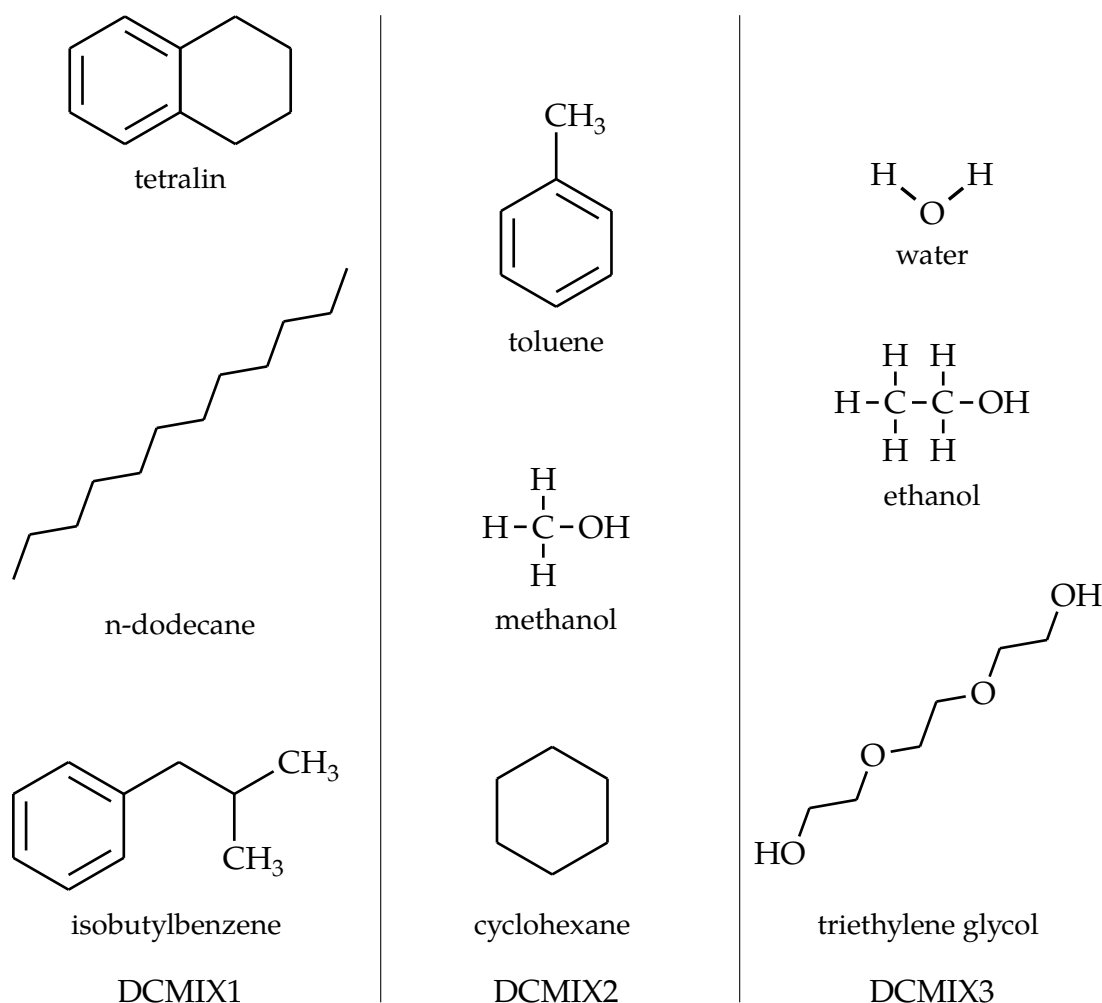


**Figure 3.1:** The molecules for the DCMIX campaigns.

tion phase, to guarantee complete mixing of all components, an almost instantaneous temperature gradient is applied. This gradient is kept constant on a sufficiently long timescale to allow the mixtures to reach a quasi-stationary condition ( $j_i = 0 \forall i$ ). As mean temperatures, 25 °C and 40 °C were chosen, with temperature gradients of  $\Delta T = 10$  K to force the thermodiffusive demixing. From the quasi-stationary state, the reverse experiment is performed: a rapid switching-off of the temperature gradient back to the mean temperature. This allows to observe pure remixing by Fickian diffusion, with no external gradient forced on the system. Overall, DCMIX1 was a success, with good measurements (commonly referred to as “runs”) in all cells at different temperatures, but some problems were identified: for one, a bubble had formed in cell 1 about two weeks after start of the operations (see Fig. 3.2), which narrowed data analysis for this cell to 3 runs at 25 °C and 2 runs at 40 °C. Also, cell 5 showed distinct problems with the regulation of the experimental parameters: the temperature control of the Peltier elements did

not stabilize within the intended limits and exhibited periodic fluctuations. Furthermore, the phase shifting of the laser diodes did not work reliably in this cell. During operations, it was found that these problems could be linked to background tasks being performed on the CPUs responsible for controlling the experiments. By reducing the workload on the processors, the regulation could be improved; but the root cause, as well as why only cell 5 was affected, could not be determined. An important aspect of the work done during DCMIX1 is the comparison and evaluation of analysis methods. To form a reliable data base, analysis methods had to be consolidated and compared; also, expertise on image processing and phase evaluation in the case of SODI had to be acquired. By comparing different techniques from all DCMIX teams, a common theme emerged: even though absolute values might differ, all methods converge to results which are indistinguishable within the contrast factor problem, as formulated in Section 2.2. The Bayreuth team also participated in the analysis of DCMIX1 data, which allowed to lay groundwork necessary to perform the role of PI during DCMIX3. The results of this analysis are presented in Section 5.1.

**Table 3.1:** Compositions for the DCMIX1 cells with components tetralin ( $c_1$ ), isobutylbenzene ( $c_2$ ) and dodecane ( $c_3$ ). All compositions are given as weight fraction.

cell	$c_1$	$c_2$	$c_3$
1	0.10	0.10	0.80
2	0.10	0.80	0.10
3	0.80	0.10	0.10
4	0.45	0.10	0.45
5	0.40	0.20	0.40
6	0.50	—	0.50

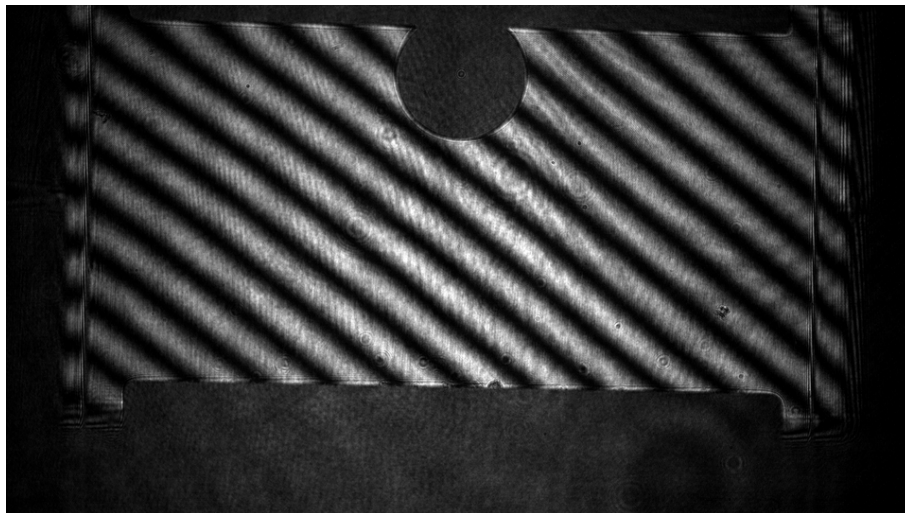


**Figure 3.2:** Bubble in DCMIX1 cell 1 around the 12th of December 2011.

## 3.2 DCMIX2

DCMIX2 focused on the system toluene, methanol and cyclohexane. Even though this is also a hydrocarbon system, DCMIX2 offers some unique properties: a broad miscibility gap exists in the ternary composition space, which allows to study phase separation when approaching this gap, i.e. a slow-down of the mass diffusion at the critical point [58, 59]. Also, the system is hydrodynamically unstable at many compositions, preventing a detailed study on earth [60]. In the timeframe 2012/2013 measurements were again performed in SODI, this time with the team of Valentina Shevtsova (Université Libre de Bruxelles, Belgium) acting as PI. One critical aspect of DCMIX2, which became already apparent during the preparations, was the choice of the sealing material of the cells. During DCMIX1 Viton<sup>®</sup> O-rings were used, but during preparations for DCMIX2 it became obvious that the new chemicals could dissolve in the material. Two alternatives were discussed at that time: Chemraz<sup>®</sup> 505 or Kalrez<sup>®</sup>; since Chemraz<sup>®</sup> was easily available, it was chosen to replace Viton<sup>®</sup>. But in hindsight, Chemraz<sup>®</sup> was not the optimal choice for the seals and already during checkout operations bubble formation could be observed in several cells.

This aggravated during operations and significantly impacted the planned experiments [61]. Even though no Soret measurements could be performed in these cells, some experiments have been made on the bubbles by applying different temperature gradients and mean temperatures. This forced Marangoni convection on the gas-liquid boundary and allowed for some qualitative observations. Also, measurements at different mean temperatures in the bubble-free cell with the binary toluene/cyclohexane mixture allowed to observe the dependence of the Soret coefficient on temperature [62].

**Table 3.2:** Compositions for the DCMIX2 cells with components toluene ( $c_1$ ), methanol ( $c_2$ ) and cyclohexane ( $c_3$ ). All compositions are given as weight fraction.

cell	$c_1$	$c_2$	$c_3$
1	0.25	0.15	0.60
2	0.45	0.15	0.40
3	0.65	0.15	0.20
4	0.20	0.40	0.40
5	0.30	0.30	0.40
6	0.40	—	0.60

## 3.3 DCMIX3

DCMIX3 was performed at the end of 2016 and focused for the first time on aqueous mixtures with water, ethanol and triethylene glycol. Since the role of PI was given to the Bayreuth team of W. Köhler (including the author), the focus of this work will be on these experiments, with the following sections giving an overview over the timeline.

### 3.3.1 DCMIX3a

Preparations for DCMIX3 started in spring 2014, as the PI team had to provide basic thermophysical information about the samples, necessary for risk assessments by NASA and ESA. Since all materials brought to the space station undergo a multitude of environmental extremes during transport, information about freezing/melting points, thermal expansion etc. are vital for flight preparation. Furthermore, all flammable chemicals aboard the space station can be a potential health hazard when leaking from containment, since in an enclosed environment even minimal amounts of liquid can produce dangerous combustions or shortages when in contact with electrical equipment. So, the PI team collected as much information about the liquids water, ethanol and triethylene glycol as possible from literature. For water and ethanol, this was possible without much effort, since these liquids are so common in everyday use. On the other hand, the literature on thermophysical properties of triethylene glycol is much scarcer and sometimes very dated. Therefore, working with lab equipment on hand or easily available from other departments, own measurements on density, melting point and freezing were conducted. Another issue which had to be worked on before any flight hardware could be assembled was the question of suitable sealing materials for the cell array. As experience from DCMIX2 had shown, a hasty choice could lead to significant problems with bubble formation, seriously hindering the operations or, in worst case, preventing planned measurements altogether. Several standard materials like Viton<sup>®</sup> (used in DCMIX1), Chemraz<sup>®</sup> (used in DCMIX2) and Kalrez<sup>®</sup> were considered and had to be tested with the sample liquids. To do this, small samples of the materials were submerged in the three pure liquids for DCMIX3 and weighed in regular intervals to test mass uptake over time. This allowed to draw conclusions about permeation in the different material/liquid combinations and make a choice for the most resilient sealing, maximizing the lifetime of the cell array. These tests showed that Kalrez<sup>®</sup> was superior in every aspect to the alternatives and consequently the appropriate material.

**Table 3.3:** Compositions for the DCMIX3 cells with components water ( $c_1$ ), ethanol ( $c_2$ ) and triethylene glycol ( $c_3$ ). All compositions are given as weight fraction.

cell	$c_1$	$c_2$	$c_3$
1	0.20	0.20	0.60
2	0.33	0.33	0.33
3	0.25	0.60	0.15
4	0.75	0.15	0.10
5	0.50	0.10	0.40
6	0.85	0.15	—

The next step in this phase was then a “breadboard” test: the three most “extreme” liquid mixtures (i.e. on the corners of the composition triangle) were filled into the Engineering Model of the DCMIX3 cell array, sealed and monitored over prolonged time for bubble formation. To do this, the Bayreuth team provided the mixtures to QinetiQ Space n.v., the company responsible for cell array manu-

facturing, which then conducted the breadboard tests. After these tests showed no bubble formation, Kalrez<sup>®</sup> was approved as sealing material and preparations could move forward to the next phase. Since all diffusive quantities of interest in the DCMIX experiments are highly sensitive to the mixture compositions, one of the most critical aspects is the sample preparation. To guarantee the desired compositions, this step was also conducted by the PI team to oversee the procurement and handling of the pure liquids as well as the mixing process itself. Beyond that, the mixed liquids had to be degassed, which was also performed in Bayreuth, since dissolved gases could again pose a danger of bubble formation at any point after cell filling.

After successful completion of all preparations, the DCMIX3 experiments were scheduled to be brought to the International Space Station aboard the automated Cygnus CRS Orb-3 spacecraft on the 28th October 2014. This spacecraft was operated by Orbital Sciences, a US-based launch provider participating in the Commercial Resupply Services (CRS) program, which enlists private companies under the auspices of NASA to provide cargo transportation services to/from the ISS. Orbital Sciences won several transport missions in its bid for CRS, and developed the Antares launch system as well as the Cygnus spacecraft for this purpose.

Launching from the Wallops Flight Facility in Virginia, the company already had made two flights to the space station. Since the development and production of rocket engines requires highly specialized knowledge, Orbital Sciences included engines from a third party for the first stage of the rocket: Aerojet Rocketdyne. The Aerojet Rocketdyne AJ26 engine has some interesting history, since it is refurbished from old Soviet NK-33 engines, which were developed in the 1960s and 1970s to provide propulsion for a possible Soviet rocket to the Moon. Since the Soviet Union lost interest in a mission to the Moon after the American landings, these engines were no longer needed and therefore put into storage until Aerojet Rocketdyne purchased a stockpile and, with significant modifications, repurposed them as AJ26 engines.

Unfortunately, during the launch of Orbital 3, a catastrophic failure of one of the turbopumps in the AJ26 engines lead to the explosion of the spacecraft and the loss of all cargo aboard [63], see Fig. 3.3. Due to the extensive damage during the explosion, the DCMIX3 cell array was considered lost, but during cleanup operations on the launch pad the containers with the DCMIX3 hardware were recovered, showing only minor scorch marks on the outside, as visible in Fig. 3.4. Closer inspection of the hardware showed some damage from impact, either on the ground or with other debris, but the cell array itself was mostly intact with the liquids still inside and free of bubbles. The hard disks for data storage even proofed to be completely undamaged, and could be reused after a re-certification by the vendor. But of course, operations were set back by this incident as a new cell array had to be built (with the old one no longer flight certifiable), new liquids prepared and a new launch opportunity to be found. In the following, all operations up to this point will be referred to as DCMIX3a.





**Figure 3.3:** Explosion of the Antares rocket carrying Cygnus CRS Orb-3 on 28th October 2014. The first DCMIX3 cell array was considered lost in this explosion. (Source: Nasa via <https://www.flickr.com/photos/nasahqphoto/>, CC BY-NC-ND 2.0)



**Figure 3.4:** The hardware of DCMIX3a recovered from the launch pad after the explosion of the Antares rocket (top: flash drives for data storage; bottom: cell array). Except for some fire damage on the stowage bags, the hardware looks undamaged. Only closer inspection revealed structural damage to the cell array, probably from the impact on the ground or collision with debris. The cells itself were not broken and still bubble-free. (Source: courtesy QinetiQ Space)

### 3.3.2 DCMIX3b

Since the damage to the DCMIX3a cell array effected an almost complete loss of hardware, a new cell array had to be built and also financed. After assessment of the situation, ESA consented to take parts originally planned for an upcoming DCMIX4 operation and use them to assemble a new DCMIX3 cell array (now called DCMIX3b). In April 2016, the new cell array was ready and new sample liquids could be prepared in Bayreuth. The process for this was analogous to the DCMIX3a preparations, so general procedures described in the following section also apply to DCMIX3a. All sample preparations took place in the time from 1st April to 13th April 2016 in the laboratories of the University of Bayreuth.

### 3.3.3 Sample Preparation

#### Mixing

To guarantee the desired concentrations and prevent contaminations, dedicated batches of ethanol and triethylene glycol were ordered from commercial suppliers:

- Ethanol Absolute 99.5 %, Extra Dry, AcroSeal® (CAS: 64-17-5) from *Acros Organics* (Lot: 1545382, Product Code: 397690025)
- Triethylene glycol 99 % (CAS: 112-27-6) from *Acros Organics* (Lot: A0364772, Product Code: 139590025)

Water was taken from a *Milli-Q*® water filtration system, which de-ionizes and filters tap water to laboratory quality (resistivity 18.5 MΩ cm, 0.22 μm PAK-filter). The mixing of the samples was done inside *Duran*® Premium bottles (borosilicate glass, capacity 100 mL, retrace code 10067727) with a PTFE screw cap. To weigh the exact amounts of liquid, the bottles were placed on a precision scale (*Sartorius* LC 620 S, MC-1 series, readability 1 mg, capacity 620 mg) and the liquids weighed out into the glasses, starting with triethylene glycol, then water and ethanol at the end. This order was followed to minimize evaporation of the liquids, and therefore concentration shifts, since the vapour pressure of the liquids increases also in this order. All handling of the samples was also done with dedicated equipment: for larger quantities, 20 mL *Brand*® *Silberbrand* AR-glass pipettes were used; smaller quantities were siphoned with 5 mL *BBraun Injekt*® single-use syringes. After the proper amounts were weighed out, the bottles were closed with the PTFE screw caps, wrapped with *Parafilm*® and shaken to ensure a complete mixing of all components. Table 3.4 gives an overview over the weighed out amounts of liquids and the resulting compositions.

#### Degassing

As already mentioned, all samples had to be degassed to prevent any bubble formation after the cell filling, so a freeze-pump-thaw technique was used to remove

any residual gases introduced during mixing. The corresponding setup is shown in Fig. 3.5. As a first step the PTFE screw caps of the bottles had to be replaced with *BOLA* PPS screw caps, equipped with a stopcock, which is necessary to connect the sample with other equipment. The degassing procedure then works as follows: first, the liquid under consideration is flash frozen in liquid nitrogen; after about 20 min, the sample is considered to be completely frozen (see Fig. 3.6). The container is then connected to a vacuum pump via the stopcock to remove any gases not frozen into the bulk. After about 20 min vacuum (below 10 mbar) the stopcock is closed again; the sample is kept under liquid nitrogen during the whole process. The third step is to slowly thaw the frozen sample in a water bath at 25 °C; during this step, bubbles can be seen rising to the surface (see Fig. 3.7). So, this technique works by lowering the partial pressure of the unwanted gases above the sample to zero, which forces gas out of the sample to maintain equilibrium. But since a single iteration is not guaranteed to remove all solved gases, the process is repeated at least three times for every sample. A good indication that the degassing is sufficient is when no bubbles appear during the last thawing step, which was the case for all samples. As last step, all sample bottles were flushed with Helium gas to prevent immediate air contact of the samples when opening them.

Also, as a quality check and reference, thermo-optical properties of all sample liquids were measured before and after degassing. The refractive index at 20 °C was measured with an *Anton Paar* Abbemat WR multi-wavelength refractometer (see Table A.1); the density of the samples was measured with an *Anton Paar* DSA 5000 M density meter (see Table A.2).

### Sample Transport

After the degassing, the samples had to be prepared for transportation, since further processing was done outside of Bayreuth. Therefore, samples had to be filled into *Hamilton* Gastight 1010 TTL syringes (10 mL capacity), to be ready for use af-

**Table 3.4:** The masses of vials and liquids, and resulting sample compositions in weight fraction for all sample cells during the mixing procedure of DCMIX3b.

cell	weight / g					$c_{\text{H}_2\text{O}}$	$c_{\text{EtOH}}$	$c_{\text{TEG}}$
	bottle	water	ethanol	TEG	total			
1	178.524	20.000	19.993	59.931	278.448	0.20015	0.20008	0.59977
2	179.478	33.326	33.350	33.266	279.420	0.33345	0.33370	0.33285
3	177.203	25.023	60.040	15.121	277.387	0.24977	0.59930	0.15093
4	179.460	74.983	14.977	9.971	279.391	0.75035	0.14987	0.09978
5	178.886	49.982	9.984	40.013	278.865	0.49993	0.09986	0.40021
6	177.923	84.962	15.005	—	277.890	0.84990	0.15010	—

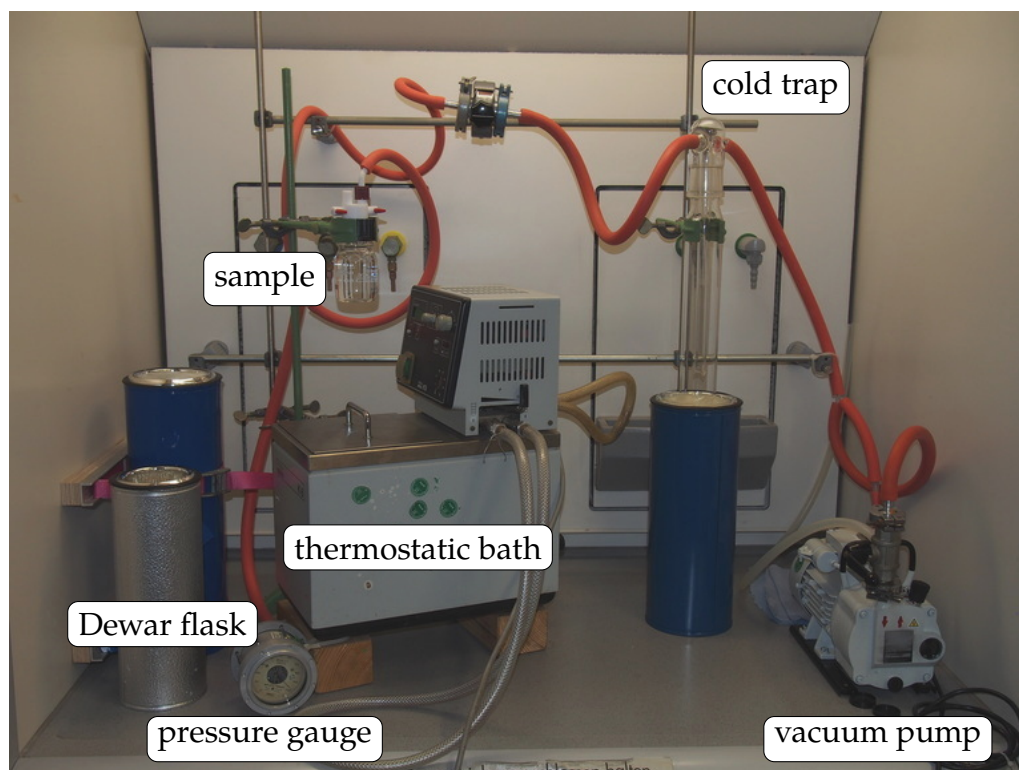


**Figure 3.5:** Degassing setup used in Bayreuth. On the left one can see the Dewar flask used for flash freezing the samples. Rubber hoses connect the sample volume (*Duran*<sup>®</sup> bottle in the middle) with the vacuum pump to the right. To prevent condensation of vapors inside the pump or reflux of oil from the pump into the hoses, a cold trap is inserted between pump and sample volume. A pressure gauge allows to control the quality of the vacuum in the sample volume. The thermostatic water bath in the middle was used in the last step to slowly thaw the mixtures.

ter shipping. These syringes were cleaned multiple times with *Milli-Q*<sup>®</sup> water and acetone and then dried under vacuum ( $< 10$  mbar) at  $50^{\circ}\text{C}$  before filling. Since the tips of the syringes are equipped with luer lock adapters, *BBraun* Discifix<sup>®</sup> stopcocks were connected, allowing to seal the syringes against leakage. To draw liquid into the syringes, a syringe pump (*World Precision Instruments* NE-1002X) was used, since manual raising of the syringes might lead to under-pressure and bubble formation. A slow pump rate of  $100\ \mu\text{L min}^{-1}$  ensured minimal friction of the plunger and a steady filling of the syringes. The connection of the syringes with the bulk of the liquids was made over *BBraun* Perfusor<sup>®</sup> Line Type IV PE connections, a  $0.22\ \mu\text{m}$  *Millipore* filter and *BBraun* Sterican<sup>®</sup> single-use needles, see Fig. 3.8. To lower the needle into the bulk, the stopcock of the bottle was opened just enough for the needle to fit through. At the end of the process, any residual air sucked into the syringes through the PE connection could be removed by moving the plunger. The stopcock of the syringe was then closed and sealed with





**Figure 3.6:** Left: The sample submerged in liquid nitrogen for flash freezing. Right: The flash-frozen sample, after evacuation and shortly before thawing.



**Figure 3.7:** The sample during thawing in the thermostatic water bath at 25 °C. In the left image, one can clearly see gas bubbles rising in the liquid. After several repetitions of the process, samples look like on the right image, when no bubbles appear during thawing. This indicates a sufficient degassing.

*Parafilm*<sup>®</sup>. Since about 5 mL of sample liquid are needed for one filling of a cell, two syringes with 10 mL each were filled from every sample to allow refilling of a cell if needed. With five ternary and one binary sample, this resulted in 12 syringes in total, see Fig. 3.9. To minimize the risk of loss of the samples, the syringes were split into two batches: the first batch was shipped by a delivery service, the second batch was transported by the PI team to the facilities for cell filling.

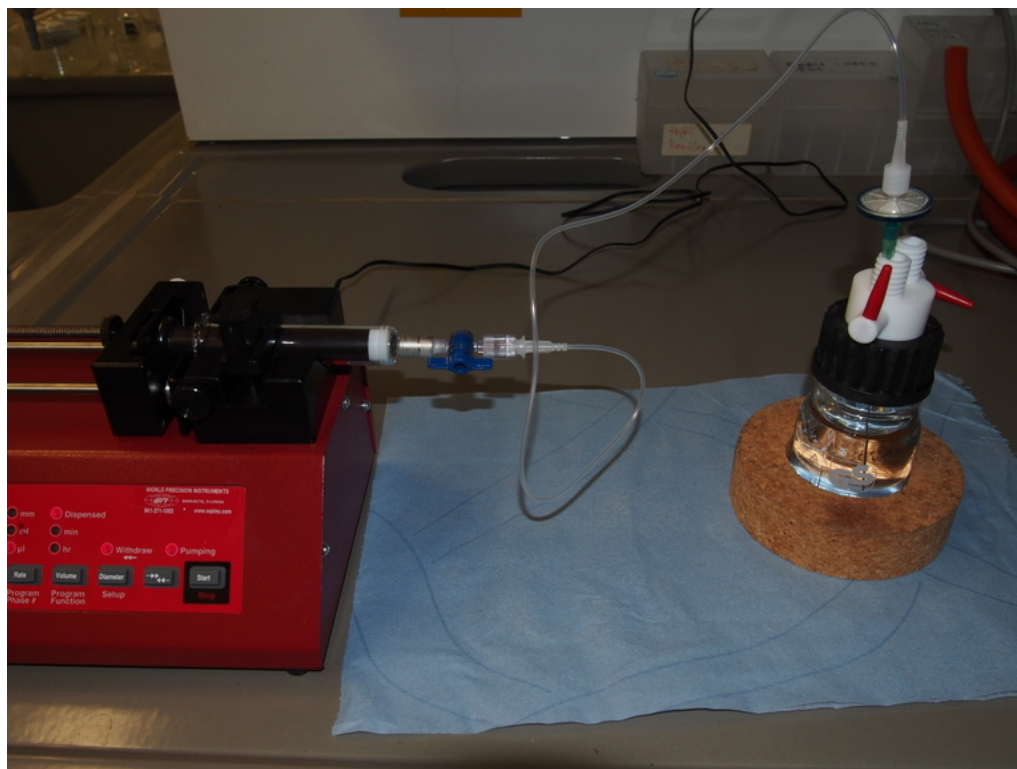


**Figure 3.8:** The setup used for filling of the syringes with the DCMIX3b sample liquids. On the left, the syringe pump is slowly raising the plunger of the syringe. Over a PE line, with a filter and a needle applied, the syringe is connected to the sample bulk through the stopcock of the bottle.

#### 3.3.4 Cell Filling

The cell filling was done in the facilities of QinetiQ Space n.v. near Antwerps, with the author present to act as consultant for the engineers, from 25th April to 29th April 2016. Since the cell design for DCMIX only allows for one filling hole on top, a special procedure had to be employed: as can be seen in Fig. 3.10, the cell is connected via hoses with a vacuum pump. Via a T junction, the syringe is connected to the system. First, the pump evacuates the cell and the hoses leading to it, with the valve to the syringe closed. Then, the valve to the pump is closed, and the valve connecting to the syringe opened. This means, that syringe and cell are connected via a evacuated hose, so the liquid gets sucked into the cell by the

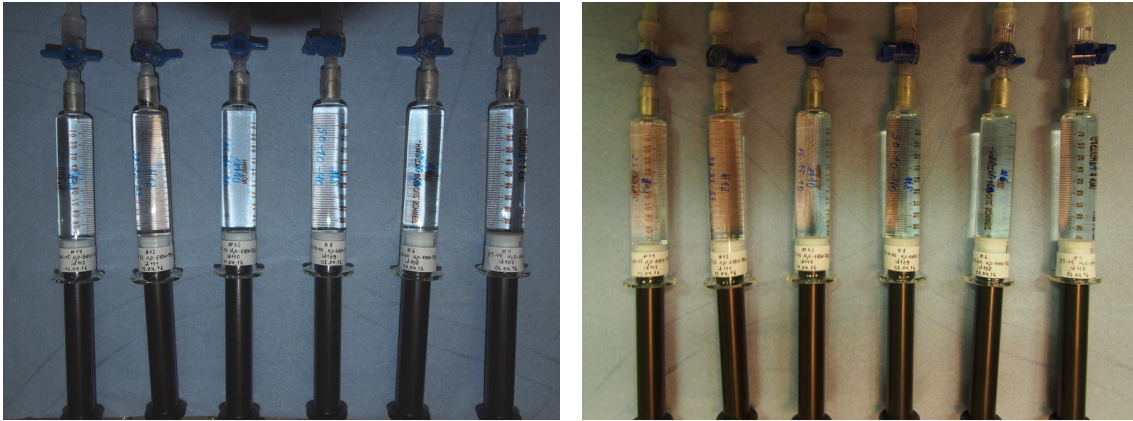


**Figure 3.9:** The filled syringes with the DCMIX3b samples, ready for shipment.

vacuum. After the liquid has entered the cell, all valves are closed. This process leads to some bubble formation; so these bubbles have to be forced out of the cell by turning the cell array, collecting all small bubbles into a large one, and letting it rise up through the filling hole. After the filling process, a close visual inspection of the cell is performed by looking through the glass windows with magnifying glasses. This step ensures that no particles or other contaminants have entered the cell during the filling procedure, or bubbles remain in some corners of the cell. Unfortunately, the visual inspection showed particles sticking to the walls inside cells 2, 3 and 5, which necessitated a refill of these cells.

Inspection of the extracted particles suggested a metallic origin. Since the material looked very similar to the thread on top of the filling hole, necessary to apply the filling adapter, the most probable explanation is that these particles were metal shaved off the thread during application of the adapter. The affected cells were emptied, thoroughly cleaned with purified water and ethanol, and dried by applying vacuum. Then, the cells were refilled using the same procedure as before, but taking special care during application of the filling adapter to avoid any abrasion. The refill was successful for all affected cells. After filling operations were completed, several integration tests were applied to the hardware by QinetiQ engineers. This includes a vacuum test, thermal cycling as well as a vibration test, to ensure that the cell array will not be impacted by ambient conditions during the flight to the space station.

### 3.3.5 Operations on the ISS

#### Delivery by SpaceX CRS-9

The DCMIX3b cell array was scheduled to be brought to the ISS with the next available resupply mission, SpaceX CRS-9. On 18th July 2016 the Falcon 9 rocket took off from Cape Canaveral, carrying a Dragon transport capsule on top, and safely arrived at the space station on 20th of July 2016, see also Fig. 3.12. After



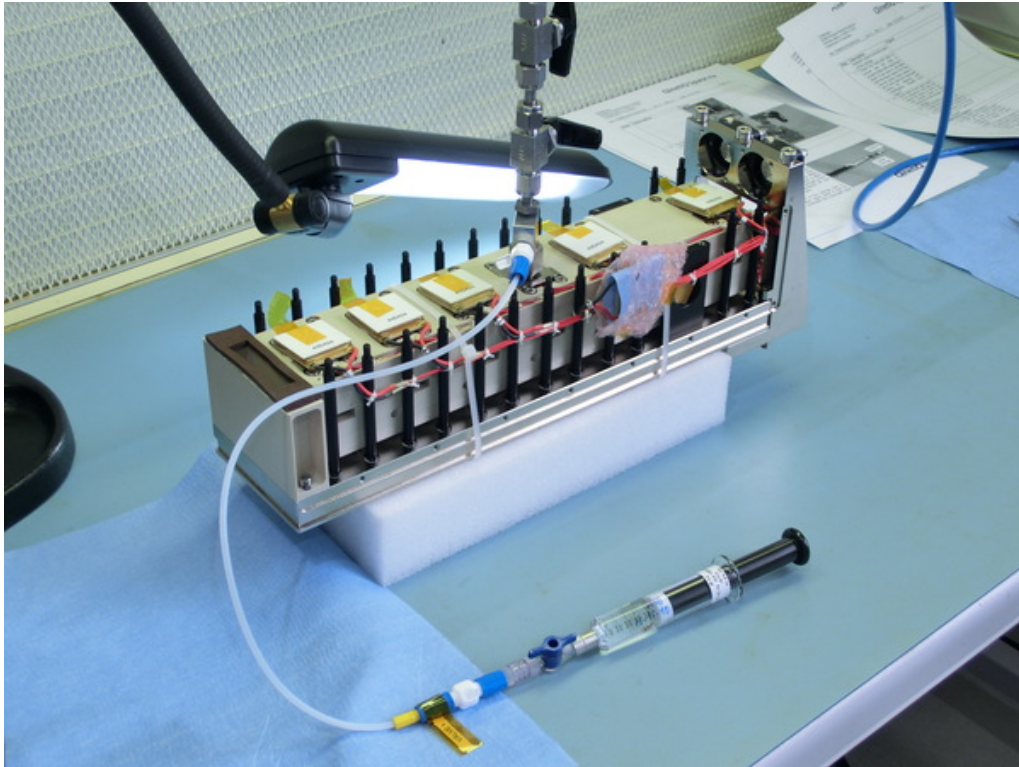


**Figure 3.10:** The system for filling of the cells. The sample syringe is connected to the filling adapter on top of the cell, which forms a T junction and is also connected to a vacuum pump. Valves allow the selective evacuation of hoses between syringe and filling adapter as well as the cell volume. The cell array itself is seen in an unfinished state, with the Peltier elements for thermal regulation not yet fixed and the outer shell missing.

docking to the ISS, the DCMIX3b hardware was put into storage until SODI could be assembled in the Microgravity Science Glovebox (MSG). MSG provides a versatile platform for different experiments, ranging from life sciences to material sciences, and is heavily utilized by a number of teams. This makes experiment time scarce and the DCMIX experiment had to wait until a timeslot became available for MSG. Figure 3.11 shows an image of the Microgravity Science Glovebox. Apart from providing an encapsulated workspace, mandatory for most experiments involving liquids on the ISS, MSG includes power outlets, controlled air flow for heat regulation and a dedicated control computer. A breadboard allows for the installation of different hardware, e.g. the SODI interferometer.

#### Hardware Checkout

In September 2016, MSG was ready for the DCMIX experiments and the hardware could be mounted inside. NASA astronaut Kathleen Rubins, together with the team at USOC Madrid, was responsible for the setup of SODI inside MSG, as well



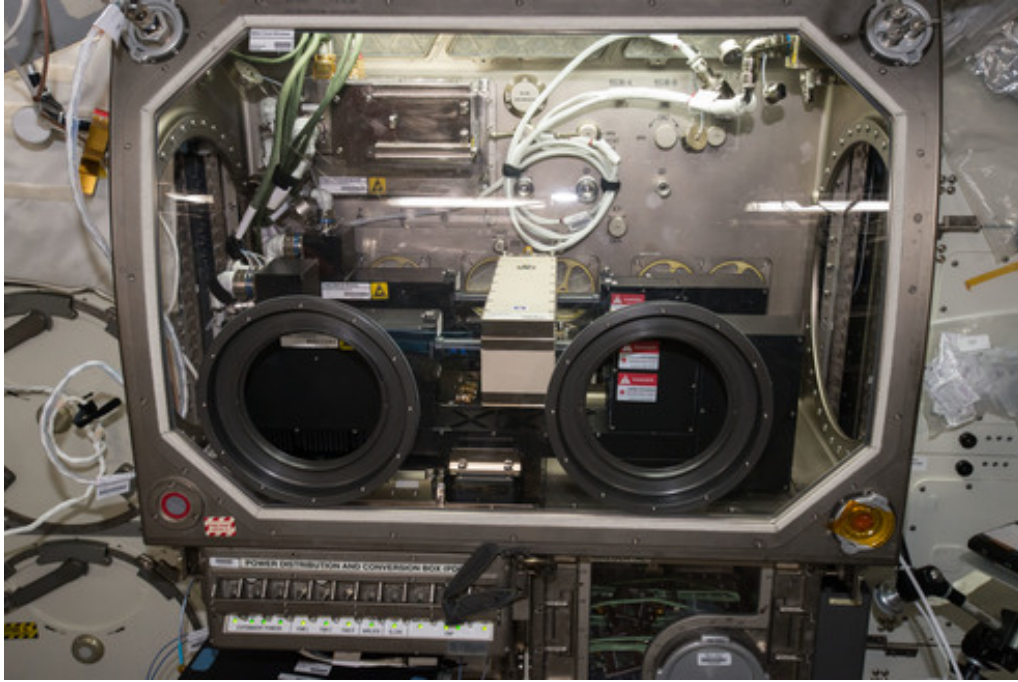


**Figure 3.11:** Image of the Microgravity Science Glovebox (MSG), a versatile experiment container inside the Destiny module of the ISS. It can provide power, cooling and control interfaces to different experiments. Here, one can see SODI with the DCMIX3b cell array inserted, shortly after setup on 13th of September 2016. The two optical modules are clearly visible, with the one in the background always being fixed on the companion cell and the one in the foreground being able to move between the different ternary cells. (Source: courtesy QinetiQ Space)



**Figure 3.12:** Left: start of SpaceX CRS-9 from Cape Canaveral on 18th July 2016. Right: arrival of the Dragon capsule carrying the DCMIX3b cell array at the ISS on 20th July 2016. (Source: SpaceX via <https://www.flickr.com/photos/spacex/>, Public Domain; NASA via <https://www.flickr.com/photos/nasa2explore/>, CC BY-NC 2.0)



**Figure 3.13:** NASA astronaut Kathleen Rubins during the setup of the SODI hardware and insertion of the DCMIX3b cell array on 13th September 2016. (Source: NASA via <https://www.flickr.com/photos/nasa2explore/>, [https://www.nasa.gov/mission\\_pages/station/research/experiments/1175.html](https://www.nasa.gov/mission_pages/station/research/experiments/1175.html), CC BY-NC 2.0)

as the integration of the DCMIX3b cell array into SODI. During this time the PI team, together with QinetiQ engineers, were present at E-USOC to monitor the operations and provide feedback as necessary. The setup of SODI started on 13th of September and could be monitored via a live video stream, see Fig. 3.13.

After insertion of the cell array, the team of E-USOC took over and downloaded images taken with the CCD cameras of SODI, to verify the field of view and the integrity of all cells, see Figs. 3.14 to 3.16. Unfortunately, this so-called optical checkout revealed some problems: first of all, a bubble had formed in cell 3. Since all other cells were bubble-free, and a continuous growth of the bubble could be observed during operations, the most probable origin was due to some leakage (Fig. 3.17). Furthermore, the field of view of cells 1 and 2 was slightly cropped, with only ca 95% and ca 97% of the cell volumes visible. The reason for this cropping could not be conclusively determined, since the design of the cell array is optimized to guarantee a reproducible positioning. But after some consideration, it was deemed acceptable, since any operations to correct the cell alignment would have had to be done by an astronaut. Scheduling additional time for such operations is very complicated and it could not be guaranteed that a repositioning of the cell array would correct the issue. Since any such attempt would have resulted in a loss of precious operation time, and since the cropped parts of the cells were close to the walls, which have to be cropped anyway during analysis, it was decided to commence with the measurements and not to try any corrections.

#### **Mandatory Runs**

The agreement of the DCMIX team with ESA about the DCMIX3 experiments, as detailed in the ESR (Experiment Scientific Requirements) document [51], defined 20 mandatory runs to be conducted at 25 °C, measuring the cells in con-

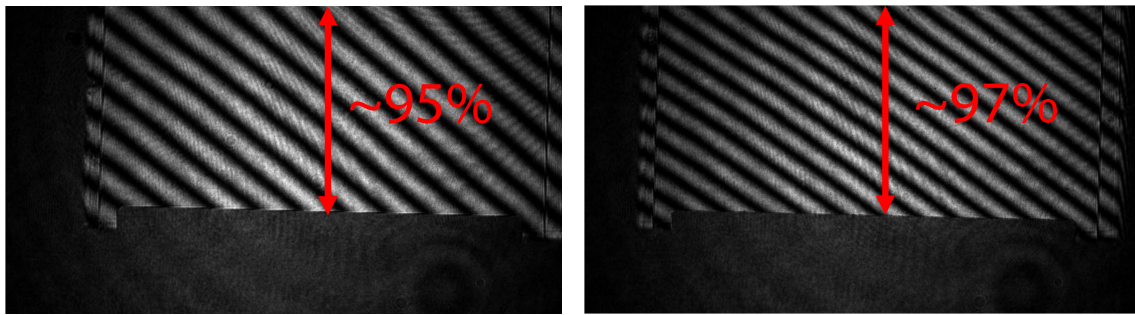


**Figure 3.14:** Status of the cells 1 and 2 during checkout operations.

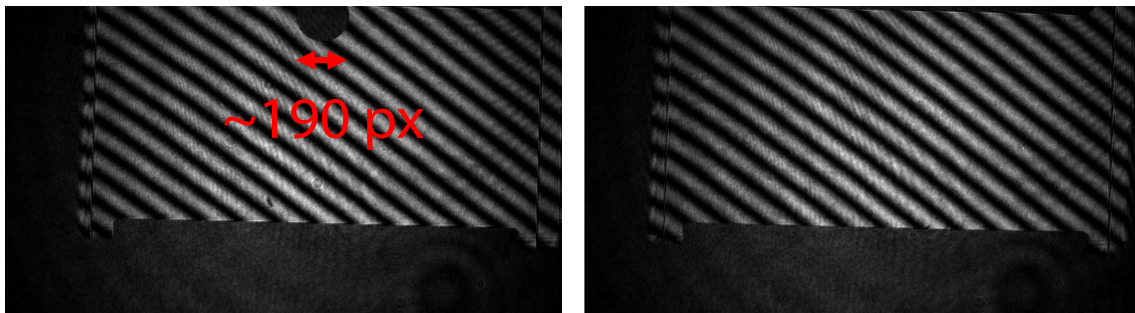


**Figure 3.15:** Status of the cells 3 and 4 during checkout operations.

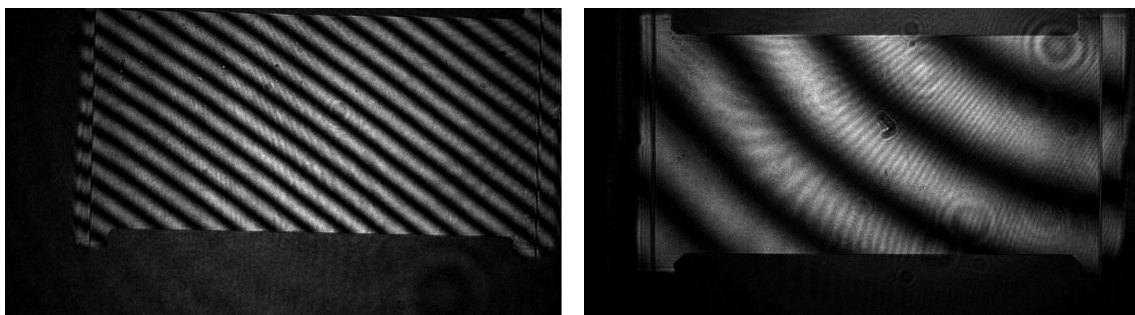


**Figure 3.16:** Status of the cells 5 and 6 during checkout operations.



secutive order (1,2,3,4,5). Since a bubble had formed in cell 3, some adjustments had to be made about the measurement processes. As tests during optical checkout revealed, the bubble was immobile under different temperature gradients, but could be removed when raising the mean temperature of the cell to 30 °C. The most probable explanation for this is, that the increased pressure in the cell forced the bubble through the filling hole into the compensation volume. When cooling down again to 25 °C, the bubble would reappear with approximately the same size as before. To avoid disturbances in cell 3 by Maragoni convection at the liquid-gas boundary, measurements in this cell were conducted at 30 °C. Also, to start measurements with the cell providing an optimal field of view, runs were reordered to start with cell 5. Together with necessary equilibration times after a completed measurement, this led to a reordering of the runs as defined in the ESR.

Operations for the mandatory runs lasted from 19th September to 20th October 2016. After completion of the optical checkout and initial run configuration, the PI team returned to Bayreuth and monitored operations via telemetry. As already mentioned, the complete data set of the experiments is too large for downlinking from the ISS. Thus, only a limited amount of data was downlinked to evaluate a run and make decisions about upcoming experiments. This telemetry data is comprised of 42 image stacks per laser and run, as well as temperature readings from the sensors inside the cell array. Special software provided by NASA (TReK, "Telescience Resource Kit"), see Fig. 3.18, and E-USOC enabled a real-time data-link between the PI team and the operators at E-USOC, which received telemetry data via Marshall Space Flight Center and streamed this data to Bayreuth. Based on this information, the PI team discussed with E-USOC the most promising actions on a weekly basis, after which the team at E-USOC would prepare the experiments. These operations were successful and, due to efficient utilization of the allotted time by E-USOC, 21 mandatory runs were completed, with 5 runs in cell 5 and 4 runs each for all other cells.

#### **Additional Experiments ("nice-to-have" Runs)**

Originally, operations would have ended on 20th October, but since another experiment scheduled for MSG had to be cancelled, DCMIX3b was granted additional time for some "nice-to-have" runs. The ESR document had already planned ahead for such an opportunity, defining some additional runs with an extended duration. But since the bubble in cell 3 had already necessitated some deviations from ESR, it was agreed that the most useful data to have would be additional runs in the other cells also performed at 30 °C. This would provide a complete data-set of all cells at identical mean temperature, making possible comparisons between the different mixtures. The "nice-to-have" runs lasted from 20th October to 22nd November 2016. After backup of the data, SODI was removed from MSG and stored on 30th November 2016. The hard disks were prepared for transportation with SpaceX CRS-10, which docked at the ISS on 23rd February 2017 and returned

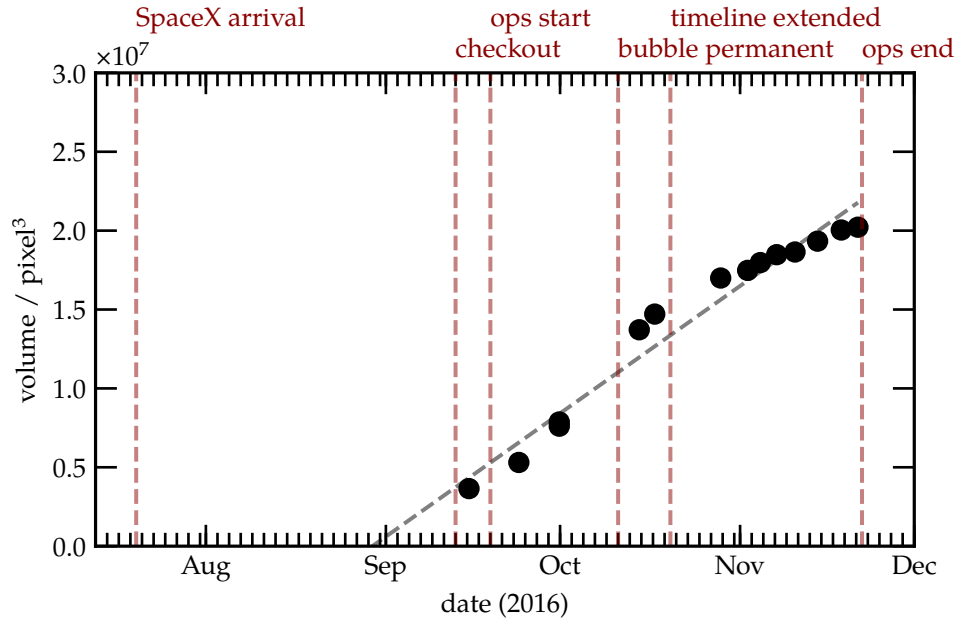


**Figure 3.17:** Plot of the bubble volume in cell 3 over time, with marks for important dates during operation. The volume has been estimated from images taken between runs, so the mean temperature was identical to the ambient temperature ( $\sim 22^\circ\text{C}$ ). A linear regression of the volume (dashed line) suggests that the bubble appeared around end of August / start of September, while the cell array was stored aboard the ISS. Minor ticks in the plot are in two-day intervals.

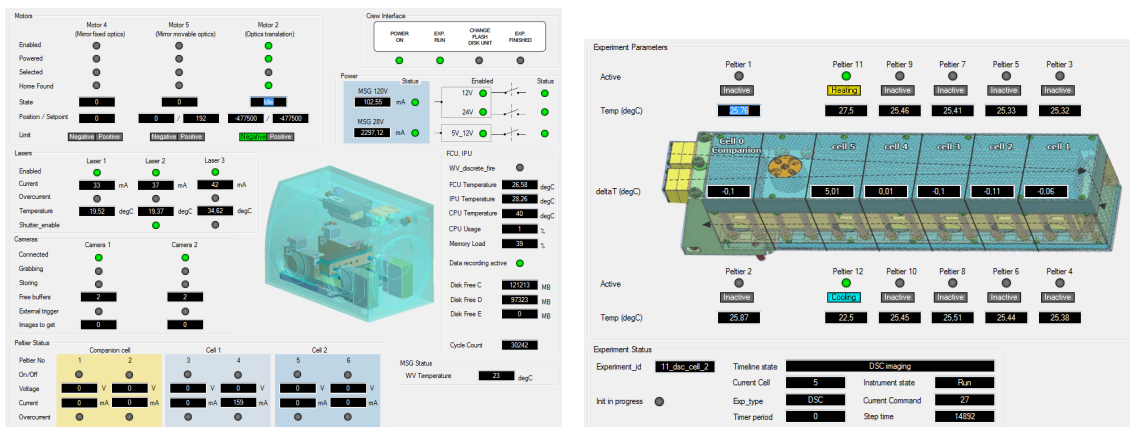


**Figure 3.18:** TReK software provided by NASA for telemetry monitoring. The left screenshot shows information provided by MSG, the right one shows the status of the Peltier elements as well as measured temperatures in the cell array.

back safely to earth on 18th March 2017. After the landing, the hard disks were transported to Madrid, where the E-USOC team performed the readout operations and uploaded the files to a FTP server. In June 2017, the PI team was given access to the full data set of DCMIX3b. Analysis of this data will be presented in Section 5.2.

#### **Notable Events**

During operations of DCMIX3b another notable event occurred, apart from the bubble in cell 3. In the course of run 08 in cell 3, a sudden shift of the camera was noticeable between the two downlinked images with timestamps at 12:59 UTC and 15:13 UTC. After the full data set became available, the exact time frame could be narrowed down to between 14:46 UTC and 14:49 UTC. Since the cell array itself is fixed, a shift of the movable camera module was the most plausible explanation. So, the cause of this had to be found to exclude any re-occurrence, which was possible since, to monitor ambient conditions, several acceleration sensors are mounted inside the MSG. Sifting through the data provided by these sensors the team at E-USOC, together with the team of Xavier Ruiz, soon identified the origin of the shift: a short, low frequency jitter on the MSG was registered in the time-frame under consideration [64]. What caused this jitter could not be determined, but probably some slow-moving object collided with the MSG, leading to the shift of the camera. This was a singular event, which was not observed again during operations, so no negative influence on the experiments is to be expected. Furthermore, the IVIDIL experiments, which were done some years before in SODI, have shown that low intensity vibrations do not disturb diffusive processes in microgravity [56]. The only consequence from this event was to redefine the Region of Interest (ROI) for image cropping, to adjust to the new camera position.

## **3.4 DCMIX4**

The latest campaign, which is under preparation during the time of writing, is DCMIX4. Since this will probably be the last DCMIX effort under the original agreement with ESA, several ideas how to best utilize this opportunity were discussed: for one, the DCMIX2 measurements were severely hindered by bubble formation, preventing most of the planned measurements, which called for a repeat of at least some DCMIX2 samples (with improved sealing). Secondly, bearing in mind that the main goal of DCMIX is to characterize a wide range of model systems, ternary polymer mixtures (meaning one polymer mixed with two solvents) would make a useful addition; especially since the future experiment “Giant Fluctuations” [65–67] (formerly named NEUF-DIX) will investigate non-equilibrium fluctuations in the ternary polymer mixture polystyrene/toluene/hexane, this offers a good opportunity to cross-reference and validate results from two different experimental methods. Thirdly, a ternary nanofluid (tetralin/toluene/fullerene)

would expand reference data to another highly interesting model system, with possible applications ranging from photovoltaics to biotechnology [68, 69]. The result from these discussions was that all of the three mentioned systems would be included in the cell array, maximizing the scientific impact of DCMIX4; the planned compositions of all cells are listed in Table 3.5.

**Table 3.5:** Planned compositions for the DCMIX4 cells, given as weight fraction.

cell	$c_1$ (toluene)	$c_2$ (methanol)	$c_3$ (cyclohexane)
1	0.20	0.25	0.55
2	0.35	0.25	0.40
3	0.55	0.25	0.20
	$c_1$ (tetralin)	$c_2$ (toluene)	$c_3$ (fullerene)
4	0.60	0.3993	0.0007
	$c_1$ (polystyrene)	$c_2$ (toluene)	$c_3$ (hexane)
5	0.02	0.49	0.49
6	0.02	0.98	—





## 4 Experimental Methods

This chapter will explain the experimental methods relevant to this work, including ground-based setups used in Bayreuth, as well as the DCMIX experiments performed on the ISS. For measurements of (thermo)diffusion coefficients, the Optical Beam Deflection (OBD) method is well established in Bayreuth, with previous works successfully employing it for binary as well as ternary systems. Since details of the implementation of this method are described in the works of Meier [70], Königer [71] and Gebhardt [13], focus in the first section will be laid on the dimensionless formulation introduced by Haugen and Firoozabadi [14]. This formulation is also the basis of the detailed analysis of stable quantities presented by Gebhardt [13, 15], which informs the data analysis in this work for both ground and microgravity measurements. All methods employed in Bayreuth rely on the precise determination of optical contrast factors, so the experiments for measurements of these will also be explained. The last section will then give details about SODI, the instrument used for microgravity measurements on the ISS, as well as some basic concepts of Phase-Shifting Interferometry in general.

### 4.1 Optical Beam Deflection

Measurements of diffusion and thermodiffusion coefficients with an Optical Beam Deflection setup have already been performed by Giglio and Vendramini in the 1970s for different polymers in solution as well as aniline/cyclohexane near the consolute critical point [25, 72, 73]. The basic principle is quite simple and leverages the fact that concentration shifts inside a sample also lead to refractive index shifts. In turn, a laser beam passing through a transparent medium with a refractive index gradient perpendicular to the beam axis is subject to deflection. This deflection of the laser beam can be detected with a simple line camera and analyzing its time dependence allows to deduce the (thermo)diffusive coefficients. Figure 4.1 shows a sketch of the basic principle.

#### 4.1.1 Setup

The setup used in Bayreuth is based on the design by Piazza [74, 75] and has first been implemented by Meier and Königer [70, 76]. This first iteration relied on a single laser source at 637 nm, enabling measurements in binary mixtures of water/ethanol [26], water/isopropanol [55] as well as toluene/methanol/cyclohexane [77]. Later, Königer and Gebhardt expanded the setup to include two beams

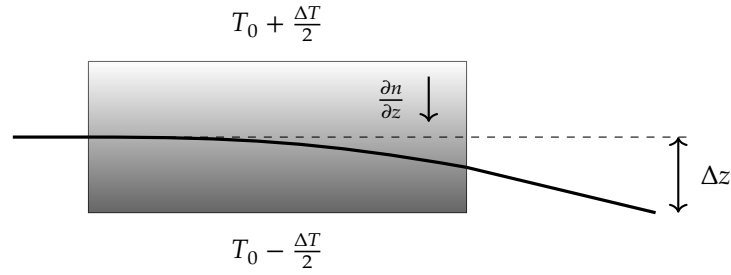


**Figure 4.1:** A simple sketch of the OBD principle: in typical experiments, the sample is heated from above, which means that a gradient  $\Delta T$  is applied symmetrically to the sample with mean temperature  $T_0$ . In most (binary) mixtures, this leads to an accumulation of the denser component on the bottom of the sample, increasing the local refractive index. Vice versa, the lighter component accumulates on the warmer (top) side, decreasing the refractive index. A light beam passing through the medium with refractive index gradient  $\frac{\partial n}{\partial z}$  perpendicular to the optical axis is deflected towards higher refractive index, leading to the detectable deflection  $\Delta z$ .

with different wavelengths (405 nm and 635 nm), following a proposition by Haugen and Firoozabadi [14]. This opened up the possibility to measure ternary mixtures, which has successfully been done in the systems tetralin/n-dodecane/isobutylbenzene [31, 78–80] and 1-methylnaphthalene/octane/decan [78]. This ternary setup has also been used in this work for measurements in the DCMIX3 system water/ethanol/triethylene glycol and will be described in the following.

Figure 4.2 shows the main components of the OBD instrument. All parts whose respective distances can influence the detected deflection (light source – sample – camera) are mounted on a profile rail (*Linus X95*) made from aluminium, to minimize changes of the relative positions due to fluctuations of the ambient temperature. Two diode lasers (*Sharp GH04P21A2GE* at 405 nm and *Schäfter und Kirchhoff 51nanoFCM* at 635 nm) are used as light sources. To guarantee that both beams enter the sample on the identical axis, they are first combined into a common optical single-mode fiber (*Schäfter und Kirchhoff SMC-400-2,6-NA012-3-APC-0-300* with collimator 60FC-4-A11-02) and directed to a collimator (*Schäfter und Kirchhoff 60FC-4-M5-33*) on the profile rail. After passing through the sample cell, the beams are detected on a line camera (*Spectronic Devices TCD1304*, 3648 pixel of  $8.25 \mu\text{m} \times 200 \mu\text{m}$  size each). Since the camera records a beam profile with finite width, the position is determined by fitting a Gaussian curve on this profile and taking the position of the maximum. This allows the measurement of the beam position with sub-pixel precision.

The core of the setup is the Soret cell with the sample, since its design directly influences the performance of the instrument. The general layout of a Soret cell is well established, with similarities across different experimental methods: to enable the application of a temperature gradient across the bulk, the sample is

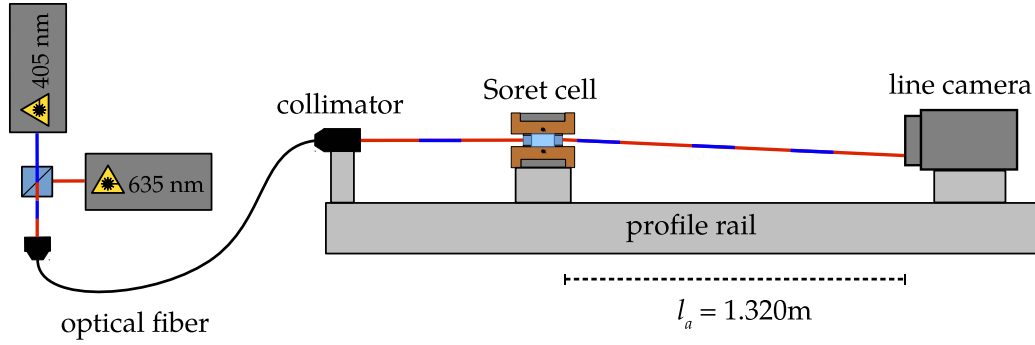


**Figure 4.2:** The 2-color Optical Beam Deflection setup as implemented in Bayreuth. Both lasers are coupled into a common fiber to guarantee an identical beam path to the sample cell. To track the laser position on the camera independently for both wavelengths, the lasers are switched on and off alternately with a frequency of around 1 Hz. Mounting the end of the optical fiber, the Soret cell and the line camera on the same profile rail minimizes changes in the important distances, especially the distance  $l_a$  between cell and camera.

sandwiched between two metal plates with high thermal conductivity (copper in the case of OBD), with a glass frame enclosing the volume. This allows to observe the sample in a direction perpendicular to the thermal gradient (and gravity) with a laser beam. In order to obtain an ideal temperature profile, i.e. free of distortions in the plane of the beam, the exact method of sealing the sample volume and filling/cleaning the cell requires careful consideration. Figure 4.3 shows the cell design used in Bayreuth, which was optimized over the years. The copper plates form a flat surface on the side of the cell volume, to prevent any dead volumes, with a rectangular glass frame (*Hellma* 690.295-OS, custom build) in between. Inside the frame, a total geometric path length of 10 mm through the sample is achieved. To seal the volume, two Teflon<sup>®</sup> foils of 100  $\mu\text{m}$  thickness, cut out to fit the glass frame, are sandwiched between frame and copper plates. This leads to total height of the cell volume of around 1.43 mm and an aspect ratio of 0.143 between cell height and geometric path length. To ensure a tight sealing between all parts, four screws connect the two copper plates on the corners. By tightening the screws with a torque wrench, only applying a specific amount of torque on each screw, excessive loads on the glass frame can be avoided. When a sample cell has been assembled like this, the sample can then be filled into the glass frame via capillaries leading through the copper plates to the corners of the sample volume.

The other important design constraint is the regulation of the applied temperature gradient, which is done via a feedback loop. Cut-outs on the copper plates allow the application of Peltier devices (*Quick Cool* QC-71-1.4-8.5-M), providing the necessary heat flux for temperature regulation. Additionally, through small

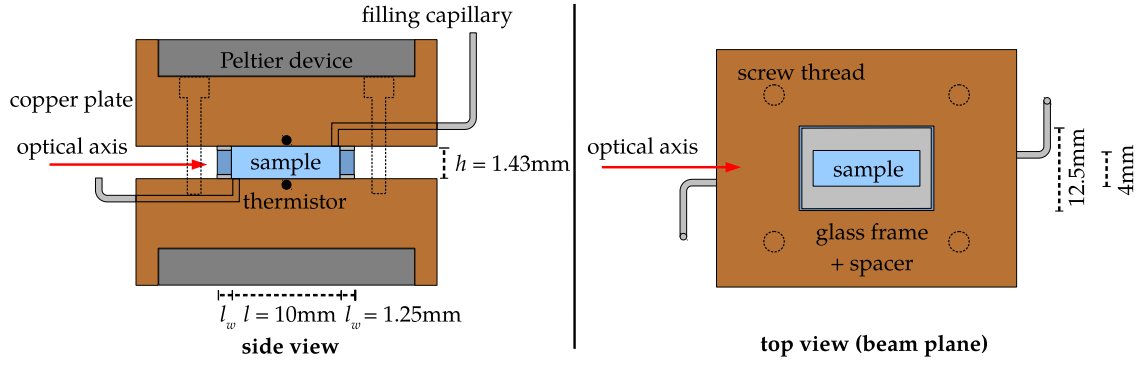


**Figure 4.3:** Soret cell design as employed for Optical Beam Deflection in Bayreuth.

holes in the copper plates close to the sample volume, thermistors (*Epcos* NTC B57540G0103F00, 10 k $\Omega$  nominal resistance at 25 °C) allow to determine the temperatures on the upper and lower walls of the sample volume, completing the feedback loop. After calibration with a precision thermometer, absolute accuracy is around 0.03 K, with differences between the two thermistors in the mK range. Now, in an ideal experiment, the application of the temperature gradient should be modelled after a Heaviside function: after an equilibration phase of several hours (to allow the sample to completely mix and to equilibrate the setup), keeping the whole sample bulk at a fixed temperature, the gradient is applied almost instantly and kept constant for sufficient long times. Typical temperature differences are around 1 K, with measurement durations of around 10 000 s. In the first iterations of the setup, the whole temperature regulation, including the gradient switching, was implemented as a PID feedback loop, which lead to overshooting during the switching. Therefore, Gebhardt devised a new “ballistic” method for this process [17], improving the temperature profile significantly: for the gradient application, the PID feedback loop is first switched off completely. Then the Peltier devices are set to maximum current for a short duration (typically around 0.5 s), heating/colling the copper plates to move the temperatures in a ballistic way close to the desired set-points. Followed by a short equilibration phase (also around 0.5 s) with a lower constant current, the PID feedback loop is then switched on again. Since the temperatures are now much closer to the target gradient, the PID regulation needs to react in a much narrower range, preventing most of the overshooting and allowing to establish constant temperature differences (in the mK range) within only a few seconds, as detailed in Gebhardt’s work [13]. The exact parameters, i.e. the durations for the individual steps just explained, are highly dependent on the sample, mean temperature and ambient conditions. They are therefore determined by experience and trial and error for each experiment.

For analysis, a working equation has to be formulated to connect the measured deflection  $\Delta z_\lambda$  ( $\lambda = 405$  nm and 635 nm for the two lasers) to the refractive index

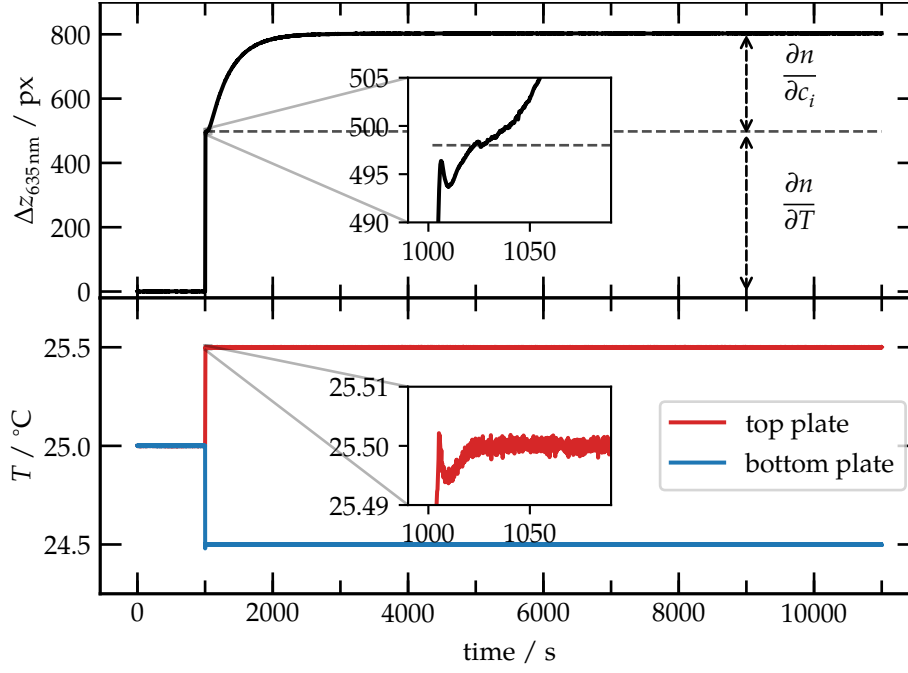


**Figure 4.4:** Plot of a typical OBD signal of the equi-mass mixture of tetralin and dodecane, together with the applied temperature gradient of 1 K. This mixture shows the expected behaviour of most binary mixtures, as described in Fig. 4.1. The two contributions to the signal from the contrast factors  $\partial n/\partial c_i$  and  $\partial n/\partial T$  are clearly discernible. Note: the beam position during the equilibration phase is taken as position 0, with deflection towards the lower end of the camera counted as positive.

gradient  $\partial n_\lambda/\partial z$  inside the sample [81]:

$$\Delta z_\lambda = l \frac{\partial n_\lambda}{\partial z} \left( \frac{l}{2n_\lambda} + \frac{l_w}{n_{w,\lambda}} + \frac{l_a}{n_{a,\lambda}} \right) \frac{1}{l_{\text{px}}} := A_\lambda \frac{\partial n_\lambda}{\partial z}, \quad (4.1)$$

with  $l = 10$  mm the geometric path length inside the sample,  $l_w = 1.25$  mm the window thickness — with respective refractive index  $n_{w,\lambda}$  — and  $l_a = 1.320$  m the distance between window and camera, with  $n_{a,\lambda}$  the refractive index of air (see Fig. 4.2). Since the deflection is measured as pixels on the camera, the pixel size  $l_{\text{px}}$  has to be accounted for (about  $8.25 \mu\text{m}/\text{px}$ ). The so-called instrument amplitude  $A_\lambda$  is almost identical for both wavelengths and can be approximated by

$$A_\lambda = A \approx l \frac{l_a}{l_{\text{px}}} = -1600 \text{ m} \times \text{px} \quad \forall \lambda. \quad (4.2)$$

This value has been used for all measurements.

Equation (4.1) only assumes a geometric ray, thereby neglecting the Gaussian profile of a real laser. To account for this, Kolodner et al. were the first to propose

an averaging of the deflection across the beam profile [34]:

$$\langle \Delta z_\lambda \rangle = A \left\langle \frac{\partial n_\lambda}{\partial z} \right\rangle, \quad (4.3)$$

where

$$\left\langle \frac{\partial n_\lambda}{\partial z} \right\rangle = \frac{\int_{-h/2}^{+h/2} I_\lambda(z) \frac{\partial n_\lambda}{\partial z} dz}{\int_{-h/2}^{+h/2} I_\lambda(z) dz}. \quad (4.4)$$

The function  $I_\lambda(z)$  describes the Gaussian profile of the laser with wavelength  $\lambda$ , whose width is given by the alignment of the collimator. To simplify notation, this averaging is implicitly assumed in the following.

Now, the refractive index gradient  $\partial n_\lambda / \partial z$  inside the sample is determined by the local temperature and the concentration gradients,

$$\frac{\partial n_\lambda}{\partial z} = \frac{\partial n_\lambda}{\partial T} \frac{\partial T}{\partial z} + \sum_{k=1}^{K-1} \frac{\partial n_\lambda}{\partial c_k} \frac{\partial c_k}{\partial z}, \quad (4.5)$$

with  $\frac{\partial n_\lambda}{\partial T}$  and  $\frac{\partial n_\lambda}{\partial c_k}$  being the optical contrast factors. Therefore, when inserting Eq. (4.5) into Eq. (4.1) the measured deflection can be written as

$$\Delta z_\lambda = A \frac{\partial n_\lambda}{\partial T} \frac{\partial T}{\partial z} + A \sum_{k=1}^{K-1} \frac{\partial n_\lambda}{\partial c_k} \frac{\partial c_k}{\partial z}. \quad (4.6)$$

As already discussed in Section 2.2, the optical contrast factors are sample-specific parameters, which have to be known beforehand from measurements explained in Section 4.2. Figure 4.4 shows a typical OBD measurement with the two contributions from temperature and concentration gradient clearly visible. For analyzing an OBD signal, it is important to be able to separate these two signals, since only the concentration signal contains the diffusion coefficients of interest. Given a high performance temperature regulation as described above, this is no problem due to the low Lewis number of liquids (see also Section 2.1.3).

### 4.1.2 Dimensionless Analysis

To extract the diffusion coefficients from the transient deflection Eq. (4.6), an analytical description of the time-dependence  $\partial c_i(t) / \partial z$  has to be found. As presented in Section 2.1.3, a general solution for a rectangular Soret cell was deduced by Haugen in the form of Eq. (2.25). Similarly, we rewrite Eq. (4.6) with a new subscript

$$\Delta z_i = A \frac{\partial n_i}{\partial T} \frac{\partial T}{\partial z} + A \sum_{k=1}^{K-1} \frac{\partial n_i}{\partial c_k} \frac{\partial c_k}{\partial z}. \quad (4.7)$$

To be able to insert Eq. (2.25) into Eq. (4.7), we have to take the transformations Eqs. (2.19) to (2.21) into account:

$$\Delta z_i = \underbrace{A \frac{\partial n_i}{\partial T} \frac{\partial T}{\partial z}}_{\Delta z_{T,i}} + A \frac{1}{h} \sum_{k=1}^{K-1} \frac{\partial n_i}{\partial c_k} V_{ik} \Delta C_{\infty,k} \frac{\partial \tilde{C}_k}{\partial \tilde{z}}. \quad (4.8)$$

The first term contains solely experimental parameters (instrument amplitude  $A$ , applied gradient  $\partial T / \partial z \approx \Delta T / h$ ) and the thermal contrast factor. So it is convenient to normalize the deflection signal on this quasi-constant thermal amplitude  $\Delta z_{T,i}$ ,

$$\begin{aligned} \frac{\Delta z_i}{\Delta z_{T,i}} &= 1 + \sum_{k=1}^{K-1} \left( \frac{\partial n_i}{\partial T} \right)^{-1} \frac{1}{\Delta T} \frac{\partial n_i}{\partial c_k} V_{ik} \Delta C_{\infty,k} \frac{\partial \tilde{C}_k}{\partial \tilde{z}} \\ &= 1 + \sum_{k=1}^{K-1} M_{ik} \frac{\partial \tilde{C}_k}{\partial \tilde{z}}. \end{aligned} \quad (4.9)$$

This description is not restricted to OBD, but can be applied to most optical experiments, as detailed in the publication of Gebhardt and Köhler [15]. The general form of a multi-color signal in an optical experiment is given by

$$s_i(t) = 1 + \sum_{k=1}^{K-1} M_{ik} f_k(t), \quad (4.10)$$

with  $f_k(t)$  being the applicable time-dependent solution of the diffusion equation Eq. (2.23) for the diffusion eigenvalue  $\hat{D}_k$ . In the case of OBD:

$$\begin{aligned} f_{\text{OBD},k}(t) &= 1 + \frac{1}{2} \sum_{n=-N}^N (-1)^n \left[ \operatorname{erf} \left( \frac{2\tilde{z} - 2n - 1}{4\sqrt{\frac{t}{\tau_k}}} \right) - \operatorname{erf} \left( \frac{2\tilde{z} - 2n + 1}{4\sqrt{\frac{t}{\tau_k}}} \right) \right] + \\ &+ \sum_{n=-N}^N (-1)^n \frac{1}{4\sqrt{\frac{\pi t}{\tau_k}}} \left[ \exp \left( -\frac{(2\tilde{z} - 2n - 1)^2}{\frac{16t}{\tau_k}} \right) + \exp \left( -\frac{(2\tilde{z} - 2n + 1)^2}{\frac{16t}{\tau_k}} \right) \right], \end{aligned} \quad (4.11)$$

which is Eq. (2.25) with time constants  $\tau_k = h^2 / \hat{D}_k$ , see also Eq. (2.22). A fitting routine based on Eqs. (4.10) and (4.11) has been implemented by Gebhardt in his PhD thesis [13] and successfully applied to the DCMIX1 system. In comparison, for TDFRS the solution is of the form

$$f_{\text{TDFRS},k}(t) = 1 - \exp \left( -\frac{t}{\tau_k} \right) = 1 - \exp \left( -t \frac{4\pi^2 \hat{D}_k}{d^2} \right), \quad (4.12)$$

with a grating vector of  $q = 2\pi/d$  (grating period  $d$ ) and time constants  $\tau_k = d^2 / (4\pi^2 \hat{D}_k)$ .

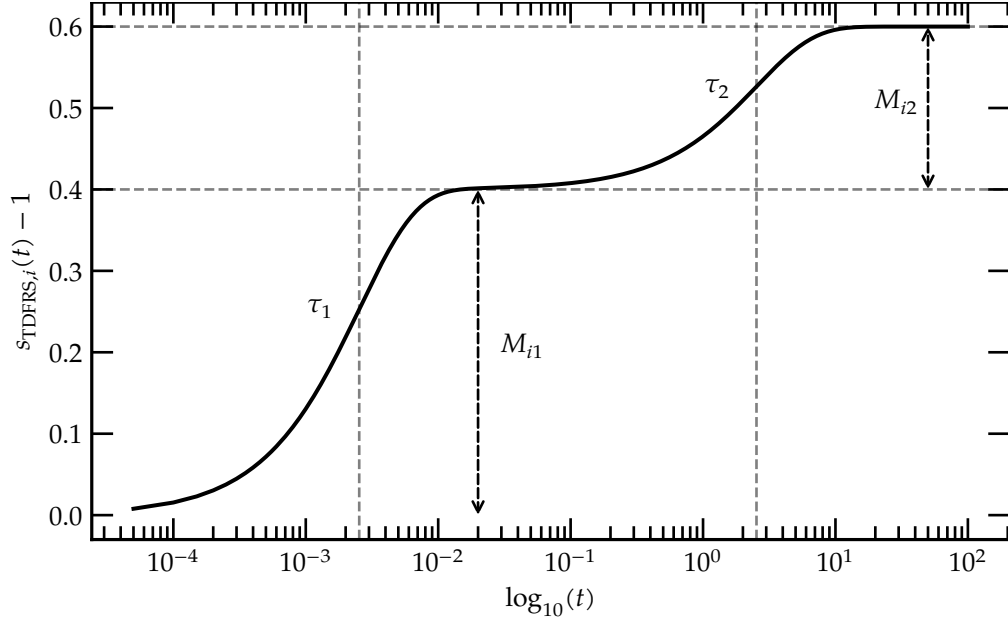


**Figure 4.5:** Plot of a hypothetical TDFRS signal for wavelength  $\lambda_i$  according to Eq. (4.10) with Eq. (4.12). For emphasis, two widely different diffusion eigenvalues of  $\hat{D}_1 = 1 \times 10^{-9} \text{ m}^2 \text{ s}^{-1}$  and  $\hat{D}_2 = 1 \times 10^{-12} \text{ m}^2 \text{ s}^{-1}$  have been chosen. The grating period  $d$  is of the order of  $10 \mu\text{m}$ .

This makes it obvious that ternary optical signals are generally described by a set of six fit parameters

$$\{M_{11}, M_{12}, M_{21}, M_{22}, \hat{D}_1, \hat{D}_2\}.$$

The general number of free parameters of a multi-color signal is  $((K - 1)^2 + (K - 1))$ . In Fig. 4.5, a resulting signal is plotted for a hypothetical ternary TDFRS experiment. Even though the general description is identical for TDFRS and OBD, the transient solution  $f(t)$  in the case of TDFRS allows for a significantly better separation of the two time constants and lends itself for visualization. But this is not only a problem in visualization, but also in signal fitting itself: if the time constants are very close, a clear separation of the amplitudes  $M_{ik}$  is no longer possible. This means that multiple sets of  $M$  and  $\hat{D}$  are compatible with the same transient  $f(t)$ . Refs. [15] and [13] therefore contain a detailed analysis about which quantities can be reliably extracted from ternary optical signals. By looking at the two limits  $s_i(t \rightarrow \infty)$  and  $s_i(t \rightarrow 0)$  it can be shown that, even though the individual parameters  $M$  and  $\hat{D}$  are ambiguous, five  $(2(K - 1) + 1)$  in general) unique combi-



nations can be found:

$$\begin{aligned} a_i &= \sum_{k=1}^{K-1} M_{ik}, \\ b_i/q^2 &= \sum_{k=1}^{K-1} M_{ik} \hat{D}_k, \\ \bar{D} &= \left[ \frac{1}{K-1} \sum_{i=1}^{K-1} \frac{\sum_{k=1}^{K-1} M_{ik} \hat{D}_k}{\sum_{k=1}^{K-1} M_{ik}} \right]^{-1}. \end{aligned} \quad (4.13)$$

It should be noted that the grating vector  $q$  is first defined in the context of a TDFRS experiment and reappears since these derivations are most easily obtained in the case of TDFRS. But nevertheless, above definitions are valid for all optical experiments compatible with Eq. (4.10). An intuitive meaning can be assigned to these quantities from the way they are defined: the  $a_i$  are the total amplitudes of the quasi-stationary plateau for  $s_i(t \rightarrow \infty)$ , the  $b_i$  the initial slopes for  $s_i(t \rightarrow 0)$  of a TDFRS signal. The coefficient  $\bar{D}$  can be interpreted as a quasi-binary averaged diffusion coefficient. What is important to note is that these quantities are

- unique for every transient  $f(t)$ ,
- independent of experimental parameters,
- independent of the measured contrast factors (but dependent on the employed wavelengths).

Therefore, in contrast to the quantities  $M$  and  $\hat{D}$ , they are robust during fitting and establish a consistent description of multi-color experiments.

To be able to extract transport coefficients of interest, and make comparisons to other experiments not evaluated with this approach, the definitions

$$\begin{aligned} a_i &= - \left( \frac{\partial n_i}{\partial T} \right)^{-1} \sum_{k=1}^{K-1} N_{c,ik} S'_{T,k}, \\ b_i/q^2 &= - \left( \frac{\partial n_i}{\partial T} \right)^{-1} \sum_{k=1}^{K-1} N_{c,ik} D'_{T,k}, \end{aligned} \quad (4.14)$$

with the inverse transformations

$$\begin{aligned} S'_{T,i} &= - \sum_{k=1}^{K-1} N_{c,ik}^{-1} \frac{\partial n_k}{\partial T} a_k, \\ D'_{T,i} &= - \sum_{k=1}^{K-1} N_{c,ik}^{-1} \frac{\partial n_k}{\partial T} b_k/q^2, \end{aligned} \quad (4.15)$$

are necessary. The  $N_{c,ik}^{-1}$  are the elements of the inverse contrast factor matrix, see also Section 2.2. It should be emphasized that the individual elements of the

diffusion matrix are not accessible by multi-color experiments and have to be determined differently. Suitable experiments include Sliding Symmetric Tubes [82] and Taylor Dispersion [83].

## 4.2 Contrast Factor Measurements

As discussed in Section 2.2, optical experiments like OBD or TDFRS rely on the optical contrast factors  $(\partial n_\lambda / \partial T)_{p, c_i}$  and  $(\partial n_\lambda / \partial c_j)_{p, T, c_{k \neq j}}$  to connect measured refractive index changes to concentration changes. In Bayreuth, both thermal and solutal contrast factors can be measured, which has also been done in this work for the DCMIX3 system.

### 4.2.1 Solutal Contrast Factor

The solutal contrast factors  $(\partial n_\lambda / \partial c_j)_{p, T, c_{k \neq j}}$  describe the variation of refractive index for slight changes in one of the independent concentrations  $c_j$  (while keeping the remaining  $c_{k \neq j}$  fixed). So for determination, the refractive indices of samples with different concentrations are measured and a multivariate polynomial (with the concentrations  $c_j$  as variables) is approximated to this refractive index data. In the ternary case:

$$n_\lambda(c_1, c_2) = \sum_{i,j=0}^{i+j=P} A_{ij} c_1^i c_2^j, \quad (4.16)$$

with  $A$  a  $(P+1) \times (P+1)$  matrix of polynomial coefficients, containing the coefficients for the powers  $c_1^i$  and  $c_2^j$  in row  $i$  and column  $j$ .  $P$  signifies the maximum power in the univariate as well as the multivariate terms, so the full polynomial is of the power  $P^2$ . The derivatives of this polynomial  $n_\lambda(c_1, c_2, \dots)$  then give the sought contrast factors  $\partial n / \partial c_j$ . In this work, refractive index measurements have been carried out with two commercial refractometers (*Anton Paar* Abbemat WR). One of these is a re-fitted model with a diode laser of 404.9 nm wavelength, while the other is capable of measuring consecutively at multiple wavelengths (437 nm, 487.7 nm, 532.3 nm, 589.3 nm, 632.6 nm and 684.4 nm). The precision is specified as  $4 \times 10^{-5}$  by the manufacturer, but in practice the accuracy of the measurements is on the order of  $1 \times 10^{-4}$ .

It is important to note, since these measurements aim at absolute refractive index values, the instruments have to be calibrated with a reference sample. Unfortunately, calibration has only been done at 20 °C by the manufacturer, so measurements with high precision are restricted to this temperature. If absolute values are needed at different temperatures, the thermal contrast factor has to be integrated:

$$n_\lambda(T) = n_\lambda(T_0) + \int_{T_0}^T \frac{\partial n_\lambda}{\partial T'} dT', \quad (4.17)$$

with  $T_0 = 20^\circ\text{C}$  in this case. To make direct measurements at different temperatures possible, as well as to increase the accuracy of the measurements, two different setups are currently being tested in Bayreuth as part of Master theses. The first setup is a multi-wavelength Michelson interferometer, which would enable the simultaneous determination of absolute refractive indices at different wavelengths inside the same sample, at a temperature of choice. First measurements have shown that the accuracy is on the order of  $1 \times 10^{-5}$ , a significant improvement to the Abbemat instruments. The second setup consists of a differential refractometer, enabling the precise measurement of the solutal contrast factor [84]. Here also, first tests are very promising.

### 4.2.2 Thermal Contrast Factor

The principle for thermal contrast factor measurements is the same as described in Ref. [85], relying on interferometry. Figure 4.6 shows a simple sketch: a glass cell (*Hellma*) is filled with the sample liquid and placed inside a metal block made from brass. This block is connected to a thermostatic bath, allowing to regulate the temperature of the metal and (in extension) the cell. Due to the high heat capacity of the metal block, small fluctuations in the heat regulation are damped and the cell can be maintained at isothermal conditions. A laser (either 632.8 nm or 405 nm) enters the cell and is reflected twice: once on the front (interface air–glass) and once on the back window (interface glass–air), leading to interference between the two wavefronts. The reflections between glass–liquid and liquid–glass can be neglected, due to the similar refractive indices. The interfering wavefronts are then reflected out of the original beam-path by a beam-splitter (a simple slab of glass) and directed onto a photodiode. Due to a slight angle between the wavefronts, a sinusoidal fringe pattern will show on the diode.

Now, by varying the optical path length inside the cell, this fringe pattern will shift continuously, leading to a sinusoidal intensity variation on the diode. Since the accumulated phase difference is given by

$$\Phi = kn2l, \quad (4.18)$$

with  $2l$  accounting for the double-pass characteristic, the tuning of the optical path is done via the refractive index  $n(T)$  of the sample. By slowly increasing/decreasing the temperature of the thermostatic bath,  $n(T)$  is changed in a controlled manner. Since thermal expansion and the refractive index of the windows has to be accounted for, the full working equation is given by [85, 86]

$$\left( \frac{\partial n_\lambda}{\partial T} \right)_{p, c_i} = \frac{\lambda}{4\pi l} \frac{\partial \Phi}{\partial T} - 2 \frac{l_w}{l} \frac{\partial n_w}{\partial T} - 2 \frac{n_w}{l} \frac{\partial l_w}{\partial T} - \frac{n}{l} \frac{\partial l}{\partial T}. \quad (4.19)$$

$l_w$  and  $n_w$  are the thickness and refractive index of the cell windows. Their values, as well as temperature dependences  $\partial l_w / \partial T$  and  $\partial n_w / \partial T$ , are provided by the manufacturer.

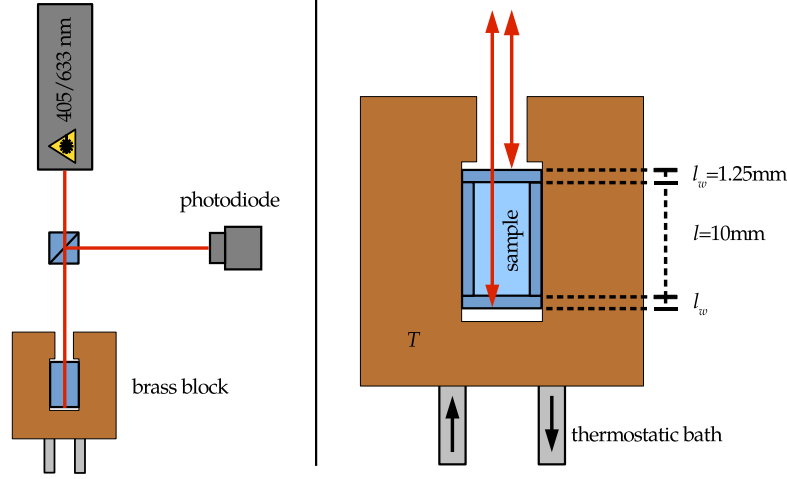


**Figure 4.6:** A sketch of the interferometric setup used in Bayreuth for measuring  $(\partial n / \partial T)_{p, c_i}$ .

$\partial \Phi / \partial T$  can be determined from the intensity signal on the diode, since the temperature variation is a controlled external parameter. By plotting the intensity versus temperature, simply counting the oscillations yields  $\Phi(T)$  as multiples of  $2\pi$ ; this can then be approximated by a polynomial to find  $\partial \Phi / \partial T$  and therefore  $\partial n / \partial T$  as a function of  $T$ .

Mostly, quadratic or cubic polynomials are sufficient for  $\Phi(T)$ , leading to linear or quadratic expressions in  $\partial n / \partial T$ . In the ternary case:

$$\left. \frac{\partial n_\lambda}{\partial T} \right|_T = \sum_{i=0}^Q b_i(c_1, c_2) T^i, \quad (4.20)$$

which describes the contrast factor  $\partial n / \partial T$  as a polynomial of order  $Q$ , evaluated at a certain temperature  $T$ . This measurement is done for different sample compositions in a system, which then allows to determine the concentration dependence  $b_i(c_1, c_2)$  for the coefficients, again by polynomial approximation:

$$b_i(c_1, c_2) = \sum_{k, l=0}^{k+l=R} B_{kl}^i c_1^k c_2^l. \quad (4.21)$$

This means that every coefficient  $b_i$  in Eq. (4.20) has its unique  $(R + 1) \times (R + 1)$  matrix  $B_{kl}^i$ .

Typical values for the thermal contrast factor are around  $-5 \times 10^{-4} \text{ K}^{-1}$ . For error estimation, the measurement is repeated over several heating/cooling cycles within the same temperature range, which also allows to check for hysteresis effects and sample aging. The resulting accuracy of the experiment is normally better than one percent of the value. It should also be noted that the validity of the

polynomial approximation is restricted to the central region of the temperature interval, between which the measurements have been performed, to avoid oscillatory behaviour on the edges. For example, since the temperature of interest in most experiments is around 25 °C, the measurements are performed in the interval 15 °C to 35 °C.

### 4.2.3 Refractive Index Parametrization

Since the described contrast factor measurements yield polynomial approximations of all relevant dependencies, a full parametrization of the absolute refractive index can be constructed. By combining Eqs. (4.17), (4.20) and (4.21), this can be written as

$$n_{\lambda}(c_1, c_2, T) = \sum_{i,j=0}^{i+j=P} A_{ij} c_1^i c_2^j + \sum_{m=0}^Q \sum_{k,l=0}^{k+l=R} B_{kl}^m c_1^k c_2^l \frac{(T^{m+1} - T_0^{m+1})}{m+1}, \quad (4.22)$$

which has to be done independently for every wavelength  $\lambda$  of interest. From these multivariate polynomial approximations, it is straightforward to determine necessary refractive index or contrast factor values at arbitrary concentrations and temperatures (within the validity range of the approximation). But of course, since polynomial approximations of high degrees can be prone to oscillations, care has to be taken in the choice of the polynomial degrees  $P$ ,  $Q$  and  $R$ , to avoid over- or under-fitting and ill-conditioning of the contrast factor matrix (see also Section 2.2 and Ref. [28]).

## 4.3 Selectable Optical Diagnostics Instrument

This section gives an overview of the instrument utilized for measurements aboard the ISS during DCMIX operations, as well as Interferogram Analysis (or more general Fringe Pattern Analysis), as it relates to this work. Most of the information about SODI itself is taken from design documents provided by the manufacturer QinetiQ Space n.v. (formerly Verhaert Space) [87–89]. Basic methods, like temporal and spatial phase stepping and phase unwrapping are discussed, as well as specific implementations for the analysis of SODI data. The last section explains the extraction of diffusive quantities from the phase data. For this, a signal similar to Optical Beam Deflection experiments has been deduced from the image data and fitted with the analytic solution of the extended diffusion equation.

### 4.3.1 Components

Onboard the International Space Station (ISS) several instruments are available, to enable scientists from different fields to study samples under long-term microgravity conditions. The Selectable Optical Diagnostics Instrument (SODI) incorporates a Mach-Zehnder interferometer, operating at two different wavelengths

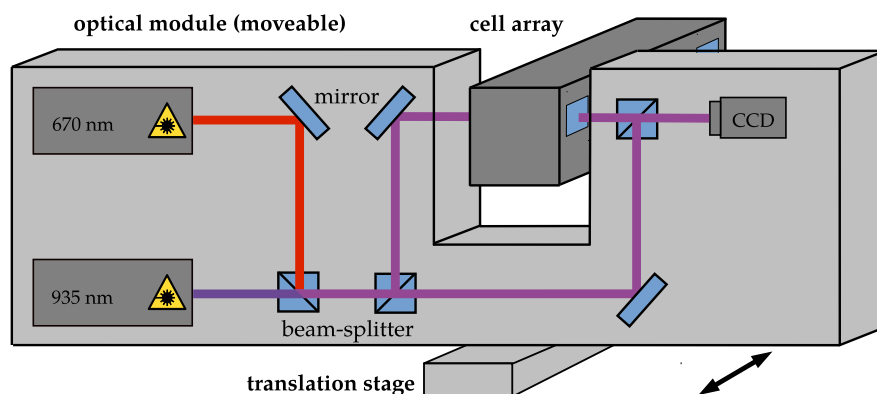


**Figure 4.7:** Schematics of SODI. The (movable) optical module contains a Mach-Zehnder interferometer working at two wavelengths (670 nm and 935 nm). This can be used to probe different samples inside the cell array. Another (fixed) optical module, always probing a so-called companion cell, is not shown. The internal optics are identical, but with only one laser at 670 nm.

(670 nm and 935 nm), see Fig. 4.7, allowing to probe refractive index changes in transparent (ternary) liquids. Since SODI is a multi-purpose instrument which is only assembled when in use, its design is modular, to allow a simple setup and insertion of different types of cell arrays; but this work will focus on the configuration used for the DCMIX operations. The main components are two optical modules, each housing an independent interferometer. One of these modules contains only one laser operating at 670 nm (*Hitachi 6714G*) and is fixed, always probing a so-called “companion cell”, mostly filled with a well-understood reference sample. The other module operates as a two-color interferometer with 670 nm (*Hitachi 6714G*) and 935 nm (*Nanoplus DFB*) lasers. This module is mounted on a rail, which allows lateral movements along the cell array actuated by a linear stage. Thus, different sample cells can be probed consecutively. In each module, all optical components necessary for the interferometric beam path are contained, including beam splitters and mirrors, to allow a reference and an object path of the light. Lenses inside the beam path widen the wavefronts to illuminate the whole sample volume (20 mm beam diameter); furthermore, the magnification of the imaging system is specified as 1.14. The two beams are then recombined and form a two-dimensional interferogram, which is recorded by a CCD camera (*DALSA Pantera SA 2M30*, one for each module); see Fig. 4.10. This camera has a resolution of  $1920 \times 1080$  pixels ( $7.4 \mu\text{m}$  size), with 8-bit grayscale-color depth.

The cell array containing the samples is made specifically for every experiment, filled on ground and brought to the ISS, the process of which has been detailed in Section 3.3.2. It can accommodate five ternary sample cells, probed by the movable two-color interferometer, and one binary companion cell, probed by the fixed one-color interferometer. The sample volume of a cell is  $5 \text{ mm} \times 10 \text{ mm} \times 10 \text{ mm}$

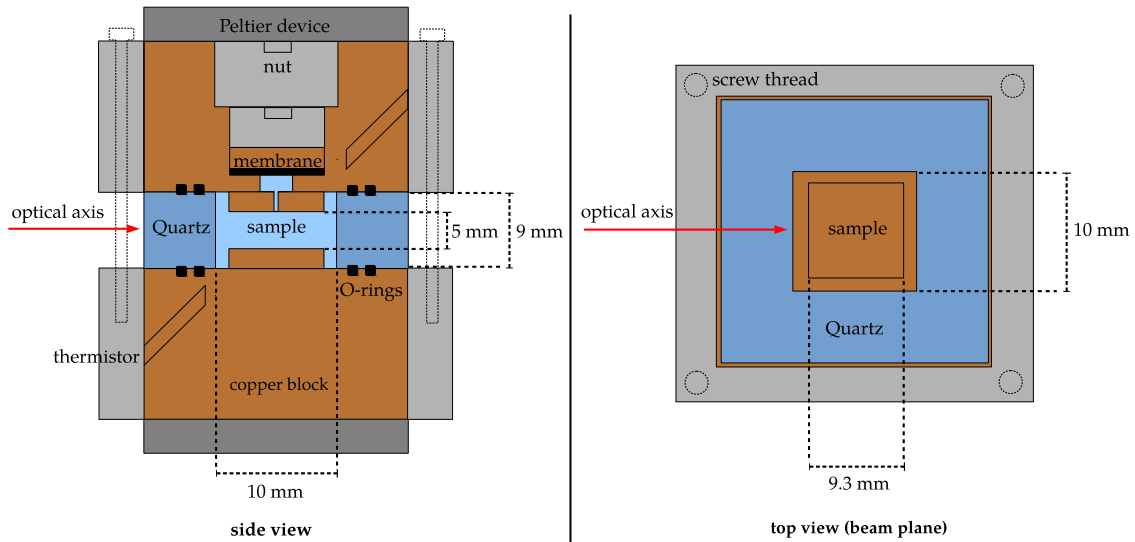


**Figure 4.8:** Schematics of the sample cells for SODI.

(height  $\times$  length  $\times$  depth), realized as a cut-out from a 9 mm thick quartz cube (see Fig. 4.8). This results in an aspect ratio of 0.5 between geometric path in the sample and height of the cell. The quartz cube itself is sandwiched between two copper blocks, connected by titanium spacers to keep them at a constant distance and avoid excessive loads on the quartz. Filling of the cell (see also Section 3.3.4) is done via a hole in one of the copper walls. Since containment and transport requirements prescribe a complete sealing of the cells, a compensation volume above this filling hole is necessary, to equilibrate any pressure changes inside the cells (i.e. when raising the cell temperature). Also, each cell is equipped with two Peltier elements (*SCTB Nord TM-71-1.4-3.7*) together with thermistors (*Betatherm NTC 50K6A1A*, 50 k $\Omega$  nominal resistance at 25  $^{\circ}\text{C}$ ) in opposite ends, to allow the establishing of a (ideally) linear temperature gradient across the sample volume via a PID feedback loop; absolute accuracy of this system after calibration is specified as 0.1 K, with a measurement resolution of 1.5 mK. To avoid an irregular temperature distribution around the compensation volume and to guarantee a full field-of-view into the sample volume, the cells are designed in such a way that protrusions extend from the copper walls, forming cavities on the lateral glass walls (see Fig. 4.8).

For DCMIX, five ternary and one binary sample cells are grouped into a lateral stack, constituting a cell array as shown in Fig. 3.10. But this is still a stripped-down stage of the complete module, since the Peltiers require electrical connections, as well as heat sinks. These heat sinks in turn have to be cooled by an air flow, generated by fans at the end of the cell array. To keep the cell array as compact as possible and to channel the air flow, additional walls made from PEEK are mounted around the cells, with cut-outs providing a line of sight into the cells.

Mounting of the complete cell array into SODI has to be reproducible, to allow easy insertion by the astronauts in microgravity and minimize errors, since re-alignment of the optics is not possible. Therefore, alignment pins on the end of the cell array allow to insert it into a mounting bracket on the fixed optical module. The complete cell array, as later inserted into SODI, is shown in Fig. 4.9.

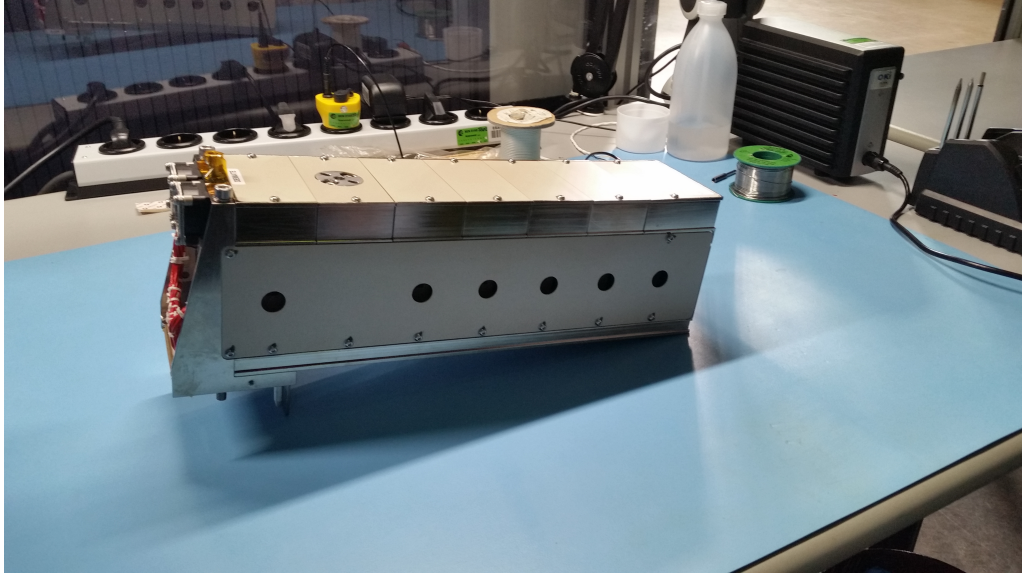


**Figure 4.9:** Complete DCMIX3b cell array. The circular cut-outs provide a field-of-view into the different cells, with the outlying one on the left belonging to the companion cell. The metal rods below the companion cell are used as alignment pins, to fixate the cell array in a reproducible position inside SODI. (Source: courtesy QinetiQ Space)

### 4.3.2 Phase-Shifting Interferometry

In SODI, as in most interferometric experiments, one can observe the generation of fringe patterns, i.e. alternating areas of low and high light intensity. As is evident from basic considerations, the governing quantity of such fringe generation is the optical path difference (or phase difference) between two wavefronts. The complex amplitude of a light wave can be written as:

$$C = Ae^{i\varphi}. \quad (4.23)$$

Let us consider two waves,  $C_1$  and  $C_2$ , propagating along the  $z$ -direction.

$$C_1 = A_1 e^{i\varphi_1(x,y)} \quad (4.24)$$

$$C_2 = A_2 e^{i\varphi_2(x,y)}. \quad (4.25)$$





**Figure 4.10:** Typical grayscale interferogram taken with a CCD camera in SODI. One can clearly see the cell volume, with protrusions on the upper and lower ends of the volume. The main sample volume is sandwiched between these protrusions, with the cavities on the left and right mostly avoided during analysis, to exclude distortion effects due to an irregular temperature gradient.

For clarity, we omit the  $z$ -dependency and just look at the behavior of the waves in the cross-subsection perpendicular to the  $z$ -axis. Due to the principle of superposition, the complex amplitudes of the two (coherent) waves just add up:

$$C = C_1 + C_2 = A_1 e^{i\varphi_1(x,y)} + A_2 e^{i\varphi_2(x,y)}. \quad (4.26)$$

The detectable physical quantity, the intensity  $I$ , has to be real, which leads to the expression

$$I(x,y) = CC^* = |A_1|^2 + |A_2|^2 + A_1 A_2 e^{i\Phi(x,y)} \quad (4.27)$$

with

$$\Phi(x,y) = \varphi_1(x,y) - \varphi_2(x,y) = knL \quad (4.28)$$

being the phase difference between the two waves. The optical path difference  $nL$  contains information either about geometric variations (changes in the geometric path difference  $L$ ), or refractive index changes of the transparent medium inside the path of the object beam. In the case of mass (thermo)diffusion experiments, optical techniques rely upon the changes of  $n$  to detect changes of the local sample compositions. But this leads to the problem, that the detectable physical quantity in the case of optical experiments is not the phase difference  $\Phi$  itself, but the intensity  $I$ . And since the amplitudes  $A_1$  and  $A_2$  are in general not known, one cannot map singular intensity values to distinct phase values. So one is faced with a

single equation Eq. (4.27), but three unknowns. To recover the phase information  $\Phi$ , the solution is to superimpose a known artificial reference phase  $\Phi_R$ :

$$\Phi' = \Phi + \Phi_R \quad (4.29)$$

This is commonly referred to as Phase-Shifting or Phase-Stepping Interferometry (PSI) in the literature (see the textbooks of Malacara [90], Hariharan [91] or Robinson and Reid [92] for good introductions to the field). A distinction can be made based on the method for introducing the phase shift  $\Phi_R$ , either in the temporal or spatial dimension [92, 93], which will be explained in the next sections.

### Temporal Phase-Shifting Interferometry

Temporal phase shifting is evident in the case of a moving mirror: every movement at a time  $t$  leads to a change in geometric path length and an alteration in the interference pattern:

$$\Phi'(x, y, t) = \Phi(x, y) + \Phi_R(t) = \Phi(x, y) + 2\pi\nu t \quad (4.30)$$

where  $\nu$  is the frequency of the phase shifting, often called a temporal carrier frequency. These different interference patterns  $I(x, y, t)$  can then be recorded after each step, allowing to solve the resulting system of equations. The exact choice of  $\Phi_R$  is not fixed, therefore different algorithms are known in the literature to calculate  $\Phi(x, y)$  from a set of measured intensities  $I(x, y, t)$  [93]. A general approach for deriving such algorithms will be given below, with the description mostly following the textbooks of Kreis [94] and Robinson [92]. Originally, this approach was introduced in the paper of Greivenkamp [95].

The set of intensities generated via temporal phase stepping, with a total number of discrete steps  $m$ , is re-written in a real equation (cf. Eq. (4.27)):

$$I_n(x, y) = a(x, y) + b(x, y) \cos(\Phi(x, y) + \Phi_{Rn}) \quad (4.31)$$

with  $n = 1, \dots, m$ .  $\Phi_{Rn}$  describes the reference phase at step  $n$ .  $a(x, y)$  and  $b(x, y)$  are the additive ( $|A_1|^2 + |A_2|^2$ ) and multiplicative ( $A_1 \cdot A_2$ ) offsets in the intensity. Assuming a constant change of the reference phase for every step  $n$

$$\Delta\Phi_{Rn} = \Phi_{Rn+1} - \Phi_{Rn} = \text{const} \quad \forall n, \quad (4.32)$$

Eq. (4.31) results in a nonlinear system of equations one has to solve to recover  $\Phi$ . To simplify this system, we define

$$u = b \cos(\Phi) \quad v = -b \sin(\Phi) \quad (4.33)$$

to write Eq. (4.31) in this way:

$$I_n = a + b \cos(\Phi + \Phi_{Rn}) = a + u \cos \Phi_{Rn} + v \sin \Phi_{Rn}. \quad (4.34)$$

The sought phase is given by:

$$\Phi = \arctan\left(\frac{-v}{u}\right). \quad (4.35)$$

Different approaches are available to solve the system of equations, e.g. the Gauß-Newton minimization of the sum of errors:

$$\sum_{n=1}^m (a + \cos \Phi_{Rn} + v \sin \Phi_{Rn} - I_n)^2 = \text{Min}. \quad (4.36)$$

With  $\frac{\partial}{\partial a} \sum (...)^2 = 0$ ,  $\frac{\partial}{\partial u} \sum (...)^2 = 0$  and  $\frac{\partial}{\partial v} \sum (...)^2 = 0$  we get:

$$\begin{pmatrix} m & \sum \cos \Phi_{Rn} & \sum \sin \Phi_{Rn} \\ \sum \cos \Phi_{Rn} & \sum \cos^2 \Phi_{Rn} & \sum \sin \Phi_{Rn} \cos \Phi_{Rn} \\ \sum \sin \Phi_{Rn} & \sum \sin \Phi_{Rn} \cos \Phi_{Rn} & \sum \sin^2 \Phi_{Rn} \end{pmatrix} \begin{pmatrix} a \\ u \\ v \end{pmatrix} = \begin{pmatrix} \sum I_n \\ \sum I_n \cos \Phi_{Rn} \\ \sum I_n \sin \Phi_{Rn} \end{pmatrix}. \quad (4.37)$$

This has to be solved for  $u$  and  $v$ . In the case of SODI, the number of phase steps is  $m = 5$ , the initial reference phase is  $\Phi_{R1} = 0^\circ$  and the individual steps are  $\Delta\Phi_R = 90^\circ$ . Therefore:

$$\begin{pmatrix} 5 & 1 & 0 \\ 1 & 3 & 0 \\ 0 & 0 & 2 \end{pmatrix} \begin{pmatrix} a \\ u \\ v \end{pmatrix} = \begin{pmatrix} I_1 + I_2 + I_3 + I_4 + I_5 \\ I_1 - I_3 + I_5 \\ I_2 - I_4 \end{pmatrix}. \quad (4.38)$$

This results in:

$$\Phi(x, y) = \arctan\left(\frac{7(I_4 - I_2)}{4I_1 - I_2 - 6I_3 - I_4 + 4I_5}\right). \quad (4.39)$$

From this equation the phase map  $\Phi(x, y)$  for SODI can be calculated, using a set of five fringe images  $I_1 \dots I_5$ , with a phase shift of  $90^\circ$  between successive images. As mentioned above, one could introduce this phase shift just by moving a mirror and changing the optical path. But in the case of SODI, which is permanently stored aboard the ISS, without much options for adjustment, one tries to avoid moving parts as much as possible. Instead, a slight tuning of the nominal wavelength  $\lambda_0$  is used to introduce the known phase shift

$$\Phi_R = \frac{2\pi}{\lambda_0^2} \Delta\lambda nL, \quad (4.40)$$

assuming a Taylor expansion of the wavenumber  $k$ . Since the lasers in SODI are diode lasers, this can be reproducibly accomplished by changes in the driving current of the diodes [90, 91, 96]. As Hariharan elaborated in [97], the wavelength of a laser diode (assuming operation in a single mode) is a linear function of the driving current, and accompanying errors due to simultaneous changes in output power are non-consequential for most applications. For example, the 935 nm laser

in SODI shows a wavelength change of 0.0074 nm/mA; with an optical path difference  $nL \approx 3$  cm, this translates to current steps of 1 mA [87]. The typical output power change is around 0.11 mW/mA (according to the datasheet of a comparable laser diode from the same manufacturer); with a nominal output power of 10 mW, this translates to changes of around 1 % during phase stepping. Figure 4.11 shows the resulting error for Eq. (4.39), which is well below 1 %.

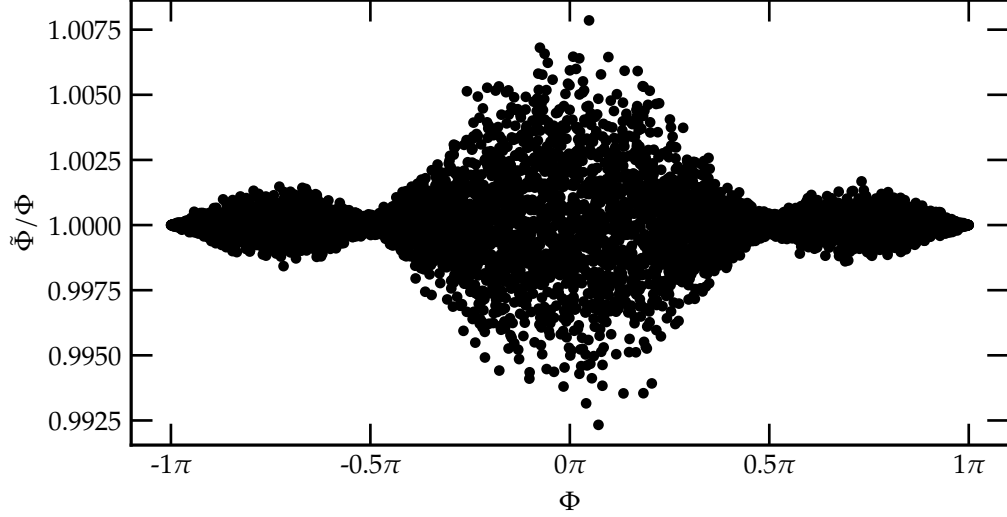


**Figure 4.11:** Phase error for Eq. (4.39), assuming an laser output change of 1 % during phase stepping. For estimation, 1 % random error has been added to the intensity values, resulting in  $\tilde{\Phi}$ .

### Spatial Phase-Shifting Interferometry

Spatial phase shifting keeps the reference phase constant in time, but introduces local phase differences:

$$\Phi'(x, y) = \Phi(x, y) + \Phi_R(x) = \Phi(x, y) + 2\pi f_0 x. \quad (4.41)$$

For simplicity, it is assumed that the reference phase only varies along the  $x$ -direction, with  $f_0$  the spatial carrier frequency. For example, by tilting reference and object beam against each other, one introduces slightly different phase shifts across the geometric path length. A simple example would be to tilt a mirror in the reference beam path of a Mach-Zehnder interferometer. This is also the case in SODI, as is obvious in Fig. 4.10, showing a tilted non-contour type fringe pattern. Assuming that the carrier frequency  $f_0$  is considerably higher than the variations in the phase  $\Phi$  [93],

$$|2\pi f_0| > |\nabla \Phi|, \quad (4.42)$$

one can look at the fringe pattern as a spatially multiplexed phase signal. Therefore, already one interferogram is sufficient to reconstruct the phase information via spatial methods.

Several approaches for this are known in the literature, e.g. the Fast Fourier Transform (FFT) method, as first introduced by Takeda et al. [98]: The fringe pattern in complex notation can be written:

$$\begin{aligned} I(x, y) &= a(x, y) + b(x, y) \cos(\Phi(x, y) + 2\pi f_0 x) \\ &= a(x, y) + c(x, y)e^{2\pi i f_0 x} + c^*(x, y)e^{-2\pi i f_0 x} \end{aligned} \quad (4.43)$$

with

$$c(x, y) = \frac{1}{2}b(x, y)e^{i\Phi(x, y)}. \quad (4.44)$$

Taking the Fourier Transform of Eq. (4.43) gives:

$$\mathfrak{F}\{I(x, y)\} = A(f, y) + C(f - f_0, y) + C^*(f + f_0, y) \quad (4.45)$$

$f$  is the spatial frequency in  $x$ -direction. Obviously, this yields two peaks around the frequencies  $(f + f_0)$  and  $(f - f_0)$ , both containing the same information. Assuming a sufficiently large difference between  $f$  and  $f_0$ , applying a band-pass filtering process can easily separate  $C$  (or  $C^*$ ) from the background noise  $A$ . The inverse Fourier transformation then only contains information about  $c$  (or  $c^*$ ), with  $a$  filtered out. Now, looking at Eq. (4.44), the phase information  $\Phi$  is obtained from the ratio of imaginary and real part of  $c$ :

$$\Phi(x, y) = \arctan\left(\frac{\mathfrak{I}\{c(x, y)\}}{\mathfrak{R}\{c(x, y)\}}\right). \quad (4.46)$$

Although this analysis was restricted to a carrier frequency solely in  $x$ -direction, the approach is identical for a carrier with components in both directions, leading to a 2-dimensional Fourier analysis.

### Phase Unwrapping

No matter if one applies a temporal or spatial PSI method, as is obvious from Eqs. (4.39) and (4.46), the phase calculation always involves the arctangent function. Normally, the range of  $\arctan(x)$  would be  $(-\frac{\pi}{2}, \frac{\pi}{2}]$ , restricted to two quadrants in the Cartesian coordinate plane; but in the case of Eqs. (4.39) and (4.46), one looks at the function  $\arctan(y/x)$ , also called  $\arctan2$  or four-quadrant arctangent. This function returns values in the range  $(-\pi, \pi]$ , see Fig. 4.12. To recover the full phase information, which can contain values outside this range, a so-called *unwrapping* process has to be applied, which transforms the phase values from the wrapped range  $(-\pi, \pi]$  to a continuous range. As with PSI, this is a known problem in literature, with several algorithms available [99]. One very easy to implement, yet effective algorithm has been proposed by Itoh [100], which shall be summarized shortly for the 1-dimensional case. Typically, one defines two operators  $W$  and  $\Delta$  for describing phase unwrapping algorithms:

$$\Phi(n) = W[\varphi(n)] = \varphi(n) \pm 2\pi k(n) \quad (4.47)$$

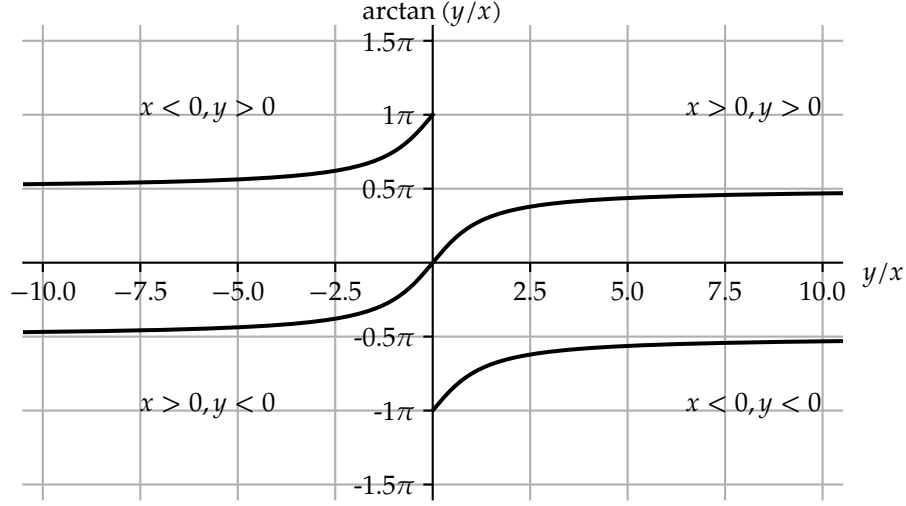


**Figure 4.12:** Plot of the four-quadrant arctangent function (arctan2 in most programming languages). Depending on the signs of the arguments, the function returns values in the range  $(-\pi, \pi]$ .

and

$$\Delta[\varphi(n)] = \varphi(n) - \varphi(n-1). \quad (4.48)$$

$\varphi(n)$  describes a discretely sampled continuous phase.  $k(n)$  is an integer, so that  $-\pi < W[\varphi(n)] \leq \pi$ . So,  $W$  describes the wrapping of the phase into  $(-\pi, \pi]$  and  $\Delta$  the backward difference. One can show now [100], that the phase at a point  $m$  can be written as

$$\varphi(m) = \varphi(0) + \sum_{n=1}^m W_2[\Delta[W_1[\varphi(n)]]]. \quad (4.49)$$

This represents the integration of the wrapped differences of the wrapped phase. For this, it is important that

$$-\pi < \Delta[\varphi(n)] \leq \pi \quad (4.50)$$

holds true. Due to noise in the signal, this is not always the case, which leads to distortions in the unwrapped phase if not accounted for. Since the Itoh algorithm integrates the signal along a given path (e.g. along a row in an image), such distortions propagate along the path. A lot of different algorithms have been proposed over the years to remedy this problem, but these are mostly computational intensive. In cases where the region of interest is essentially free of artifacts, which holds true most of the time with SODI, the Itoh algorithm offers good performance.

### 4.3.3 Phase-Shifting Interferometry in the Case of SODI

The previous subsection gave a general overview about Phase-Shifting Interferometry methods. This subsections focus will be on the application of PSI in SODI,

explaining the image processing and also the extraction of thermodiffusive quantities as employed in this work.

### Stack File Format

As already mentioned, SODI also employs PSI in the form of a Mach-Zehnder interferometer, which records 2-dimensional interferograms of a Soret cell. The operational mode of SODI is configured in such a way that, by slight tuning of the wavelength of the diode lasers, a consecutive phase-shift of  $\pi/2$  is introduced, acting as temporal carrier. Starting with a reference phase of  $\Phi_R = 0$ , the phase is shifted by  $2\pi$  in total, leading to 5 distinct phase-shifted states of the interferogram. SODI records each of these states, only about a fraction of a second apart, as RAW 8-bit grayscale images with  $1920 \times 1080$  pixels resolution and stores these five images together in a so-called Stack-file format (STK in the following). This file format not only stores the RAW image information, but also the associated filenames, which encode a timestamp among other information to allow correct ordering of all images, see also Fig. 4.13. A typical filename of a single RAW image is given like this [89]:

11\_0\_5D2B@0018\_FR\_RAW\_140621\_133058\_9.raw

The first part gives information about the **measurement process** generating the image file:

- **11**: experiment ID
- **0**: cell number (here, 0 signifies the companion cell)
- **5D2B**: checksum of the measurement script generating the file
- **0018**: current step in the measurement script

This is followed by information about the **light source**:

- **FR**: laser (FR meaning fixed red)
- **RAW**: type of image (RAW camera image)

The last part is a **unique timestamp**:

- **140621**: date (21st of June 2014)
- **133058**: time (13:30 and 58 seconds)
- **9**: increment counter to distinguish two files with identical timestamp

The resulting STK filename, containing five such RAW images, follows the same convention, with the only difference that RAW is replaced by DSC and a file extension “.stk” instead of “.raw”. An in-depth description of the file format is also provided in the SODI Software Manual [89].

The rationale behind the STK file format is to allow easy application of a five-image temporal PSI algorithm, as the one presented in Eq. (4.39). But it is not the only option, since a slight tilt in the beam path leads to a spatial carrier frequency, as seen in Fig. 4.10. If this frequency is sufficiently high with respect to the spatial phase variations in the sample, one is not limited to temporal algorithms, but can employ spatial algorithms as presented in Section 4.3.2. In fact, different groups in the DCMIX team, which are tasked with the analysis of the SODI data, apply different algorithms. For example, the groups of T. Lyubimova and I. Ryzhkov specialized in the Fourier Transform method, while the groups of V. Shevtsova and W. Köhler apply temporal algorithms (spatial algorithms are also currently being implemented in Bayreuth). This has a clear advantage: for one, comparison of the evaluation of the same dataset by different groups allows to cross-check for errors in the methods, enhancing confidence in the results. Also, applying the temporal and spatial methods in parallel guarantees that the data can be evaluated even in case of a failure of the phase-shifting, which would be a minor problem on ground, but catastrophic in microgravity, since repetition of an experiment after the fact is not possible.

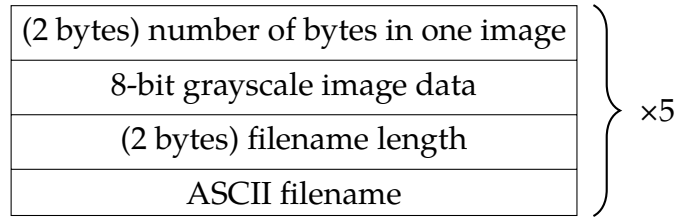


**Figure 4.13:** General layout of a STK file.

Since data storage capacity on the ISS is limited, and each STK file requires 10 MB disk space, image acquisition with a constant high frame rate over the duration of a run (about 75 000 s) is not feasible. But since the timescales of the involved processes are different, with the concentration gradient evolving much slower than the temperature gradient, a dynamic frame rate during the different experiment stages can drastically reduce storage requirements.

### Image Processing

An important step in the analysis is the image processing, i.e. the cropping and rotating of the RAW images within one image stack. The camera in SODI is fixed within the optical module and allows only lateral alignment to the cell under study and the cell volume fills only about half of the image. Also, the cell is not perfectly horizontal with respect to the image borders. This necessitates a rotation



and cropping of the image, to only include the cell volume and align the  $y$ -axis of the image with the temperature gradient (see Fig. 4.14). After this step, either via applying Eq. (4.39) to all five RAW images in a stack or via Eq. (4.46) applied to single RAWs (or any other suitable phase stepping algorithm), the wrapped phase image can be recovered.

The next important step in the processing is the subtraction of a reference phase image. Since all phase values recovered via Eqs. (4.39) and (4.46) only describe differences between the object and reference wavefronts, whose absolute phase states are unknown, these values are per se not meaningful. They only gain meaning when compared to a known reference state. Therefore, a reference image stack within one experimental run is chosen, processed in the same manner as above, and the resulting wrapped phase values subtracted from the phase image under study. The resulting difference image describes changes in the phase relative to this reference state, allowing to observe the temporal evolution of the wavefront phase under controlled variation of experimental parameters.

These wrapped images offer a complete view of the cell as well as regions outside of it. But for further analysis, a region of interest (ROI) has to be defined within the cell volume, as the cell design leads to some dead volume on the lateral walls (see Section 4.3.1). Detailed studies by Mialdun et al. [101–103] have shown that these lateral dead volumes can even lead to convective vortices in the corners of the cell if used under normal gravity conditions. Even though this problem does not arise in microgravity, the deformation of the temperature gradient introduced by this cell design is significant near the walls. Therefore, the region of interest is restricted to a smaller stripe of 600 px along the  $x$ -axis to restrict analysis to a region with an approximately linear temperature distribution. Along the  $y$ -axis, a similar problem arises near the protrusions, since the temperature gradient is non-linear along the border between the cell material and the sample liquid. So the ROI does not extend up to the full height of the cell ( $H_p \approx 760$  px), but is slightly smaller (700 px), see Fig. 4.14.

## Software

The analysis process described above has to be applied to all STK files of a run ( $\sim 600$  for DCMIX3), amounting to 6 GB of consecutive image data per laser. In total, DCMIX3 yielded  $\sim 470$  GB of data, so a comprehensive approach to image processing and signal recovery is needed. With the experience from participating in the analysis of DCMIX1 data, a software package was written for this work, offering a reproducible and automated process for phase calculation, image manipulation and signal recovery. This software comprises a core library offering basic functionality, written in C and utilizing the open source FreeImage library, as well as a Python interface with several commandline programs for automation. A more detailed description of the software is given in the appendix Appendix D.

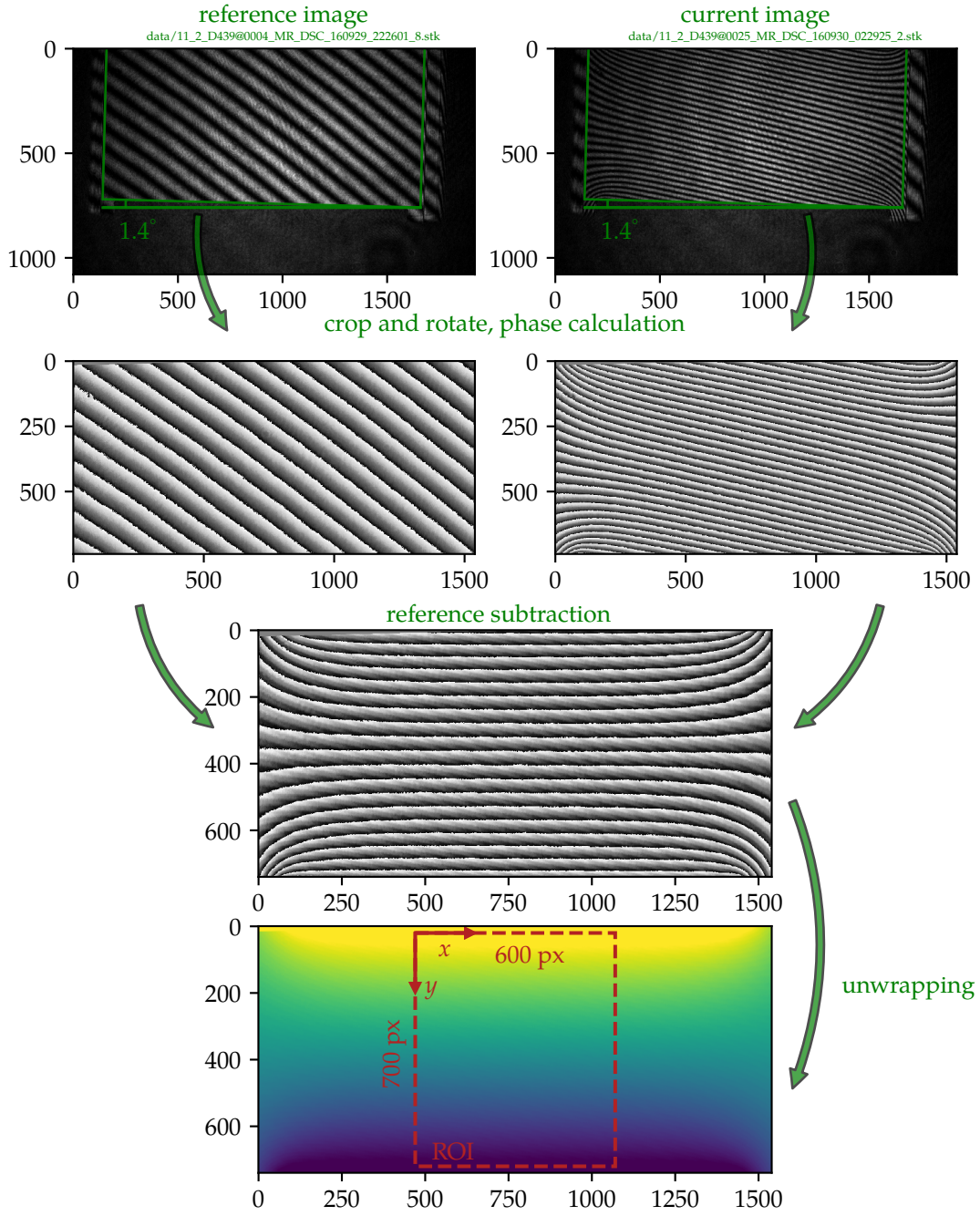


**Figure 4.14:** Image processing steps, from top to bottom, on example images from DCMIX3 run 07, cell 2. First, the raw images need to be cropped and rotated, to focus on the cell volume. In this example, a rotation of  $1.4^\circ$  is necessary. In the second step, Eq. (4.39) is applied to the cropped and rotated RAW images, resulting in a wrapped phase image. Then, the reference image is subtracted from the image under study. After unwrapping of this difference image, a regular phase map of the visible cell volume is obtained. For signal extraction, one wants to avoid regions with a non-uniform temperature gradient. Therefore, the ROI for further processing is restricted to 600 px in  $x$ -direction and 700 px in  $y$ -direction, centered on the middle of the cell.

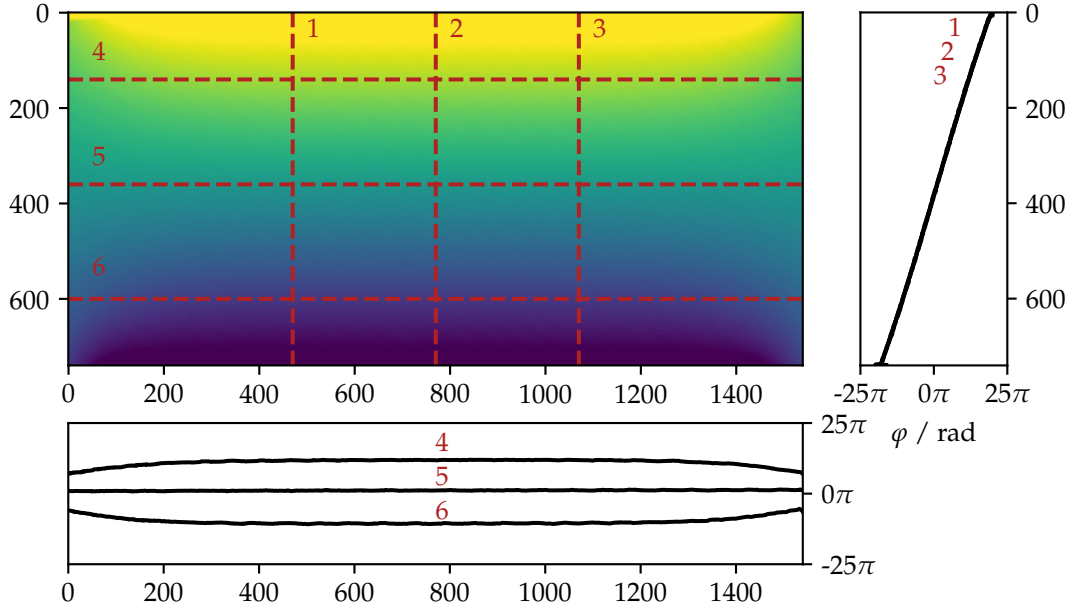


**Figure 4.15:** Phase gradient in the unwrapped image from Fig. 4.14 along the dashed lines. Along the vertical axis, all three cuts (lines 1, 2 and 3) are practically indistinguishable. Only outside the ROI, on approach of the lateral walls, a significant deformation of the phase gradient is visible (see lines 4, 5 and 6). The image is taken from the last stage of the run, in the quasi-steady state, cf. Fig. 4.16.

#### 4.3.4 Dimensionless Analysis

For extraction of transport coefficients, the same reasoning as for all optical experiments conducted in parallelepipedic Soret cells applies (see Section 2.1.3 and Section 2.2) and the same solution Eq. (2.25) as in OBD is valid for the case of SODI. Since the OBD signal has been studied extensively and is well understood, cf. Section 4.1.2, an identical approach is taken in the evaluation of SODI data in this work. Specifically, this allows to reuse the fitting routines developed by Gebhardt for OBD, significantly simplifying comparison between ground- and microgravity-based experiments. In OBD, the signal is defined by the refractive index gradient along the cell height normalized to the thermal amplitude, see Eq. (4.9). Phase and refractive index are connected by a simple multiplicative factor,

$$n_\lambda = \varphi \frac{\lambda}{2\pi L}, \quad (4.51)$$

with  $L$  the geometric light path along the cell, which allows to write the equivalent of Eq. (4.9) in the case of SODI:

$$\frac{\Delta\varphi_i}{\Delta\varphi_{T,i}} = 1 + \sum_{k=1}^{K-1} M_{ik} \frac{\partial \tilde{C}_k}{\partial \tilde{z}}, \quad (4.52)$$

with  $\Delta\varphi_T$  the purely thermal portion of the phase gradient.

This means that, by extracting the phase gradient  $d\varphi/dy$  in the middle of the cell for every unwrapped phase image in a SODI run (see Fig. 4.15), a signal analogous to OBD can be recovered, which is then subjected to the same fitting routine. To determine the gradient reliably, a polynomial is fitted to the phase information along 700 px parallel to the temperature gradient for all 600 columns in the ROI. The resulting 600 polynomials are averaged, to minimize the influence of artifacts in the image. The phase gradient can now be computed, by taking the derivative of this averaged polynomial and evaluating it at the center  $H_p/2$  of the cell. Doing this for all phase images in a run and taking the timestamps of the files as time axis, a signal as shown in Fig. 4.16 can be recovered.

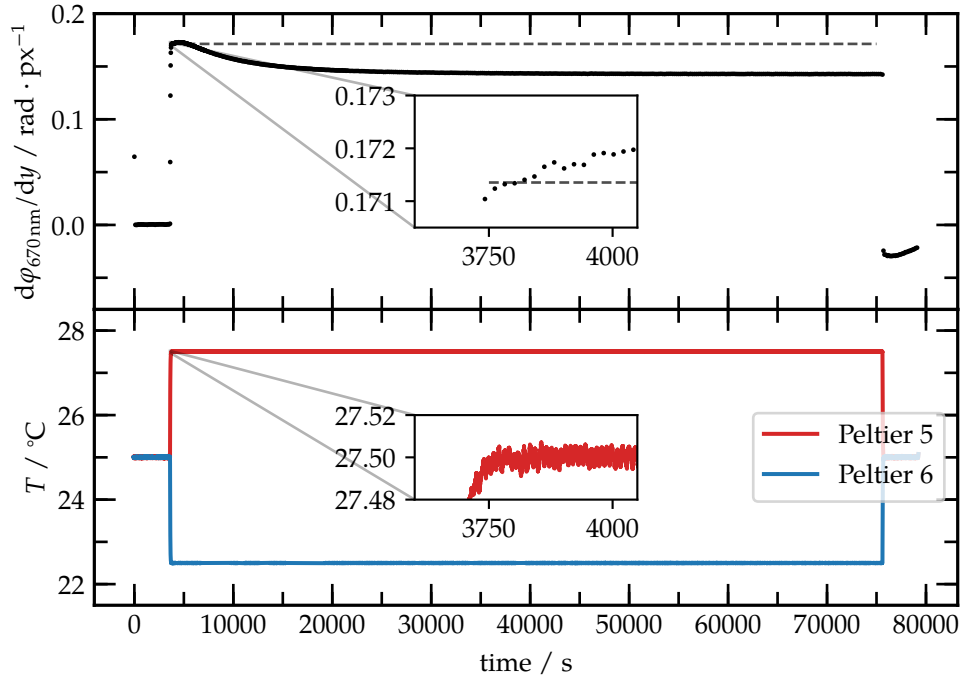


**Figure 4.16:** Phase gradient in the center of the cell for DCMIX3 run 07, cell 2, MR laser. The signal shows similar behaviour as in the case of OBD, see also Fig. 4.4. But due to a different cell height (5 mm vs. 1.42 mm), the timeconstants for thermal and mass diffusivity are about 12 times longer ( $\sim h_{\text{SODI}}^2/h_{\text{OBD}}^2$ ). It is also important to note that the amplitudes  $M_{ik}$  can be negative, as is the case in this sample.

### Thermal Amplitude

The insets in Fig. 4.16 show the zoomed signal and temperature data on Peltier 5 around the time when the thermal gradient has stabilized. Switching of the gradient happens around time mark 3600 s, stabilization is finished around 3820 s (in contrast to OBD, no special ballistic heating is employed in SODI, solely relying

on PID regulation). By comparing temperature data and the signal, the thermal plateau can still be determined quite reliably, as is marked in the insets. During signal fitting, the data is normalized on the thermal amplitude determined this way. To compensate for the relatively slow gradient buildup, the start time for the fitting algorithm can be shifted. Instead of starting analysis at the time of reaching the thermal amplitude, time zero can be shifted to earlier times during the gradient buildup, which corresponds more with the physical reality, since mass diffusion already starts in this phase. From experience, by estimating the time when the areas under the thermal signal as well as between thermal signal and its plateau are equal, one can choose this as new effective starting time  $t_{0,\text{eff}}$  for fitting, see Fig. 4.17.

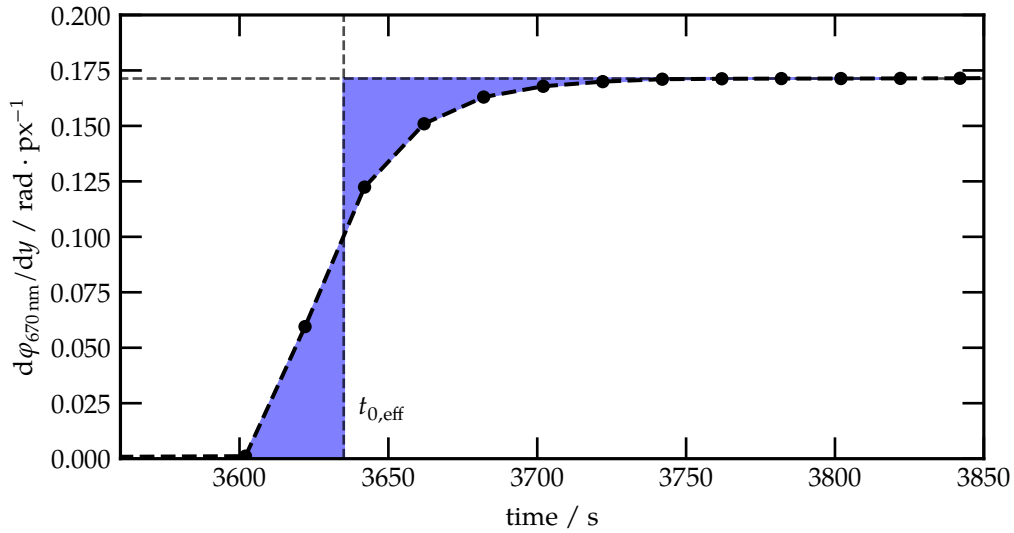


**Figure 4.17:** Zoomed plot of the thermal signal from Fig. 4.16. For determining the effective start time  $t_{0,\text{eff}}$  for fitting of the concentration signal, one has to keep in mind that diffusion starts already during gradient switching. By estimating the time when the two shaded areas are equal, a good compromise for this effective value can be found.



## 5 Results and Discussion

The previous chapters introduced basic concepts and the experimental methods. Special focus has been given to the DCMIX project, since it constitutes the framework binding ground-based and microgravity related activities together. This chapter summarizes the results gathered from analysing SODI-DCMIX1 data compared to literature, as well as SODI-DCMIX3 data compared to OBD experiments conducted in Bayreuth.

### 5.1 DCMIX1

As detailed in Section 3.1, SODI-DCMIX1 operations were successfully concluded in 2011/2012, but analysis of the gathered data is still ongoing. Since this was the first iteration of the project, providing reliable reference data on one of the model ternary systems for the first time, special care is taken about the evaluation process to identify systematic error sources. Therefore, when the first work of the Bayreuth team on DCMIX3 started in 2013/2014, participating in the analysis of DCMIX1 data provided a good opportunity to test the implemented software. Most importantly, first ternary data from OBD measurements became available through the work of Gebhardt [79], allowing a direct comparison to values obtained on ground; this is especially true when using the OBD fitting routine, as described in Sections 4.1.2 and 4.3.4. So, via the group of V. Shevtsova, access to the full data set of DCMIX1 was provided to the Bayreuth group. This section will first summarize the available literature data on contrast factors for SODI as well as OBD; after that the data quality of SODI-DCMIX1 will be quantified, as this has important consequences for the evaluation. Finally, utilizing available reference values for SODI data from other teams, as well as OBD and TGC measurements, a comprehensive comparison of microgravity and ground measurements will be presented.

#### 5.1.1 Contrast Factors

For the conversion between refractive index space and concentration space, a precise knowledge of the optical contrast factors is necessary, cf. Section 2.2. Refractive indices of tetralin, isobutylbenzene and dodecane have already been measured by Sechenyh et al. in Ref. [104] for the SODI wavelengths at 25 °C; the employed infrared laser of 925 nm does not exactly match the SODI wavelength of 935 nm, but dispersion in the infrared range is negligible, making them equivalent

for this use case. Using the parametrization given in [104], the contrast factors and condition numbers for the DCMIX1 compositions can be calculated, see Table 5.1 and Fig. 5.1. In ternary systems, the choice of the independent concentrations  $c_1$  and  $c_2$  is important for interpretation, so in the remainder of this chapter  $c_1$  will always be THN,  $c_2$  will be IBB. The dependent concentration  $c_3$  is nC12. Literature data given in different systems can be transformed accordingly (see the appendix of Ref. [78] for an explanation of such transformations).

Since OBD measurements in this system have been performed earlier by Gebhardt, a parametrization of the refractive index at 405 nm and 633 nm is also available in the literature, see [31], as well as data on the (thermo)diffusion coefficients, see [79]. The calculated contrast factors and condition numbers are also given in Table 5.1 and Fig. 5.1. Furthermore, measurements with TGC have been performed by Larrañaga et al. [105]. In this reference, values for the thermodiffusion and diffusion coefficients as well as the Soret coefficients are given for all DCMIX1 mixtures. As with the optical techniques, concentration determination in ternary TGC measurements has to be performed via contrast factors. But contrary to OBD or SODI, since with TGC the determination is performed ex-situ, they need not be purely optical. In fact, the conversion to concentration space can be performed via refractive index derivatives as first contrast factor and the density ( $\rho$ ) derivatives as second contrast factor:

$$\begin{pmatrix} \Delta n_\lambda \\ \Delta \rho \end{pmatrix} = \underbrace{\begin{pmatrix} \partial n_\lambda / \partial c_1 & \partial n_\lambda / \partial c_2 \\ \partial \rho / \partial c_1 & \partial \rho / \partial c_2 \end{pmatrix}}_{N_c} \cdot \begin{pmatrix} \Delta c_1 \\ \Delta c_2 \end{pmatrix}. \quad (5.1)$$

This is the equivalent of Eq. (2.29) in the case of TGC. The relevant contrast factor values for the DCMIX1 mixtures measured in Ref. [105] were kindly provided by the authors and are also summarized in Table 5.1.

Ternary plots for the resulting condition numbers across the whole composition space of THN, IBB and nC12 for the wavelength combinations 405/633 nm and 670/925 nm are shown in Fig. 5.1; the compositions of the SODI-DCMIX1 measurements are marked with red dots. For the choice of compositions the DCMIX team had to compromise on mixtures with relatively low condition numbers, while still retaining a reasonable coverage of the composition space. It is obvious from these plots that the OBD wavelengths result in much lower condition numbers, well below 150, while for the SODI wavelengths condition numbers can rise up to 1000. This can be attributed mainly to dispersion: on approach of the infrared range, as is the case with SODI, the weak dispersion leads to very similar values for the elements of the contrast factor matrix  $N_c$ ; in turn, the determinant  $\det(N_c)$  approaches zero. But one of the necessary prerequisites for the matrix  $N_c$  to be invertible is  $\det(N_c) \neq 0$  [28]. So the high condition numbers in the case of SODI are a consequence of a numerical deviation from this prerequisite due to almost similar refractive indices in the red to infrared range. In turn, this means that determination of concentration changes (and therefore diffusive quantities) is affected with a higher uncertainty in SODI (Section 2.2). Of course, one



**Table 5.1:** Contrast factors and condition numbers for the DCMIX1 cells with components tetralin ( $c_1$ ), isobutylbenzene ( $c_2$ ) and dodecane ( $c_3$ ) (compositions in weight fraction) in the case of OBD, SODI and TGC, all at 25 °C. Contrast factors and condition numbers were computed from parametrized refractive index values taken from [31] and [104] in the case of OBD and SODI. Values for TGC were kindly provided by the authors of [105]; note the different reference system.

cell	$c_1$	$c_2$	$c_3$	$N_{c,11}$	$N_{c,12}$	$N_{c,21}$	$N_{c,22}$	cond( $N_c$ )
OBD								
				$\left(\frac{\partial n_{405 \text{ nm}}}{\partial c_1}\right)_{c_2}$	$\left(\frac{\partial n_{405 \text{ nm}}}{\partial c_2}\right)_{c_1}$	$\left(\frac{\partial n_{633 \text{ nm}}}{\partial c_1}\right)_{c_2}$	$\left(\frac{\partial n_{633 \text{ nm}}}{\partial c_2}\right)_{c_1}$	
1	0.10	0.10	0.80	0.112030	0.068551	0.097228	0.056518	90
2	0.10	0.80	0.10	0.145390	0.091405	0.125660	0.075728	107
3	0.80	0.10	0.10	0.166800	0.105970	0.143610	0.088186	133
4	0.45	0.10	0.45	0.134860	0.084175	0.116630	0.069951	114
5	0.40	0.20	0.40	0.136300	0.085178	0.117850	0.070758	114
6	0.50	—	0.50	0.133430	—	0.115430	—	—
SODI								
				$\left(\frac{\partial n_{670 \text{ nm}}}{\partial c_1}\right)_{c_2}$	$\left(\frac{\partial n_{670 \text{ nm}}}{\partial c_2}\right)_{c_1}$	$\left(\frac{\partial n_{925 \text{ nm}}}{\partial c_1}\right)_{c_2}$	$\left(\frac{\partial n_{925 \text{ nm}}}{\partial c_2}\right)_{c_1}$	
1	0.10	0.10	0.80	0.095980	0.054747	0.926410	0.052127	342
2	0.10	0.80	0.10	0.124820	0.075771	0.119800	0.071440	254
3	0.80	0.10	0.10	0.142710	0.088696	0.137370	0.083768	241
4	0.45	0.10	0.45	0.114890	0.068594	0.110740	0.065510	495
5	0.40	0.20	0.40	0.116350	0.069607	0.112010	0.066732	1092
6	0.50	—	0.50	0.113240	—	0.109490	—	—
TGC								
				$\left(\frac{\partial n_{589 \text{ nm}}}{\partial c_1}\right)_{c_3}$	$\left(\frac{\partial n_{589 \text{ nm}}}{\partial c_3}\right)_{c_1}$	$\left(\frac{\partial \rho}{\partial c_1}\right)_{c_3}$	$\left(\frac{\partial \rho}{\partial c_3}\right)_{c_1}$	
1	0.10	0.10	0.80	0.089227	-0.094189	0.040406	-0.057614	16
2	0.10	0.80	0.10	0.105245	-0.122807	0.048842	-0.077341	16
3	0.80	0.10	0.10	0.117569	-0.145028	0.054968	-0.090423	17
4	0.45	0.10	0.45	0.101875	-0.115505	0.046719	-0.071311	17
5	0.40	0.20	0.40	0.102365	-0.116189	0.047269	-0.071804	17

has to bear in mind that SODI is a multi-purpose instrument: by design, it was always meant to fulfill other roles besides the Mach-Zehnder configuration used for DCMIX (i.e. IVIDIL and COLLOID experiments), including Particle Image Velocimetry and Near Field Scattering [29, 88, 106]. So, the choice of wavelengths was influenced by multiple factors, and even though a more favourable combination for DCMIX could be argued for, this does not prevent the extraction of useful reference data in any way.

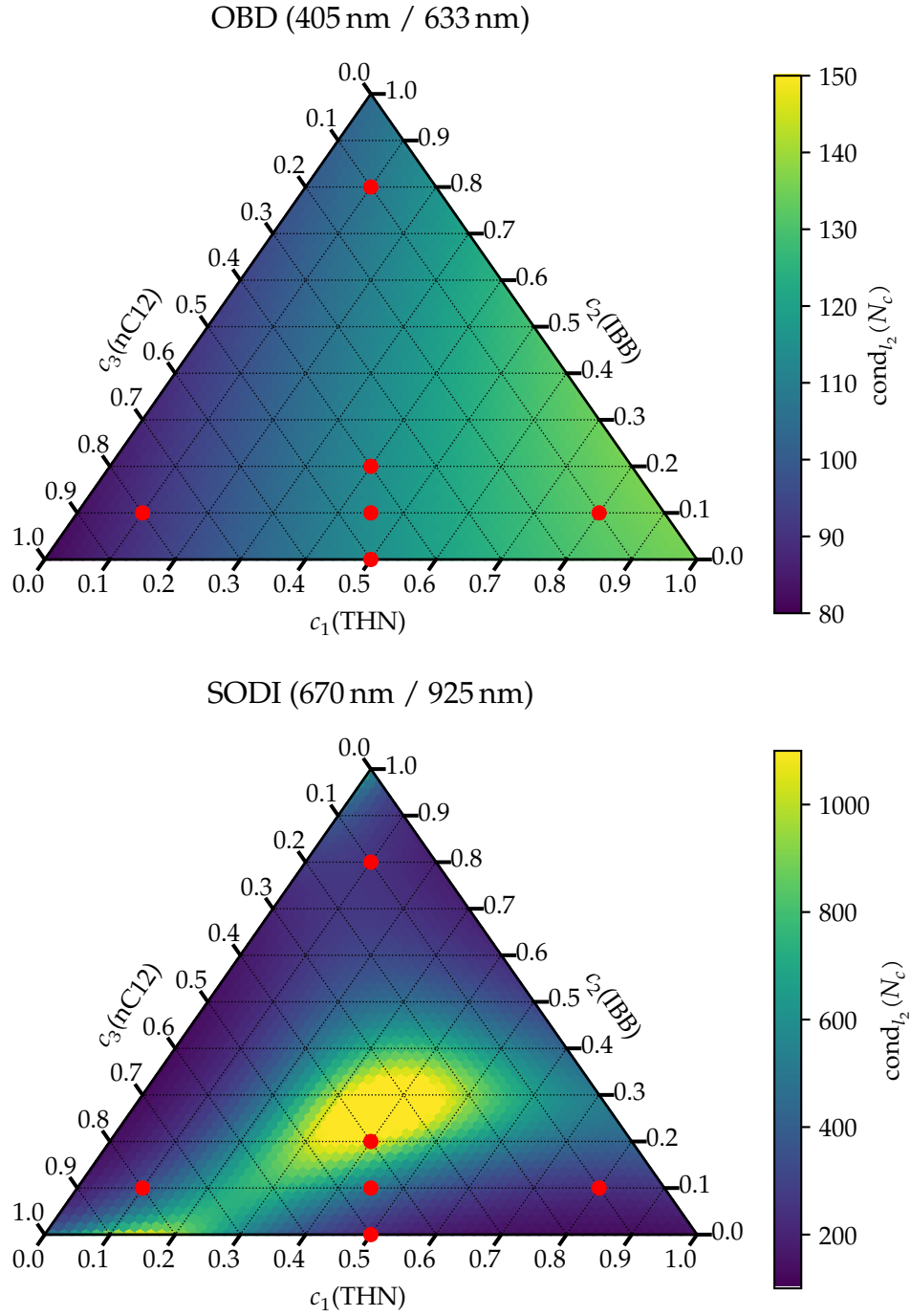


**Figure 5.1:** Condition numbers for OBD (top) and SODI (bottom) experiments. Computed from parametrized refractive indices at 25 °C given in [31] for OBD and in [104] for SODI wavelengths. Red dots mark the mixtures chosen for SODI-DCMIX1 measurements. Notice the different scales in the colour map, with the SODI configuration yielding higher condition numbers.

### 5.1.2 SODI-DCMIX1

For processing of the SODI-DCMIX1 data, a timeline of all runs was necessary to correctly assign STK files to the respective run based on their timestamps. Furthermore, extraction of the temperature data from the database of all housekeeping data collected by MSG is also based on the timestamps. Such a timeline was prepared by the team at MARS USOC, which was responsible for operations of DCMIX1. In total, 55 runs were performed, 34 of which were conducted at a mean temperature of 25 °C and 21 at 40 °C. Unfortunately, during operations one of the SSDs of SODI failed, corrupting the data stored on that drive. Recovery efforts could restore most images, but the mirror provided to the Bayreuth team did not contain these recovered images. Also, up until the time of writing, only contrast factors for 25 °C have been published in the literature. Even though experiments in preparation in Bayreuth might be capable of providing contrast factors at different temperatures in the future, analysis has been limited to runs with 25 °C mean temperature. Taking these factors into account, 20 SODI-DCMIX1 runs have been analyzed for this work; Table 5.2 gives an overview of these runs.

The description of DCMIX1 operations given in Section 3.1 already mentioned some other problems present in the data: after the second week, a bubble had formed in cell 1 (see Fig. 3.2). Also, cell 5 exhibited a problematic phase stepping and temperature regulation; an example of such behaviour is given in Fig. 5.2. To better quantify such problems, the next section will categorize the data based on some quality criteria. Data quality in the case of SODI can be split into three sub-domains most relevant to the measuring process: the image quality of individual interferograms, the consistency of the phase-stepping between these images and the stability of the applied temperature gradient.

#### RAW Image Quality

Since SODI interferograms are 8-bit grayscale RAW images (5 per STK), the resulting phase image depends directly on their quality. In this work, quality refers to specific metrics, which will be calculated for a central region in the image, about 20 % in  $x$ -direction and 60 % in  $y$ -direction. This is the region most relevant to analysis, since on approach of the boundaries the phase map can become non-linear. Also, this is in accordance with the ESR document, formulating the scientific goals and quality metrics for DCMIX.

The first metric of interest is the dynamic range of the images. Since the color-depth is 8-bit grayscale, 256 different intensity values can be discerned. But depending on the illumination and the camera settings, excessive black or white saturation can narrow the dynamic range and lead to distortions in the phase calculation. Saturation means the relative amount of completely black (grayscale value 0) or white (grayscale value 255) pixels inside one RAW image. The black and white saturation has been determined for all analyzed runs, taking the mean across all RAWs and all STKs in a run for the different lasers (Fig. 5.3). There is an imme-

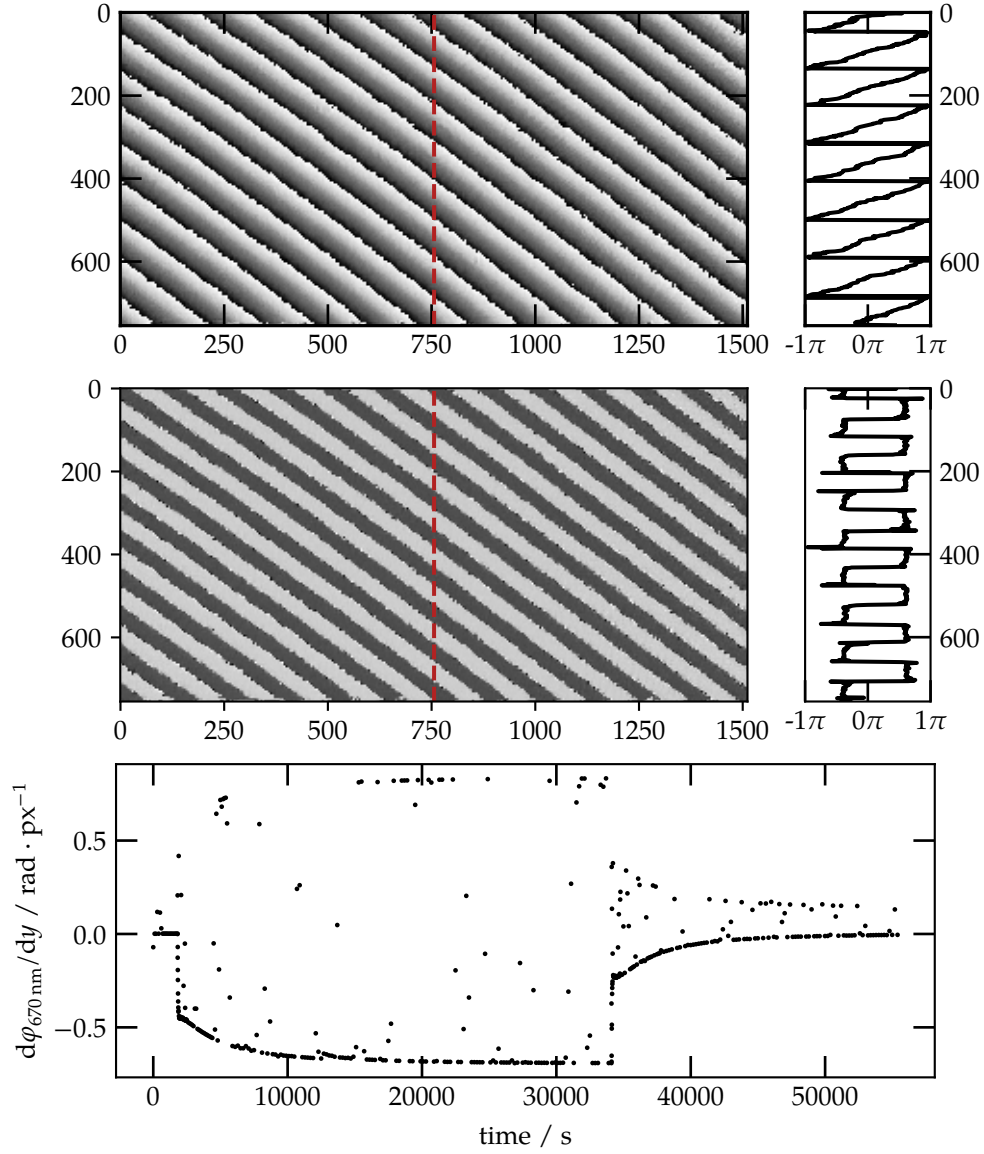


**Figure 5.2:** Phase stepping in DCMIX1 cell 5 during run 05. The top wrapped phase image shows the expected behaviour, with values inside the full range  $(-\pi, \pi]$ . The image in the middle is exemplaric for problematic phase stepping in SODI, effecting distorted wrapped phase values when applying temporal PSI algorithms. The plot on the bottom shows the resulting noisy phase gradient signal in run 05.

diagnose observation from this plot: while white saturation is well below 1 % for all runs and lasers, and black saturation as well in the case of the MR and MN laser, the FR laser shows an excessive black saturation of up to 10 % in all runs.

The second RAW quality criteria is contrast: the interferograms basically consist of a sinusoidal grayscale modulation, cf. Eq. (4.31). To reliably extract phase

**Table 5.2:** List of all DCMIX1 runs analyzed for this work.

run	start time	end time	low SNR	remarks
cell 1				
06	10-12-2011 07:74:00	10-12-2011 18:16:00	—	bubble
16	02-12-2011 00:49:19	02-12-2011 11:17:25	—	
21	04-12-2011 05:04:10	04-12-2011 15:35:00	—	
26	12-12-2011 12:26:00	12-12-2011 22:53:00	—	bubble
cell 2				
02	07-12-2011 18:01:00	08-12-2011 09:27:00	—	ext. Soret phase
17	02-12-2011 11:17:25	02-12-2011 21:44:11	—	
22	10-12-2011 18:38:00	11-12-2011 05:05:00	—	
27	12-12-2011 22:53:00	13-12-2011 09:19:00	—	
27b	15-01-2012 07:39:00	15-01-2012 19:36:00	MR	
cell 3				
03	08-12-2011 09:27:00	09-12-2011 00:53:00	—	ext. Soret phase
18	02-12-2011 21:44:11	03-12-2011 08:10:00	—	
23	11-12-2011 05:05:00	11-12-2011 15:32:00	—	
28	15-01-2012 19:36:00	16-01-2012 06:02:00	MR	
cell 4				
04	09-12-2011 00:53:00	09-12-2011 16:21:00	—	ext. Soret phase
19	03-12-2011 08:10:00	03-12-2011 18:40:00	—	
24	11-12-2011 15:32:00	12-12-2011 01:59:00	—	
cell 5				
05	09-12-2011 16:21:00	10-12-2011 07:47:00	MR,MN	ext. Soret phase
15	01-12-2011 14:21:55	02-12-2011 00:49:19	MR,MN	
20	03-12-2011 18:40:00	04-12-2011 05:04:10	MR,MN	
25	12-12-2011 01:59:00	12-12-2011 12:26:00	MR,MN	

information from this modulation, the contrast between the modulation and background, either in the temporal or spatial sense, has to be high enough. A common measure for this is the so-called Michelson contrast; since for the phase calculation in this work the temporal algorithm Eq. (4.39) is used, the Michelson contrast can be defined accordingly:

$$C_M(x, y) = \frac{I_{\max}(x, y) - I_{\min}(x, y)}{I_{\max}(x, y) + I_{\min}(x, y)}. \quad (5.2)$$

This means that, when analyzing a stack of five RAW images, the contrast is defined on a per pixel basis, evaluating the maximum and minimum intensity values

for a specific pixel across the five images. Figure 5.5 shows the resulting averaged values for all analyzed runs in DCMIX1. In general, the contrast should be well above 0.5 to guarantee a good signal-to-noise ratio for phase calculation. The contrast for the MR and MN lasers is between 0.7 and 0.8 for most of the runs, which is sufficiently high. An exception to this are the contrast values for the FR laser: they are above 0.9 for all runs. This might well be a consequence of the high black saturation in the FR images, as shown in Fig. 5.3. On the other hand, a drop in contrast is visible in runs 27b and 28 for the MR laser, with contrast values below 0.6 and a relatively high standard deviation. To further analyze the reason for this contrast drop, Fig. 5.6 also shows the grayscale variance of the individual RAWs inside the STK files. The variance of a RAW image is given by

$$\text{Var}(I) = \frac{1}{N_x N_y} \sum_{x=0}^{N_x} \sum_{y=0}^{N_y} (I(x, y) - \bar{I})^2, \quad (5.3)$$

with  $\bar{I}$  the mean of all pixel values.  $N_x$  and  $N_y$  are the total number of pixels in  $x$ - and  $y$ -direction, respectively. The variance can be interpreted in the following way: a normal sinusoidal fringe pattern will exhibit a histogram as shown in Fig. 5.4 (left). During phase stepping, this histogram should keep its bimodal distribution, except for effects from the slight output power change discussed in Section 4.3.2. As can be seen from Fig. 5.4 (right), in case of a low Michelson contrast, this no longer holds true for all RAWs in a STK file: during phase stepping, the histogram is deformed to an almost unimodal distribution; the sinusoidal fringe pattern is washed out. The variance now reflects exactly this spread in the histogram: as the sinusoidal pattern is lost, the distribution gets narrower with a lower variance. So, the low Michelson contrast in runs 27b and 28 can be understood, as Fig. 5.5 shows such a sharp drop of variance for the individual RAWs of these runs at the 670 nm wavelength. The underlying reason for this drop can only be speculated upon, but it seems rather plausible that some undesired behaviour of the light source comes into play; since only images for the MR laser are affected, the camera is probably performing as expected. For this, it is also instructive to look at the mean grayscale values, shown in Fig. 5.6: they show an almost constant behaviour in all runs, again except for the linear output change during phase-stepping. So, the interpretation of a constant mean and a dropping variance is, that the overall intensity of the light source stays constant, but the modulation introduced by interference is depressed. This could be attributed for example to a broadening of the wavelength spectrum, negatively affecting the coherence of the beams, or other instabilities of the laser diode.

The consequences of this become clear when calculating the transient phase gradient signals: the phase is affected with a high error, making interpretation of the signal almost impossible. But as mentioned, other runs also show a noisy phase gradient signal, most notably in cell 5, without any obvious deviations in the contrast (cf. Fig. 5.2). This indicates that laser instabilities do not always manifest themselves in the quality of the individual RAWs.

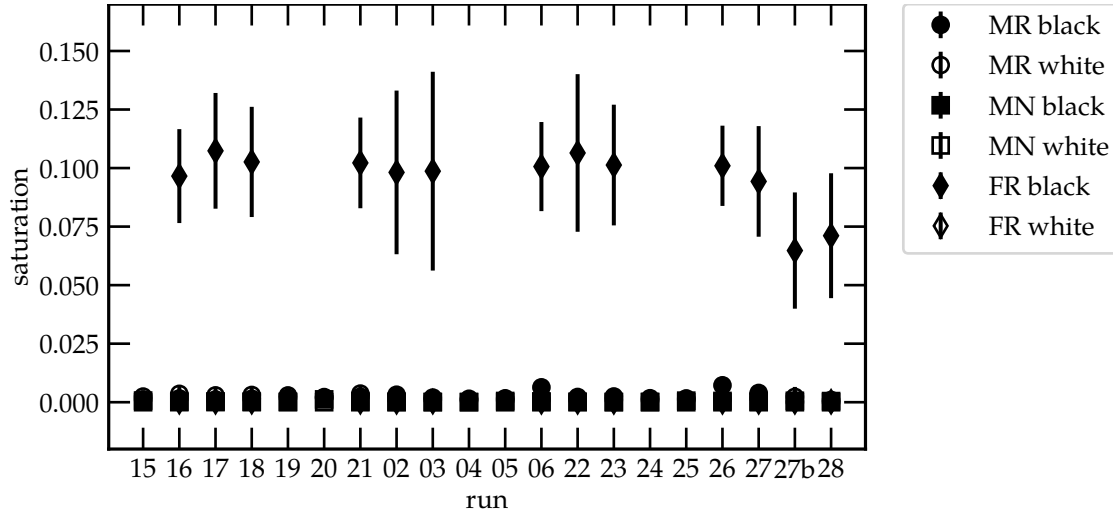


**Figure 5.3:** Percentage of black and white saturation in analyzed DCMIX1 runs; runs are given in chronological order. The saturation has been calculated from the RAW image histograms, averaged over all STKs in a run; the bars represent the standard deviation.

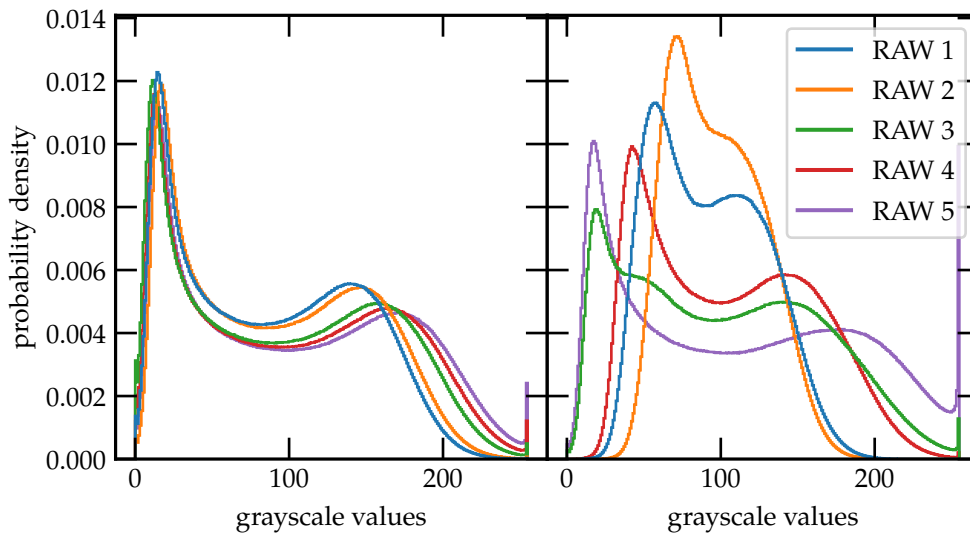


**Figure 5.4:** Histograms from DCMIX1, left run 05, right run 27b. Run 05 shows the expected bimodal distribution for a sinusoidal interferogram. During run 27b, the distribution especially of the first two RAWs is almost unimodal.

### Phase Step Estimation

Another possible consequence of problems with the laser stability, which would influence the phase calculation, is the consistency of the phase-stepping. That the low signal-to-noise ratio in the phase gradient in cell 5 is indeed a result of defective phase stepping can be verified by estimating the phase step between RAW images inside a stack. An algorithm for this was first proposed by Carré [93,

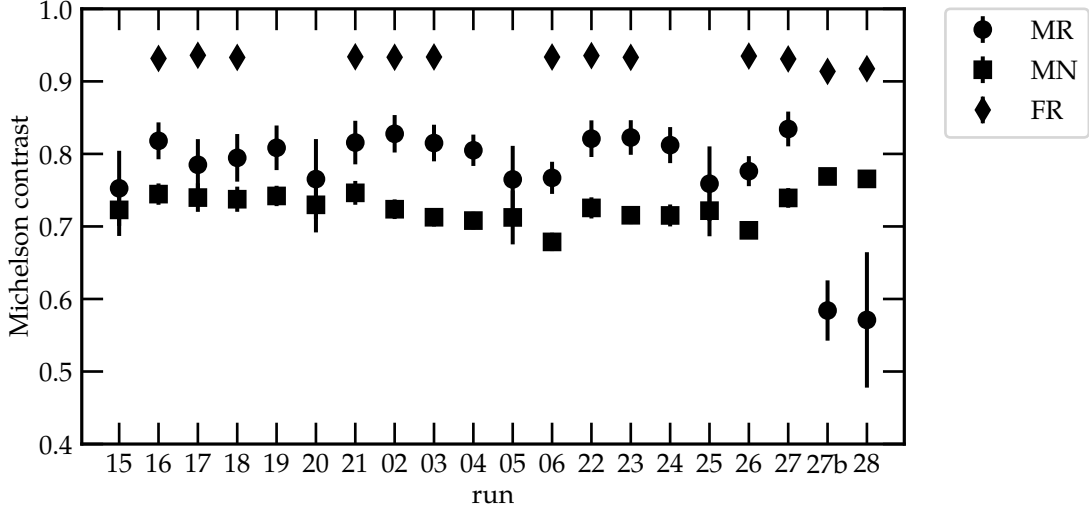


**Figure 5.5:** Michelson contrast of all analyzed runs in DCMIX1 as defined in Eq. (5.2); runs are given in chronological order. Values have been averaged over all STKs in a run, the bars represent the standard deviation.

107] and is still used today. Starting from four interferograms with an unknown phase-shift between them, it is able to estimate this temporal phase-shift without a priori knowledge:

$$\tan(\Delta\Phi_R/2) = \sqrt{\frac{3(I_2 - I_3) - I_1 + I_4}{I_1 + I_2 - I_3 - I_4}}, \quad (5.4)$$

with  $\Delta\Phi_R$  being the estimated phase-shift for a certain pixel  $(x, y)$ . Normally, the only requirement for the algorithm would be that these phase-shifts are the same between all images ( $\Delta\Phi_{R,n} = \text{const } \forall n$ ), which cannot be guaranteed for the problem at hand. But still, even for varying phase-shifts, using Eq. (5.4) across all pixels in all STK files of a run, and averaging the results, can give a good indication of problematic phase stepping. Since the algorithm requires only four images, but STK files from SODI contain five phase-shifted images, the calculation can be applied twice per STK: for images  $I_1$  to  $I_4$  or for  $I_2$  to  $I_5$ . Applying this estimation to SODI-DCMIX1 data results in Fig. 5.7. In the textbook of Servin [93], several phase-step algorithms are analyzed in detail, including their robustness against deviations from the nominal phase-step. For five-step algorithms as the one used in this work, Eq. (4.39), an error of 1 % is reached as soon as the phase-step deviates by circa  $\pi/16$ . Dashed lines in Fig. 5.7 mark this deviation of  $\pi/16$ , so points outside these indicate a problematic phase-stepping behaviour during a run.

Comparison with Table 5.2 shows that all runs in cell 5 with a low signal-to-noise ratio stand out in both estimations; so, for this cell a defective phase-stepping can be identified as reason for the problems during phase calculation. Runs 27b and 28, which already exhibited a low Michelson contrast, also show deviations in the phase-stepping for one of the estimations. The ultimate cause for the dis-



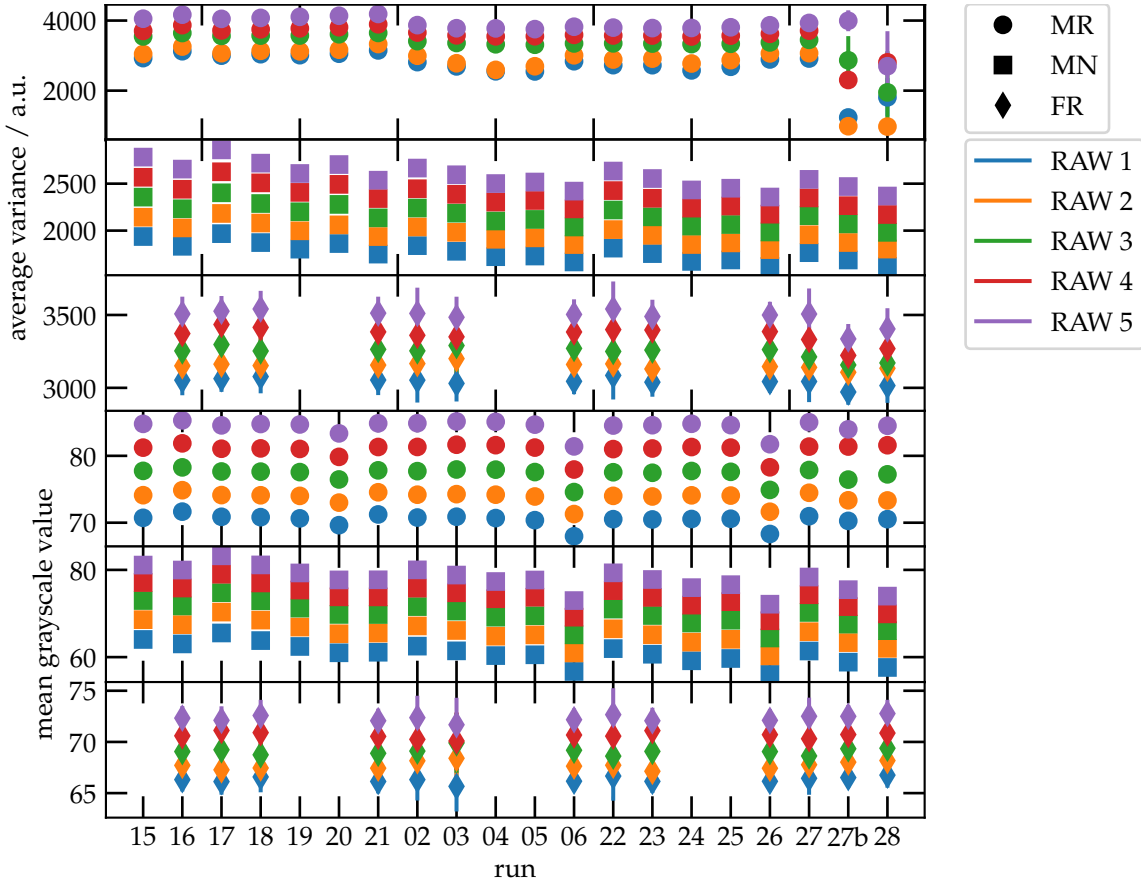


**Figure 5.6:** Variance (see Eq. (5.3)) and mean values in the grayscale levels for the individual RAWs within stack files, across all runs in DCMIX1; runs are given in chronological order. Values have been averaged over all STKs in a run, the bars represent the standard deviation.

cussed laser instabilities remains unclear, but it is curious that cell 5 is affected almost exclusively in all analyzed runs. Also, whereas in runs 27b and 28 only the MR laser is affected, the phase-stepping problems in cell 5 affect both lasers, even though the MN to a lesser degree.

### Temperature Regulation

The last important quality criterion is the stability of the temperature regulation. The regulation has two important aspects: for one, the temperature gradient has to be applied in a good approximation to a Heaviside-function; good in this case means, that the characteristic timescale of the application of the gradient should be much shorter than the typical timescale of the fastest diffusive process. Secondly, the applied gradient has then to be kept stable during the diffusion process, since large variations would effect a change in the driving force of the thermomodification process.

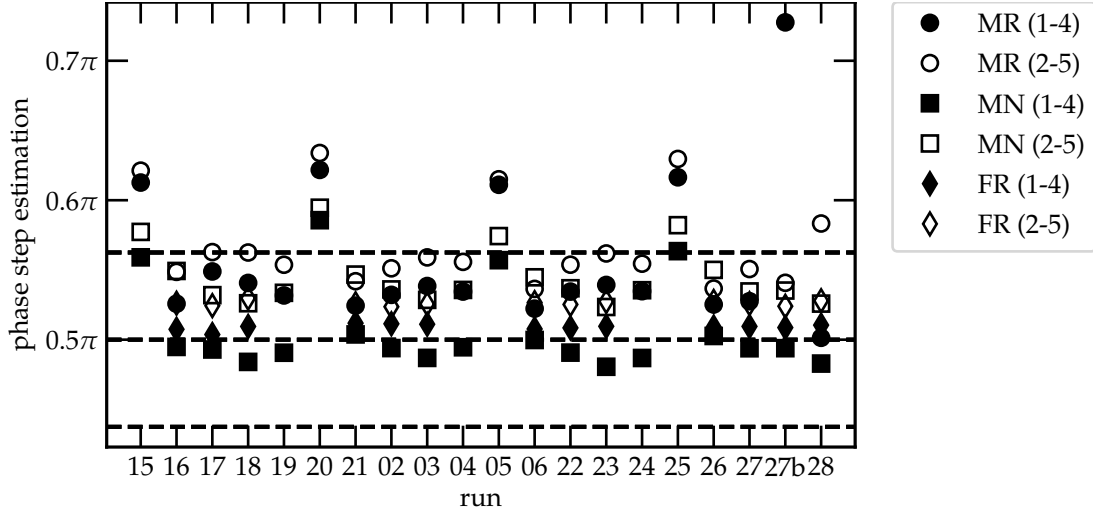


**Figure 5.7:** Estimated phase steps for all analyzed runs in DCMIX1, according to Eq. (5.4). Dashed lines represent a deviation of  $\pi/16$  from the desired phase step of  $\pi/2$ , translating to around 1 % error in phase calculation.

As explained in Section 4.3.1, temperature control in SODI is implemented via Peltier elements. In contrast to OBD, no ballistic heating/cooling is employed, with the regulation solely relying on a PID feedback loop. Naturally, this leads to a longer timescale for establishing the gradient, but since the cell height is much larger in SODI (5 mm instead of 1.43 mm in OBD), also the timescale for diffusion is much larger. A simple estimation

$$\tau = \frac{h^2}{\pi^2 D}, \quad (5.5)$$

with a typical diffusion coefficient  $D$  of  $5 \times 10^{-10} \text{ m}^2 \text{ s}^{-1}$  of aqueous solutions and  $h = 5 \text{ mm}$ , gives a timescale of 5066 s. In contrast, the typical time constant for gradient application in SODI is around 22 s for all DCMIX1 runs, so the gradient switching can still be considered as quasi-instantaneous.

To quantify the stability of the temperature gradient, the standard deviation of the temperature data after gradient buildup can be considered, as shown in Table 5.3. Typical values range from 0.6 mK to 3 mK, with exception of cell 4: here the standard deviation on the hot plate (Peltier number 9) is around 8 mK. Still, these noise levels are well within acceptable limits. The exception lies again with cell 5: additionally to the laser stability issues discussed above, also the temperature control exhibits abnormal behaviour. Values for the standard deviation range between 24 mK and 93 mK, an order of magnitude higher than in all other cells. Closer inspection of the temperature data revealed that this is not due to instrument noise but periodic fluctuations affecting both Peltiers, see Fig. 5.8. These fluctuations happen randomly during runs, with the temperature deviating up to 0.5 K from the set-point; after about 100 s, the set-point is reached again. If this

is related to some hardware issues or problems in the software feedback loop is hard to tell.

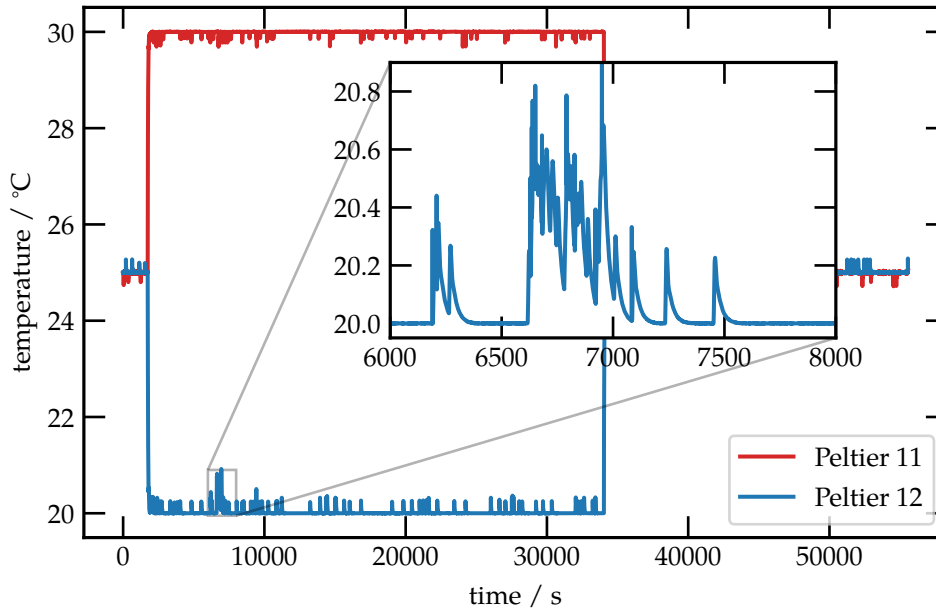


**Figure 5.8:** Temperature fluctuations in cell 5 during run 05. Even though these can lead to deviations of up to 0.5 K from the set-point, they decay much faster than the diffusion timescale.

### 5.1.3 Comparison Microgravity and Ground Results

The quality analysis above guides the subsequent determination of thermodiffusion coefficients from the data. Whereas the low contrast in runs 27b (cell 2) and 28 (cell 3) makes an analysis of these runs with available techniques impossible, all other runs in these cells show a stable contrast and phase-stepping behaviour. The obvious exception is cell 5, where all performed runs struggle with phase-stepping issues. Still, since not all images within a run are affected (cf. the transient phase gradient in Fig. 5.2), and the MN laser is significantly less prone to these problems, recovery of an analyzable signal seems possible. For this, offending STK files were removed by hand, mostly guided by comparing MR and MN signals to identify obvious outliers. This led to the purging of around 100 STK files per run, leaving between 200 and 300 ones (depending if the run featured an extended Soret phase or not) for analysis. Another problem is the bubble formation in cell 1, which happened after the second week of operations. This means that runs 06 and 26, even though performing well regarding the quality metrics, had to be excluded from this analysis, since the bubble can influence the diffusion process via a distorted temperature profile and Marangoni convection on the gas-liquid interface.

**Table 5.3:** Standard deviations of the temperature in SODI-DCMIX1, calculated after gradient stabilization.  $\delta T_{+/-}$  describes the standard deviation on the hot/cold plate.

run	$T_0/^\circ\text{C}$	$\Delta T/\text{K}$	$\delta T_{+}/\text{K}$	$\delta T_{-}/\text{K}$
<b>cell 1</b>				
06	25	10	0.0024 (0.0025)	0.0009 (0.0006)
16	25	10	0.0021 (0.0020)	0.0022 (0.0006)
21	25	10	0.0021 (0.0020)	0.0023 (0.0006)
26	25	10	0.0024 (0.0025)	0.0009 (0.0006)
<b>cell 2</b>				
02	25	10	0.0022 (0.0026)	0.0006 (0.0006)
17	25	10	0.0024 (0.0026)	0.0006 (0.0006)
22	25	10	0.0020 (0.0025)	0.0006 (0.0006)
27	25	10	0.0026 (0.0024)	0.0006 (0.0006)
27b	25	10	0.0026 (0.0021)	0.0022 (0.0009)
<b>cell 3</b>				
03	25	10	0.0024 (0.0026)	0.0006 (0.0006)
18	25	10	0.0027 (0.0019)	0.0024 (0.0006)
23	25	10	0.0025 (0.0026)	0.0006 (0.0006)
28	25	10	0.0020 (0.0023)	0.0021 (0.0013)
<b>cell 4</b>				
04	25	10	0.0081	0.0019
19	25	10	0.0081	0.0021
24	25	10	0.0080	0.0011
<b>cell 5</b>				
05	25	10	0.0239	0.0585
15	25	10	0.0382	0.0424
20	25	10	0.0825	0.0926
25	25	10	0.0263	0.0747

The general approach for extracting relevant quantities was described in Section 4.3.4: by leveraging the similarities between the transient phase gradients in SODI and OBD, the OBD fitting routines can be applied. Of course, this also means that, just as with ternary OBD (and TGC) experiments, the Fickian diffusion matrix cannot be extracted. Instead, only the stable quantities defined in Section 4.1.2 are reliable quantities; the resulting values are given in Table B.1. To test the applicability of the proposed approach, comparisons with results from other teams are necessary, which are mostly published in the form of Soret coefficients. For DCMIX1, data from Galand (Université Libre de Bruxelles) and Mialdun (Université Libre de Bruxelles) were available for cells 1, 2, 3 and 5, as well as from Ryzhkov (Federal Research Center KSC SB RAS) for cells 1–3. Results for cell 3

by these teams were already published earlier as benchmark efforts [30, 31, 80, 82, 108–110] together with OBD and TGC measurements on ground, while data for the other cells was exchanged during DCMIX team meetings; this data is summarized in Tables 5.4 and 5.5. The next paragraphs will give a short summary of the different methods employed by these other DCMIX teams.

The method used by Galand et al. is similar to the one described in this work (temporal phase stepping), but relying on recovering the absolute concentration distribution instead of the gradient [109]. Soret coefficients are extracted either from stationary state amplitudes or fitting of the transients. Since the fitting of the transients is more reliable, because it can account for the experiment not completely reaching the stationary state, those values are chosen for comparison in this work.

Mialdun et al. also employ temporal phase stepping algorithms; in fact, first implementations of the image processing described in this work are based on samples kindly provided by Mialdun, for which the author wishes to express his gratitude. Similar to Galand et al., a fitting procedure is applied to the concentration values extracted from the phase stepping algorithms. What sets the method of Mialdun apart from all other is the application of a tomographic reconstruction [111]. The authors of Ref. [111] identify two contributions, which can lead to a substantial underestimation of Soret coefficients: first, the two-dimensional phase images only represent an integrated view along the optical path through the cell. This means that non-uniformities in the concentration gradient, which are always present near the glass walls, are also integrated over. Secondly, the design of SODI necessitates a compensation volume above the heated plate, see Section 4.3.1. Therefore, during demixing a constant diffusion flux exists between the bulk and the compensation volume (which contains the average composition of the mixture) disturbing the concentration profile in the middle of the cell. These combined effects lead to a general under-estimation of Soret coefficients around 10 %, which can be corrected by tomography [110]. For tomographic reconstruction, Mialdun et al. exploit the symmetric geometry of the SODI cell design, assuming that the two-dimensional view into the cell is equivalent for all sides and reusing the same phase image twice.

The analysis chosen by Ryzhkov et al. relies on the spatial carrier frequency, utilizing a Fourier Transform method [30]. Two different parts of each run are analyzed: SODI-DCMIX1 experiments were performed in such a way that, after the Soret phase, the gradient was switched off and remixing by Fickian diffusion recorded, so values can be extracted both from the Soret and the diffusion phase. Since the system gives a linear response, both phases are in principle equivalent; but for easier visualization, only values extracted from the Soret phase are used for comparison.

Lastly, a paper by Ahadi and Saghir [112] analyzes cells 1–4; however, this publication is not consistent with the other results. Even though the authors cite the work of Sechenyh [104] as source for the contrast factors necessary to calculate Soret coefficients, the values for cells 1, 2 and 4 given in [112] differ markedly

from those in Table 5.1 (and therefore those used by the other DCMIX teams). Interestingly, these differences always occur for the values of  $\partial n_{670\text{nm}}/\partial c_2$ . Since values have to be computed from the parametrization of the refractive index, it is reasonable to assume that an error in those calculations leads to the discrepancies. Fortunately, Ref. [112] also provides values for  $\Delta n_i$  (the measured refractive index gradient), which allows to recalculate  $S'_{T,i}$  with the correct contrast factors. The original and corrected values from the publication of Ahadi are also provided in Table 5.5. Note: the exponents on values in Tab. 3 of [112] seem to be given with an erroneous sign; we assume a negative exponent. Furthermore, Soret coefficients are computed with a reduced temperature gradient, compatible with the cropped heights given in Tab. 3.

Apart from different analysis of the microgravity data provided by SODI, literature data measured on ground is available: Gebhardt performed extensive measurements over the whole ternary composition space with OBD [13, 79] and Larraña measured the DCMIX1 compositions with TGC [105].

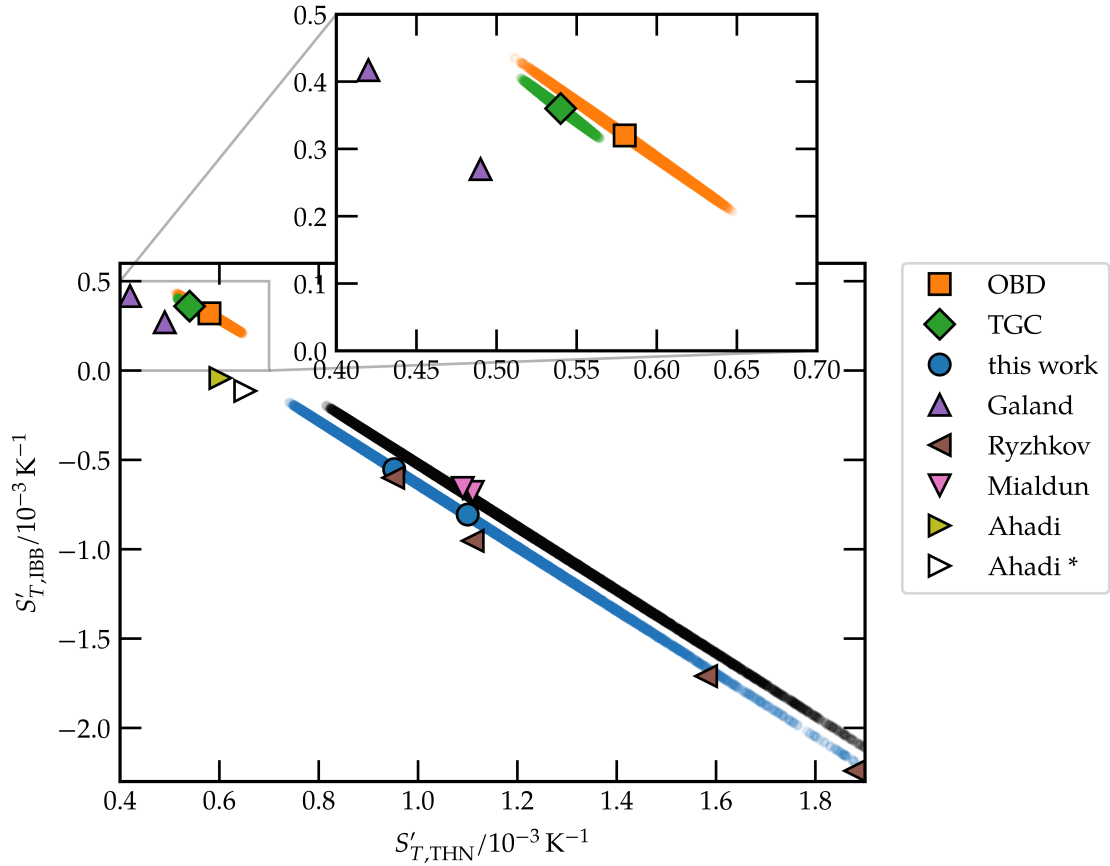


**Figure 5.9:** Soret coefficients cell 1 DCMIX1. The elongated regions represent the compatibility space calculated via a Monte-Carlo approach (see text for details). The black region contains the tomographic correction for this work. Values “Ahadi\*” were calculated with contrast factors from Table 5.1.

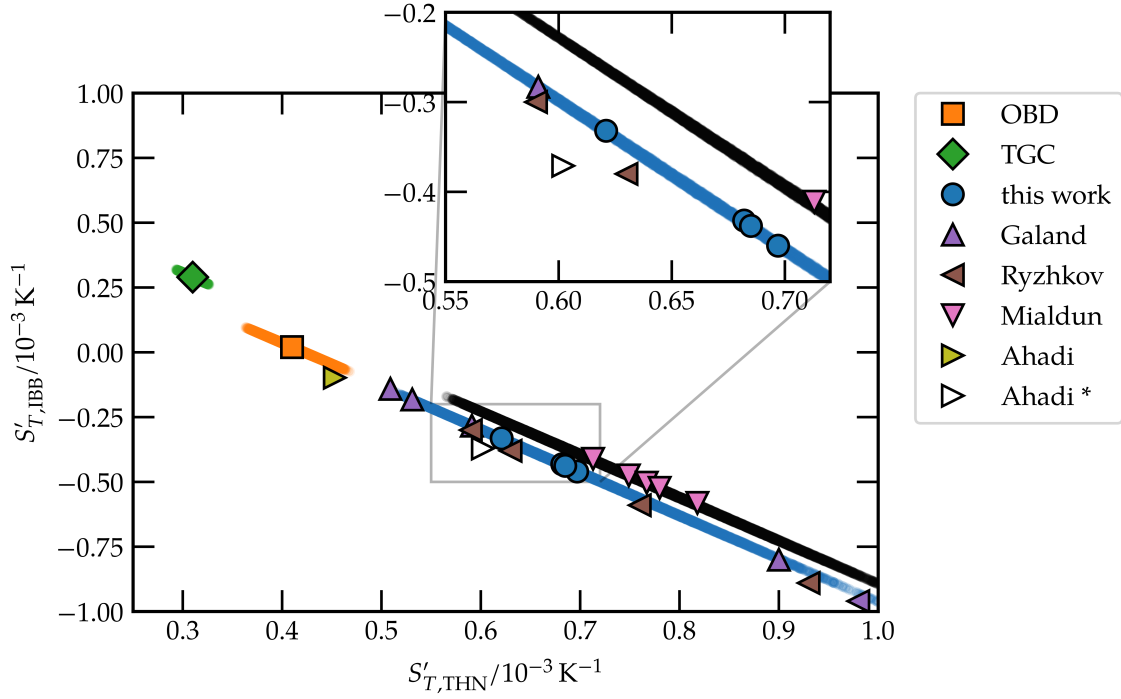


**Figure 5.10:** Soret coefficients cell 2 DCMIX1. The elongated regions represent the compatibility space calculated via a Monte-Carlo approach (see text for details). The black region contains the tomographic correction for this work. Values “Ahadi\*” were calculated with contrast factors from Table 5.1.

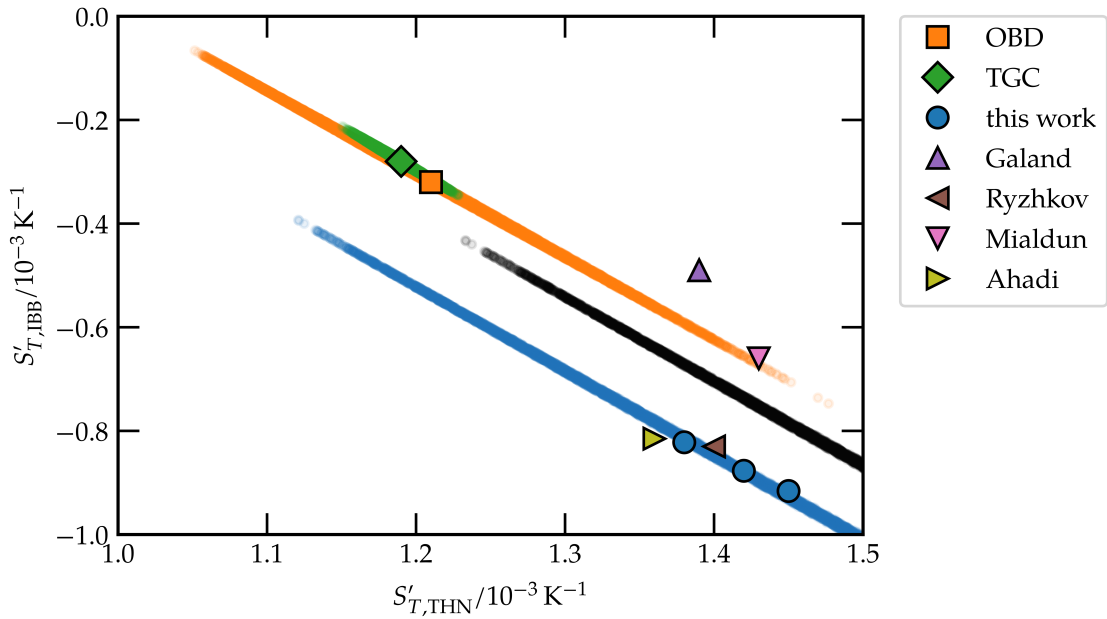


**Figure 5.11:** Soret coefficients cell 3 DCMIX1. The elongated regions represent the compatibility space calculated via a Monte-Carlo approach (see text for details). The black region contains the tomographic correction for this work.

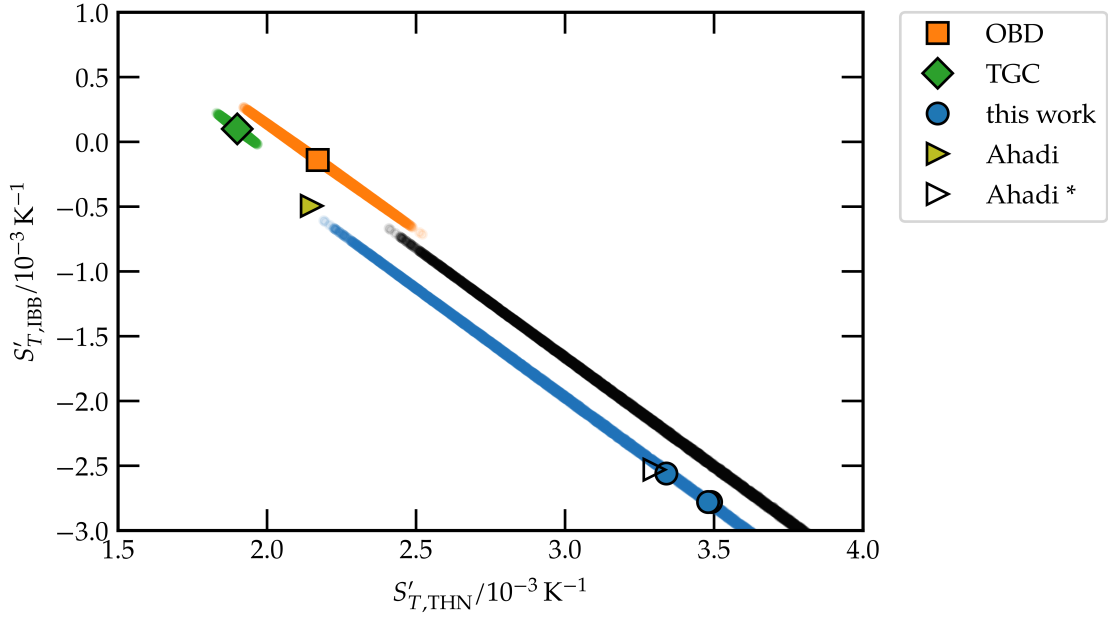


**Figure 5.12:** Soret coefficients cell 4 DCMIX1. The elongated regions represent the compatibility space calculated via a Monte-Carlo approach (see text for details). The black region contains the tomographic correction for this work. Values “Ahadi \*” were calculated with contrast factors from Table 5.1.

When comparing values from different experiments, at first glance no coherent picture emerges. Values sometimes differ by more than an order of magnitude, even changing signs. To understand this, the error propagation discussed in Section 2.2 has to be considered; the high condition numbers of the contrast factor matrix in the case of SODI elongate the space of possible values significantly during inversion from refractive index to concentration space. This was already discussed in the literature during benchmark processing of cell 3 [30, 31]: by adding artificial noise to the contrast factor matrix, and calculating the resulting Soret coefficients, a region in  $S'_{T,1}$ - $S'_{T,2}$ -space can be visualized, which contains all Soret coefficients compatible within the contrast factor problem. A similar Monte Carlo approach was also chosen for this work: by adding uniform noise to the contrast factor values and recalculating the Soret coefficients around 10000 times, a compatibility region is constructed. The amplitude of the noise has been fixed to 0.5 %, which is a realistic value for experimental uncertainty in the determination of contrast factors; as a starting point for calculations, the averaged values of  $a_1$  and  $a_2$  as defined in Section 4.1.2 were chosen (cf. Table B.1). This can be done for values extracted from SODI, as well as literature data from OBD and TGC measurements, utilizing the contrast factors given in Table 5.1. Resulting plots for all cells are shown in Figs. 5.9 to 5.13; for simplicity, “cell” in this context signifies measurements performed on the corresponding mixture given in Table 5.1, regardless of method.



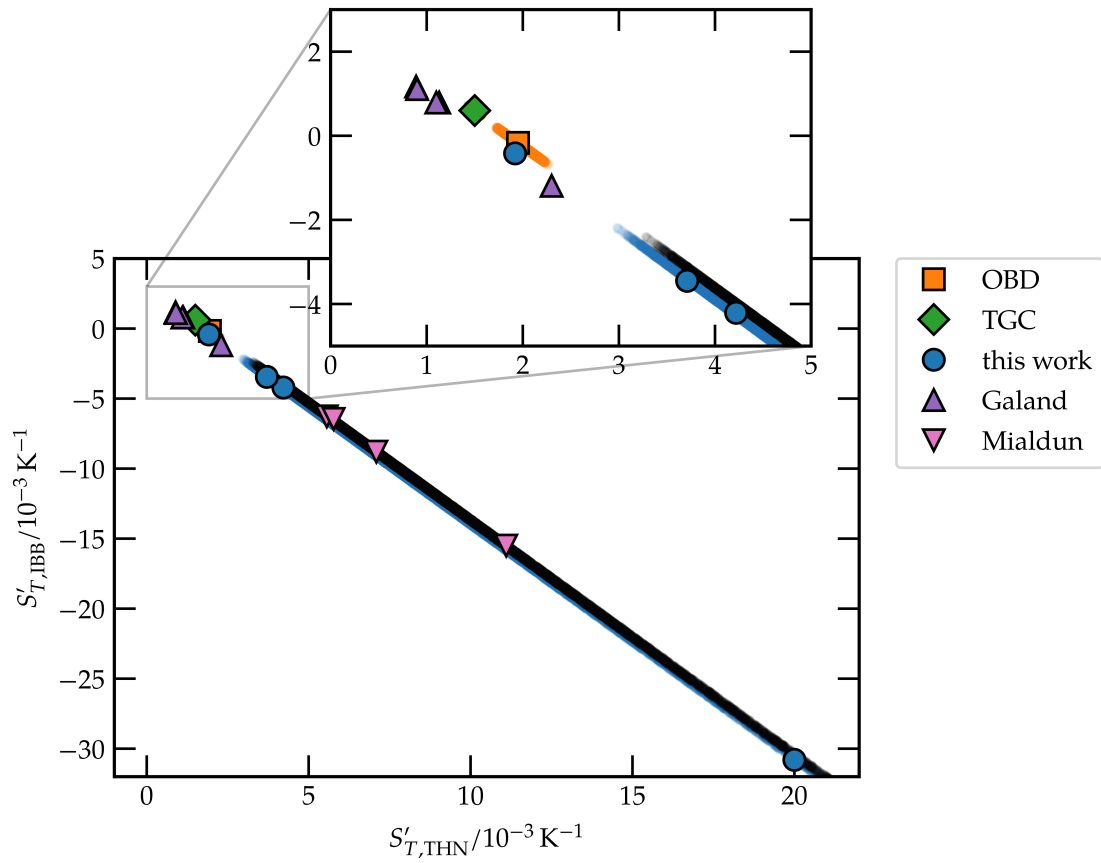


**Figure 5.13:** Soret coefficients cell 5 DCMIX1. The elongated regions represent the compatibility space calculated via a Monte-Carlo approach (see text for details). The black region contains the tomographic correction for this work.

The first important observation from these plots is, that the compatibility space defined from the average amplitudes encompasses all runs, meaning that SODI runs are reproducible within the contrast factor problem. SODI data from other teams also aggregate around the same compatibility space, meaning that the different methods are compatible to each other, too. This is even true for cell 5, where the high condition number leads to a spread-out error region.

When comparing ground and space results, one distinct feature emerges: the asymmetrical nature of error propagation gives special importance to deviations perpendicular to the main axis of the compatibility region. Here, the results by Mialdun stand out in particular: his values consistently correct these lateral deviations present in other SODI-DCMIX1 results, leading to an overlap between the compatibility regions in ground and space experiments. Because all other processing steps are more or less equivalent, this seems to be an effect from the applied tomographic correction. If true, this tomographic correction should be a multiplicative factor, applicable across the different cells, since it mainly depends on the geometry of the cells, and not so much on the properties of the sample. As a test, Figs. 5.9 to 5.13 contain also a second compatibility region, again computed from averaged values of the amplitudes  $a_1$  and  $a_2$ , but with a corrective factor of 10 % applied. Obviously, this shifts the region consistently closer to the ground measurements, mostly coinciding with values from Mialdun. Therefore, the tomographic correction seems plausible, leading to compatible results between microgravity and ground measurements.

Overall, the analysis of DCMIX1 data provides the following conclusions, which are also important for the subsequent analysis of DCMIX3:

- the presented analysis of SODI data is consistent with established methods in the literature
- the high condition numbers in SODI require a Monte-Carlo approach to error propagation, similar to the one in Ref. [30]
- the tomographic correction factor of around 10 % proposed in Ref. [110] is necessary to avoid an under-estimation of separation in SODI; this applies to all methods
- for practical purposes, the complex tomographic reconstruction can be replaced by a simple multiplication with an empirical factor of 1.1
- within the contrast factor problem, ground and space experiments provide compatible values

**Table 5.4:** DCMIX1 literature data from ground measurements at 25 °C.  $c_1$  is THN,  $c_2$  is IBB. OBD results are taken from the works of Gebhardt [13, 79], TGC results from the works of Larrañaga [105].

	OBD		TGC	
	$S'_{T,1}$	$S'_{T,2}$	$S'_{T,1}$	$S'_{T,2}$
	$/10^{-3} \text{ K}^{-1}$			
cell 1	0.58	0.32	0.54	0.36
cell 2	0.41	0.02	0.31	0.29
cell 3	1.21	-0.32	1.19	-0.28
cell 4	2.17	-0.14	1.90	0.10
cell 5	1.95	-0.17	1.50	0.60

**Table 5.5:** Results for SODI-DCMIX1 measurements from this work and other DCMIX teams at 25 °C (kindly provided for this work).  $c_1$  is THN,  $c_2$  is IBB. Values from Ahadi are taken from Ref. [112]; corrected values "Ahadi \*" were calculated with contrast factors from Table 5.1. Benchmark values for cell 3 were already published in Ref. [80].

	this work		Galand		Ryzhkov		Mialdun		Ahadi [112]		Ahadi * (corrected $N_c$ )	
	$S'_{T,1}$	$S'_{T,2}$	$S'_{T,1}$	$S'_{T,2}$	$S'_{T,1}$	$S'_{T,2}$	$S'_{T,1}$	$S'_{T,2}$	$S'_{T,1}$	$S'_{T,2}$	$S'_{T,1}$	$S'_{T,2}$
$/10^{-3} \text{ K}^{-1}$												
<b>cell 1</b>												
run 06					1.11	-0.953			0.602	-0.042	0.652	-0.114
run 11												
run 16	1.10	-0.806	0.42	0.417	1.88	-2.24	1.11	-0.679				
run 21	0.952	-0.552	0.49	0.27	1.58	-1.71	1.09	-0.657				
run 26					0.950	-0.60						
<b>cell 2</b>												
run 02	0.682	-0.432	0.509	-0.141	0.59	-0.30	0.713	-0.411	0.453	-0.098	0.602	-0.371
run 07			0.531	-0.182			0.818	-0.581				
run 12			0.90	-0.80								
run 17	0.621	-0.332			0.93	-0.89	0.749	-0.475				
run 22	0.697	-0.460	0.591	-0.283	0.63	-0.38	0.767	-0.503				
run 27	0.685	-0.438			0.76	-0.59	0.780	-0.523				
run 27j					0.98	-0.96						
<b>cell 3</b>												
run 03	1.38	-0.822	1.39	-0.490	1.40	-0.83	1.43	-0.660	1.36	-0.815		
run 18	1.45	-0.916										
run 23	1.42	-0.877										

Table 5.5 continued from previous page

	this work		Galand		Ryzhkov		Mialdun		Ahadi [112]		Ahadi * (corrected $N_c$ )	
	$S'_{T,1}$	$S'_{T,2}$	$S'_{T,1}$	$S'_{T,2}$	$S'_{T,1}$	$S'_{T,2}$	$S'_{T,1}$	$S'_{T,2}$	$S'_{T,1}$	$S'_{T,2}$	$S'_{T,1}$	$S'_{T,2}$
$/10^{-3} \text{ K}^{-1}$												
<b>cell 4</b>												
run 04	3.49	-2.78							2.15	-0.494	3.30	-2.53
run 19	3.48	-2.78										
run 24	3.34	-2.56										
<b>cell 5</b>												
run 05	4.22	-4.21	1.13	0.79			11.1	-15.5				
run 10	—	—	0.89	1.17								
run 15	3.71	-3.45	1.10	0.79			5.56	-6.27				
run 20	20.0	-30.8	0.90	1.11			5.77	-6.45				
run 25	1.92	-0.419	2.30	-1.19			7.09	-8.79				

## 5.2 DCMIX3

This section will now summarize the results from DCMIX3, gathered via SODI during the 2016 campaign, as well as OBD measurements performed in Bayreuth. As already demonstrated for SODI-DCMIX1 data, quantifying some select quality metrics for SODI allows to identify runs which will likely be problematic during phase reconstruction. Consequently, the same procedure has been applied to DCMIX3 images when the full data set became available in summer 2017. Most of these evaluations have already been published in a joint paper of the DCMIX team, which gives a summary of the SODI-DCMIX3 operations as reference for future analysis, see Ref. [113]. For completeness, these results are reproduced in the following, again focusing on RAW image quality, phase step estimation and temperature control. The comparison of DCMIX1 data showed, that the analysis method presented in this work performs comparably to other methods currently in use; additionally, established routines from OBD can be utilized, simplifying implementation. This allows for a comprehensive study of the SODI-DCMIX3 data alongside OBD measurements, which will also be presented together with the necessary contrast factor measurements. Furthermore, TGC reference values for two mixtures were kindly provided by Lapeira and Bou-Ali.

### 5.2.1 Contrast Factors

To calculate concentration changes from measured data, contrast factors for the employed wavelengths have to be known. For SODI (670 nm and 935 nm), these were already measured by Sechenyh et al. and published in [114]. In the case of OBD (405 nm and 635 nm), contrast factors have been determined for this work according to the methods outlined in Section 4.2: by parametrization of the refractive index as a function of concentration and temperature, contrast factors can be calculated across the whole composition space and within a limited temperature range. The necessary measurements of refractive indices at 20 °C have been performed on a grid of 46 samples along the binary edges as well as in the ternary space (see Fig. 5.14). Overall, the differences between the parametrization and the measured values do not exceed  $4 \times 10^{-4}$  in absolute values. Measurements of the temperature derivative  $\partial n / \partial T$ , which require more time, have been performed for a total of 22 different samples; here, maximal differences between parametrization and measured values are  $8 \times 10^{-6} \text{ K}^{-1}$  (note: a quadratic temperature dependence was chosen, consistent with a polynomial of order  $Q = 2$  in Eq. (4.20)). The resulting matrices for parametrization, cf. Section 4.2, as well as the measured refractive indices and values for  $\partial n / \partial T$ , are summarized in the appendix Tables A.3 to A.5, C.1 and C.2.

In addition to values for OBD and SODI, contrast factors for TGC at two concentrations have been provided for this work, courtesy of Lapeira and Bou-Ali (University of Mondragon, Spain). The contrast factors for these different experiments are summarized in Tables 5.6 and 5.7. From the parametrizations, one can again

calculate the condition numbers across the whole concentration space, which is shown in Fig. 5.15. The high condition numbers for the OBD wavelengths, obvious from these plots and Table 5.6, run counter to intuition; normally, one would expect to see much smaller condition numbers than in the case of SODI, due to the more favourable dispersion at lower wavelengths. But here, condition numbers for OBD are well above 1000, with the exception of cell 1. Since the quality of the employed parametrization is not different to other examples in the literature, e.g. Refs. [31, 104, 114], one possible conclusion is, that this general approach is no longer sufficient for the OBD wavelengths in this system. Instead, a close sampling and parametrization of thermophysical properties around the select concentrations of interest, as normally necessary for TGC, should be employed in future studies. Furthermore, to exclude discrepancies between different experiments at different wavelengths, a simultaneous measurement with all necessary wavelengths on the same sample at 25 °C would greatly enhance confidence in results. Such a measurement system is currently under development in Bayreuth as part of a Master thesis, utilizing a multi-wavelength Michelson interferometer.

Nevertheless, even though the high condition numbers for OBD lead to large uncertainties in concentration space, this does not preclude comparison between the different experiments, as demonstrated by DCMIX1.

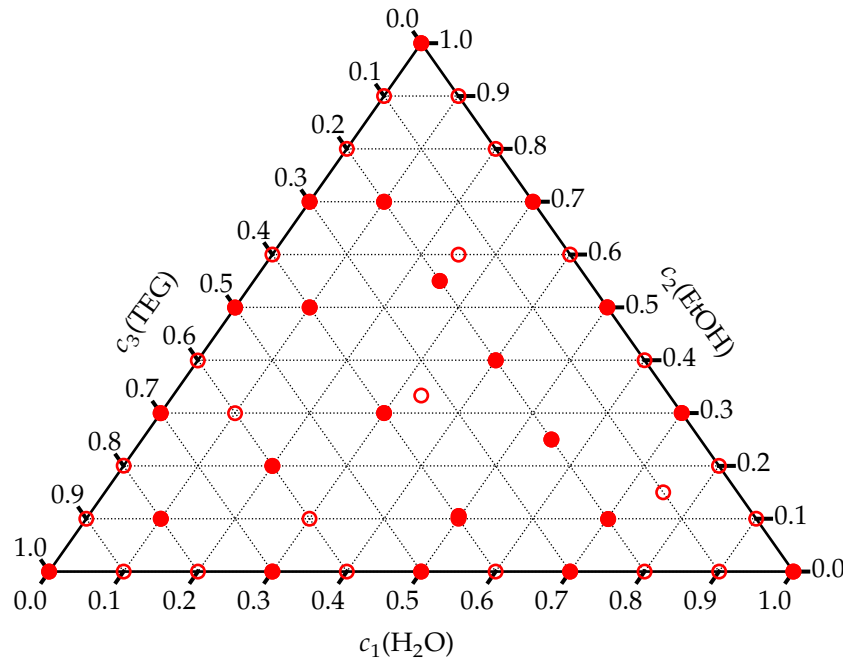


**Figure 5.14:** Compositions of the measured samples for parametrization of the refractive index (weight fraction). Open circles signify refractive index measurements at 20 °C, filled circles additional measurements of the temperature derivative  $\left(\frac{\partial n_{\lambda}}{\partial T}\right)_{p,c_1,c_2}$ .

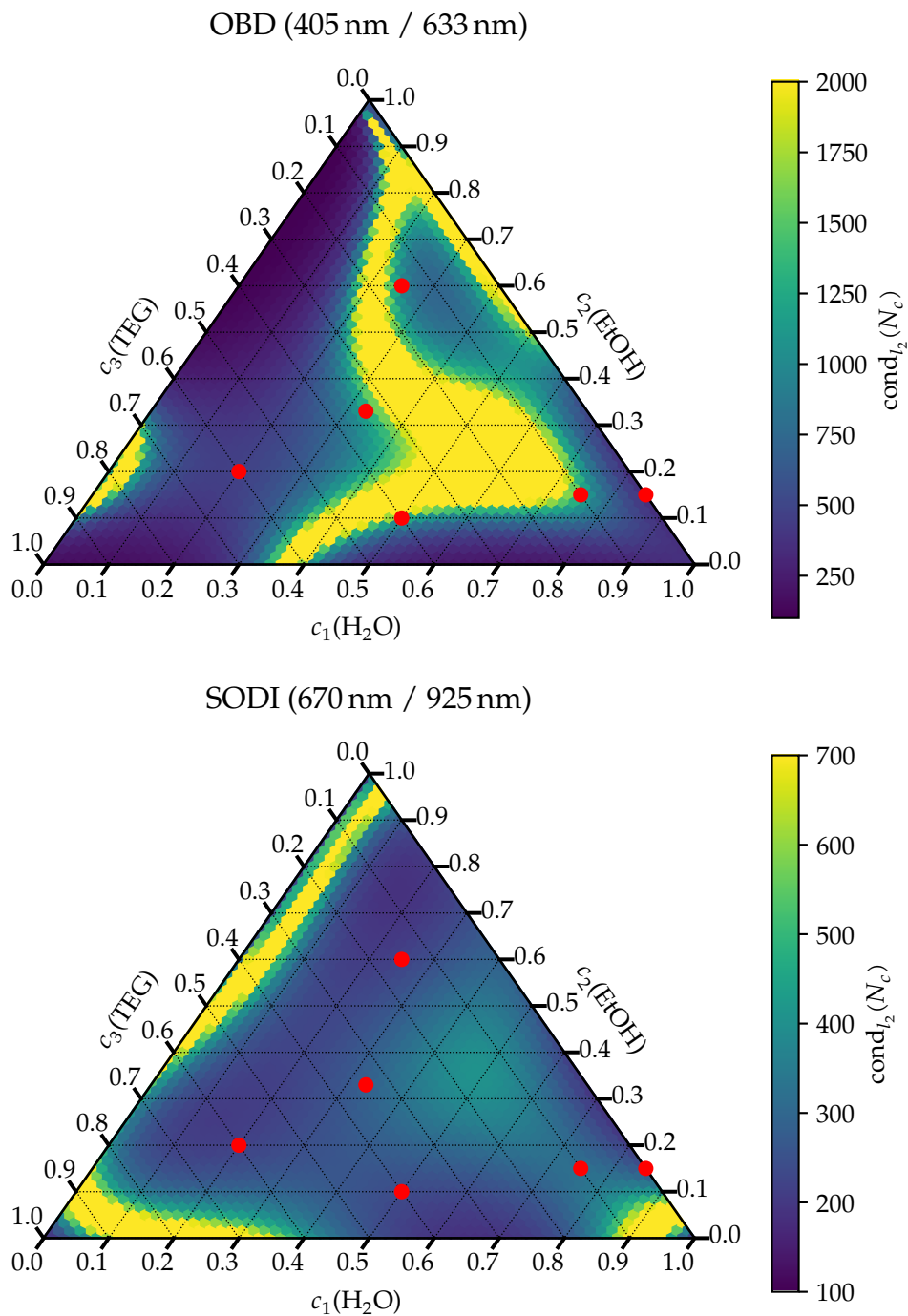


**Figure 5.15:** Condition numbers for OBD (top) and SODI (bottom) experiments. Computed from parametrized refractive indices at 25 °C; results for SODI are taken from Ref. [114]. Red dots mark the mixtures chosen for SODI-DCMIX3 measurements. Notice the different scales in the colour map, with the OBD configuration yielding markedly higher condition numbers. Note: a similar plot for SODI in Ref. [16] gives different absolute values, probably due to some issues with interpolation.



**Table 5.6:** Solutal contrast factors and condition numbers for the DCMIX3 cells with components water ( $c_1$ ), ethanol ( $c_2$ ) and triethylene glycol ( $c_3$ ) (compositions in weight fraction) in the case of OBD, SODI and TGC, all at 25 °C. Contrast factors and condition numbers for SODI were computed from parametrized refractive index values taken from [114]. Values for TGC were kindly provided by Lapeira and Bou-Ali. Measurements for OBD were performed in Bayreuth, according to the methods described in Section 4.2.

cell	$c_1$	$c_2$	$c_3$	$N_{c,11}$	$N_{c,12}$	$N_{c,21}$	$N_{c,22}$	cond( $N_c$ )
OBD								
				$\left(\frac{\partial n_{405 \text{ nm}}}{\partial c_1}\right)_{c_2}$	$\left(\frac{\partial n_{405 \text{ nm}}}{\partial c_2}\right)_{c_1}$	$\left(\frac{\partial n_{633 \text{ nm}}}{\partial c_1}\right)_{c_2}$	$\left(\frac{\partial n_{633 \text{ nm}}}{\partial c_2}\right)_{c_1}$	
1	0.20	0.20	0.60	-0.105384	-0.097078	-0.101496	-0.094308	465
2	0.33	0.33	0.33	-0.103223	-0.085633	-0.099777	-0.083039	1279
3	0.25	0.60	0.15	-0.084002	-0.081073	-0.081125	-0.077996	1041
4	0.75	0.15	0.10	-0.124167	-0.055696	-0.120550	-0.053852	1312
5	0.50	0.10	0.40	-0.127096	-0.075620	-0.123428	-0.073202	1421
6	0.85	0.15	—	-0.126765	—	-0.122218	—	—
SODI								
				$\left(\frac{\partial n_{670 \text{ nm}}}{\partial c_1}\right)_{c_2}$	$\left(\frac{\partial n_{670 \text{ nm}}}{\partial c_2}\right)_{c_1}$	$\left(\frac{\partial n_{925 \text{ nm}}}{\partial c_1}\right)_{c_2}$	$\left(\frac{\partial n_{925 \text{ nm}}}{\partial c_2}\right)_{c_1}$	
1	0.20	0.20	0.60	-0.099605	-0.093685	-0.099956	-0.092303	218
2	0.33	0.33	0.33	-0.099657	-0.081940	-0.099866	-0.080935	283
3	0.25	0.60	0.15	-0.083074	-0.079075	-0.084234	-0.078725	219
4	0.75	0.15	0.10	-0.120113	-0.055526	-0.121027	-0.055022	316
5	0.50	0.10	0.40	-0.122472	-0.072570	-0.122236	-0.071052	239
6	0.85	0.15	—	-0.124378	—	-0.123684	—	—
TGC								
				$\left(\frac{\partial n_{589 \text{ nm}}}{\partial c_1}\right)_{c_3}$	$\left(\frac{\partial n_{589 \text{ nm}}}{\partial c_3}\right)_{c_1}$	$\left(\frac{\partial \rho}{\partial c_1}\right)_{c_3}$	$\left(\frac{\partial \rho}{\partial c_3}\right)_{c_1}$	
2	0.33	0.33	0.33	0.016014	0.098295	-0.267395	0.070267	3
3	0.25	0.60	0.15	0.003968	0.081870	-0.258715	0.041175	3

**Table 5.7:** Measured thermal contrast factors (quadratic dependency) for the DCMIX3 cells with components water ( $c_1$ ), ethanol ( $c_2$ ) and triethylene glycol ( $c_3$ ) (compositions in weight fraction) in the case of OBD at 25 °C.

cell	$c_1$	$c_2$	$c_3$	$\frac{\partial n_{405 \text{ nm}}}{\partial T}$	$\frac{\partial n_{633 \text{ nm}}}{\partial T}$
$/10^{-4} \text{ K}^{-1}$					
1	0.20	0.20	0.60	-3.3632	-3.2826
2	0.33	0.33	0.33	-3.3912	-3.3097
3	0.25	0.60	0.15	-3.7709	-3.6939
4	0.75	0.15	0.10	-1.9632	-1.9335
5	0.50	0.10	0.40	-2.7275	-2.6534

### 5.2.2 Optical Beam Deflection

Accompanying ground measurements with Optical Beam Deflection have been performed for all five ternary DCMIX3 compositions at 25 °C, as well as 30 °C for the cell 3 mixture, see Section 4.1 for experimental details. The resulting signals are presented in Figs. 5.16 to 5.21. Section 2.3 already explained that special care has to be taken in ground measurements to avoid gravitational instabilities, as can also be seen from the plots exhibiting different modes of instabilities, which shall be discussed briefly.

Figs. 5.17 and 5.19 make it obvious that, by applying a gradient in the thermally unstable configuration above a certain threshold (between  $-0.5$  K and  $-1$  K in the case of cell 3), an oscillatory mode occurs. After the initial 1000 s to 2000 s of the demixing, seemingly following the same diffusion path as in a stable configuration, a turning point is reached: the achieved density stratification becomes gravitationally unstable and a sudden remixing occurs, which eventually settles again, allowing the process to start over. In both mixtures, the oscillations die off relatively fast, leaving the system in a kind of intermediate state, no longer prone to oscillations, but also not settling in a plateau.

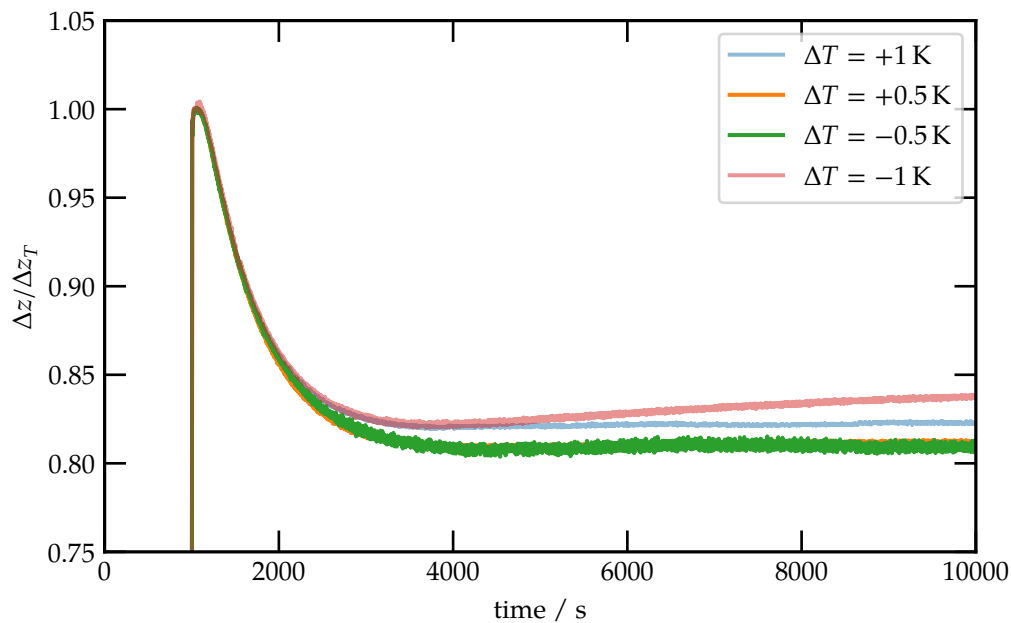


**Figure 5.16:** Measured OBD signals (635 nm) for cell 1, 25 °C.

Of course, apart from their general interest to further studies, these instabilities are easy to discern and avoid, especially since they only occur in the thermally unstable situation of heating from below. In the cases of cells 1, 4 and 5, cf. Figs. 5.16, 5.20 and 5.21, the situation is not as unambiguous: instabilities also occur in the thermally stable configuration (heating from above), necessitating much more care during measurements. One approach to avoid convection onset in these cases

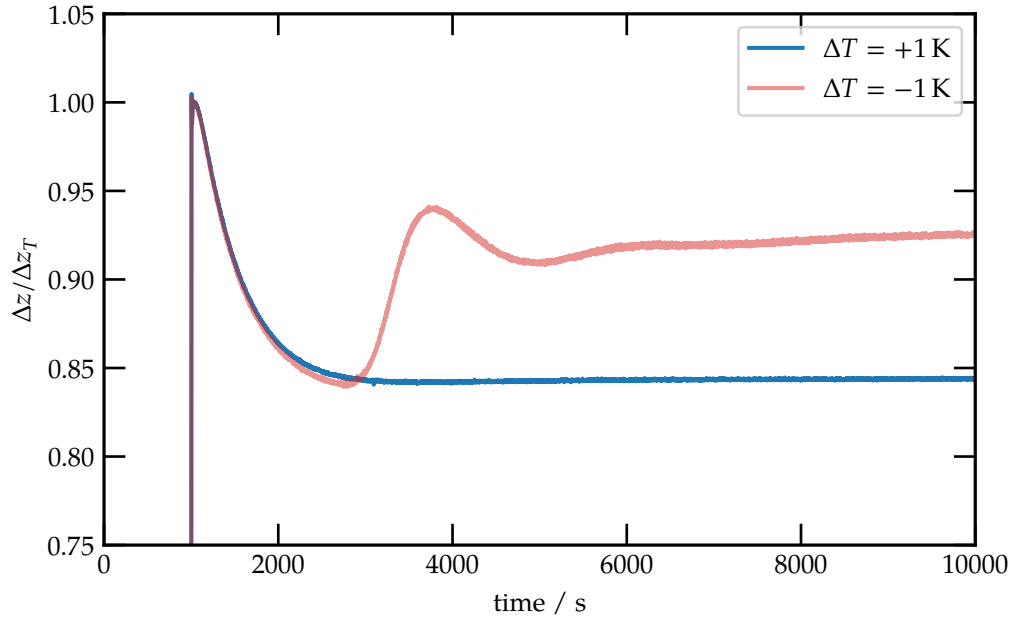


**Figure 5.17:** Measured OBD signals (635 nm) for cell 2, 25 °C.

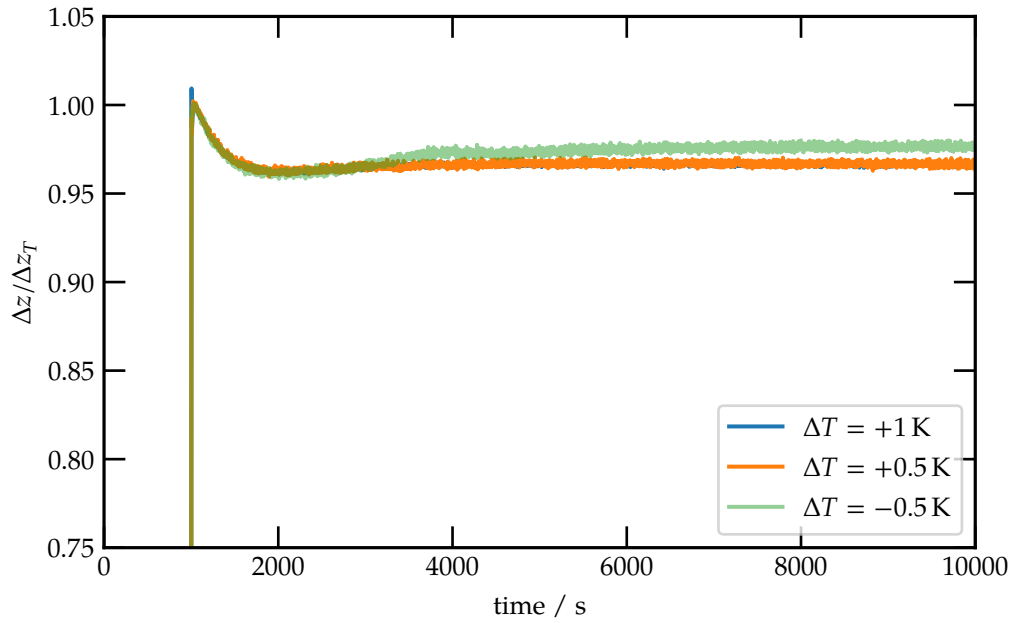


**Figure 5.18:** Measured OBD signals (635 nm) for cell 3, 25 °C

is to measure with lower temperature gradients, since, as evidenced by the expression for the solutal Rayleigh number, Eq. (2.33), the threshold for convection onset is directly proportional to the applied temperature gradient  $\Delta T$ . But lowering the applied temperature gradient also directly decreases the signal-to-noise ratio, since the magnitude of the measured separation is also directly proportional to  $\Delta T$ , cf. Eqs. (2.10) and (4.6), which necessitates multiple measurements at differ-

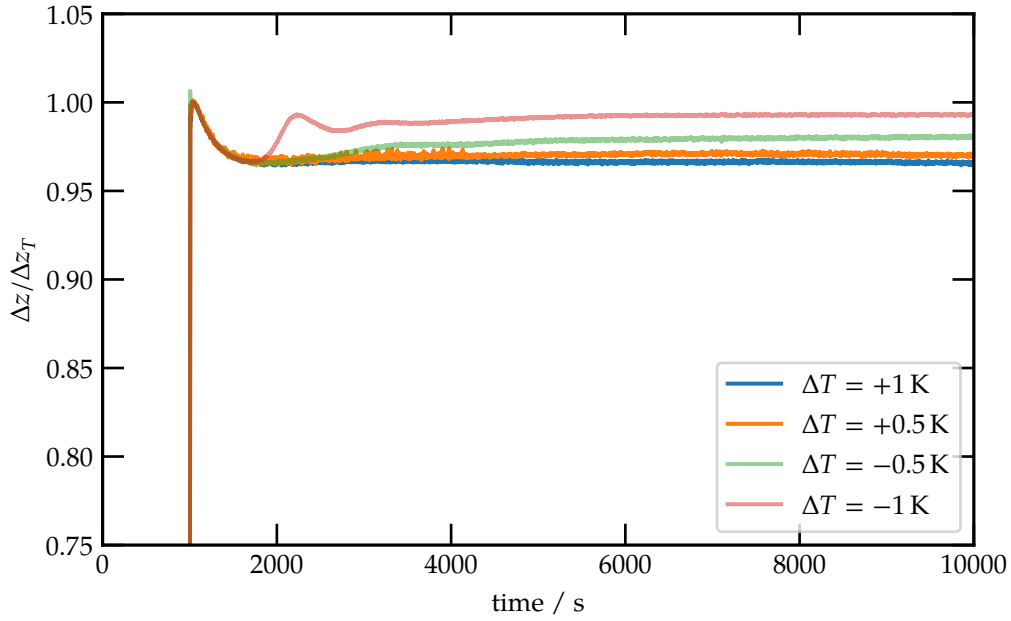


**Figure 5.19:** Measured OBD signals (635 nm) for cell 3, 30 °C

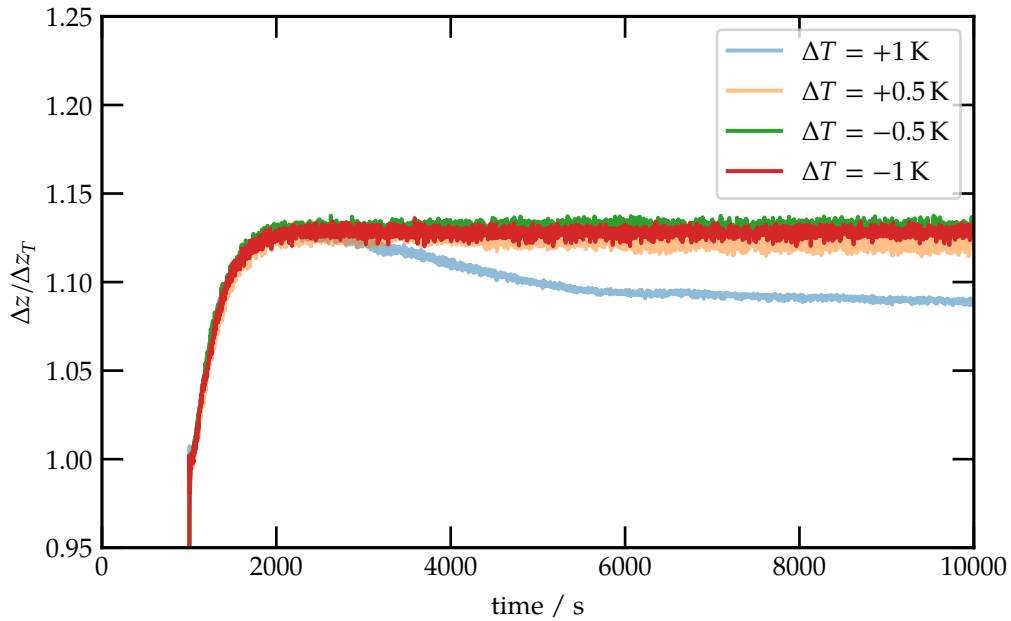


**Figure 5.20:** Measured OBD signals (635 nm) for cell 4, 25 °C.

ent gradients to find suitable configurations. Cell 4 (Fig. 5.20) demonstrates that this approach is also limited; even a lower gradient of +0.5 K exhibits a slow drift, probably due to advective fluxes. Even more critical, cell 1 (Fig. 5.16) might appear stable in the case of  $\Delta T = +1$  K, but only further measurements reveal, that the achieved plateau seems to be too low. So, against intuition, another method to avoid instabilities is to switch to a thermally unstable configuration of heating from

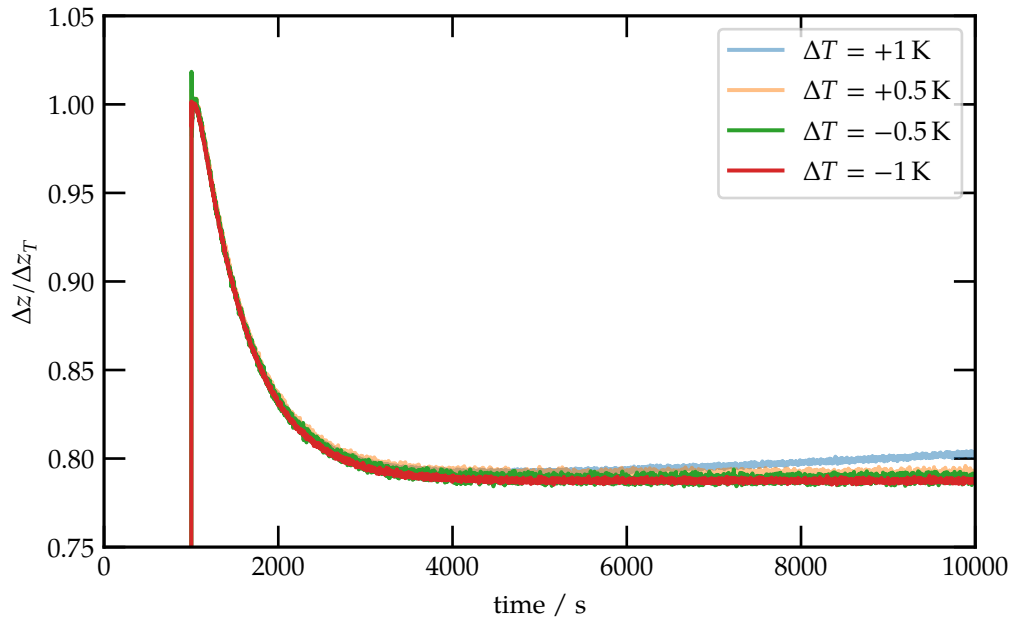


**Figure 5.21:** Measured OBD signals (635 nm) for cell 5, 25 °C.

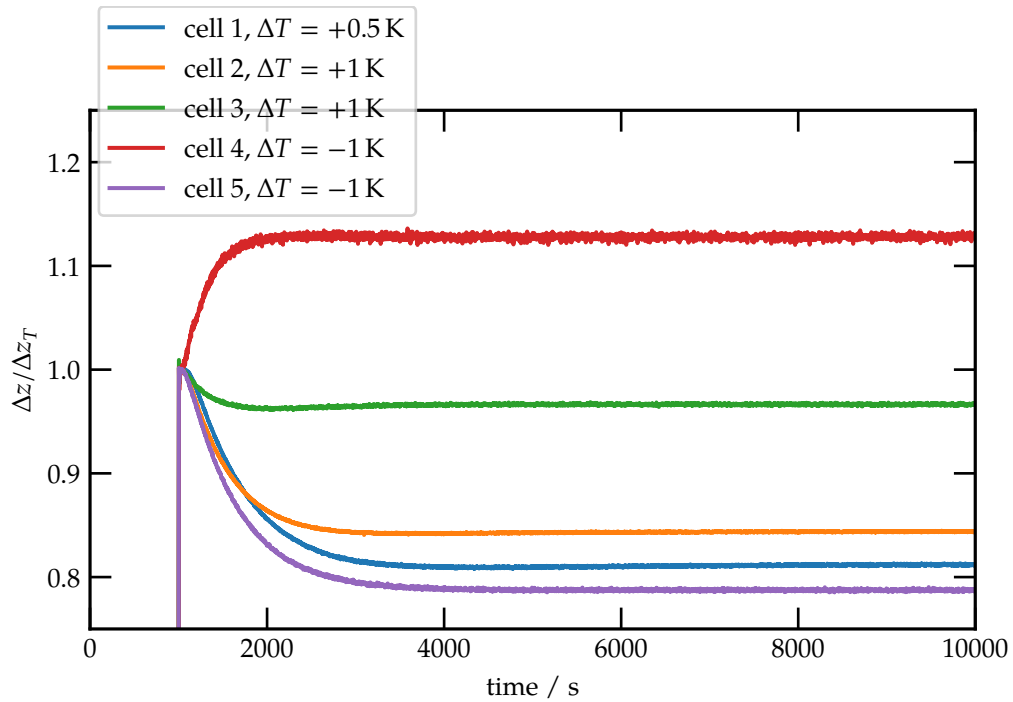


**Figure 5.22:** Comparison of all stable OBD signals (635 nm) at 25 °C.

below. Depending on the Soret coefficients of the individual components, a stable density stratification can be achieved even though thermal expansion would dictate otherwise [33]. But this depends on a balance of the competing processes as well as the magnitude of the applied gradient, as again evidenced by Fig. 5.16.

Generally, by careful choice of experimental parameters, seemingly stable signals could be measured for all DCMIX3 mixtures; see Fig. 5.22 for a comparison between all mixtures. But as already mentioned, there are some caveats in the analysis: as made clear by comparing different gradient configurations in the same mixture, a slow advective flux can be almost indiscernible in a signal, easily leading to misinterpretations. This reinforces the general tenet of the DCMIX project: only a reference base of microgravity data can eliminate such ambiguities.

### 5.2.3 SODI-DCMIX3

The general timeline of SODI-DCMIX3 was already described in Section 3.3.2 and Table 5.8 gives a summary of all performed runs, marking those with low signal-to-noise ratio as well as runs in cell 3 containing a bubble. As for DCMIX1, an overview of image quality and temperature data is given first.

#### RAW Image Quality

Dynamic range is again assessed via black/white saturation of the RAWs, which is summarized in Fig. 5.23 for SODI-DCMIX3. For all runs the percentage of completely black or white pixels is below 4 % and therefore negligible. The black saturation of the MR laser is slightly elevated compared to the other two lasers, but — even considering the standard deviation — does not extend above 4 %. So the dynamic range is more than sufficient in all cases to perform phase calculations and is well within the limits set by the ESR [51]. The Michelson contrast for SODI-DCMIX3, as defined in Eq. (5.2), is shown in Fig. 5.24. From this, it can be seen that the FR laser suffered from considerable contrast problems during operations, most evidently in runs 08, 13, 17 and 19. It is also interesting to note that this drop in contrast has a clear temporal evolution, starting with run 03 and also recovering after run 17, which was not evident in DCMIX1. This behaviour is again mirrored by the variance, cf. Fig. 5.25, with the normally linear rise of variance during phase-stepping severely disturbed in runs with low contrast. Again, as with the MR laser during DCMIX1 operations, the reason for this contrast problems of the FR laser is not traceable from the available housekeeping data, and can only be attributed to some general instability in the laser diode operation.

Another feature visible in the variance, as well as mean grayscale values, is a drift in all lasers during the time of operations; this is most noticeable for the MN laser, with values decreasing about 15 % between start and end of operations. Most probably, this is due to a slight drift of the output efficiency of the diodes, since they are operated almost constantly across several weeks, but without noticeable consequences for the analysis.

**Table 5.8:** List of all DCMIX3 runs.

run	start time	end time	low SNR	remarks
<b>cell 1</b>				
01	22-09-16 01:23	22-09-16 23:23	—	
06	27-09-16 04:21	28-09-16 02:21	—	
11	05-10-16 22:23	06-10-16 20:23	—	
16	12-10-16 04:59	13-10-16 02:59	—	
23	03-11-16 05:22	04-11-16 03:22	—	
28	16-11-16 03:03	17-11-16 01:03	—	
<b>cell 2</b>				
02	21-09-16 03:23	22-09-16 01:23	—	
07	29-09-16 22:21	30-09-16 20:21	—	
12	05-10-16 00:23	05-10-16 22:23	—	
17	19-10-16 23:46	20-10-16 21:46	FR	
22	02-11-16 07:22	03-11-16 05:22	—	
25	08-11-16 05:26	09-11-16 03:26	—	
30	22-11-16 03:41	23-11-16 01:41	—	
<b>cell 3</b>				
03	28-09-16 02:21	29-09-16 00:21	—	
08	11-10-16 06:59	12-10-16 04:59	FR	bubble
13	13-10-16 02:59	14-10-16 00:59	FR	bubble
18	19-10-16 01:46	19-10-16 23:46	—	bubble
<b>cell 4</b>				
04	20-09-16 05:23	21-09-16 03:23	MR	
09	26-09-16 06:21	27-09-16 04:21	—	
14	29-09-16 00:21	29-09-16 22:21	—	
19	18-10-16 03:46	19-10-16 01:46	FR, MR	
21	27-10-16 14:33	28-10-16 12:33	FR	
26	09-11-16 03:26	10-11-16 01:26	MR, MN	
29	17-11-16 01:04	17-11-16 23:04	—	
<b>cell 5</b>				
05	19-09-16 07:22	20-09-16 05:22	MR, MN	
10	22-09-16 23:23	23-09-16 21:23	MR, MN	
15	04-10-16 02:23	05-10-16 00:23	MR	
20	06-10-16 20:23	07-10-16 18:23	—	
20a	20-10-16 21:46	21-10-16 19:46	—	
24	07-11-16 07:26	08-11-16 05:26	—	
27	15-11-16 05:03	16-11-16 03:03	—	



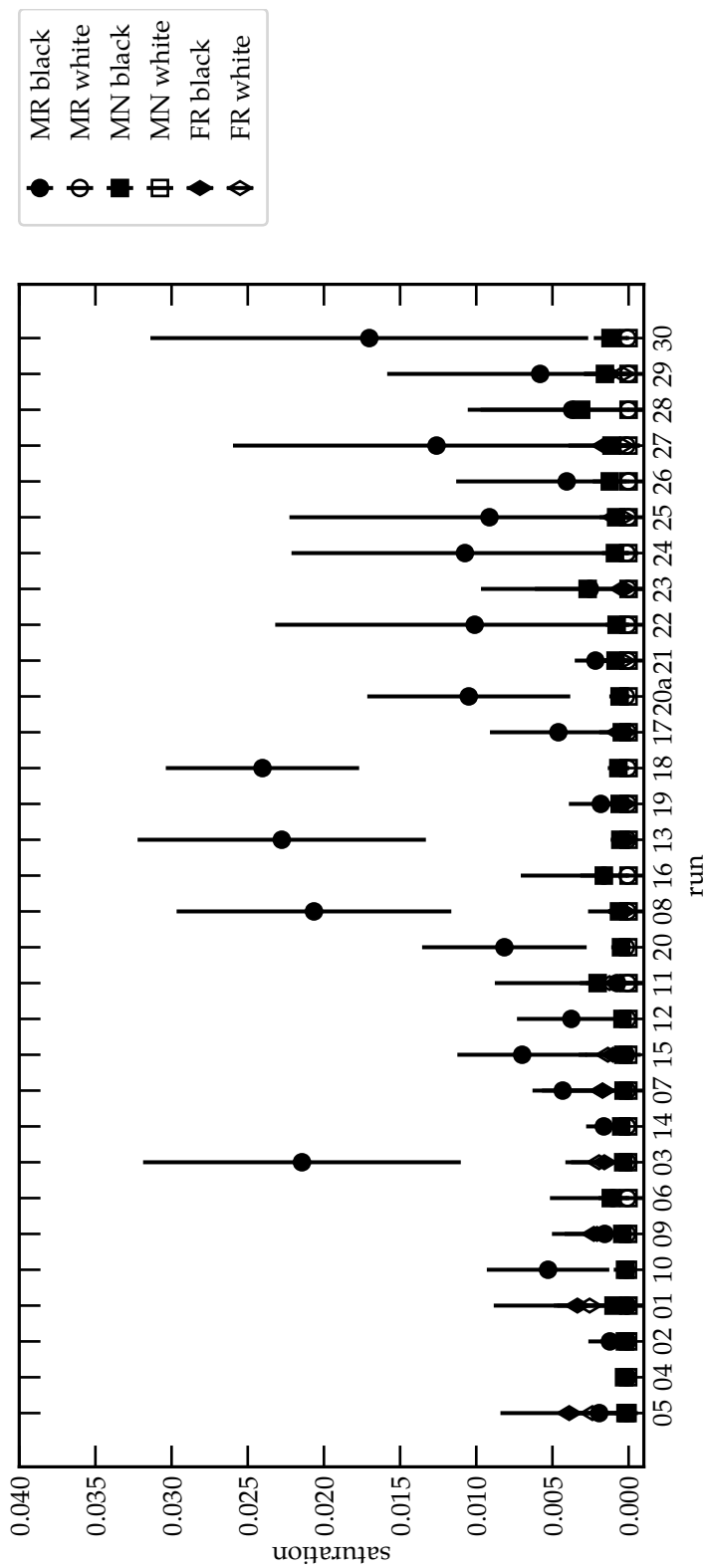


**Figure 5.23:** Percentage of black and white saturation in analyzed DCMIX3 runs; runs are given in chronological order. The saturation has been calculated from the RAW image histograms, averaged over all STKs in a run; the bars represent the standard deviation.

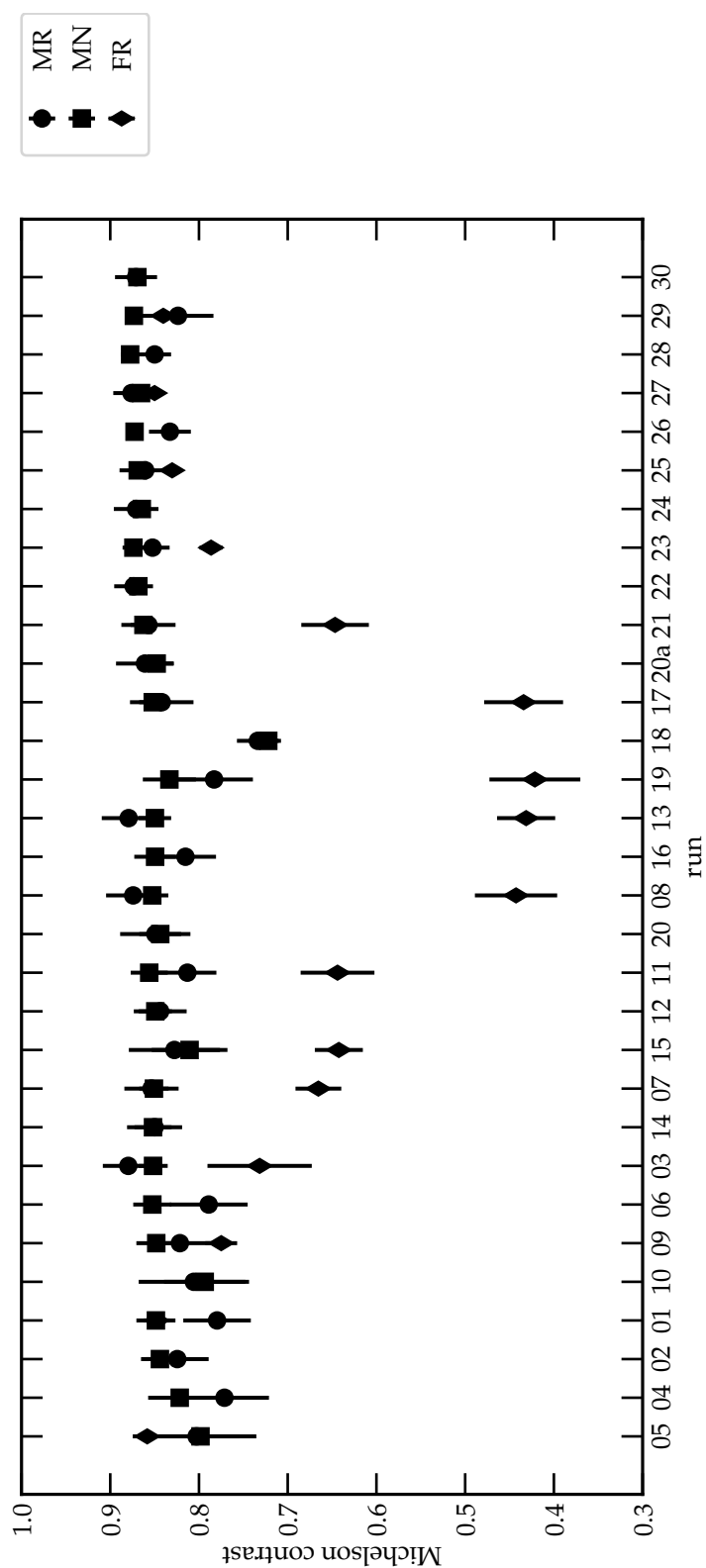


**Figure 5.24:** Michelson contrast of all analyzed runs in DCMIX3 as defined in Eq. (5.2); runs are given in chronological order. Values have been averaged over all STKs in a run, the bars represent the standard deviation. A similar plot was first published in Ref. [113].

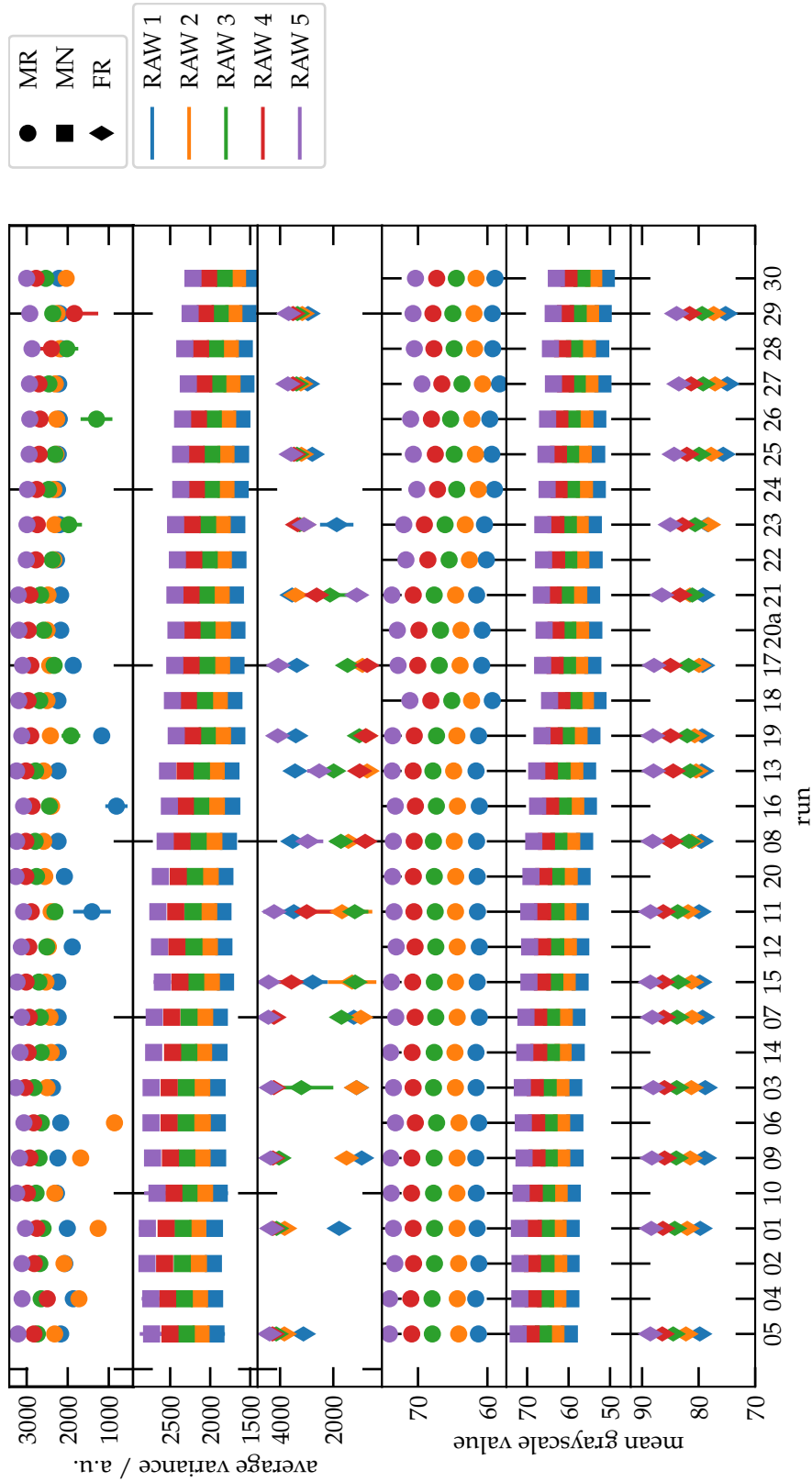


**Figure 5.25:** Variance (see Eq. (5.3)) and mean values in the grayscale levels for the individual RAWs within stack files, across all runs in DCMIX3; runs are given in chronological order. Values have been averaged over all STKs in a run, the bars represent the standard deviation.

### Phase Step Estimation

To estimate the average phase steps between RAW images, Eq. (5.4) is used again; the resulting values are shown in Fig. 5.26. As before, the dashed lines mark a deviation of  $\pi/16$  from the nominal phase step of  $\pi/2$ , which can be seen as a soft threshold for a breakdown of the phase-step algorithm Eq. (4.39). The two values for each laser again result from the possibility to apply Eq. (5.4) twice to each STK, since only four images are required.

First of all, Fig. 5.26 shows a strong deviation of the phase-step for runs of the FR laser, which are also affected by a low contrast. This confirms the observation from DCMIX1, that drops in contrast are accompanied by errors in phase-stepping. In turn, several runs with no obvious contrast problems stand out in the phase-step estimation: during runs 05 and 10, both the MR and MN lasers lie above the threshold; this is also true for several other runs in the case of the MR laser. What is striking about this is, that — as in DCMIX1 — these problems surface prominently in cell 5. But contrary to DCMIX1 operations, where reducing background tasks on the controlling CPU could alleviate this somewhat, no such correlation was evident in DCMIX3. Where possible, a manual comparison between MR and MN lasers has been applied to identify and sort out affected STKs. Since in the runs 05, 10 and 26 almost all STKs in both lasers suffer from phase-stepping issues, this approach could not be applied. These runs need to be analyzed by some spatial instead of temporal algorithm, requiring only one image; at the time of writing, such an analysis method is being implemented and tested in Bayreuth as part of a Master thesis.

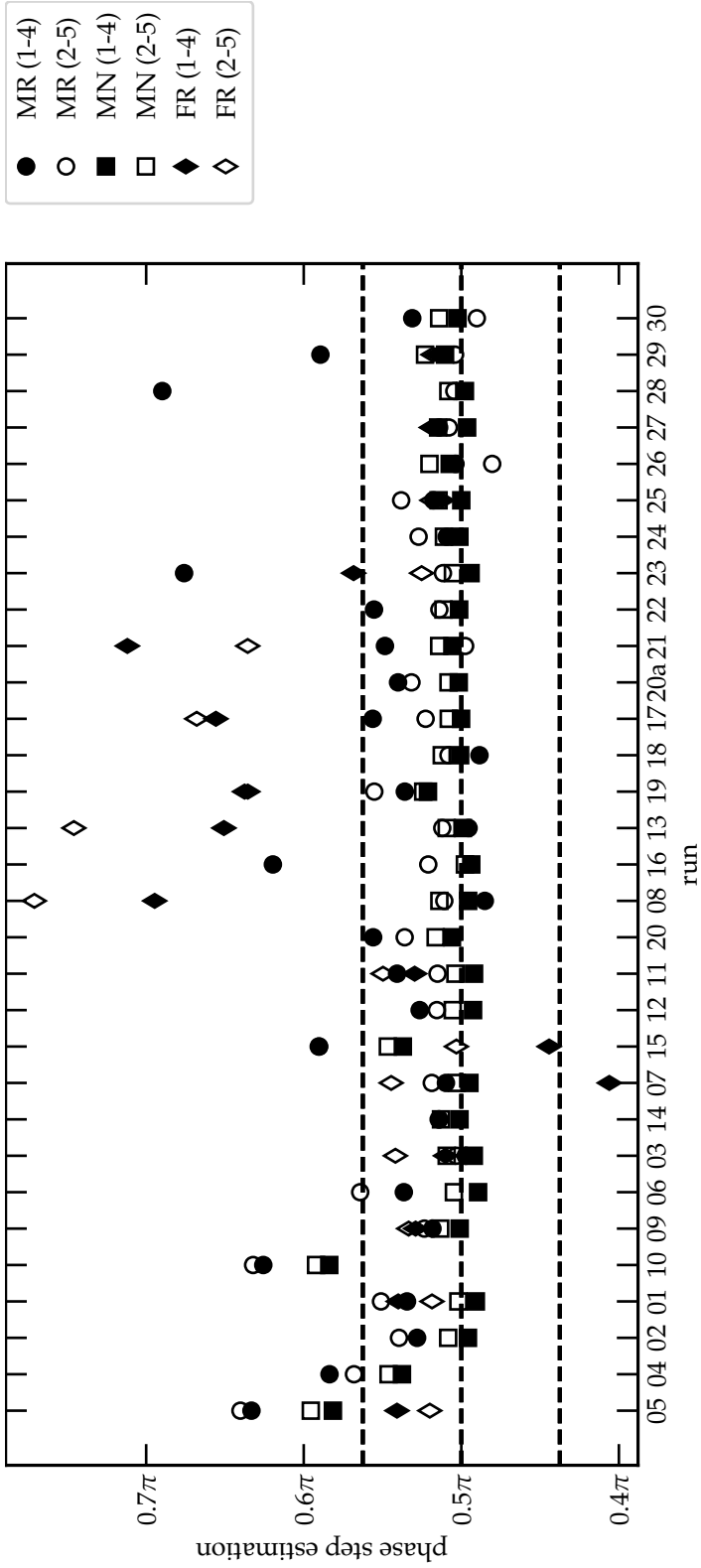


**Figure 5.26:** Estimated phase steps for all analyzed runs in DCMIX3, according to Eq. (5.4). Dashed lines represent a deviation of  $\pi/16$  from the desired phase step of  $\pi/2$ , translating to around 1 % error in phase calculation. A similar plot was first published in Ref. [113].

### Temperature Regulation

The stability of temperature regulation is quantified in the same way as in Section 5.1.2 by calculating the standard deviation of the temperature readouts after gradient buildup. Corresponding results for DCMIX3 are summarized in Table 5.9. As one can see, noise levels are typically around 3 mK or below. But curiously, Peltier 9 on cell 4 is again the exception, as in DCMIX1, with the standard deviation of all runs at 25 °C amounting to 23 mK. An example for this is shown in Fig. 5.27: as the zoomed inset shows, the noise level can be attributed to fluctuations in the range of 0.01 Hz to 0.1 Hz. Still, invoking the electrical analogy, the sample itself can be viewed as a low-pass filter and should not be affected by such high frequency noise. Another important observation is, that these fluctuations drop considerably for runs at 30 °C and, in contrast to DCMIX1, are not present in cell 5.

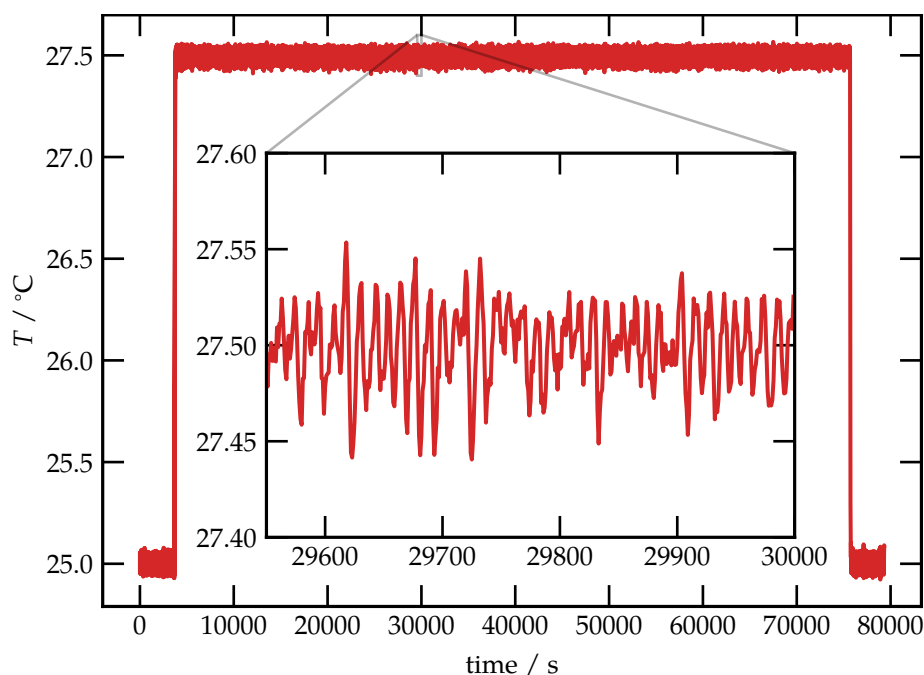


**Figure 5.27:** Temperature fluctuations on Peltier 9 during run 04. A similar plot was first published in Ref. [113].

**Table 5.9:** Standard deviations of the temperature in SODI-DCMIX3, calculated after gradient stabilization.  $\delta T_{+/-}$  describes the standard deviation on the hot/cold plate. Values in parenthesis are for the binary companion cell. A similar table was first published in Ref. [113].

run	$T_0/^\circ\text{C}$	$\Delta T/\text{K}$	$\delta T_{+}/\text{K}$	$\delta T_{-}/\text{K}$
<b>cell 1</b>				
01	25 (25)	5 (5)	0.0032 (0.0022 )	0.0020 (0.0022)
06	25	5	0.0031	0.0020
11	25 (25)	5 (10)	0.0029 (0.0026)	0.0021 (0.0006)
16	25	5	0.0027	0.0019
23	30 (30)	5 (5)	0.0025 (0.0025)	0.0058 (0.0049)
28	30	5	0.0022	0.0054
<b>cell 2</b>				
02	25	5	0.0033	0.0019
07	25 (25)	5 (5)	0.0031 (0.0022)	0.0019 (0.0021)
12	25	5	0.0031	0.0018
17	25 (25)	5 (10)	0.0025 (0.0024)	0.0019 (0.0006)
22	30	5	0.0029	0.0044
25	30 (30)	5 (5)	0.0026 (0.0026)	0.0045 (0.0047)
30	30	5	0.0027	0.0060
<b>cell 3</b>				
03	30 (25)	5 (5)	0.0026 (0.0022)	0.0061 (0.0022)
08	30 (25)	5 (5)	0.0025 (0.0022)	0.0062 (0.0020)
13	30 (25)	5 (10)	0.0025 (0.0026)	0.0063 (0.0006)
18	30	5	0.0022	0.0021
<b>cell 4</b>				
04	25	5	0.0222	0.0020
09	25 (25)	5 (5)	0.0223	0.0020
14	25	5	0.0232	0.0020
19	25 (25)	5 (10)	0.0233 (0.0025)	0.0020 (0.0006)
21	30 (30)	5 (5)	0.0071 (0.0021)	0.0062 (0.0050)
26	30	5	0.0072	0.0061
29	30 (30)	5 (5)	0.0071 (0.0022)	0.0063 (0.0050)
<b>cell 5</b>				
05	25 (25)	5 (5)	0.0029 (0.0024)	0.0018 (0.0020)
10	25	5	0.0031	0.0018
15	25 (25)	5 (10)	0.0029 (0.0026)	0.0018 (0.0006)
20	25	5	0.0029	0.0019
20a	30	5	0.0030	0.0052
24	30	5	0.0022	0.0048
27	30 (30)	5 (5)	0.0026 (0.0023)	0.0045 (0.0050)

### Transient Phase Signal

The general image processing has been explained in detail in Section 4.3: from the recovered phase maps, an OBD-like signal can be extracted for further fitting. The resulting signals are shown in Fig. 5.28 for all cells at 25 °C and 30 °C mean temperature. Unfortunately, no measurement without bubble could be performed in cell 3 at 25 °C, making only the dataset at 30 °C complete; nevertheless, the recorded runs with the bubble visible inside cell 3 could still be of future interest, especially regarding Marangoni-convection at the liquid-gas interface.

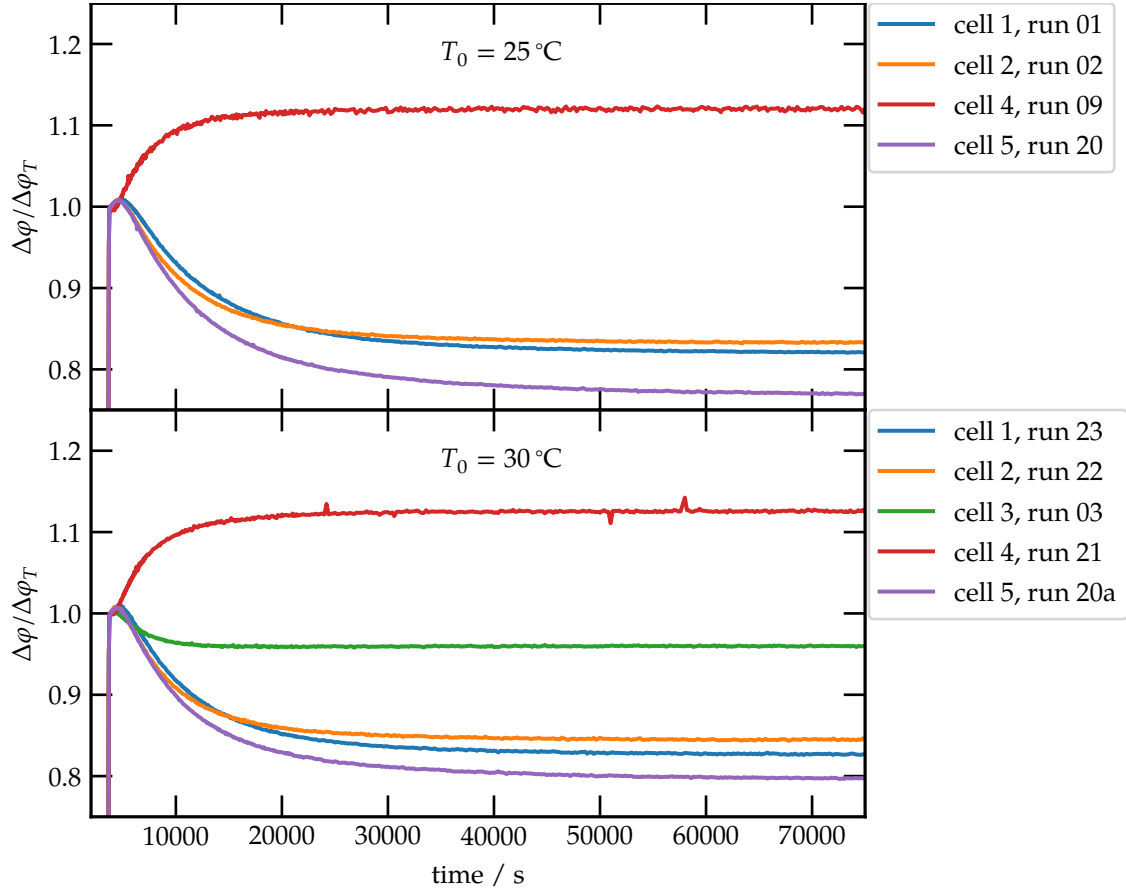


**Figure 5.28:** Comparison of measured SODI signals (670 nm) for all cells. Note: due to the growing bubble in cell 3, only one bubble-free measurement at 30 °C could be performed.

What is immediately obvious from Fig. 5.28 is a qualitative similarity to Fig. 5.22: the signs, as well as relative magnitudes of the amplitudes are comparable between all cells. Of course, such observations do not allow to make assumptions about the resulting Soret coefficients, since the individual contrast factors are necessary for conversion into concentration space. Another important aspect is the timing of the runs: all SODI-DCMIX3 runs lasted about 72 000 s, a time determined by the smallest diffusion eigenvalues of the mixtures, which were mea-



sured on ground beforehand [83]. In general, this time seems sufficient, with all signals reaching a quasi-stationary plateau; only in cell 5, there is still a slight tendency discernible on approach of the end of the run.

#### 5.2.4 Comparison Microgravity and Ground Results

Taking the measured signals from OBD and SODI data, the OBD fitting routine as described in Sections 4.1.2 and 4.3.4 can be applied; the resulting fit coefficients are summarized in Tables B.2 and B.3. Furthermore, values for the thermodiffusion coefficients  $D'_{T,i}$  were measured via TGC by Lapeira and Bou-Ali in the laboratories of the University of Mondragon (Spain); results for the mixtures 33-33-33 wt% H<sub>2</sub>O-EtOH-TEG (cell 2) and 25-60-15 wt% H<sub>2</sub>O-EtOH-TEG (cell 3) were kindly provided for this work. To include TGC values in the comparison, Soret coefficients can be computed from thermodiffusion coefficients via Eq. (2.11), using the diffusion matrices published in Ref. [83] (see Table 5.10).

Due to the bubble in cell 3, which could only be measured at 30 °C, this presents a problem: until now, no contrast factors at 30 °C have been published for the SODI wavelengths 670 nm and 935 nm. This precludes a comparison in the Soret space for these measurements.

Figures 5.29 to 5.33 show the Soret coefficients for all cells at 25 °C. As already explained in Section 5.1, the error propagation in ternary mixtures can spread values across a wide range, even changing signs. Therefore, by adding 0.5 % noise to the contrast factors, a compatibility region is again constructed, taking average amplitudes  $a_1$  and  $a_2$  as starting points (see Section 4.1.2). Additionally, the tomographic correction proposed by Mialdun et al. [111] is considered as a second region marked in black. Note: due to the extremely low condition numbers (see Table 5.6) for the TGC contrast factors, no Monte-Carlo approach was tried on these results, since the resulting region would be exceedingly small. In general, a similar picture emerges from these plots as in DCMIX1: the trends of the compatibility space for SODI and OBD are very similar for all cells. Of course, due to the ill-conditioning of both OBD and SODI contrast factors matrices, a wide range of possible values is covered in all cases and making statements about definite values becomes very difficult. But still, the highly asymmetric nature of the error-propagation allows to indicate possible over- or underestimations of Soret coefficients.

When looking at the effect of the tomographic correction (around 10 % of the amplitudes, cf. Section 5.1.3), a slight correction of SODI values in direction of the OBD space is visible, as was already observed in DCMIX1. This is especially apparent in cell 1, with the corrected SODI values almost coinciding with the OBD region. Another obvious property of the plots, which is best observed in cell 4, is the gap in the compatibility regions near zero; this is another consequence of the numerical ill-conditioning of the contrast factors, making comparisons around small values difficult. In cell 2, values for TGC are quite small and outside of the regions for SODI and OBD. But by extrapolating the trends, which is justified due

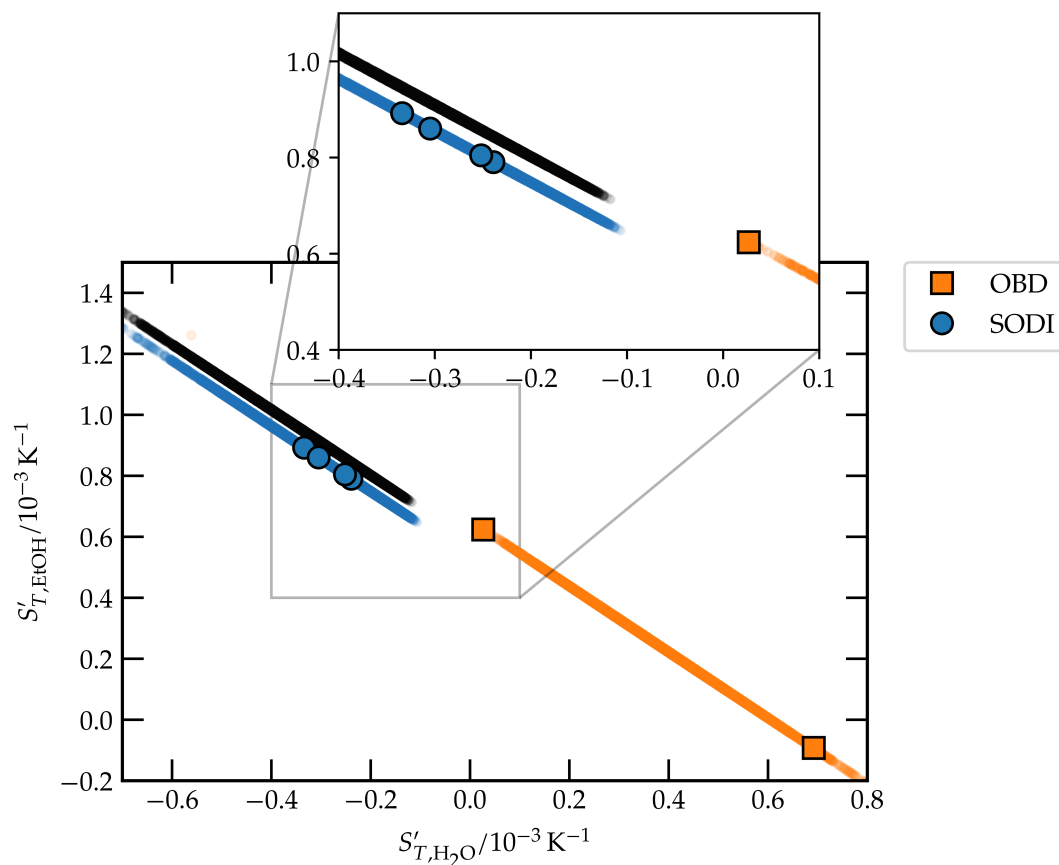


**Figure 5.29:** Soret coefficients cell 1 DCMIX3 at 25 °C. The elongated regions represent the compatibility space calculated via a Monte-Carlo approach. The black region contains the tomographic correction for this work. Filled symbols represent individual measurements via SODI or OBD.

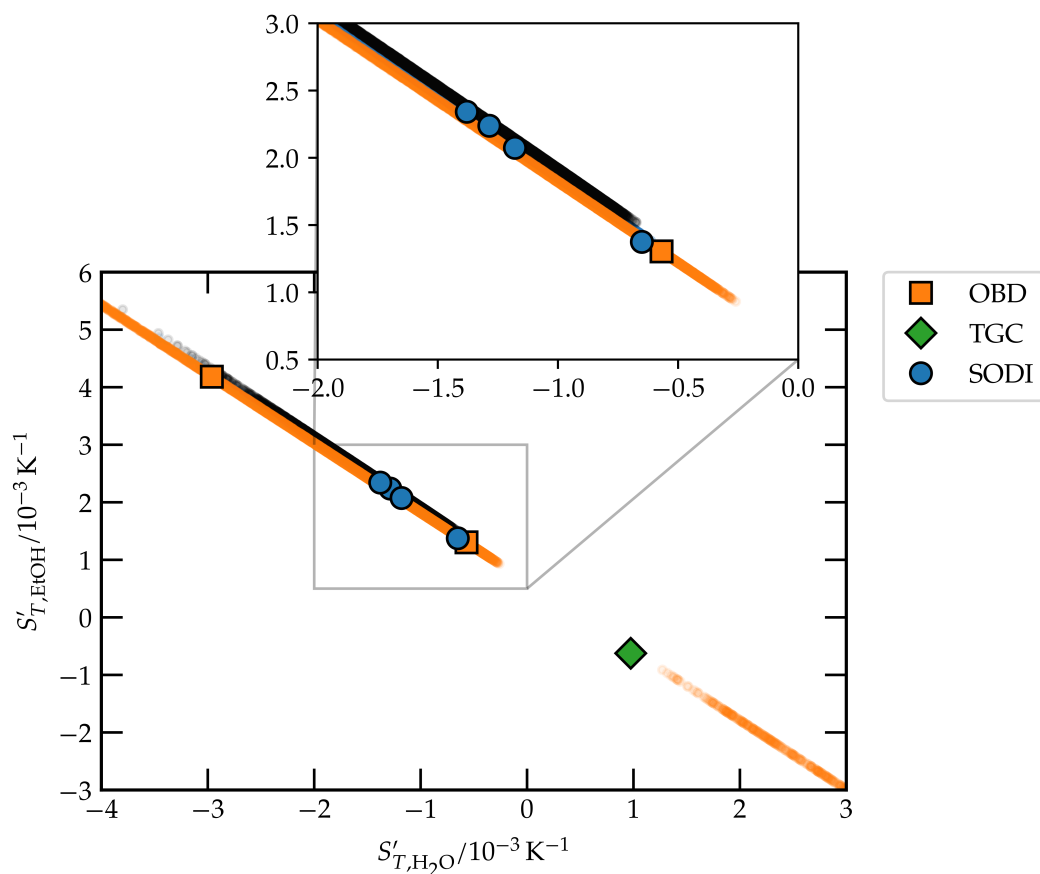


**Figure 5.30:** Soret coefficients cell 2 DCMIX3 at 25 °C. The elongated regions represent the compatibility space calculated via a Monte-Carlo approach. The black region contains the tomographic correction for this work. Filled symbols represent individual measurements via SODI or OBD.

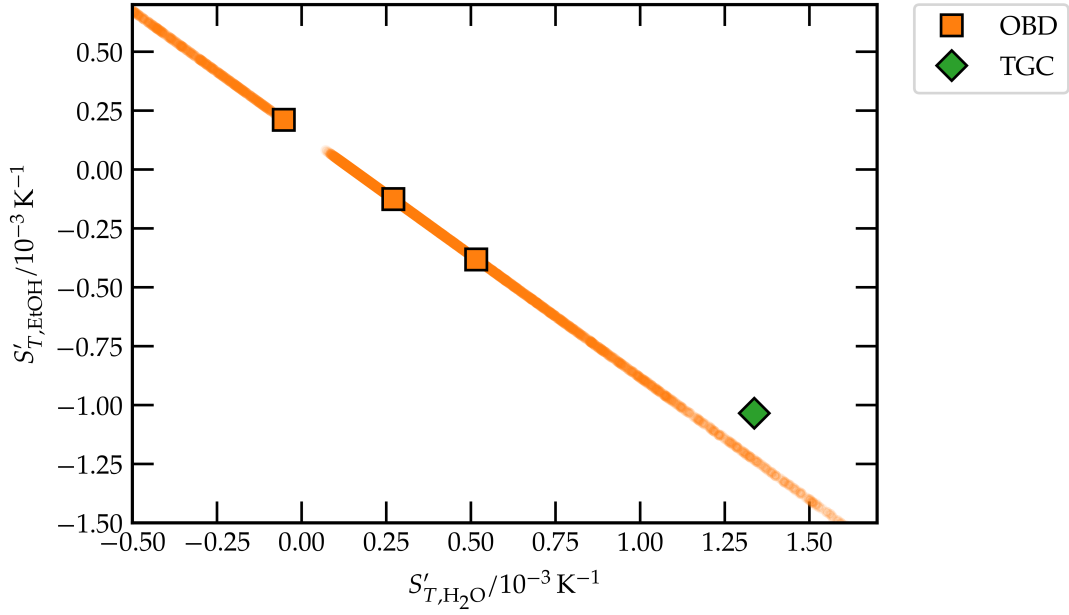


**Figure 5.31:** Soret coefficients cell 3 DCMIX3 at 25 °C. Due to the bubble in this cell, no results from SODI can be presented. The elongated regions represent the compatibility space calculated via a Monte-Carlo approach. The black region contains the tomographic correction for this work. Filled symbols represent individual measurements via SODI or OBD.

to fact that the magnitude of the applied noise is more or less arbitrary, SODI and OBD values always aggregate around the same line; this is a strong argument for the general compatibility of SODI and OBD measurements.

Including the TGC values for cells 2 and 3 in the considerations, this impression is reinforced. For cell 2, even though TGC values are considerably smaller, they still lie on the hypothetical extrapolation of the SODI/OBD compatibility spaces, which means that all three methods are compatible for this cell, increasing confidence in the results. For cell 3 — which lacks values from SODI — OBD and TGC show a lateral displacement, but bearing in mind the narrow scale on Fig. 5.31, this might very well be within margins of experimental errors. Fortunately, due to the properties of the OBD fitting algorithm, another way of comparison is available: the fitting coefficients  $b_i/q^2$  presented in Section 4.1.2 are stable and in themselves not dependent on the conditioning of the contrast factor matrix. Of course, they still depend on the utilized wavelengths, so direct comparison e.g. between SODI and OBD values should be treated with care. But in the case of TGC, this becomes less problematic for two reasons: first, contrast factors for TGC have very low condition numbers, leading to negligible errors in concentration space. Second, via Eq. (4.14) one can now transform the provided  $D'_{T,i}$  to  $b_i/q^2$  utilizing the OBD contrast factors. Since this does not involve any inversion of the contrast factor matrix, no error amplification should be expected, resulting in a set of comparable quantities, see Tables 5.10 and 5.11. The differences between OBD and TGC are

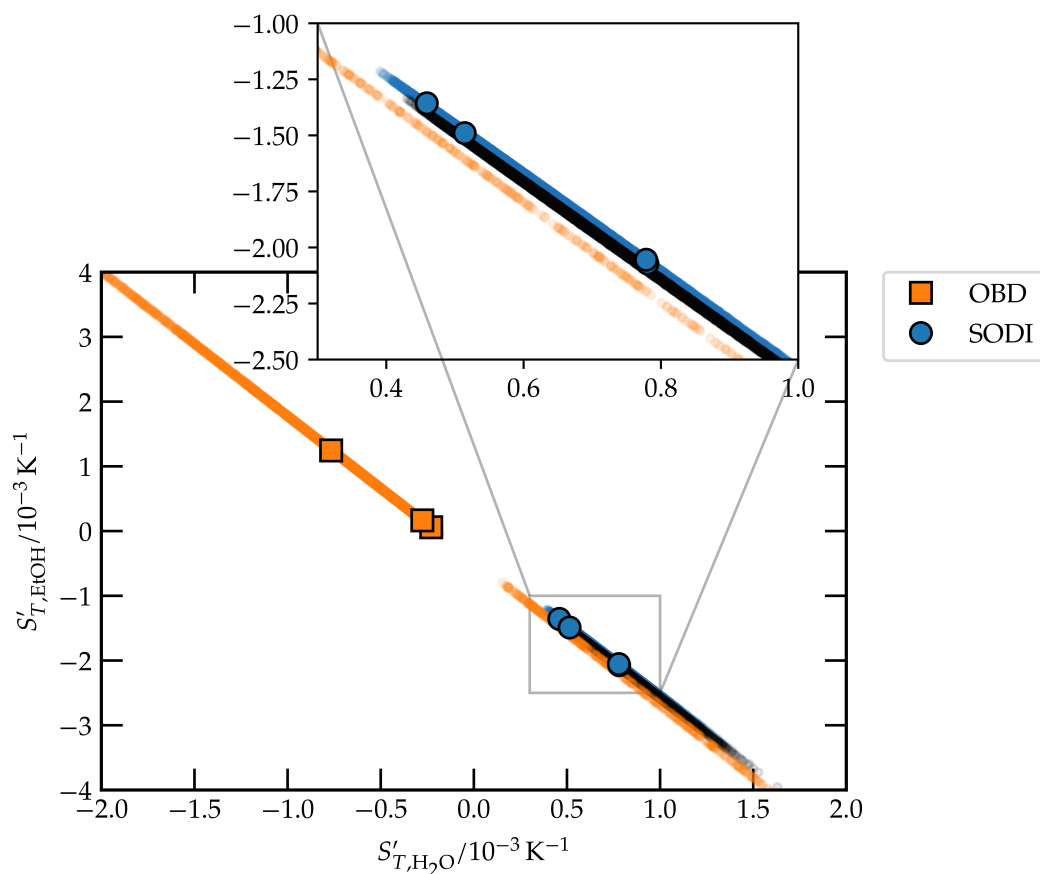


**Figure 5.32:** Soret coefficients cell 4 DCMIX3 at 25 °C. The elongated regions represent the compatibility space calculated via a Monte-Carlo approach. The black region contains the tomographic correction for this work. Filled symbols represent individual measurements via SODI or OBD.

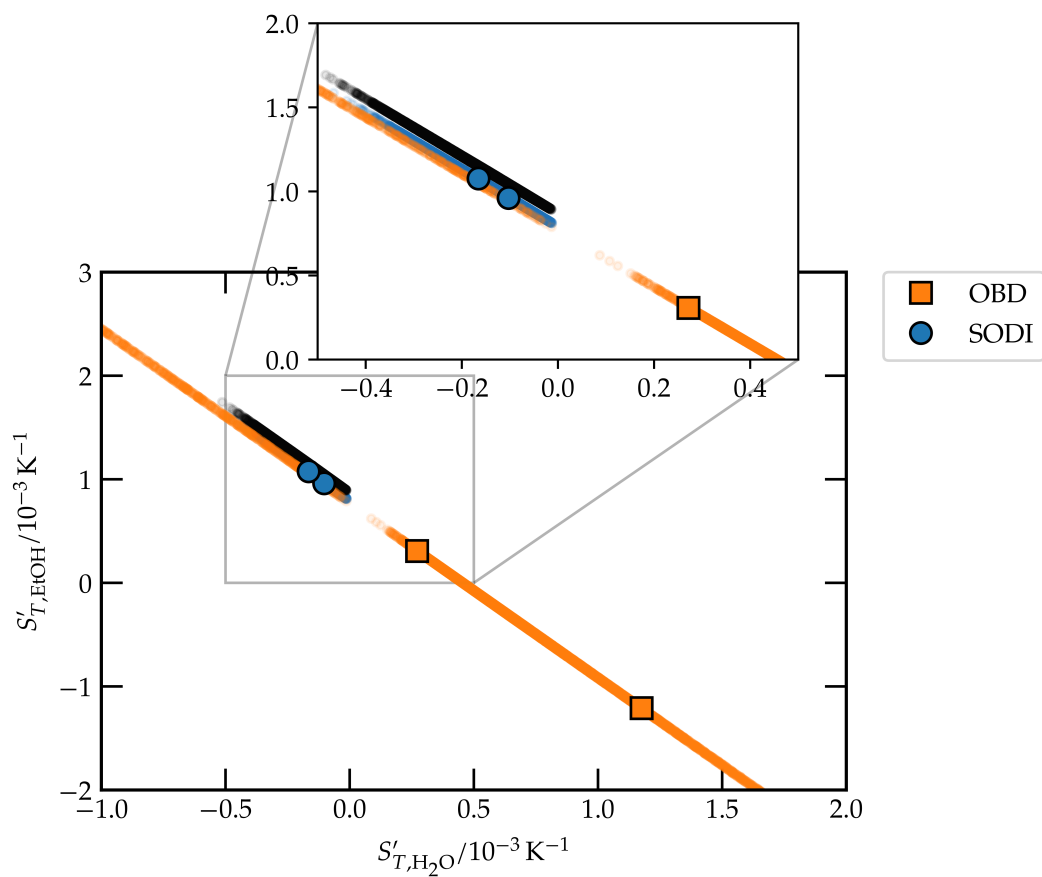


**Figure 5.33:** Soret coefficients cell 5 DCMIX3 at 25 °C. The elongated regions represent the compatibility space calculated via a Monte-Carlo approach. The black region contains the tomographic correction for this work. Filled symbols represent individual measurements via SODI or OBD.

**Table 5.10:** Thermodiffusion coefficients  $D'_{T,i}$  measured with TGC at 25 °C, kindly provided by Lapeira and Bou-Ali (University of Mondragon). Values for  $S'_{T,i}$  were calculated via Eq. (2.11), utilizing diffusion matrices given in Ref. [83]. The  $b_i/q^2$  in turn were calculated from Eq. (4.14). For this, contrast factors from OBD, not TGC, were used to allow these values to be comparable with OBD measurements.

cell	$c_1$	$c_2$	$c_3$	$D'_{T,H_2O}$	$D'_{T,EtOH}$	$b_1/q^2$	$b_2/q^2$	$S'_{T,H_2O}$	$S'_{T,EtOH}$
				/ $10^{-13} \text{ m}^2 \text{ s}^{-1} \text{ K}^{-1}$		/ $10^{-11} \text{ m}^2 \text{ s}^{-1}$		/ $10^{-3} \text{ K}^{-1}$	
2	0.33	0.33	0.33	3.67	-1.93	-6.30	-6.22	0.97	-0.62
3	0.25	0.60	0.15	4.36	-3.30	-2.61	-2.61	1.34	-1.03

below 10 % for cell 2 and below 1 % for cell 3. For one, this testifies to the value of the stable quantities introduced in Ref. [15]; furthermore, this similarity between the two methods bodes well for future studies in the system, especially measurements at 30 °C, allowing to include SODI results.

In summary, the presented results verify the value of the DCMIX project as a nucleus for important studies in ternary systems. The studies performed in this work allow to provide a comprehensive comparison between ground and microgravity measurements in the system water/ethanol/triethylene glycol for the first time, indicating a general compatibility between all considered experiments. Also, the observed contrast factor problem, especially for OBD, reinforces the importance of the associated condition numbers for the choice of molecules.

**Table 5.11:** Averaged  $b_i/q^2$  and  $S'_{T,i}$  from OBD measurements at 25 °C. Full results are given in Table B.3.

cell	$c_1$	$c_2$	$c_3$	$b_1/q^2$	$b_2/q^2$	$S'_{T,H_2O}$	$S'_{T,EtOH}$
				/ $10^{-11} \text{ m}^2 \text{ s}^{-1}$		/ $10^{-3} \text{ K}^{-1}$	
1	0.20	0.20	0.60	$-5.910 \pm 0.003$	$-6.0 \pm 0.1$	$0.4 \pm 0.5$	$0.3 \pm 0.5$
2	0.33	0.33	0.33	$-6.830 \pm 0.006$	$-6.82 \pm 0.04$	$-1.8 \pm 1.7$	$2.7 \pm 2.0$
3	0.25	0.60	0.15	$-2.61 \pm 0.02$	$-2.59 \pm 0.01$	$0.2 \pm 0.4$	$-0.1 \pm 0.4$
4	0.75	0.15	0.10	$9.54 \pm 0.16$	$9.49 \pm 0.22$	$-0.4 \pm 0.4$	$0.5 \pm 1.0$
5	0.50	0.10	0.40	$-7.98 \pm 0.02$	$-7.90 \pm 0.06$	$0.7 \pm 0.6$	$-0.5 \pm 1.1$





## 6 Summary and Conclusions

This work presents the first analysis of diffusive properties of the ternary system water/ethanol/triethylene glycol under microgravity conditions, combining results from measurements conducted during the DCMIX3 campaign on the ISS, as well as ground measurements performed by Optical Beam Deflection. Of special interest for this work is the Soret effect, which describes the diffusive demixing of mixtures under a temperature gradient. Chapter 2 explains the theoretical foundations of the Soret effect in the field of (linear) non-equilibrium thermodynamics, presenting the phenomenological equations used to describe transport phenomena in non-equilibrium conditions. Building on this framework, the general governing equations for optical experiments are recapitulated, with focus on the dimensionless solution of the extended diffusion equation. Most importantly, the role of the so-called contrast factors in ternary experiments, connecting detectable refractive index changes to concentration shifts in a sample, as currently understood in the literature is explained. Especially the concept of the condition number of the contrast factor matrix, which acts as a measure of the error-propagation during transformation between refractive index and concentration space, and the asymmetric nature of the error-propagation gain importance in the ternary case. Building on this, a general concept for comparing different experimental results can be defined: values are compatible if the compatibility spaces, resulting from high condition numbers, overlap. From this property of ternary measurements, the general need for microgravity data can be made clear. Since in many cases gravitational instabilities, which are always a concern in Soret effect measurements on ground, cannot be separated from instrument drifts — and are possible even in configurations which would normally be assumed to be stable — only measurements in a environment guaranteed to be free of convection can yield unambiguous reference data.

This need for microgravity reference data initiated the DCMIX project, a cooperation of multiple international research teams with ESA. Since measurements in several systems have already been performed and DCMIX being the foundation for measurements in this work, the history and rationale of the project are explained in detail in Chapter 3. Special focus is given to the DCMIX3 campaign, the system water/ethanol/triethylene glycol, since most of the presented work revolves around the preparations and operations of DCMIX3, with the author being part of the PI team. Apart from the sample preparations, a detailed timeline of events and experimental protocols is given, which can act as necessary reference for future work on DCMIX3 data. During DCMIX3 operations, a total of 31 experimental runs were performed; the unexpected occurrence of a bubble in cell

3 prevented measurements at 25 °C for this mixture. But by elevating the mean measurement temperature to 30 °C, the bubble could be forced out of the visible volume, allowing one bubble-free run in cell 3. Furthermore, a complementary set of measurements at 30 °C in all cells could be accomplished.

Experimental details of the relevant techniques are explained in Chapter 4, including the necessary contrast factor measurements for transformation of the measurements into concentration space. A common trait between all employed methods is the use of a Soret cell: a sample is sandwiched between plates with high thermal conductivity, which allows to force a homogeneous temperature gradient along the fluid bulk. Transparent windows allow monitoring of the refractive index changes of the sample. For ground measurements, Optical Beam Deflection (OBD) is used, which relies on the deflection of a laser beam when traveling through the refractive index gradient. Deduction of the governing equations from the dimensionless solution of the extended diffusion equations is presented, incorporating the latest results from literature regarding stable quantities of these descriptions. The microgravity experiment SODI (Selectable Optical Diagnostics Instrument), which was used during the DCMIX3 campaign on the ISS, is another variant of such an optical instrument, but relying on a phase-shifting Mach-Zehnder interferometer for detection of refractive index changes. Recovery of the phase maps of the images necessitates application of Phase-Shifting algorithms, details of which are given in Sections 4.3.2 and 4.3.3. From these phase maps, a signal very similar to the one found in Optical Beam Deflection can be generated, which allows the application of the same fitting routines and simplifies comparisons.

Before SODI-DCMIX3 data can be analyzed, the proposed methods of fitting an OBD-equivalent signal has to be tested on data with references available. The DCMIX1 campaign, investigating tetralin/n-dodecane/isobutylbenzene, was already performed in 2011/2012; therefore, Section 5.1 focuses on DCMIX1 data, first summarizing housekeeping data and quantifying image quality. Employing a phase-step estimation, low signal-to-noise ratios can be traced to a defective phase-stepping of the lasers during some runs. Next, the fitted results are compared to ground measurements from literature, as well as the other established methods. This shows, that the proposed method performs comparably with the ones already in use by other teams, but yields a general underestimation with respect to ground results. A tomographic correction proposed in the literature can compensate almost completely for this discrepancy, taking into account the design details of the sample cell.

Having validated the employed method on DCMIX1 data, Section 5.2 summarizes the results on DCMIX3. Utilizing OBD, the five ternary DCMIX3 mixtures were measured, with a special focus on potential gravitational instabilities; by carefully choosing stable temperature gradient configurations, reference values for all mixtures could be generated. Interestingly, this study reveals that some of the mixtures are prone to instabilities in the thermally stable configuration of heating from above. Instead, stable measurements were only achieved in the

---

counterintuitive situation of heating from below, which is normally more susceptible to instability. For SODI, the same summary of housekeeping data and image quality is given as in the case of DCMIX1, again identifying experimental runs affected by laser instabilities. Applying the OBD-equivalent analysis, a comprehensive comparison between SODI and OBD results, as well as values from Thermo-Gravitational Column measurements kindly provided by Lapeira and Bou-Ali, can be achieved. Even though the ill-conditioning of the contrast factor matrices for both SODI and OBD leads to a wide range of possible values, it can be shown that both microgravity and ground experiments yield compatible results. Unfortunately, lacking contrast factors for SODI at 30 °C, this comparison can only be conducted at 25 °C. But the presented data lays the necessary groundwork for future analysis in this system as soon as SODI contrast factors become available, such as a comparison of provided OBD and SODI data for cell 3 at 30 °C, respectively a comparison for all other SODI measurements at 30 °C, utilizing the provided fit coefficients. Furthermore, future improvements in measuring these factors can directly be applied to refine the results of this work.



# Appendix A Thermophysical Data

**Table A.1:** Refractive index of the DCMIX3b mixtures at 633 nm and 20 °C, measured before and after degassing. The changes are within the precision of the measurement device, which indicates that sample composition has not changed noticeably during degassing.

cell	$c_{\text{H}_2\text{O}}$	$c_{\text{EtOH}}$	$c_{\text{TEG}}$	$n_{633\text{ nm}}$		difference
				undegassed	degassed	
1	0.20	0.20	0.60	1.38915	1.38925	$1 \cdot 10^{-4}$
2	0.33	0.33	0.33	1.41431	1.41452	$2.1 \cdot 10^{-4}$
3	0.25	0.60	0.15	1.37541	1.37540	$0.1 \cdot 10^{-4}$
4	0.75	0.15	0.10	1.35452	1.35452	0
5	0.50	0.10	0.40	1.38869	1.38880	$1.1 \cdot 10^{-4}$
6	0.85	0.15	—	1.34233	1.34237	$0.4 \cdot 10^{-4}$

**Table A.2:** Density of the DCMIX3b mixtures measured before and after degassing at 25 °C. For all mixtures, the density increases after degassing, as should be expected after the removal of solved gases.

cell	$c_{\text{H}_2\text{O}}$	$c_{\text{EtOH}}$	$c_{\text{TEG}}$	$\rho_{25\text{ °C}}/\text{g cm}^{-3}$		difference / $\text{g cm}^{-3}$
				undegassed	degassed	
1	0.20	0.20	0.60	1.030979	1.031535	$5.6 \cdot 10^{-4}$
2	0.33	0.33	0.33	0.975060	0.975788	$7.3 \cdot 10^{-4}$
3	0.25	0.60	0.15	0.894754	0.895093	$3.4 \cdot 10^{-4}$
4	0.75	0.15	0.10	0.988196	0.988362	$1.7 \cdot 10^{-4}$
5	0.50	0.10	0.40	1.039238	1.039785	$5.5 \cdot 10^{-4}$
6	0.85	0.15	—	0.973348	0.973396	$0.5 \cdot 10^{-4}$

**Table A.3:** Measured refractive index data for DCMIX3 parametrization at 20 °C.

sample ID	c(H <sub>2</sub> O)	c(EtOH)	c(TEG)	$n_{405\text{ nm}}$	$n_{437\text{ nm}}$	$n_{488\text{ nm}}$	$n_{532\text{ nm}}$	$n_{589\text{ nm}}$	$n_{633\text{ nm}}$	$n_{684\text{ nm}}$
id092	1.00	0.00	0.00	1.343034	1.340533	1.337540	1.335483	1.333486	1.332177	1.330980
id075	0.90	0.10	0.00	1.349750	1.347190	1.344138	1.342055	1.340050	1.338705	1.337529
id076	0.90	0.00	0.10	1.355165	1.352512	1.349390	1.347278	1.345255	1.343892	1.342691
id074	0.80	0.20	0.00	1.357093	1.354561	1.351427	1.349313	1.347277	1.345945	1.344764
id077	0.80	0.00	0.20	1.367959	1.365149	1.361922	1.359770	1.357679	1.356295	1.355066
id124	0.75	0.15	0.10	1.366017	1.363318	1.360104	1.357958	1.355888	1.354525	1.353319
id073	0.70	0.30	0.00	1.363865	1.361172	1.357966	1.355830	1.353787	1.352447	1.351267
id099	0.70	0.10	0.20	1.375116	1.372300	1.369013	1.366814	1.364716	1.363323	1.362091
id078	0.70	0.00	0.30	1.381208	1.378305	1.374965	1.372742	1.370604	1.369194	1.367942
id071	0.60	0.40	0.00	1.368578	1.365829	1.362602	1.360459	1.358407	1.357054	1.355870
id079	0.60	0.00	0.40	1.394760	1.391797	1.388366	1.386067	1.383852	1.382423	1.381150
id100	0.55	0.25	0.20	1.384355	1.381436	1.378092	1.375852	1.373717	1.372324	1.371100
id114	0.50	0.50	0.00	1.371829	1.369045	1.365800	1.363658	1.361588	1.360241	1.359072
id098	0.50	0.11	0.40	1.401019	1.398023	1.394551	1.392215	1.389983	1.388550	1.387281
id123	0.50	0.10	0.40	1.401047	1.398060	1.394584	1.392262	1.390020	1.388580	1.387316
id080	0.50	0.00	0.50	1.408573	1.405392	1.401860	1.399499	1.397214	1.395763	1.394456
id115	0.40	0.60	0.00	1.373985	1.371197	1.367927	1.365776	1.363709	1.362371	1.361199
id096	0.40	0.40	0.20	1.389276	1.386333	1.382946	1.380685	1.378543	1.377152	1.375946
id081	0.40	0.00	0.60	1.422064	1.418853	1.415197	1.412738	1.410399	1.408920	1.407602
id113	0.33	0.33	0.33	1.401704	1.398632	1.395139	1.392822	1.390588	1.389173	1.387936
id067	0.30	0.70	0.00	1.375329	1.372478	1.369202	1.367034	1.364983	1.363642	1.362493
id095	0.30	0.30	0.40	1.407957	1.404789	1.401279	1.398911	1.396655	1.395239	1.393971
id122	0.30	0.10	0.60	1.425858	1.422659	1.418962	1.416496	1.414114	1.412638	1.411326

Continued on next page

**Table A.3:** Measured refractive index data for DCMIX3 parametrization at 20 °C.

sample ID	c(H <sub>2</sub> O)	c(EtOH)	c(TEG)	$n_{405\text{ nm}}$	$n_{437\text{ nm}}$	$n_{488\text{ nm}}$	$n_{532\text{ nm}}$	$n_{589\text{ nm}}$	$n_{633\text{ nm}}$	$n_{684\text{ nm}}$
id082	0.30	0.00	0.70	1.435021	1.431823	1.428046	1.425510	1.423092	1.421588	1.420253
id128	0.25	0.60	0.15	1.387255	1.384391	1.380993	1.378758	1.376615	1.375262	1.374084
id101	0.25	0.55	0.20	1.391443	1.388423	1.385020	1.382754	1.380606	1.379228	1.378029
id065	0.20	0.80	0.00	1.375758	1.372854	1.369565	1.367403	1.365357	1.364029	1.362883
id127	0.20	0.20	0.60	1.427992	1.424594	1.420866	1.418379	1.415999	1.414530	1.413222
id083	0.20	0.00	0.80	1.447375	1.444060	1.440150	1.437541	1.435058	1.433517	1.432154
id116	0.10	0.90	0.00	1.374930	1.372115	1.368821	1.366672	1.364625	1.363307	1.362177
id105	0.10	0.70	0.20	1.390920	1.387869	1.384458	1.382196	1.380051	1.378692	1.377516
id097	0.10	0.50	0.40	1.408422	1.405137	1.401581	1.399209	1.396959	1.395559	1.394324
id121	0.10	0.30	0.60	1.428346	1.424978	1.421206	1.418700	1.416312	1.414858	1.413588
id093	0.10	0.10	0.80	1.448246	1.444811	1.440882	1.438260	1.435781	1.434242	1.432880
id084	0.10	0.00	0.90	1.458933	1.455452	1.451415	1.448736	1.446183	1.444606	1.443226
id054	0.00	1.00	0.00	1.372153	1.369225	1.365952	1.363795	1.361791	1.360492	1.359389
id120	0.00	0.90	0.10	1.380173	1.377215	1.373883	1.371688	1.369613	1.368294	1.367161
id048	0.00	0.80	0.20	1.388656	1.385688	1.382230	1.379930	1.377808	1.376482	1.375379
id042	0.00	0.70	0.30	1.398202	1.394651	1.391173	1.388827	1.386653	1.385298	1.384126
id046	0.00	0.60	0.40	1.407227	1.403766	1.400120	1.397653	1.395394	1.394061	1.392962
id066	0.00	0.50	0.50	1.416420	1.413236	1.409581	1.407126	1.404819	1.403416	1.402190
id047	0.00	0.40	0.60	1.427158	1.423328	1.419641	1.417209	1.414924	1.413352	1.412034
id064	0.00	0.30	0.70	1.436643	1.433278	1.429445	1.426882	1.424468	1.422979	1.421672
id119	0.00	0.20	0.80	1.447134	1.443573	1.439625	1.437015	1.434515	1.432998	1.431655
id118	0.00	0.10	0.90	1.458232	1.454740	1.450668	1.447990	1.445428	1.443866	1.442500
id061	0.00	0.00	1.00	1.469950	1.466333	1.462146	1.459377	1.456776	1.455169	1.453749

**Table A.4:** Measured  $\partial n/\partial T$  data at 405 nm for DCMIX3, with linear and quadratic coefficients. See Section 4.2.2 for details.

sample ID	c(H2O)	c(EtOH)	c(TEG)	$b_{\text{lin},0}$		$b_{\text{quad},0}$		$b_{\text{lin},1}$		$b_{\text{quad},1}$		$b_{\text{quad},2}$		$\partial n/\partial T_{\text{lin},25^\circ\text{C}}$		$\partial n/\partial T_{\text{quad},25^\circ\text{C}}$	
				$/10^{-4}\text{K}^{-1}$		$/10^{-4}\text{K}^{-1}$		$/10^{-6}\text{K}^{-2}$		$/10^{-8}\text{K}^{-3}$		$/10^{-4}\text{K}^{-1}$		$/10^{-4}\text{K}^{-1}$			
id053	1.00	0.00	0.0	-0.341	-0.130	-3.058	-4.766	3.367	-1.105	-1.111							
id073	0.70	0.30	0.0	-2.195	-2.179	-1.676	-1.801	0.246	-2.614	-2.614							
id099	0.70	0.10	0.2	-1.643	-2.225	-1.635	2.942	-8.953	-2.052	-2.049							
id078	0.70	0.00	0.3	-1.406	-1.327	-1.846	-2.475	1.239	-1.867	-1.869							
id100	0.55	0.25	0.2	-2.652	-2.672	-1.075	-0.953	-0.163	-2.921	-2.921							
id069	0.50	0.50	0.0	-3.156	-3.211	-1.037	-0.597	-0.875	-3.415	-3.415							
id098	0.50	0.11	0.4	-2.487	-2.479	-0.965	-1.015	0.083	-2.728	-2.727							
id080	0.50	0.00	0.5	-2.255	-2.342	-1.004	-0.300	-1.391	-2.506	-2.504							
id096	0.40	0.40	0.2	-3.197	-3.454	-0.843	1.248	-4.183	-3.408	-3.403							
id067	0.30	0.70	0.0	-3.599	-3.689	-1.054	-0.326	-1.457	-3.863	-3.861							
id095	0.30	0.30	0.4	-3.199	-3.141	-0.710	-1.215	1.066	-3.377	-3.378							
id082	0.30	0.00	0.7	-2.889	-2.852	-0.435	-0.737	0.603	-2.998	-2.999							
id101	0.25	0.55	0.2	-3.235	-2.493	-2.074	-7.832	11.110	-3.753	-3.757							
id094	0.20	0.20	0.6	-3.241	-3.322	-0.491	0.160	-1.306	-3.363	-3.363							
id105	0.10	0.70	0.2	-3.606	-3.855	-1.458	0.429	-3.596	-3.970	-3.972							
id097	0.10	0.50	0.4	-3.614	-3.416	-0.556	-2.167	3.209	-3.753	-3.757							
id093	0.10	0.10	0.8	-3.229	-3.049	-0.528	-1.985	2.869	-3.361	-3.366							
id054	0.00	1.00	0.0	-4.093	-4.290	-0.554	0.903	-2.665	-4.232	-4.231							
id042	0.00	0.70	0.3	-3.901	-3.788	-0.350	-1.253	1.768	-3.988	-3.990							
id066	0.00	0.50	0.5	-3.714	-3.761	-0.348	0.035	-0.759	-3.801	-3.800							
id043	0.00	0.30	0.7	-3.600	-3.585	-0.128	-0.091	-0.382	-3.632	-3.632							
id061	0.00	0.00	1.0	-3.382	-3.484	0.075	0.899	-1.626	-3.364	-3.361							



**Table A.5:** Measured  $\partial n/\partial T$  data at 633 nm for DCMIX3, with linear and quadratic coefficients. See Section 4.2.2 for details.

sample ID	c(H <sub>2</sub> O)	c(EtOH)	c(TEG)	$b_{\text{lin},0}$ / $10^{-4} \text{ K}^{-1}$	$b_{\text{quad},0}$ / $10^{-6} \text{ K}^{-2}$	$b_{\text{lin},1}$ / $10^{-6} \text{ K}^{-2}$	$b_{\text{quad},1}$ / $10^{-8} \text{ K}^{-3}$	$\partial n/\partial T_{\text{lin},25^\circ\text{C}}$ / $10^{-4} \text{ K}^{-1}$	$\partial n/\partial T_{\text{quad},25^\circ\text{C}}$
id053	1.00	0.00	0.0	-0.297	-0.079	-3.063	4.816	-1.063	-1.065
id073	0.70	0.30	0.0	-2.117	-2.115	-1.655	-1.665	-2.531	-2.531
id099	0.70	0.10	0.2	-1.501	-1.482	-1.946	-2.099	-1.987	-1.987
id078	0.70	0.00	0.3	-1.348	-1.350	-1.842	-1.820	-1.809	-1.809
id100	0.55	0.25	0.2	-2.548	-2.534	-1.144	-1.258	-2.834	-2.834
id069	0.50	0.50	0.0	-3.062	-3.110	-1.030	-0.646	-3.319	-3.319
id098	0.50	0.11	0.4	-2.398	-2.385	-1.020	-1.123	-2.653	-2.653
id080	0.50	0.00	0.5	-2.184	-2.219	-1.013	-0.726	-2.437	-2.436
id096	0.40	0.40	0.2	-3.108	-2.919	-0.852	-2.370	-3.321	-3.325
id067	0.30	0.70	0.0	-3.497	-3.536	-1.007	-0.687	-3.749	-3.748
id095	0.30	0.30	0.4	-3.104	-2.812	-0.798	-3.153	-3.304	-3.309
id082	0.30	0.00	0.7	-2.807	-2.813	-0.457	-0.410	-2.922	-2.921
id101	0.25	0.55	0.2	-3.420	-3.277	-0.841	-1.987	-3.631	-3.633
id094	0.20	0.20	0.6	-3.151	-3.305	-0.534	0.701	-3.285	-3.283
id105	0.10	0.70	0.2	-3.724	-3.790	-0.525	-0.014	-3.855	-3.854
id097	0.10	0.50	0.4	-3.522	-3.752	-0.490	1.358	-3.645	-3.641
id093	0.10	0.10	0.8	-3.203	-3.251	-0.222	0.169	-3.259	-3.258
id054	0.00	1.00	0.0	-3.980	-4.036	-0.515	-0.063	-4.109	-4.108
id042	0.00	0.70	0.3	-3.835	-3.876	-0.161	0.173	-3.875	-3.874
id066	0.00	0.50	0.5	-3.625	-3.640	-0.295	-0.173	-3.699	-3.698
id043	0.00	0.30	0.7	-3.549	-3.495	0.035	-0.390	-3.540	-3.541
id061	0.00	0.00	1.0	-3.275	-3.268	0.013	-0.042	-3.272	-3.272

**Table A.6:** Measured density data (*Anton Paar DSA 5000 M*) for DCMIX3 for 10 °C to 35 °C. Missing values are due to bubble formation during measurement.

sample ID	c(H <sub>2</sub> O)	c(EtOH)	c(TEG)	$\rho_{10\text{ }^{\circ}\text{C}}$	$\rho_{15\text{ }^{\circ}\text{C}}$	$\rho_{20\text{ }^{\circ}\text{C}}$	$\rho_{25\text{ }^{\circ}\text{C}}$	$\rho_{30\text{ }^{\circ}\text{C}}$	$\rho_{35\text{ }^{\circ}\text{C}}$
/g cm <sup>-3</sup>									
id092	1.00	0.00	0.00	0.999714	0.999124	0.998233	0.997081	0.995686	0.994071
id075	0.90	0.10	0.00	0.983933	0.983052	0.981878	0.980442	0.978759	0.976856
id076	0.90	0.00	0.10	1.015234	1.014268	1.013046	1.011600	1.009940	1.008075
id107	0.85	0.15	0.00	0.978003	0.976706	0.975150	0.973348	0.971333	0.969110
id074	0.80	0.20	0.00	0.972502	0.970672	0.968630	0.966388	0.963955	0.961341
id077	0.80	0.00	0.20	1.031942	1.030503	1.028861	1.027034	1.025028	1.022850
id124	0.75	0.15	0.10	0.994762	0.992753	0.990565	0.988208	0.985686	0.983007
id073	0.70	0.30	0.00	0.959774	0.956864	0.953829	0.950678	0.947413	0.944035
id099	0.70	0.10	0.20	1.017810	1.015636	1.013312	1.010842	1.008230	1.005480
id078	0.70	0.00	0.30	1.049296	1.047327	1.045206	1.042947	1.040548	1.038007
id071	0.60	0.40	0.00	0.942398	0.938840	0.935207	0.931504	0.927724	0.923866
id079	0.60	0.00	0.40	1.066704	1.064207	1.061602	1.058898	1.056092	1.053182
id100	0.55	0.25	0.20	0.993628	0.990259	0.986814	0.983297	0.979702	0.976020
id114	0.50	0.50	0.00	0.921822	0.917969	0.914049	0.910064	0.906001	0.901885
id098	0.50	0.11	0.40	1.047528	1.044312	1.041022	1.037667	1.034242	1.030732
id123	0.50	0.10	0.40	1.049017	1.045822	1.042557	1.039223	1.035817	1.032327
id080	0.50	0.00	0.50	1.083367	1.080397	1.077352	1.074239	1.071039	1.067778
id115	0.40	0.60	0.00	0.899492	0.895468	0.891381	0.887232	0.883012	0.878737
id096	0.40	0.40	0.20	0.960316	0.956426	0.952514	0.948539	0.944524	0.940389
id081	0.40	0.00	0.60	1.098418	1.095069	1.091668	1.088223	1.084726	1.081175
id113	0.33	0.33	0.33	0.987032	0.983157	0.979231	0.975260	0.971241	0.967158

Continued on next page

**Table A.6:** Measured density data (*Anton Paar* DSA 5000 M) for DCMIX3 for 10 °C to 35 °C. Missing values are due to bubble formation during measurement.

sample ID	c(H <sub>2</sub> O)	c(EtOH)	c(TEG)	$\rho_{10\text{ }^{\circ}\text{C}}$	$\rho_{15\text{ }^{\circ}\text{C}}$	$\rho_{20\text{ }^{\circ}\text{C}}$	$\rho_{25\text{ }^{\circ}\text{C}}$	$\rho_{30\text{ }^{\circ}\text{C}}$	$\rho_{35\text{ }^{\circ}\text{C}}$
/g cm <sup>-3</sup>									
id067	0.30	0.70	0.00	0.876138	0.871996	0.867793	0.863536	0.859220	0.854826
id095	0.30	0.30	0.40	1.000749	0.996869	0.992944	0.988980	0.984968	0.980898
id122	0.30	0.10	0.60	1.072781	1.069069	1.065318	1.061534	1.057710	1.053836
id082	0.30	0.00	0.70	1.110945	1.107337	1.103695	1.100024	1.096317	1.092572
id117	0.25	0.60	0.15	0.907471	0.903373	0.899225	0.895027	0.890774	0.886457
id101	0.25	0.55	0.20	0.922392	0.918320	0.914199	0.910018	0.905794	0.901517
id065	0.20	0.80	0.00	0.852089	0.847864	0.843584	0.839254	0.834852	0.830400
id108	0.20	0.20	0.60	1.042699	1.038824	1.034915	1.030979	1.026996	1.022994
id083	0.20	0.00	0.80	1.120375	1.116625	1.112858	1.109071	1.105261	1.101426
id116	0.10	0.90	0.00	0.826997	0.822738	0.818429	0.814067	0.809663	0.805208
id105	0.10	0.70	0.20	0.881418	0.877273	0.873078	0.868836	0.864547	0.860216
id097	0.10	0.50	0.40	0.941982	0.937897	0.933783	0.929685	0.925545	0.921372
id121	0.10	0.30	0.60	1.010425	1.006472	1.002496	0.998500	0.994476	0.990412
id093	0.10	0.10	0.80	1.085822	1.081967	1.078096	1.074212	1.070307	1.066371
id084	0.10	0.00	0.90	1.126727	1.122918	1.119094	1.115268	1.111425	1.107558
id055	0.00	1.00	0.00	0.797859	0.793624	0.789361	0.785076	0.780745	0.776395
id120	0.00	0.90	0.10	0.824432	0.820227	0.815996	0.811744	0.807451	0.803132
id048	0.00	0.80	0.20	0.851325	0.847150	0.842951	0.838733	0.834477	0.830201
id042	0.00	0.70	0.30	0.880242	0.876099	0.871934	0.867752	0.863551	0.859321
id046	0.00	0.60	0.40	0.910415	0.906306	0.902181	0.898039	0.893875	0.889679
id041	0.00	0.50	0.50	0.942310	0.938236	0.934148	0.930045	0.925928	0.921787

Continued on next page

**Table A.6:** Measured density data (*Anton Paar DSA 5000 M*) for DCMIX3 for 10 °C to 35 °C. Missing values are due to bubble formation during measurement.

sample ID	c(H <sub>2</sub> O)	c(EtOH)	c(TEG)	$\rho_{10\text{ }^{\circ}\text{C}}$	$\rho_{15\text{ }^{\circ}\text{C}}$	$\rho_{20\text{ }^{\circ}\text{C}}$	$\rho_{25\text{ }^{\circ}\text{C}}$	$\rho_{30\text{ }^{\circ}\text{C}}$	$\rho_{35\text{ }^{\circ}\text{C}}$
/g cm <sup>-3</sup>									
id047	0.00	0.40	0.60	0.976599	0.972569	0.968521	0.964464	0.960387	0.956285
id043	0.00	0.30	0.70	1.011838	1.007845	1.003835	0.999821	0.995794	0.991753
id119	0.00	0.20	0.80	1.049515	1.045564	1.041601	1.037633	1.033645	1.029653
id118	0.00	0.10	0.90	1.089379	1.085463	1.081543	1.077621	1.073680	1.069741
id057	0.00	0.00	1.00	1.131010	1.127123	1.123237	1.119354	1.115472	1.111585

**Table A.7:** Measured density data (*Anton Paar* DSA 5000 M) for DCMIX3 for 40 °C to 60 °C. Missing values are due to bubble formation during measurement.

sample ID	c(H <sub>2</sub> O)	c(EtOH)	c(TEG)	$\rho_{40\text{ }^{\circ}\text{C}}$	$\rho_{45\text{ }^{\circ}\text{C}}$	$\rho_{50\text{ }^{\circ}\text{C}}$	$\rho_{55\text{ }^{\circ}\text{C}}$	$\rho_{60\text{ }^{\circ}\text{C}}$
/g cm <sup>-3</sup>								
id092	1.00	0.00	0.00	0.992116	0.989793	0.987203	—	—
id075	0.90	0.10	0.00	0.974746	0.972441	0.969954	0.966691	—
id076	0.90	0.00	0.10	1.006034	1.003820	1.001446	0.998876	—
id107	0.85	0.15	0.00	0.966695	0.964097	0.961329	0.958400	0.955320
id074	0.80	0.20	0.00	0.958549	0.955607	0.952514	0.949280	0.945909
id077	0.80	0.00	0.20	1.020521	1.018043	1.015424	1.012667	1.009778
id124	0.75	0.15	0.10	0.980167	0.977194	0.974086	0.970848	0.967484
id073	0.70	0.30	0.00	0.940536	0.936945	0.933251	0.929460	0.925568
id099	0.70	0.10	0.20	1.002590	0.999582	0.996452	0.993204	0.989840
id078	0.70	0.00	0.30	1.035347	1.032562	1.029659	1.026639	1.023506
id071	0.60	0.40	0.00	0.919921	0.915912	0.911827	0.907664	0.903419
id079	0.60	0.00	0.40	1.050166	1.047059	1.043862	1.040566	1.037179
id100	0.55	0.25	0.20	0.972276	0.968454	0.964558	0.960584	0.956535
id114	0.50	0.50	0.00	0.897701	0.893448	0.889124	0.884730	0.880260
id098	0.50	0.11	0.40	1.027164	1.023523	1.019812	1.016031	1.012176
id123	0.50	0.10	0.40	1.028777	1.025155	1.021462	1.017698	1.013860
id080	0.50	0.00	0.50	1.064443	1.061033	1.057554	1.053998	1.050371
id115	0.40	0.60	0.00	0.874396	0.869982	0.865505	0.860955	0.856325
id096	0.40	0.40	0.20	0.936262	0.932045	—	—	—
id081	0.40	0.00	0.60	—	1.073903	1.070192	1.066425	1.062603
id113	0.33	0.33	0.33	0.963033	0.958857	0.954624	0.950334	0.945984

Continued on next page

**Table A.7:** Measured density data (*Anton Paar* DSA 5000 M) for DCMIX3 for 40 °C to 60 °C. Missing values are due to bubble formation during measurement.

sample ID	c(H <sub>2</sub> O)	c(EtOH)	c(TEG)	$\rho_{40\text{ °C}}$	$\rho_{45\text{ °C}}$	$\rho_{50\text{ °C}}$	$\rho_{55\text{ °C}}$	$\rho_{60\text{ °C}}$
/g cm <sup>-3</sup>								
id067	0.30	0.70	0.00	0.850377	0.845859	0.841274	0.836618	0.831884
id095	0.30	0.30	0.40	0.976792	0.972634	0.968427	0.964166	0.959849
id122	0.30	0.10	0.60	1.049932	1.045986	1.041999	1.037965	1.033884
id082	0.30	0.00	0.70	1.088781	1.084959	1.081100	1.077199	1.073252
id117	0.25	0.60	0.15	0.882091	0.877668	0.873181	0.868630	0.864012
id101	0.25	0.55	0.20	0.897183	0.892791	0.888337	0.883822	0.879239
id065	0.20	0.80	0.00	0.825886	0.821307	0.816662	0.811946	0.807151
id108	0.20	0.20	0.60	1.018957	1.014883	1.010772	1.006619	1.002424
id083	0.20	0.00	0.80	1.097559	1.093669	1.089752	1.085803	1.081822
id116	0.10	0.90	0.00	0.800697	0.796124	0.791486	0.786780	0.781997
id105	0.10	0.70	0.20	—	—	—	—	—
id097	0.10	0.50	0.40	—	—	—	—	—
id121	0.10	0.30	0.60	0.986329	0.982216	0.978068	0.973882	0.969659
id093	0.10	0.10	0.80	1.062428	1.058461	1.054472	1.050458	1.046414
id084	0.10	0.00	0.90	1.103689	1.099802	1.095897	1.091968	1.088015
id055	0.00	1.00	0.00	0.772004	0.767571	0.763085	—	—
id120	0.00	0.90	0.10	0.798781	0.794387	0.789946	0.785451	0.780896
id048	0.00	0.80	0.20	0.825890	0.821543	0.817156	0.812721	0.808229
id042	0.00	0.70	0.30	0.855049	0.850751	0.846417	0.842040	0.837613
id046	0.00	0.60	0.40	0.885465	0.881220	0.876941	0.872626	0.868265
id041	0.00	0.50	0.50	0.917614	0.913423	0.909203	0.904951	0.900660

Continued on next page

**Table A.7:** Measured density data (*Anton Paar* DSA 5000 M) for DCMIX3 for 40 °C to 60 °C. Missing values are due to bubble formation during measurement.

sample ID	c(H <sub>2</sub> O)	c(EtOH)	c(TEG)	$\rho_{40\text{ }^{\circ}\text{C}}$	$\rho_{45\text{ }^{\circ}\text{C}}$	$\rho_{50\text{ }^{\circ}\text{C}}$	$\rho_{55\text{ }^{\circ}\text{C}}$	$\rho_{60\text{ }^{\circ}\text{C}}$
/g cm <sup>-3</sup>								
id047	0.00	0.40	0.60	0.952173	0.948039	0.943879	0.939690	0.935472
id043	0.00	0.30	0.70	0.987684	0.983605	0.979506	0.975385	0.971238
id119	0.00	0.20	0.80	1.025650	1.021631	1.017598	1.013544	1.009473
id118	0.00	0.10	0.90	1.065793	1.061835	1.057867	1.053886	1.049889
id057	0.00	0.00	1.00	1.107688	1.103796	1.099898	1.095987	1.092069





# Appendix B Fit Coefficients

**Table B.1:** Fitted stable quantities for the analyzed SODI-DCMIX1 runs.  $A_{\text{th}}$  describes the thermal amplitude of the recovered signal.

	$A_{\text{th},670\text{ nm}}$	$A_{\text{th},935\text{ nm}}$	$a_1$	$a_2$	$b_1/q^2$	$b_2/q^2$	$\overline{D}$
	$/\text{rad px}^{-1}$				$/10^{-10} \text{ m}^2 \text{ s}^{-1}$		
<b>cell 1</b>							
run 16	-0.4456	-0.3191	0.1691	0.1649	1.85	1.81	8.32
run 21	-0.4452	-0.3191	0.1696	0.1648	1.87	1.81	8.30
<b>cell 2</b>							
run 02	-0.4883	-0.3484	0.1325	0.1291	1.44	1.40	8.13
run 17	-0.4879	-0.3483	0.1323	0.1285	1.39	1.39	8.26
run 22	-0.4887	-0.3488	0.1316	0.1283	1.45	1.41	8.45
run 27	-0.4882	-0.3483	0.1321	0.1288	1.46	1.43	8.52
<b>cell 3</b>							
run 03	-0.4678	-0.3332	0.3274	0.3202	2.16	2.11	5.02
run 18	-0.4677	-0.3335	0.3297	0.3227	2.13	2.09	4.79
run 23	-0.4664	-0.3333	0.3287	0.3208	2.16	2.11	5.00
<b>cell 4</b>							
run 04	-0.4466	-0.3197	0.5802	0.5640	4.49	4.37	5.86
run 19	-0.4465	-0.3184	0.5760	0.5620	4.54	4.43	6.11
run 24	-0.4465	-0.3197	0.5750	0.5582	4.53	4.40	6.13
<b>cell 5</b>							
run 05	-0.4542	-0.3252	0.5434	0.5263	4.52	4.37	5.59
run 15	-0.4481	-0.3197	0.5180	0.5026	4.98	4.84	7.22
run 20	-0.4985	-0.3204	0.4730	0.5325	4.29	4.90	7.09
run 25	-0.4533	-0.3234	0.5275	0.5084	4.46	4.27	6.23

**Table B.2:** Fitted stable quantities for the analyzed SODI-DCMIX3 runs.  $A_{\text{th}}$  describes the thermal amplitude of the recovered signal.

	$A_{\text{th},670\text{nm}}$	$A_{\text{th},935\text{nm}}$	$a_1$	$a_2$	$b_1/q^2$	$b_2/q^2$	$\bar{D}$
	/rad px <sup>-1</sup>				/10 <sup>-10</sup> m <sup>2</sup> s <sup>-1</sup>		
<b>cell 1</b>							
run 01	-0.1715	-0.1222	-0.1811	-0.1771	-0.50	-0.52	2.96
run 06	-0.1713	-0.1225	-0.1810	-0.1771	-0.50	-0.52	2.96
run 11	-0.1709	-0.1222	-0.1816	-0.1777	-0.51	-0.52	2.97
run 16	-0.1710	-0.1220	-0.1813	-0.1773	-0.51	-0.52	2.97
run 23	-0.1716	-0.1226	-0.1750	-0.1713	-0.60	-0.60	3.47
run 28	-0.1723	-0.1229	-0.1737	-0.1702	-0.60	-0.59	3.48
<b>cell 2</b>							
run 02	-0.1716	-0.1223	-0.1988	-0.1907	-0.62	-0.61	0.69
run 07	-0.1714	-0.1223	-0.1888	-0.1812	-0.63	-0.61	1.14
run 12	-0.1714	-0.1223	-0.1959	-0.1873	-0.63	-0.62	0.76
run 17	-0.1713	-0.1220	-0.1721	-0.1677	-0.62	-0.61	3.60
run 22	-0.1731	-0.1235	-0.1670	-0.1600	-0.70	-0.68	2.31
run 25	-0.1735	-0.1235	-0.1660	-0.1609	-0.71	-0.69	2.26
run 30	-0.1731	-0.1234	-0.1661	-0.1607	-0.71	-0.69	2.52
<b>cell 3</b>							
run 03	-0.1907	-0.1360	-0.0428	-0.0402	-0.34	-0.32	10.0
<b>cell 4</b>							
run 04	-0.1000	-0.0699	0.1313	0.1236	1.10	0.99	6.18
run 09	-0.1001	-0.0704	0.1246	0.1199	0.87	0.84	6.97
run 14	-0.1003	-0.0701	0.1267	0.1189	0.91	0.86	6.45
run 19	-0.1000	-0.0703	0.1294	0.1242	0.87	0.84	6.75
run 21	-0.1061	-0.0747	0.1304	0.1258	1.01	0.97	6.03
run 29	-0.1061	-0.0745	0.1288	0.1221	0.98	0.92	6.30
<b>cell 5</b>							
run 15	-0.1385	-0.0985	-0.2545	-0.2500	-0.75	-0.73	1.35
run 20	-0.1386	-0.0984	-0.2576	-0.2529	-0.75	-0.73	1.24
run 20a	-0.1415	-0.1004	-0.2220	-0.2181	-0.77	-0.75	1.70
run 24	-0.1417	-0.1008	-0.2217	-0.2178	-0.77	-0.75	1.70
run 27	-0.1415	-0.1006	-0.2232	-0.2177	-0.77	-0.75	1.57

**Table B.3:** Fitted stable quantities for OBD measurements in the DCMIX3 system.  $A_{\text{th}}$  describes the thermal amplitude of the recovered signal. It derives from the measured deflection in pixel by dividing through the instrument amplitude  $A = -1600 \text{ m} \times \text{px}$ . ID values refer to internal IDs given to each sample.

	$A_{\text{th},405\text{ nm}}$	$A_{\text{th},635\text{ nm}}$	$a_1$	$a_2$	$b_1/q^2$	$b_2/q^2$	$\overline{D}$
	/ $\text{m}^{-1}$				/ $10^{-10}\text{ m}^2\text{ s}^{-1}$		
<b>20-20-60 wt% (cell 1)</b>							
id126, $T_0 = 25^\circ\text{C}$							
$\Delta T = -0.5\text{ K}$	-0.1204	-0.1169	-0.1902	-0.1875	-0.59	-0.61	3.55
$\Delta T = +0.5\text{ K}$	-0.1206	-0.1173	-0.1884	-0.1874	-0.59	-0.60	3.68
id127, $T_0 = 30^\circ\text{C}$							
$\Delta T = +0.5\text{ K}$	-0.1206	-0.1177	-0.1820	-0.1787	-0.58	-0.60	3.73
<b>33-33-33 wt% (cell 2)</b>							
id113, $T_0 = 25^\circ\text{C}$							
$\Delta T = +1\text{ K}$	-0.2427	-0.2360	-0.1561	-0.1557	-0.68	-0.68	4.96
$\Delta T = +2\text{ K}$	-0.4718	-0.4856	-0.1545	-0.1564	-0.68	-0.69	5.22
<b>25-60-15 wt% (cell 3)</b>							
id117, $T_0 = 25^\circ\text{C}$							
$\Delta T = +0.5\text{ K}$	-0.1348	-0.1307	-0.0333	-0.0330	-0.26	-0.26	39.4
$\Delta T = +1\text{ K}$	-0.2702	-0.2627	-0.0335	-0.0330	-0.26	-0.26	34.9
$\Delta T = +2\text{ K}$	-0.5405	-0.5256	-0.0327	-0.0326	-0.26	-0.26	36.3
id128, $T_0 = 30^\circ\text{C}$							
$\Delta T = +1\text{ K}$	-0.2733	-0.2657	-0.0347	-0.0340	-0.23	-0.23	10.1
$\Delta T = +2\text{ K}$	-0.5468	-0.5314	-0.0314	-0.0312	-0.27	-0.27	14.1
<b>75-15-10 wt% (cell 4)</b>							
id124, $T_0 = 25^\circ\text{C}$							
$\Delta T = -2\text{ K}$	0.2848	0.2747	0.1281	0.1265	0.95	0.95	8.37
$\Delta T = -1\text{ K}$	0.1422	0.1379	0.1281	0.1264	0.94	0.92	8.01
$\Delta T = -0.5\text{ K}$	0.0707	0.0682	0.1313	0.1309	0.98	0.98	8.36
<b>50-10-40 wt% (cell 5)</b>							
id123, $T_0 = 25^\circ\text{C}$							
$\Delta T = -1\text{ K}$	0.1940	0.1882	-0.2123	-0.2131	-0.80	0.80	3.70
$\Delta T = -0.5\text{ K}$	0.0969	0.0942	-0.2117	-0.2110	-0.80	0.78	3.69



# Appendix C Parametrization

As explained in Section 4.2.3, the refractive index  $n$  of a multi-component system can be parametrized as a function of the independent concentrations  $c_1$  and  $c_2$ , as well as the temperature  $T$ :

$$n_\lambda(c_1, c_2, T) = \sum_{i,j=0}^{i+j=P} A_{ij} c_1^i c_2^j + \sum_{m=0}^Q \sum_{k,l=0}^{k+l=R} B_{kl}^m c_1^k c_2^l \frac{(T^{m+1} - T_0^{m+1})}{m+1},$$

see also Eq. (4.22). The following tables give the resulting matrix elements  $A_{ij}$  and  $B_{kl}^m$  for the system water/ethanol/triethylene glycol at wavelengths  $\lambda = 405$  nm and 633 nm. The indices refer to the corresponding power of the concentrations  $c_1$  and  $c_2$ :

$$A = \begin{pmatrix} A_{00} & \dots & A_{05} \\ \vdots & \ddots & \vdots \\ A_{50} & \dots & A_{55} \end{pmatrix}$$

So the element  $A_{32}$  is the coefficient for the term  $c_1^3 c_2^2$ . Parametrization has been done in the system  $c_1$  (H<sub>2</sub>O) and  $c_2$  (EtOH).

Since the temperature dependence can be parametrized for different choices of  $Q$ , the elements of the matrices  $B_{kl}^m$  are given for the linear case  $Q = 1$  as well as the quadratic case  $Q = 2$ . The respective matrices are called  $B_{\text{lin}}$  and  $B_{\text{quad}}$ .

**Table C.1:** Matrices for refractive index parametrization, 405 nm.

index	$A$	$B_{\text{lin}}^0$	$B_{\text{quad}}^0$	$B_{\text{lin}}^1$	$B_{\text{quad}}^1$	$B_{\text{quad}}^2$
		$/10^{-4} \text{ K}^{-1}$		$/10^{-6} \text{ K}^{-2}$		$/10^{-8} \text{ K}^{-3}$
00	1.469959	-3.341471	-3.417106	-0.061150	0.553486	-1.223039
01	-0.123913	-1.111888	-1.277706	1.757683	3.723154	-5.203663
02	0.068277	1.255424	2.877969	-7.244117	-21.747703	31.681837
03	-0.102328	-0.890707	-2.527261	5.000253	18.837718	-28.808313
04	0.085566	0	0	0	0	0
05	-0.025485	0	0	0	0	0
10	-0.108097	0.370433	2.342065	-1.193112	-17.229039	32.060982
11	0.194579	1.536092	0.235174	-12.051153	-2.905118	-15.153925
12	-0.529446	-1.196714	-1.147476	9.209483	11.354079	-9.262705
13	0.639616	0	0	0	0	0
14	-0.228090	0	0	0	0	0
15	0	0	0	0	0	0
20	-0.013416	4.717681	-1.381001	-0.795219	48.627703	-98.554099
21	-0.410349	-5.832027	-4.058416	15.559808	1.427764	27.301426
22	1.055231	0	0	0	0	0
23	-0.735816	0	0	0	0	0
24	0	0	0	0	0	0
25	0	0	0	0	0	0
30	-0.080124	-2.033613	2.380806	-1.120827	-36.843247	71.116968
31	0.590717	0	0	0	0	0
32	-0.561053	0	0	0	0	0
33	0	0	0	0	0	0
34	0	0	0	0	0	0
35	0	0	0	0	0	0
40	0.116949	0	0	0	0	0
41	-0.314264	0	0	0	0	0
42	0	0	0	0	0	0
43	0	0	0	0	0	0
44	0	0	0	0	0	0
45	0	0	0	0	0	0
50	-0.042238	0	0	0	0	0
51	0	0	0	0	0	0
52	0	0	0	0	0	0
53	0	0	0	0	0	0
54	0	0	0	0	0	0
55	0	0	0	0	0	0

**Table C.2:** Matrices for refractive index parametrization, 633 nm.

index	$A$	$B_{\text{lin}}^0$	$B_{\text{quad}}^0$	$B_{\text{lin}}^1$	$B_{\text{quad}}^1$	$B_{\text{quad}}^2$
		$/10^{-4} \text{ K}^{-1}$		$/10^{-6} \text{ K}^{-2}$		$/10^{-8} \text{ K}^{-3}$
00	1.455182	-3.265298	-3.253399	0.021347	-0.074351	0.189097
01	-0.120730	-0.555573	-0.751890	-0.753850	0.914246	-3.455536
02	0.075815	-0.617240	-0.621226	1.226004	0.998314	0.914228
03	-0.139687	0.463911	0.586311	-1.008959	-1.815896	1.283775
04	0.140169	0	0	0	0	0
05	-0.050310	0	0	0	0	0
10	-0.102689	0.174070	-0.362648	-0.693677	3.654938	-8.627977
11	0.170909	-0.199905	4.961612	-4.298081	-46.225937	83.633648
12	-0.490744	0.660081	-3.430731	1.216969	34.584573	-66.848820
13	0.671753	0	0	0	0	0
14	-0.280741	0	0	0	0	0
15	0	0	0	0	0	0
20	-0.019224	5.419966	6.310887	-3.430512	-10.658291	14.302918
21	-0.311258	-4.096102	-9.403599	8.366043	51.379481	-85.621785
22	0.864578	0	0	0	0	0
23	-0.671220	0	0	0	0	0
24	0	0	0	0	0	0
25	0	0	0	0	0	0
30	-0.070712	-2.584994	-2.756445	0.983188	2.394154	-2.753268
31	0.456618	0	0	0	0	0
32	-0.417514	0	0	0	0	0
33	0	0	0	0	0	0
34	0	0	0	0	0	0
35	0	0	0	0	0	0
40	0.109205	0	0	0	0	0
41	-0.255669	0	0	0	0	0
42	0	0	0	0	0	0
43	0	0	0	0	0	0
44	0	0	0	0	0	0
45	0	0	0	0	0	0
50	-0.039593	0	0	0	0	0
51	0	0	0	0	0	0
52	0	0	0	0	0	0
53	0	0	0	0	0	0
54	0	0	0	0	0	0
55	0	0	0	0	0	0





# Appendix D Software and Sources

## D.1 Plots

All plots in this work have been done with the Python programming language, version 3.4<sup>1</sup>, utilizing several specialized open source packages for scientific programming and visualization:

- Numpy[115]
- Matplotlib [116]
- Pandas [117]
- python-ternary [118]

The necessary data for all plots is part of the source code of this thesis (`~/tex/Dissertation/plots/data`).

## D.2 Data Analysis

For analysis of SODI data, a C library implementing core phase-stepping algorithms and image manipulation routines has been written. Image manipulation routines depend on the FreeImage library<sup>2</sup>. On top of the core C library, a Python package (based on version 3.4) for convenient use has also been written, which interfaces with the library via ctypes. Apart from the Python standard library, some additional open source packages are utilized for this, especially:

- Numpy[115]
- pyqtgraph<sup>3</sup>

Since the complete data sets of DCMIX1 and DCMIX3 contain several hundred GB each, GNU parallel [119] was used for parallel data analysis to speed up the processing.

The necessary parametrization of refractive index measurements was done in Jupyter notebooks [120], utilizing the statsmodels package [121] for fitting, as well as Numpy and Pandas.

<sup>1</sup><http://www.python.org/>

<sup>2</sup><http://freeimage.sourceforge.net>

<sup>3</sup><http://www.pyqtgraph.org/>

## D.3 Source Paths

To allow reproduction of all results in this work, a list of storage locations for raw data as well as utilized software is given below. Of course, this can only be a snapshot of the current situation “as is”. Longterm reproducibility of these storage locations are outside of the influence of the author and cannot be guaranteed.

### D.3.1 Software

- source code of this thesis:  
`~/tex/Dissertation`
- SODI analysis:  
`/home/local2/git/SODI and ~/src/SODI`
- OBD measurement:  
`/home/local2/git/OBD/Messprogramme`
- OBD data preparation:  
`/home/local2/git/OBD/Auswertung/prepare_data_ternary.git`
- OBD fitting routine:  
`/home/local2/git/OBD/Auswertung/fit_signal_ternary.git`

### D.3.2 Data

- thermophysical data:  
`~/data/DCMIX3`
- Jupyter notebooks for parametrization of thermophysical data:  
`~/analysis/DCMIX3`
- recovered signals SODI-DCMIX1:  
`~/analysis/DCMIX1/signals`
- temperature data SODI-DCMIX1:  
`~/analysis/DCMIX1/temperature_data`
- recovered signals SODI-DCMIX3:  
`~/analysis/DCMIX3/SODI/signals`
- temperature data SODI-DCMIX3:  
`~/analysis/DCMIX3/SODI/temperature`
- OBD measurements DCMIX3:  
`~/analysis/DCMIX3/OBD/signals`

# Bibliography

- [1] A. Fick. "Ueber Diffusion". In: *Ann. Phys.* 170.1 (1855), pp. 59–86.  
doi: 10.1002/andp.18551700105 (cit. on p. 1).
- [2] S. R. de Groot and P. Mazur. *Non-Equilibrium Thermodynamics*. New York: Dover Publications, 1984.  
ISBN: 0486647412 (cit. on pp. 1, 5, 8, 10).
- [3] D. G. Miller. "The origins of Onsager's key role in the development of linear irreversible thermodynamics". In: *J. Stat. Phys.* 78.1 (1995), pp. 563–573.  
doi: 10.1007/BF02183365 (cit. on pp. 1, 7).
- [4] C. Ludwig. "Diffusion zwischen ungleich erwärmten Orten gleich zusammengesetzter Lösungen". In: *Sitzungsbericht. Kaiser. Akad. Wiss. (Mathem.-Naturwiss. Cl.)* 20 (1856), p. 539 (cit. on pp. 1, 6).
- [5] C. Soret. "Sur l'état d'équilibre que prend, du point de vue de sa concentration, une dissolution saline primitivement homogène, dont deux parties sont portées à des températures différentes". In: *Arch. Genève* II (1879), p. 48 (cit. on pp. 1, 6).
- [6] D. Braun and A. Libchaber. "Thermal force approach to molecular evolution". In: *Phys. Biol.* 1.1 (2004), P1.  
doi: 10.1088/1478-3967/1/1/P01 (cit. on p. 1).
- [7] H. E. Huppert and J. S. Turner. "Double-diffusive convection". In: *J. Fluid Mech.* 106 (1981), pp. 299–329.  
doi: 10.1017/S0022112081001614 (cit. on p. 1).
- [8] S. Van Vaerenbergh et al. "Multicomponent transport studies of crude oils and asphaltenes in DSC program". In: *Microgravity Sci. Technol.* 18.3 (2006), pp. 150–154. ISSN: 1875-0494.  
doi: 10.1007/BF02870399 (cit. on p. 1).
- [9] W. Köhler and K. I. Morozov. "The Soret Effect in Liquid Mixtures—A Review". In: *J. Non-Equilib. Thermodyn.* 41.3 (2016), pp. 151–197.  
doi: 10.1515/jnet-2016-0024 (cit. on p. 1).
- [10] R. Taylor and R. Krishna. *Wiley series in chemical engineering*. Vol. 2: *Multi-component mass transfer*. New York, Chichester, and Brisbane: John Wiley & Sons, 1993.  
ISBN: 0471574171 (cit. on pp. 5–7).

- [11] W. M. Deen. *Analysis of transport phenomena*. 2nd ed. New York and Oxford: Oxford University Press, 2013.  
ISBN: 9780199740253 (cit. on pp. 5, 6, 10–12).
- [12] M. Hartung. “A Detailed Treatment of the Measurement of Transport Coefficients in Transient Grating Experiments”. PhD thesis. Universität Bayreuth, 2007.  
URN: urn:nbn:de:bvb:703-opus-3806 (cit. on p. 5).
- [13] M. Gebhardt. “Thermodiffusion in ternären organischen Flüssigkeiten”. PhD thesis. Universität Bayreuth, 2015.  
URN: urn:nbn:de:bvb:703-epub-2485-4 (cit. on pp. 5, 43, 46, 49, 50, 88, 93).
- [14] K. B. Haugen and A. Firoozabadi. “On Measurement of Molecular and Thermal Diffusion Coefficients in Multicomponent Mixtures”. In: *J. Phys. Chem. B* 110.35 (2006), pp. 17678–17682.  
DOI: 10.1021/jp062382m (cit. on pp. 5, 11–13, 43, 44).
- [15] M. Gebhardt and W. Köhler. “What can be learned from optical two-color diffusion and thermodiffusion experiments on ternary fluid mixtures?” In: *J. Chem. Phys.* 142.8, 084506 (2015).  
DOI: 10.1063/1.4908538 (cit. on pp. 5, 14, 43, 49, 50, 121).
- [16] V. Shevtsova et al. “Analysis of the application of optical two-wavelength techniques to measurement of the Soret coefficients in ternary mixtures”. In: *Philos. Mag.* 91.26 (2011), pp. 3498–3518.  
DOI: 10.1080/14786435.2011.586376 (cit. on pp. 5, 14, 98).
- [17] M. Gebhardt et al. “Diffusion, thermal diffusion, and Soret coefficients and optical contrast factors of the binary mixtures of dodecane, isobutylbenzene, and 1,2,3,4-tetrahydronaphthalene”. In: *J. Chem. Phys.* 138.11, 114503 (2013).  
DOI: 10.1063/1.4795432 (cit. on pp. 5, 14, 46).
- [18] P. K. Gupta and A. R. Cooper Jr. “The [D] Matrix for Multicomponent Diffusion”. In: *Physica* 54.1 (1971), pp. 39–59.  
DOI: 10.1016/0031-8914(71)90062-0 (cit. on pp. 6, 8, 11).
- [19] T. Allie-Ebrahim et al. “Maxwell-Stefan diffusion coefficient estimation for ternary systems: an ideal ternary alcohol system”. In: *Phys. Chem. Chem. Phys.* 19.24 (2017), pp. 16071–16077.  
DOI: 10.1039/C7CP02582C (cit. on p. 6).
- [20] L. Onsager. “Reciprocal Relations in Irreversible Processes I”. In: *Phys. Rev.* 37.4 (1931), pp. 405–426.  
DOI: 10.1103/PhysRev.37.405 (cit. on p. 7).
- [21] L. Onsager. “Reciprocal Relations in Irreversible Processes II”. In: *Phys. Rev.* 38.12 (1931), pp. 2265–2279.  
DOI: 10.1103/PhysRev.38.2265 (cit. on p. 7).

- [22] D. G. Miller. "Some comments on multicomponent diffusion: negative main term diffusion coefficients, second law constraints, solvent choices, and reference frame transformations". In: *J. Phys. Chem.* 90.8 (1986), pp. 1509–1519. doi: doi:10.1021/j100399a010 (cit. on p. 8).
- [23] J. W. Mutoru and A. Firoozabadi. "Form of multicomponent Fickian diffusion coefficients matrix". In: *J. Chem. Thermodyn.* 43.8 (2011), pp. 1192–1203. doi: 10.1016/j.jct.2011.03.003 (cit. on p. 8).
- [24] J. A. Bierlein. "A Phenomenological Theory of the Soret Diffusion". In: *J. Chem. Phys.* 23.1 (1955), pp. 10–14. doi: 10.1063/1.1740504 (cit. on p. 10).
- [25] M. Giglio and A. Vendramini. "Thermal-diffusion measurements near a consolute critical point". In: *Phys. Rev. Lett.* 34.10 (1975), p. 561. doi: 10.1103/PhysRevLett.34.561 (cit. on pp. 10, 43).
- [26] A. Königer, B. Meier, and W. Köhler. "Measurement of the Soret, diffusion and thermal diffusion coefficients of three binary organic benchmark mixtures and of ethanol-water mixtures using a beam deflection technique". In: *Philos. Mag.* 89.10 (2009), pp. 907–923. doi: 10.1080/14786430902814029 (cit. on pp. 10, 43).
- [27] K. B. Haugen and A. Firoozabadi. "On the unsteady-state species separation of a binary liquid mixture in a rectangular thermogravitational column". In: *J. Chem. Phys.* 124.5, 054502 (2006). doi: 10.1063/1.2150431 (cit. on pp. 11, 12).
- [28] L. N. Trefethen and D. Bau III. *Numerical linear algebra*. Philadelphia: SIAM, 1997. ISBN: 0898713617 (cit. on pp. 14, 15, 55, 74).
- [29] V. Shevtsova et al. "IVIDIL: on-board g-jitters and diffusion controlled phenomena". In: *J. Phys: Conf. Ser.* 327.1, 012031 (2011). doi: 10.1088/1742-6596/327/1/012031 (cit. on pp. 15, 20, 75).
- [30] O. A. Khlybov, I. I. Ryzhkov, and T. P. Lyubimova. "Contribution to the benchmark for ternary mixtures: Measurement of diffusion and Soret coefficients in 1,2,3,4-tetrahydronaphthalene, isobutylbenzene, and dodecane onboard the ISS". In: *Eur. Phys. J. E* 38, 29 (2015). doi: 10.1140/epje/i2015-15029-0 (cit. on pp. 15, 87, 90, 92).
- [31] M. Gebhardt and W. Köhler. "Contribution to the benchmark for ternary mixtures: Measurement of the Soret and thermodiffusion coefficients of tetralin+isobutylbenzene+n-dodecane at a composition of (0.8 / 0.1 / 0.1) mass fractions by two-color optical beam deflection". In: *Eur. Phys. J. E* 38, 24 (2015). doi: 10.1140/epje/i2015-15024-5 (cit. on pp. 15, 44, 74–76, 87, 90, 97).

- [32] J. K. Platten. "The Soret Effect: A Review of Recent Experimental Results". In: *J. Appl. Mech.* 73.5 (2006), pp. 5–15.  
doi: 10.1115/1.1992517 (cit. on p. 16).
- [33] V. Shevtsova, D. Melnikov, and J. C. Legros. "Onset of convection in Soret-driven instability". In: *Phys. Rev. E* 73.4, 047302 (2006).  
doi: 10.1103/PhysRevE.73.047302 (cit. on pp. 16, 104).
- [34] P. Kolodner, H. Williams, and C. Moe. "Optical measurement of the Soret coefficient of ethanol / water solutions". In: *J. Chem. Phys.* 88.10 (1988), pp. 6512–6524.  
doi: 10.1063/1.454436 (cit. on pp. 16, 48).
- [35] D. T. J. Hurle and E. Jakeman. "Soret-driven thermosolutal convection". In: *J. Fluid Mech.* 47.4 (1971), pp. 667–687.  
doi: 10.1017/S0022112071001319 (cit. on p. 16).
- [36] R. Schechter, I. Prigogine, and J. Hamm. "Thermal diffusion and convective stability". In: *Phys. Fluids* 15.3 (1972), pp. 379–386.  
doi: 10.1063/1.1693920 (cit. on pp. 16, 19).
- [37] M. Velarde and R. Schechter. "Thermal diffusion and convective stability. II. An analysis of the convected fluxes". In: *Phys. Fluids* 15.10 (1972), pp. 1707–1714.  
doi: 10.1063/1.1693766 (cit. on pp. 16, 19).
- [38] M. Giglio and A. Vendramini. "Optical study of a convective instability in a binary liquid mixture heated from above". In: *Opt. Commun.* 20.3 (1977), pp. 438–440.  
doi: 10.1016/0030-4018(77)90224-3 (cit. on p. 16).
- [39] A. La Porta and C. Surko. "Convective instability in a fluid mixture heated from above". In: *Phys. Rev. Lett.* 80.17 (1998), p. 3759.  
doi: 10.1103/PhysRevLett.80.3759 (cit. on p. 16).
- [40] D. Jung and M. Lücke. "Traveling wave fronts and localized traveling wave convection in binary fluid mixtures". In: *Phys. Rev. E* 72.2, 026307 (2005).  
doi: 10.1103/PhysRevE.72.026307 (cit. on p. 16).
- [41] I. I. Ryzhkov and V. Shevtsova. "On the Cross-diffusion and Soret Effect in Multicomponent Mixtures". In: *Microgravity Sci. Technol.* 21 (2009), pp. 37–40.  
doi: 10.1007/s12217-008-9081-9 (cit. on p. 17).
- [42] I. I. Ryzhkov and V. Shevtsova. "Long-Wave instability of a multicomponent fluid layer with the Soret effect". In: *Phys. Fluids* 21, 014102 (2009).  
doi: 10.1063/1.3054154 (cit. on p. 17).
- [43] I. I. Ryzhkov and V. Shevtsova. "Convective stability of multicomponent fluids in the thermogravitational column". In: *Phys. Rev. E* 79, 026308 (2009).  
doi: 10.1103/PhysRevE.79.026308 (cit. on p. 17).

- [44] S. Wiegand. "150 Jahre Ludwig-Soret-Effekt". In: *Bunsen-Magazin* 5 (2006), pp. 130–134. ISSN: 0005–9021 (cit. on p. 19).
- [45] J. K. Platten et al. "Benchmark values for the Soret, thermal diffusion and diffusion coefficients of three binary organic liquid mixtures". In: *Philos. Mag.* 83.17-18 (2003), pp. 1965–1971.  
DOI: 10.1080/0141861031000108204 (cit. on p. 19).
- [46] P. Costesèque and J.-C. Loubet. "Measuring the Soret coefficient of binary hydrocarbon mixtures in packed thermogravitational columns (contribution of Toulouse University to the benchmark test)". In: *Philos. Mag.* 83.17-18 (2003), pp. 2017–2022.  
DOI: 10.1080/0141861031000108187 (cit. on p. 19).
- [47] M. M. Bou-Ali et al. "Determination of the thermodiffusion coefficient in three binary organic liquid mixtures by the thermogravitational method (contribution of the Universidad del Pais Vasco, Bilbao, to the benchmark test)". In: *Philos. Mag.* 83.17-18 (2003), pp. 2011–2015.  
DOI: 10.1080/0141861031000113299 (cit. on p. 19).
- [48] J. K. Platten, M. M. Bou-Ali, and J. F. Dutrieux. "Precise determination of the Soret, thermodiffusion and isothermal diffusion coefficients of binary mixtures of dodecane, isobutylbenzene and 1,2,3,4-tetrahydronaphthalene (contribution of the University of Mons to the benchmark test)". In: *Philos. Mag.* 83.17-18 (2003), pp. 2001–2010.  
DOI: 10.1080/0141861031000108196 (cit. on p. 19).
- [49] C. Leppla and S. Wiegand. "Investigation of the Soret effect in binary liquid mixtures by thermal-diffusion-forced Rayleigh scattering (contribution to the benchmark test)". In: *Philos. Mag.* 83.17-18 (2003), pp. 1989–1999.  
DOI: 10.1080/0141861031000108222 (cit. on p. 19).
- [50] G. Wittko and W. Köhler. "Precise determination of the Soret, thermal diffusion and mass diffusion coefficients of binary mixtures of dodecane, isobutylbenzene and 1,2,3,4-tetrahydronaphthalene by a holographic grating technique". In: *Philos. Mag.* 83.17-18 (2003), pp. 1973–1987.  
DOI: 10.1080/0141861031000108213 (cit. on p. 19).
- [51] D. Voss. *SCI-ESA-HSO-ESR-DCMIX3 i2r0\_version 2. DCMIX3 Experiment Scientific Requirements*. 2014 (cit. on pp. 20, 36, 105).
- [52] M. A. Rahman and M. Z. Saghir. "Thermodiffusion or Soret effect: Historical review". In: *Int. J. Heat Mass Transfer* 73 (2014), pp. 693–705.  
DOI: 10.1016/j.ijheatmasstransfer.2014.02.057 (cit. on p. 20).
- [53] V. Shevtsova et al. "The IVIDIL experiment onboard the ISS: Thermodiffusion in the presence of controlled vibrations". In: *Comptes Rendus Mécanique* 339.5 (2011), pp. 310–317.  
DOI: 10.1016/j.crme.2011.03.007 (cit. on p. 20).

- [54] S. Mazzoni et al. "Vibrating liquids in space". In: *Europhys. News* 41.6 (2010), pp. 14–16.  
doi: 10.1051/epn/2010601 (cit. on p. 20).
- [55] A. Mialdun et al. "A comprehensive study of diffusion, thermodiffusion, and Soret coefficients of water-isopropanol mixtures". In: *J. Chem. Phys.* 136.24, 244512 (2012).  
doi: 10.1063/1.4730306 (cit. on pp. 20, 43).
- [56] V. Shevtsova et al. "Dynamics of a binary mixture subjected to a temperature gradient and oscillatory forcing". In: *J. Fluid Mech.* 767 (2015), pp. 290–322.  
doi: doi:10.1017/jfm.2015.50 (cit. on pp. 20, 40).
- [57] S. Van Vaerenbergh, S. Srinivasan, and M. Z. Saghir. "Thermodiffusion in multicomponent hydrocarbon mixtures: Experimental investigations and computational analysis". In: *J. Chem. Phys.* 131.11, 114505 (2009).  
doi: 10.1063/1.3211303 (cit. on p. 21).
- [58] V. Sechenyh, J. C. Legros, and V. Shevtsova. "Measurement of Optical Properties in Binary and Ternary Mixtures Containing Cyclohexane, Toluene, and Methanol". In: *J. Chem. Eng. Data* 57 (2012), pp. 1036–1043.  
doi: 10.1021/je201277d (cit. on p. 24).
- [59] I. Nagata. "Liquid-liquid equilibria for four ternary systems containing methanol and cyclohexane". In: *Fluid Phase Equilib.* 18.1 (1984), pp. 83–92.  
doi: 10.1016/0378-3812(84)80023-0 (cit. on p. 24).
- [60] V. Shevtsova et al. "Diffusion and Soret in Ternary Mixtures. Preparation of the DCMIX2 Experiment on the ISS". In: *Microgravity Sci. Technol.* 25.5 (2014), pp. 275–283.  
doi: 10.1007/s12217-013-9349-6 (cit. on p. 24).
- [61] C. Santos et al. "Sorption equilibria and diffusion of toluene, methanol, and cyclohexane in/through elastomers". In: *J. Appl. Polym. Sci.* 133, 43449 (2016).  
doi: 10.1002/app.43449 (cit. on p. 24).
- [62] A. Mialdun and V. Shevtsova. "Temperature dependence of Soret and diffusion coefficients for toluene–cyclohexane mixture measured in convection-free environment". In: *J. Chem. Phys.* 143.22, 224902 (2015).  
doi: 10.1063/1.4936778 (cit. on p. 24).
- [63] NASA Independent Review Team. *Orb-3 Accident Investigation Report. Executive Summary*. 9, 2015. URL: [https://www.nasa.gov/sites/default/files/atoms/files/orb3\\_irt\\_execsumm\\_0.pdf](https://www.nasa.gov/sites/default/files/atoms/files/orb3_irt_execsumm_0.pdf) (visited on February 5, 2018) (cit. on p. 26).
- [64] J. Ollé et al. "Onsite vibrational characterization of DCMIX2/3 experiments". In: *Acta Astronaut.* 140 (2017), pp. 409–419.  
doi: 10.1016/j.actaastro.2017.09.007 (cit. on p. 40).



- [65] F. Croccolo et al. "Shadowgraph Analysis of Non-equilibrium Fluctuations for Measuring Transport Properties in Microgravity in the GRADFLEX Experiment". In: *Microgravity Sci. Technol.* 28.4 (2016), pp. 467–475.  
doi: 10.1007/s12217-016-9501-1 (cit. on p. 40).
- [66] P. Baaske et al. "The NEUF-DIX space project - Non-EquilibriUm Fluctuations during Diffusion in compleX liquids". In: *Eur. Phys. J. E* 39, 119 (2016).  
doi: 10.1140/epje/i2016-16119-1 (cit. on p. 40).
- [67] H. Bataller et al. "Dynamic analysis of the light scattered by the non-equilibrium fluctuations of a ternary mixture of polystyrene-toluene-n-hexane". In: *Eur. Phys. J. E* 40, 35 (2017).  
doi: 10.1140/epje/i2017-11522-8 (cit. on pp. 40, 161).
- [68] Y. He and Y. Li. "Fullerene derivative acceptors for high performance polymer solar cells". In: *Phys. Chem. Chem. Phys.* 13.6 (2011), pp. 1970–1983.  
doi: 10.1039/c0cp01178a (cit. on p. 41).
- [69] W. Yu and H. Xie. "A Review on Nanofluids: Preparation, Stability Mechanisms, and Applications". In: *J. Nanomaterials* 2012, 2070291 (2012).  
doi: 10.1155/2012/435873 (cit. on p. 41).
- [70] B. Meier. "Aufbau einer "Beam Deflection"-Apparatur zur Messung von Transportkoeffizienten in Flüssigkeiten". Diploma thesis. Universität Bayreuth, 2007 (cit. on p. 43).
- [71] A. Königer. "Optische Untersuchung diffusiver Transportvorgänge in mehrkomponentigen Fluiden". PhD thesis. Universität Bayreuth, 2012.  
URN: urn:nbn:de:bvb:703-opus4-10140 (cit. on p. 43).
- [72] M. Giglio and A. Vendramini. "Optical Measurements of Gravitationally Induced Concentration Gradients near a Liquid-Liquid Critical Point". In: *Phys. Rev. Lett.* 35.3 (1975), p. 168.  
doi: 10.1103/PhysRevLett.35.168 (cit. on p. 43).
- [73] M. Giglio and A. Vendramini. "Soret-type motion of macromolecules in solution". In: *Phys. Rev. Lett.* 38.1 (1977), p. 26.  
doi: 10.1103/PhysRevLett.38.26 (cit. on p. 43).
- [74] R. Piazza and A. Guarino. "Soret effect in interacting micellar solutions." In: *Phys. Rev. Lett.* 88.20, 208302 (2002).  
doi: 10.1103/PhysRevLett.88.208302 (cit. on p. 43).
- [75] R. Piazza. "Thermal diffusion in ionic micellar solutions". In: *Philos. Mag.* 83.17-18 (2003), pp. 2067–2085.  
doi: 10.1080/0141861031000107971 (cit. on p. 43).
- [76] A. Königer. "Bestimmung der Transportkoeffizienten binärer Mischungen mittels einer optimierten Beamdeflection-Apparatur". Diploma thesis. Universität Bayreuth, 2008 (cit. on p. 43).

- [77] E. Lapeira et al. "Transport properties of the binary mixtures of the three organic liquids toluene, methanol, and cyclohexane". In: *J. Chem. Phys.* 146.9, 094507 (2017).  
doi: 10.1063/1.4977078 (cit. on pp. 43, 161).
- [78] A. Königer, H. Wunderlich, and W. Köhler. "Measurement of diffusion and thermal diffusion in ternary fluid mixtures using a two-color optical beam deflection technique". In: *J. Chem. Phys.* 132, 174506 (2010).  
doi: 10.1063/1.3421547 (cit. on pp. 44, 74).
- [79] M. Gebhardt and W. Köhler. "Soret, thermodiffusion, and mean diffusion coefficients of the ternary mixture n-dodecane+isobutylbenzene+1,2,3,4-tetrahydronaphthalene". In: *J. Chem. Phys.* 143.16, 164511 (2015).  
doi: 10.1063/1.4934718 (cit. on pp. 44, 73, 74, 88, 93).
- [80] M. M. Bou-Ali et al. "Benchmark values for the Soret, thermodiffusion and molecular diffusion coefficients of the ternary mixture tetralin+isobutylbenzene+n-dodecane with 0.8-0.1-0.1 mass fraction". In: *Eur. Phys. J. E* 38, 30 (2015).  
doi: 10.1140/epje/i2015-15030-7 (cit. on pp. 44, 87, 94).
- [81] K. J. Zhang et al. "Optical measurement of the Soret coefficient and the diffusion coefficient of liquid mixtures". In: *J. Chem. Phys.* 104 (1996), p. 6881.  
doi: 10.1063/1.471355 (cit. on p. 47).
- [82] M. Larrañaga et al. "Contribution to the benchmark for ternary mixtures: Determination of Soret coefficients by the thermogravitational and the sliding symmetric tubes techniques". In: *Eur. Phys. J. E* 38, 28 (2015).  
doi: 10.1140/epje/i2015-15028-1 (cit. on pp. 52, 87).
- [83] J. C. Legros et al. "Investigation of Fickian diffusion in the ternary mixtures of water-ethanol-triethylene glycol and its binary pairs". In: *Phys. Chem. Chem. Phys.* 17 (2015), pp. 27713–27725.  
doi: 10.1039/C5CP04745E (cit. on pp. 52, 115, 121, 161).
- [84] X. Gong, T. Ngai, and C. Wu. "A portable, stable and precise laser differential refractometer". In: *Rev. Sci. Instrum.* 84.11, 114103 (2013).  
doi: 10.1063/1.4828350 (cit. on p. 53).
- [85] A. Becker, W. Köhler, and B. Müller. "A Scanning Michelson Interferometer for the Measurement of the Concentration and Temperature Derivative of the Refractive Index of Liquids". In: *Ber. Bunsenges. Phys. Chem.* 99.4 (1995), pp. 600–608.  
doi: 10.1002/bbpc.19950990403 (cit. on p. 53).
- [86] W. B. Li et al. "Determination of the Temperature and Concentration-dependence of the Refractive-index of A Liquid-mixture". In: *J. Chem. Phys.* 101.6 (1994), pp. 5058–5069.  
doi: 10.1063/1.467428 (cit. on p. 53).

- [87] QinetiQ Space nv. *SODI-RP-LX-09\_C0. Phase CD optical design report*. Tech. rep. 2009 (cit. on pp. 55, 62).
- [88] QinetiQ Space nv. *SODI-RP-006-VE\_D1\_SODI Design Report2. SODI design report*. Tech. rep. 2009 (cit. on pp. 55, 75).
- [89] QinetiQ Space nv. *SODI-MAN-372-VE\_B1. SODI Software User Manual*. 2010 (cit. on pp. 55, 65, 66).
- [90] D. Malacara, M. Servín, and Z. Malacara. *Interferogram Analysis for Optical Testing*. New York: Marcel Dekker, 1998.  
ISBN: 0824799402 (cit. on pp. 60, 61).
- [91] P. Hariharan. *Optical interferometry*. 2nd ed. Amsterdam and Boston: Academic Press, 2003.  
ISBN: 0123116309 (cit. on pp. 60, 61).
- [92] D. W. Robinson and G. T. Reid, eds. *Interferogram Analysis. Digital Fringe Pattern Measurement Techniques*. Bristol and Philadelphia: IOP Publishing, 1993.  
ISBN: 075030197X (cit. on p. 60).
- [93] M. Servín, J. A. Quiroga, and M. Padilla. *Fringe Pattern Analysis for Optical Metrology. Theory, Algorithms, and Applications*. Weinheim: Wiley-VCH, 2014.  
ISBN: 9783527411528 (cit. on pp. 60, 62, 81, 82).
- [94] T. Kreis. *Handbook of Holographic Interferometry*. Weinheim: Wiley-VCH, 2005.  
ISBN: 3527405461 (cit. on p. 60).
- [95] J. E. Greivenkamp. “Generalized data reduction for heterodyne interferometry”. In: *Opt. Eng.* 23.4, 234350 (1984).  
DOI: 10.1117/12.7973298 (cit. on p. 60).
- [96] Y. Ishii. “Recent developments in laser-diode interferometry”. In: *Opt. Lasers Eng.* 14.4-5 (1991), pp. 293–309.  
DOI: 10.1016/0143-8166(91)90054-W (cit. on p. 61).
- [97] P. Hariharan. “Phase-stepping interferometry with laser diodes: effect of changes in laser power with output wavelength”. In: *Appl. Opt.* 28.1 (1989), pp. 27–29.  
DOI: 10.1364/AO.28.000027 (cit. on p. 61).
- [98] M. Takeda, H. Ina, and S. Kobayashi. “Fourier-transform method of fringe-pattern analysis for computer-based topography and interferometry”. In: *J. Opt. Soc. Am.* 72.1 (1982), pp. 156–160.  
DOI: 10.1364/JOSA.72.000156 (cit. on p. 63).
- [99] D. C. Ghiglia and M. D. Pritt. *Two-dimensional Phase Unwrapping. Theory, Algorithms, and Software*. New York: Wiley, 1998.  
ISBN: 0471249351 (cit. on p. 63).

- [100] K. Itoh. "Analysis of the phase unwrapping algorithm". In: *Appl. Opt.* 21.14 (1982), pp. 2470–2470.  
doi: 10.1364/AO.21.002470 (cit. on pp. 63, 64).
- [101] A. Mialdun and V. Shevtsova. "Development of optical digital interferometry technique for measurement of thermodiffusion coefficients". In: *Int. J. Heat Mass Transfer* 51.11–12 (2008), pp. 3164–3178.  
doi: 10.1016/j.ijheatmasstransfer.2007.08.020 (cit. on p. 67).
- [102] A. Mialdun and V. Shevtsova. "Open questions on reliable measurements of Soret coefficients". In: *Microgravity Sci. Technol.* 21.1-2 (2009), pp. 31–36.  
doi: 10.1007/s12217-008-9088-2 (cit. on p. 67).
- [103] A. Mialdun et al. "Analysis of the Thermal Performance of SODI Instrument for DCMIX Configuration". In: *Microgravity Sci. Technol.* 25.1 (2013), pp. 83–94.  
doi: 10.1007/s12217-012-9337-2 (cit. on p. 67).
- [104] V. Sechenyh, J. C. Legros, and V. Shevtsova. "Optical properties of binary and ternary liquid mixtures containing tetralin, isobutylbenzene and dodecane". In: *J. Chem. Thermodyn.* 62 (2013), pp. 64–68.  
doi: 10.1016/j.jct.2013.01.026 (cit. on pp. 73–76, 87, 97).
- [105] M. Larrañaga et al. "Soret coefficients of the ternary mixture 1, 2, 3, 4-tetrahydronaphthalene + isobutylbenzene + n-dodecane". In: *J. Chem. Phys.* 143.2, 024202 (2015).  
doi: 10.1063/1.4926654 (cit. on pp. 74, 75, 88, 93).
- [106] S. Mazzoni et al. "SODI-COLLOID: A combination of static and dynamic light scattering on board the International Space Station". In: *Rev. Sci. Instrum.* 84.4, 043704 (2013).  
doi: 10.1063/1.4801852 (cit. on p. 75).
- [107] P. Carré. "Installation et utilisation du comparateur photoélectrique et interférentiel du Bureau International des Poids et Mesures". In: *Metrologia* 2.1 (1966), p. 13.  
doi: 10.1088/0026-1394/2/1/005 (cit. on p. 81).
- [108] A. Ahadi and M. Z. Saghir. "Contribution to the benchmark for ternary mixtures: Transient analysis in microgravity conditions". In: *Eur. Phys. J. E* 38, 25 (2015).  
doi: 10.1140/epje/i2015-15025-4 (cit. on p. 87).
- [109] Q. Galand and S. Van Vaerenbergh. "Contribution to the benchmark for ternary mixtures: Measurement of diffusion and Soret coefficients of ternary system tetrahydronaphthalene-isobutylbenzene-n-dodecane with mass fractions 80-10-10 at 25 °C". In: *Eur. Phys. J. E* 38, 26 (2015).  
doi: 10.1140/epje/i2015-15026-3 (cit. on p. 87).

- [110] A. Mialdun et al. "Contribution to the benchmark for ternary mixtures: Measurement of the Soret, diffusion and thermodiffusion coefficients in the ternary mixture THN/IBB/nC12 with 0.8/0.1/0.1 mass fractions in ground and orbital laboratories". In: *Eur. Phys. J. E* 38, 27 (2015).  
doi: 10.1140/epje/i2015-15027-2 (cit. on pp. 87, 92).
- [111] A. Mialdun et al. "Investigation of Fickian diffusion in the ternary mixture of 1,2,3,4-tetrahydronaphthalene, isobutylbenzene, and dodecane". In: *J. Chem. Phys.* 139.10, 104903 (2013).  
doi: 10.1063/1.4820357 (cit. on pp. 87, 115).
- [112] A. Ahadi and M. Z. Saghir. "The microgravity DSC-DCMIX1 mission on-board ISS: Experiment description and results on the measurement of the Soret coefficients for isobutylbenzene, dodecane, tetralin ternary hydrocarbons mixtures". In: *Exp. Therm Fluid Sci.* 74 (2016), pp. 296–307.  
doi: 10.1016/j.expthermflusci.2015.12.020 (cit. on pp. 87, 88, 94, 95).
- [113] T. Triller et al. "Thermodiffusion in Ternary Mixtures of Water/Ethanol/Triethylene Glycol: First Report on the DCMIX3-Experiments Performed on the International Space Station". In: *Microgravity Sci. Technol.* (2018).  
doi: 10.1007/s12217-018-9598-5 (cit. on pp. 96, 108, 111–113, 161).
- [114] V. Sechenyh, J. C. Legros, and V. Shevtsova. "Experimental and predicted refractive index properties in ternary mixtures of associated liquids". In: *J. Chem. Thermodyn.* 43 (2011), pp. 1700–1707.  
doi: 10.1016/j.jct.2011.05.034 (cit. on pp. 96–99).
- [115] S. van der Walt, S. C. Colbert, and G. Varoquaux. "The NumPy Array: A Structure for Efficient Numerical Computation". In: *Comput. Sci. Eng.* 13.2 (2011), pp. 22–30.  
doi: 10.1109/MCSE.2011.37 (cit. on p. 147).
- [116] J. D. Hunter. "Matplotlib: A 2D graphics environment". In: *Comput. Sci. Eng.* 9.3 (2007), pp. 90–95.  
doi: 10.1109/MCSE.2007.55 (cit. on p. 147).
- [117] W. McKinney. "Data Structures for Statistical Computing in Python". In: *Proceedings of the 9th Python in Science Conference*. Ed. by S. van der Walt and J. Millman. 2010, pp. 51–56 (cit. on p. 147).
- [118] M. Harper et al. *python-ternary: Ternary Plots in Python*. 2015.  
doi: 10.5281/zenodo.34938 (cit. on p. 147).
- [119] O. Tange. "GNU Parallel - The Command-Line Power Tool". In: *login: The USENIX Magazine* 36.1 (2011), pp. 42–47.  
doi: 10.5281/zenodo.16303 (cit. on p. 147).

- [120] T. Kluyver et al. “Jupyter Notebooks – a publishing format for reproducible computational workflows”. In: *Positioning and Power in Academic Publishing: Players, Agents and Agendas*. Ed. by F. Loizides and B. Schmidt. IOS Press. 2016, pp. 87–90.  
doi: 10.3233/978-1-61499-649-1-87 (cit. on p. 147).
- [121] S. Seabold and J. Perktold. “Statsmodels: Econometric and statistical modeling with python”. In: *Proceedings of the 9th Python in Science Conference*. Ed. by S. van der Walt and J. Millman. 2010, pp. 57–61 (cit. on p. 147).

# List of Publications & Funding

The following is a list of all publications authored or co-authored in the course of this work:

T. Triller et al. "Thermodiffusion in Ternary Mixtures of Water/Ethanol/Triethylene Glycol: First Report on the DCMIX3-Experiments Performed on the International Space Station". In: *Microgravity Sci. Technol.* (2018).

DOI: 10.1007/s12217-018-9598-5

H. Bataller et al. "Dynamic analysis of the light scattered by the non-equilibrium fluctuations of a ternary mixture of polystyrene-toluene-n-hexane". In: *Eur. Phys. J. E* 40, 35 (2017).

DOI: 10.1140/epje/i2017-11522-8

E. Lapeira et al. "Transport properties of the binary mixtures of the three organic liquids toluene, methanol, and cyclohexane". In: *J. Chem. Phys.* 146.9, 094507 (2017).

DOI: 10.1063/1.4977078

J. C. Legros et al. "Investigation of Fickian diffusion in the ternary mixtures of water-ethanol-triethylene glycol and its binary pairs". In: *Phys. Chem. Chem. Phys.* 17 (2015), pp. 27713–27725.

DOI: 10.1039/C5CP04745E

This work has been developed in the framework of the cooperative project DCMIX (No. AO-2009-0858/1056) of the European Space Agency and the Russian Space Agency (Roscosmos)/TsNIIMash. Operations in Bayreuth were supported by the *Deutsches Zentrum für Luft- und Raumfahrt*, grants 50WM1130 and 50WM1544.

The author was awarded the Zeldovich Medal 2016 (Section G — Material Sciences in Space), conferred by the Russian Academy of Sciences and COSPAR, for the preparations of DCMIX3 experiments performed during this work<sup>1</sup>.

<sup>1</sup><https://cosparhq.cnes.fr/awards/zeldovich>





# List of Acronyms

- CRS** *Commercial Resupply Services*: NASA program to provide transportation to ISS via commercial operators
- DCMIX** *Diffusion and thermodiffusion Coefficients Measurements in ternary mIXtures*: international collaboration under ESA auspices to further understanding of ternary mixtures
- ESR** *Experiment Scientific Requirements*: document formulating the scientific requirements for the SODI-DCMIX measurements as agreed with ESA
- E-USOC** *Spanish User Support and Operations Centre*: provided support to scientists during DCMIX2/DCMIX3 operations on behalf of ESA, located in Madrid
- FR** *Fixed Red*: fixed 670 nm laser for probing binary samples in SODI
- MARS** *Microgravity Advanced Research and Support Center*: provided support to scientists during DCMIX1 operations on behalf of ESA, located in Naples
- MN** *Moving Near-infrared*: moveable 935 nm laser for probing ternary samples in SODI
- MR** *Moving Red*: moveable 670 nm laser for probing ternary samples in SODI
- MSG** *Microgravity Science Glovebox*: experiment facility on ISS, located in Destiny module
- OBD** *Optical Beam Deflection*: optical measurement technique used on ground (Bayreuth)
- ODI** *Optical Digital Interferometry*: Mach-Zehnder interferometer used on ground (Brussels)
- PSI** *Phase-Shifting/Phase-Stepping Interferometry*: optical measurement technique used in SODI and ODI
- SODI** *Selectable Optical Diagnostics Instrument*: Mach-Zehnder interferometer on ISS, can be operated inside MSG
- STK** *Stack file*: special file format used to store SODI data

**TDFRS** *Thermal Diffusion Forced Rayleigh Scattering*: optical technique used on ground (Bayreuth)

**TGC** *Thermo-Gravitational Column*: convective coupling measurement technique used on ground (Mondragon)

To better differentiate between measurements performed on ground and on ISS during the DCMIX campaigns, data gathered with SODI will sometimes be referred to as SODI-DCMIX.

# List of Figures

2.1	Diffusive effects in binary and ternary systems . . . . .	7
2.2	Principle of Soret cell experiments . . . . .	10
2.3	Analytical solution of the diffusion equation in a Soret cell . . . . .	13
2.4	General error propagation due to contrast factor inversion . . . . .	14
2.5	Examples of instabilities in ternary mixtures . . . . .	17
3.1	DCMIX molecules . . . . .	22
3.2	Bubble in DCMIX1 cell 1 . . . . .	23
3.3	Failure of Anatres rocket carrying DCMIX3a . . . . .	27
3.4	Recovered DCMIX3a hardware . . . . .	27
3.5	Degassing setup . . . . .	30
3.6	Flash frozen sample . . . . .	31
3.7	Sample during thawing . . . . .	31
3.8	Syringe filling setup . . . . .	32
3.9	Filled syringes with DCMIX3b samples . . . . .	33
3.10	SODI cell filling setup . . . . .	34
3.11	Microgravity Science Glovebox with SODI . . . . .	35
3.12	Start SpaceX CRS-9 with DCMIX3b . . . . .	35
3.13	Astronaut Kathleen Rubins during SODI setup . . . . .	36
3.14	Checkout DCMIX3b cells 1 and 2 . . . . .	37
3.15	Checkout DCMIX3b cells 3 and 4 . . . . .	37
3.16	Checkout DCMIX3b cells 5 and 6 . . . . .	37
3.17	Bubble growth DCMIX3b cell 3 . . . . .	39
3.18	TRek software . . . . .	39
4.1	OBD principle . . . . .	44
4.2	Schematics of 2-color OBD setup . . . . .	45
4.3	Schematics of OBD sample cell . . . . .	46
4.4	Typical OBD signal . . . . .	47
4.5	Hypothetical TDFRS signal . . . . .	50
4.6	Interferometric setup for measuring $(\partial n / \partial T)_{p, c_i}$ . . . . .	54
4.7	Schematics of SODI . . . . .	56
4.8	Schematics of SODI sample cells . . . . .	57
4.9	Complete DCMIX3b cell array . . . . .	58
4.10	Typical interferogram taken with SODI . . . . .	59
4.11	Phase error due to laser output changes . . . . .	62
4.12	Four-quadrant arctangent function . . . . .	64

4.13	General layout of a STK file . . . . .	66
4.14	Processing of SODI interferograms via temporal phase-shifting . . .	68
4.15	Unwrapped phase gradient in SODI . . . . .	69
4.16	Transient phase gradient in SODI . . . . .	70
4.17	Determination of $t_{0,\text{eff}}$ for fitting . . . . .	71
5.1	Condition numbers DCMIX1 for OBD and SODI wavelengths . . . .	76
5.2	Phase stepping in DCMIX1 cell 5 . . . . .	78
5.3	Black and white saturation DCMIX1 . . . . .	81
5.4	Histograms from run 05 and run27b DCMIX1 . . . . .	81
5.5	Michelson contrast DCMIX1 . . . . .	82
5.6	Grayscale variance and mean DCMIX1 . . . . .	83
5.7	Estimated phase step DCMIX1 . . . . .	84
5.8	Temperature fluctuations cell 5 DCMIX1 . . . . .	85
5.9	Soret coefficients cell 1 DCMIX1 . . . . .	88
5.10	Soret coefficients cell 2 DCMIX1 . . . . .	89
5.11	Soret coefficients cell 3 DCMIX1 . . . . .	89
5.12	Soret coefficients cell 4 DCMIX1 . . . . .	90
5.13	Soret coefficients cell 5 DCMIX1 . . . . .	91
5.14	Compositions for refractive index parametrization DCMIX3 . . . .	97
5.15	Condition numbers DCMIX3 for OBD and SODI wavelengths . . . .	98
5.16	Measured OBD signals DCMIX3, cell 1 . . . . .	101
5.17	Measured OBD signals DCMIX3, cell 2 . . . . .	102
5.18	Measured OBD signals DCMIX3, cell 3, 25 °C . . . . .	102
5.19	Measured OBD signals DCMIX3, cell 3, 30 °C . . . . .	103
5.20	Measured OBD signals DCMIX3, cell 4 . . . . .	103
5.21	Measured OBD signals DCMIX3, cell 5 . . . . .	104
5.22	Comparison of stable OBD signals DCMIX3 . . . . .	104
5.23	Black and white saturation DCMIX3 . . . . .	107
5.24	Michelson contrast DCMIX3 . . . . .	108
5.25	Grayscale variance and mean DCMIX3 . . . . .	109
5.26	Estimated phase step DCMIX3 . . . . .	111
5.27	Temperature fluctuations on Peltier 9, run 04, DCMIX3 . . . . .	112
5.28	Comparison of SODI signals, DCMIX3 . . . . .	114
5.29	Soret coefficients cell 1 DCMIX3 . . . . .	116
5.30	Soret coefficients cell 2 DCMIX3 . . . . .	117
5.31	Soret coefficients cell 3 DCMIX3 . . . . .	118
5.32	Soret coefficients cell 4 DCMIX3 . . . . .	119
5.33	Soret coefficients cell 5 DCMIX3 . . . . .	120

# List of Tables

3.1	Compositions DCMIX1 . . . . .	23
3.2	Compositions DCMIX2 . . . . .	24
3.3	Compositions DCMIX3 . . . . .	25
3.4	Weighed out liquid masses and compositions DCMIX3b . . . . .	29
3.5	Compositions DCMIX4 . . . . .	41
5.1	Contrast factors DCMIX1 . . . . .	75
5.2	Table of all runs, DCMIX1 . . . . .	79
5.3	Temperature regulation DCMIX1 . . . . .	86
5.4	DCMIX1 literature data from ground measurements . . . . .	93
5.5	SODI-DCMIX1 microgravity results . . . . .	94
5.6	Solutal contrast factors DCMIX3 . . . . .	99
5.7	Thermal contrast factors DCMIX3 . . . . .	100
5.8	Table of all runs, DCMIX3 . . . . .	106
5.9	Temperature regulation DCMIX3 . . . . .	113
5.10	Reference values from TGC measurements, DCMIX3 . . . . .	121
5.11	Averaged coefficients for OBD, DCMIX3 . . . . .	121
A.1	Refractive indices of DCMIX3b samples . . . . .	127
A.2	Densities of DCMIX3b samples . . . . .	127
A.3	Measured refractive index data for DCMIX 3 parametrization . . .	128
A.3	Measured refractive index data for DCMIX 3 parametrization . . .	129
A.4	Measured $\partial n / \partial T$ data at 405 nm for DCMIX3 . . . . .	130
A.5	Measured $\partial n / \partial T$ data at 633 nm for DCMIX3 . . . . .	131
A.6	Measured density data 10 °C to 35 °C for DCMIX 3 . . . . .	132
A.6	Measured density data 10 °C to 35 °C for DCMIX 3 . . . . .	133
A.6	Measured density data 10 °C to 35 °C for DCMIX 3 . . . . .	134
A.7	Measured density data 40 °C to 60 °C for DCMIX 3 . . . . .	135
A.7	Measured density data 40 °C to 60 °C for DCMIX 3 . . . . .	136
A.7	Measured density data 40 °C to 60 °C for DCMIX 3 . . . . .	137
B.1	SODI fit coefficients DCMIX1 . . . . .	139
B.2	SODI fit coefficients DCMIX3 . . . . .	140
B.3	OBD fit coefficients DCMIX3 . . . . .	141
C.1	Matrices for refractive index parametrization, 405 nm . . . . .	144
C.2	Matrices for refractive index parametrization, 633 nm . . . . .	145



# Acknowledgments

Zum Abschluss möchte ich allen danken, die mir auf meinem Weg zur Promotion geholfen haben, Zeit zum Diskutieren hatten oder sich einfach nur meine Klagen angehört haben.

Werner Köhler danke ich, dass er mir als mein Doktorvater die Gelegenheit für diese Arbeit gegeben hat. Auch wenn der Weg mit vielen Unsicherheiten und ein oder zwei Explosionen gespickt war, so bin ich trotzdem froh, dass Werner mir 2012 das Angebot gemacht hat in seiner Arbeitsgruppe zu promovieren und ich es angenommen habe. Über die Jahre konnte ich darauf vertrauen bei ihm ein offenes Ohr zu finden und hatte stets die Sicherheit, dass es auch nach den größten Rückschlägen einen Weg nach vorn gibt.

Mein Dank gilt auch Matthias Weiß, der sich bereit erklärt hat das Zweitgutachten für diese Arbeit zu verfassen, trotz vollem Terminkalender.

Als ich noch blauäugig mit dieser Arbeit anfang, wurde ich schnell von den alt-ingesessenen Doktoranden über die noch bevorstehenden Hürden auf dem Weg zum Dokortitel aufgeklärt. Zwar konnten Florian Schwaiger, Daniel Schmidt und Matthias Gebhardt mich nicht davon abhalten zu promovieren, aber dafür standen sie mir stets mit Rat zur Seite. Egal ob es um Fragen zu Python, R, Beam Deflection oder auch vollkommen Uni-fremde Dinge ging, bei einer Tasse Kaffee (manchmal auch auf dem Dach vor Daniels Büro) konnte man mit ihnen über Gott und die Welt reden, wofür ich mich bedanken möchte. Gerne habe ich auch Matthias als (inoffizieller) IT-Helfer bei seiner Aufgabe unterstützt, die Rechner der Arbeitsgruppe vor alten OpenSUSE-Versionen und gewieften Hackern zu schützen. Glücklicherweise wurde nach seiner Promotion die IT der Arbeitsgruppe auf Selbstverwaltung umgestellt, so dass nachfolgenden Generationen diese Bürde erspart wurde.

Bastian Pur danke ich dafür, dass er mich die letzten Jahre als Büronachbarn ertragen hat und mir ein guter Freund ist. Ich könnte mir nicht vorstellen, wie ich ohne seine Gesellschaft den täglichen Uni-Wahnsinn ausgehalten und mit wem ich dann die wichtigen Fragen des Lebens diskutiert hätte: Soll man den roten Schalter umlegen? Was ist besser: ISA-Bus oder RS232? Woher kommt das Seil? Was macht der Bär hinter der Wand? Gibt es einen neuen Trailer zu Deadpool 2? Soll ich promovieren? Ohne die täglichen Geschichten zu nervigen Zugfahrten, nervigen Menschen, nerviger Promotion und was uns sonst so eingefallen ist, wären die letzten Jahre sehr trist gewesen. Ich hoffe Dein nächster Büronachbar weiß Deinen Humor (und "El Diffusio") so zu schätzen wie ich. Ebenso danke ich Marcel, der das "Glück" hatte mich am Mehrfarbeninterferometer zu beerben und (trotz meiner Warnungen) bald Teil unserer täglichen Doktoranden-Selbsthilfe-

Sitzungen im Büro wurde. Auch allen anderen Mitgliedern der Arbeitsgruppe und des (ehemaligen) Lehrstuhls EPIV möchte ich für die letzten Jahre und so manchen lustigen Moment danken.

Since this work gave me the special opportunity to work with a lot of endearing people from different countries, I also want to give my thanks to everyone from the DCMIX team. Through the recurring meetings and conferences, I learned to value cooperation and the chance to share results with other people. Here, my special thanks goes to Aliaksandr Mialdun. The analysis in this work benefitted a lot from his ideas and our discussions during conferences and I cannot overstate how lucky I feel to have had the chance to work with him. I thank Valentina Shevtsova for her dedication and expertise in all things microgravity; she enables the DCMIX project and, by extension, enabled this thesis. Also, I thank Mounir Bou-Ali and his team. Working and sharing time with them was a great experience, especially at conferences, no matter if during scientific sessions or when we just strolled around the city together in the evenings.

My special thanks goes to Ana Laveron and her team at E-USOC for their excellent support during DCMIX3 operations. Their hard work and dedication ensured that the science team (and myself) received good data and enabled the results in this work.

I want to thank the team from QinetiQ Space, especially Marc Dielissen, Ingmar Lafaille and Johan Buytaert, for their hospitality during my visits to Kruike and for their help making DCMIX3 a success.

Meinen Eltern möchte ich danken, dass sie mir mit ihrer Unterstützung und Geduld diesen Weg erst ermöglicht haben. Sie haben mir vermittelt, wie wertvoll es ist seine Interessen auch zum Beruf zu machen.

Zum Schluss möchte ich der wichtigsten Person von allen danken: meiner Theresa. Deine Liebe, Geduld und Verständnis waren das wichtigste in den langen Jahren der Promotion. Du hast meine Marotten ertragen, Dir mein Genörgel angehört und mir auch manchmal den Kopf wieder gerade gerückt. Und auch wenn ich oft gezweifelt habe, so hast Du mich immer wieder aufgebaut und mir Kraft gegeben. Ich liebe Dich.



# Eidesstattliche Versicherung

Hiermit versichere ich an Eides statt, dass ich die vorliegende Arbeit selbstständig verfasst und keine anderen als die von mir angegebenen Quellen und Hilfsmittel verwendet habe.

Weiterhin erkläre ich, dass ich die Hilfe von gewerblichen Promotionsberatern bzw. -vermittlern oder ähnlichen Dienstleistern weder bisher in Anspruch genommen habe, noch künftig in Anspruch nehmen werde.

Zusätzlich erkläre ich hiermit, dass ich keinerlei frühere Promotionsversuche unternommen habe.

Bayreuth, den

Unterschrift

